UNIVERSIDAD DE CANTABRIA

DEPARTAMENTO DE CIENCIAS Y TÉCNICAS

DEL AGUA Y DEL MEDIO AMBIENTE

TESIS DOCTORAL

ESTUDIO DE LA DINÁMICA OCEÁNICA SUPERFICIAL EN EL GOLFO DE BIZKAIA UTILIZANDO LA TECNOLOGÍA RADAR HF

Presentada por: LOHITZUNE SOLABARRIETA ODRIOZOLA

Dirigida por: ANNA RUBIO COMPAÑY
SONIA CASTANEDO BÁRCENA
RAÚL MEDINA SANTAMARÍA

Mayo 2015

Auritz, Eñaut eta Unairi

AGRADECIMIENTOS

Después de más de 4 años, un Proyecto increíble y muchísimas vivencias personales y profesionales, ha llegado el momento de agradecer vuestro esfuerzo a todos los que habéis hecho posible que esta Tesis haya llegado a buen puerto.

Me gustaría dar las gracias a la Fundación Centros Tecnológicos Iñaki Goenaga por haberme concedido una beca de doctorado para llevar a cabo esta Tesis. A AZTI, por haberme dado la oportunidad de llevarla a cabo en sus instalaciones y en colaboración con todo su personal. A la Universidad de Cantabria, por aceptar esta tesis dentro de su programa de doctorado. Y al Departamento de Atención y Emergencias del País Vasco (DAEM) y Euskalmet por haberme permitido usar los datos Radar HF durante la Tesis. Valentín, Javi y Jesús ¡eskerrikasko por vuestra paciencia!

A mis tres co-directores: Anna, gracias por haber hecho de mi tesis un proyecto increíblemente bonito. Las dos sabemos que esto no hubiera sido así de no ser por el entusiasmo que transmites en cada cosa que haces. Ha habido momentos buenos, no tan buenos e incluso duros. Pero siempre has estado ahí, siendo directora, amiga, compañera... Has sido la directora con la que cualquier doctorando sueña y espero haberte devuelto al menos algo de todo lo que tú me has dado; eskerrikasko. Raúl y Sonia, sabéis que habéis sido parte fundamental de mi tesis desde el primer momento. Gracias por aportar ese orden y claridad para encauzar el trabajo y no dejarme perder por el camino. Gracias también por animarme y ayudarme en cada cosa que os he pedido, siempre de una forma muy humana.

Jeff and Mike thank you for accepting me in NPS. I learned a lot about HF Radar technology and scientific career in Monterey. I also learned a lot about you and your way of life; you offered me and my family everything we needed to make our stay in the USA a wonderful experience. Thank you!

También me gustaría agradecer a todos los compañeros de AZTI, que habéis estado ahí cuando os he necesitado. Entre todos hacéis un buen equipo.

Este camino no habría sido igual sin vosotros, el resto de becarios o más bien, compañeros y amigos. Podría escribir varias páginas sobre vosotros, pero aun así no podría agradeceros todo el apoyo que he recibido por vuestra parte a lo largo de todos estos años: Nerea, Katerin, Nagore C., Iñaki, Aizkorri, Nagore Z, Jon, Carlos, Eva, Oihane M., Jorge, Natalia, Irati, Ganix, Nadia, María, Oihane E., Bea, Fuensanta; Eskerrikasko eta animo zuen bidean!!!

Ama eta aitai umetatik emondako guztiatxik; ania eta Leirei, falta eiztanin hortxe eotearren. Eskerrikasko! Enitxake nazena ixango zeuek baik.

Goiko etxekoei: esker mila denbora guzti honetan behar izan dudan laguntza emateagatik!

Unai, eskerrikasko proiektu honetan sartzera animatzeagatik eta egunero egunero, zure maitasuna eta pazientzia eskeintzeagatik. Milesker bikote izateaz gain, maitale, lagun eta konfidente izateagatik.

Eta azkenik, Auritz eta Eñaut: zuek biok izan zarete denbora guzti honetan ilusioz eta gogoz jarraitzearen arrazoi nagusia; energia eta denbora ugari eskatu arren, egunero ematen didazuen maitasuna gehiago baita. Matxe Zatxuet!

Índice

CAPÍTULO I: INTRODUCCIÓN

1.1. INTRODUCCIÓN

1.1.1. Marco de la Tesis

Esta tesis se ha realizado en la Fundación AZTI-Tecnalia en colaboración con la Universidad de Cantabria, dentro del programa de doctorado "Ciencias y tecnologías para la gestión de la costa". La tesis ha sido codirigida por la Doctora Anna Rubio Compañy (AZTI), el Catedrático Raúl Medina y la Profesora Titular Sonia Castanedo Bárcena (ambos de la Universidad de Cantabria).

El objetivo principal de esta tesis, es el estudio de las corrientes superficiales oceánicas en el Golfo de Bizkaia, utilizando datos de Radar de Alta Frecuencia (Radar HF, de sus siglas en inglés). El trabajo ha sido financiado por la Fundación de Centros Tecnológicos Iñaki Goenaga, con la beca "Corrientes superficiales en el Golfo de Bizkaia, con datos Radar HF".

1.1.2. Oportunidad de la Tesis

El sistema radar HF CODAR (Coastal Ocean Dynamics Application Radar), está operativo desde 2009, en el sureste (SE) del Golfo de Bizkaia (Figura 1). Forma parte del sistema operacional de adquisición de datos de la Dirección de Atención de Emergencias y Meteorología del Gobierno Vasco. Está compuesto por 2 antenas (una en el cabo Higer y la otra en el cabo Matxitxako) que emiten en una frecuencia de 4,86 MHz. Este sistema ofrece corrientes superficiales horarias, con 5,12 km de resolución espacial y cubre un área de estudio de 10000 km^2.

Los datos radar HF, con una gran resolución espacial y temporal, contribuyen considerablemente al estudio de patrones de corriente superficial y procesos físicos de la costa y al desarrollo de herramientas de oceanografía operacional (Paduan y Rosenfeld, 1996; Kohut y Glenn, 2003; Abascal *et al*., 2009; Gough *et al*., 2010; Schaeffer *et al*., 2011; Paduan y Washburn, 2013; Wyatt, 2014; Lorente *et al*., 2015). Teniendo en cuenta la reciente disponibilidad de estos datos y sabiendo que existen incertidumbres en el conocimiento de las corrientes superficiales, esta tesis pretende dar una nueva visión de las dinámicas oceánicas superficiales del SE del Golfo de Bizkaia. El área de estudio está recuadrado en la Figura 1.

1.2. ESTADO DEL CONOCIMIENTO

1.2.1. Geografía y Meteorología

El Golfo de Bizkaia es una región del Océano Atlántico Norte. Es la transición entre las frías aguas del norte y los mares tropicales y cubre el área entre el Cabo Finisterre (A Coruña, España) y la Punta de Penmarc'h (Bretaña, Francia) (Figura 1).

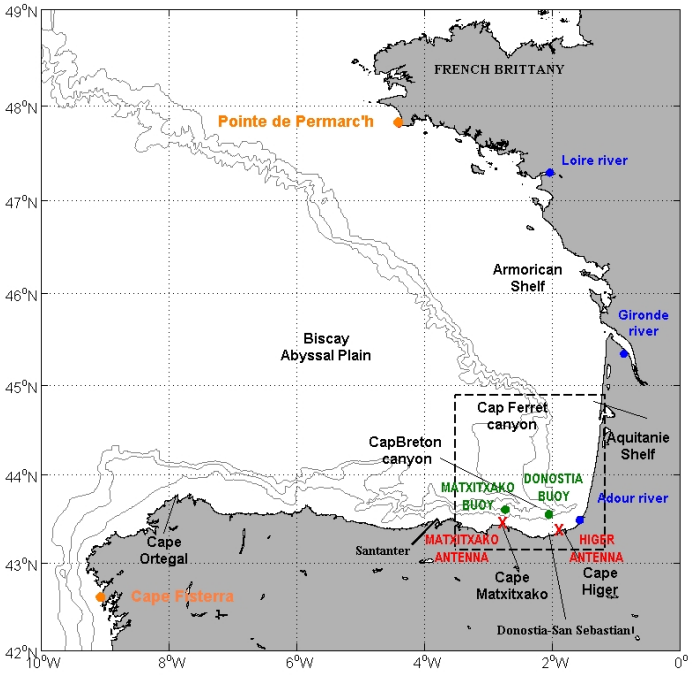

Figura 1: Geografía del Golfo de Bizkaia. Incluye las principales características referidas en esta tesis. Las antenas de radar HF Matxitxako e Higer están marcadas con una cruz roja y las boyas de Matxitxako y Donostia están señaladas con puntos verdes. El recuadro negro delimita la zona de estudio. Los principales ríos están señalados con puntos verdes.

La característica morfológica más importante de la zona es el cambio brusco de orientación de la costa, siendo ésta oeste-este en la costa española y norte-sur en la costa francesa. La plataforma continental española, llamada plataforma Cantábrica, es estrecha y uniforme (30-40 km) mientras que la anchura de la plataforma francesa aumenta hacia el norte (50-180 km). El cañón de Cap Bretón está situado entre ambas plataformas. Por su parte, la plataforma francesa está dividida entre la plataforma de Aquitania y la plataforma Armórica, por el cañón de Cap Ferret. Esta compleja batimetría de la región, afecta en gran mediad a la circulación general y condiciona a las variables medioambientales y biológicas (Bardey *et al*, 1999; Koutsikopoulos y Le Cann, 1996; Lavín *et al*., 2006).

En la parte oeste europea, la circulación atmosférica a latitudes medias del Atlántico Norte, está gobernada por la existencia de 2 centros de actividad: la anticiclónica en latitudes por debajo de 40ºN (centrada cerca de las Azores) y el área de bajas presiones (centrada a 60ªN). Entre ambas áreas, los principales vientos son del suroeste en invierno y noroeste en verano, siendo más fuertes en invierno y más débiles y menos regulares en verano (OSPAR, 2000). Además, existe una gran variabilidad intraanual, especialmente durante Marzo y Abril (Lazure 1997; González *et al*., 2002, 2004; Lavín *et al*., 2006; Fontán *et al*. 2009, 2013).

1.2.2. Masas de agua

La mayoría de las masas de agua del Golfo de Bizkaia tienen su origen en el Atlántico Norte o son el resultado de la interacción entre aguas formadas en el Atlántico con aguas de origen Mediterráneo (OSPAR, 2000). Las aguas centrales del este del Atlántico Norte (ENACW), que ocupan las capas superficiales del Golfo de Bizkaia, están afectadas por la mezcla invernal y están sujetas a variaciones estacionales de las aguas superficiales.

1.2.3. La descarga de ríos

Durante el invierno, la plataforma continental frente a los estuarios/desembocaduras de los principales ríos (Loire, Gironde y Adour), se caracteriza por aguas frías y salinas. A menudo se observan inversiones termales sobre la plataforma, relacionados con la estratificación salina. La contribución del flujo de los ríos se diluye a lo largo de la columna de agua. Esto regula la salinidad y temperatura de la plataforma interna y ayuda a preservar el gradiente entre las aguas de plataforma, que equilibran la corriente de talud (Koutsikopoulos y Le Cann, 1996; Lavín *et al*., 2005). Cabe destacar que en el área de estudio, el efecto de los ríos es puntual y poco significativo; siendo el Adour la principal fuente de agua de origen continental (Valencia *et al*., 2004; Ferrer *et al*, 2009).

1.2.4. Aspectos generales de la circulación oceánica en el Golfo de Bizkaia

Las principales características de la circulación oceánica del Golfo de Bizkaia están resumidas en la Figura 2.

1.2.4.1.Circulación general en la llanura abisal

Varios autores (Saunders, 1982; Maillard, 1986; Koutsikopoulos y Le Cann, 1996) han caracterizado la parte exterior del Golfo de Bizkaia con una circulación anticiclónica débil y variable (1-2 cm • s^{-1}) y con la presencia de remolinos tanto ciclónicos como

anticiclónicos. Estos remolinos tienen su origen en la corriente de talud (Pingree y Le Cann, 1992ª).

Pingree (1993) mostró que la ENACW penetra en el sur del golfo siguiendo la circulación anticiclónica sobre la llanura abisal a 400 m de profundidad. Las corrientes superficiales obtenidas a partir de boyas lagrangianas con velas a 15 m de profundidad (van Aken, 2002) han confirmado la tendencia del flujo hacia el sur. También confirmaron la variación estacional del flujo, con una componente hacia el este en otoño y hacia el sur en primavera y verano.

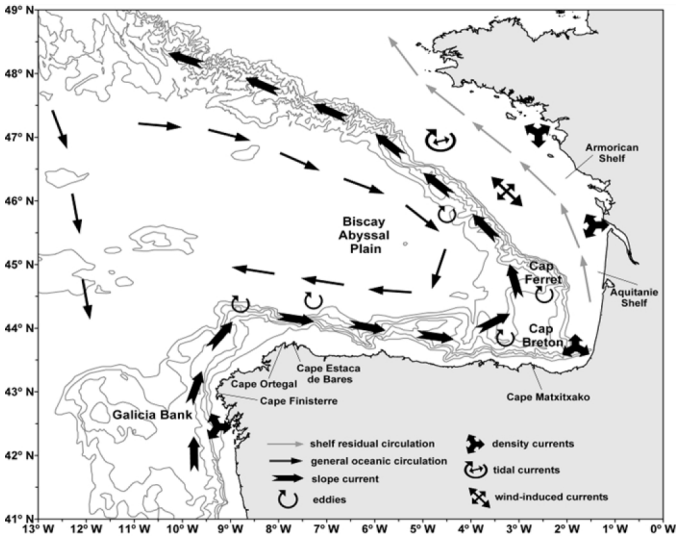

Figura 2: Circulación estacional en el Golfo de Bizkaia (Ferrer et al., 2009).

1.2.4.2. Corrientes de plataforma/talud

La circulación oceánica sobre el talud está dominada por la corriente estacional Iberian Poleward Current (IPC). En la zona de estudio circula hacia el este a lo largo de la Península Ibérica hasta que gira hacia el norte al encontrarse con el contorno francés (Frouin *et al*, 1990; Haynes y Barton, 1990, Pingree y Le Cann, 1990, 1992a, 1992b; Charria *et al*., 2013). Durante el invierno, a menudo se observa una intrusión salina cálida en la costa, atrapada a 50 km desde el borde de la plataforma y asociada a la IPC (Le Cann y Serpette, 2009; Esnaola *et al*., 2013).

Recientemente, Le Boyer *et al*. (2013) han descrito la circulación superficial, caracterizando la circulación media sobre la plataforma y parte alta del talud hacia el norte, siguiendo la topografía, con carácter estacional. Otros autores describen esta inversión con corrientes más débiles en verano con corrientes hacia el oeste en el talud español (Pingree y Le Cann, 1990; Rubio *et al*. 2013b; Charria *et al*., 2013). Charria *et*

al. (2013) mostraron una circulación esquemática donde se observa el carácter estacional de la circulación superficial (Figura 3).

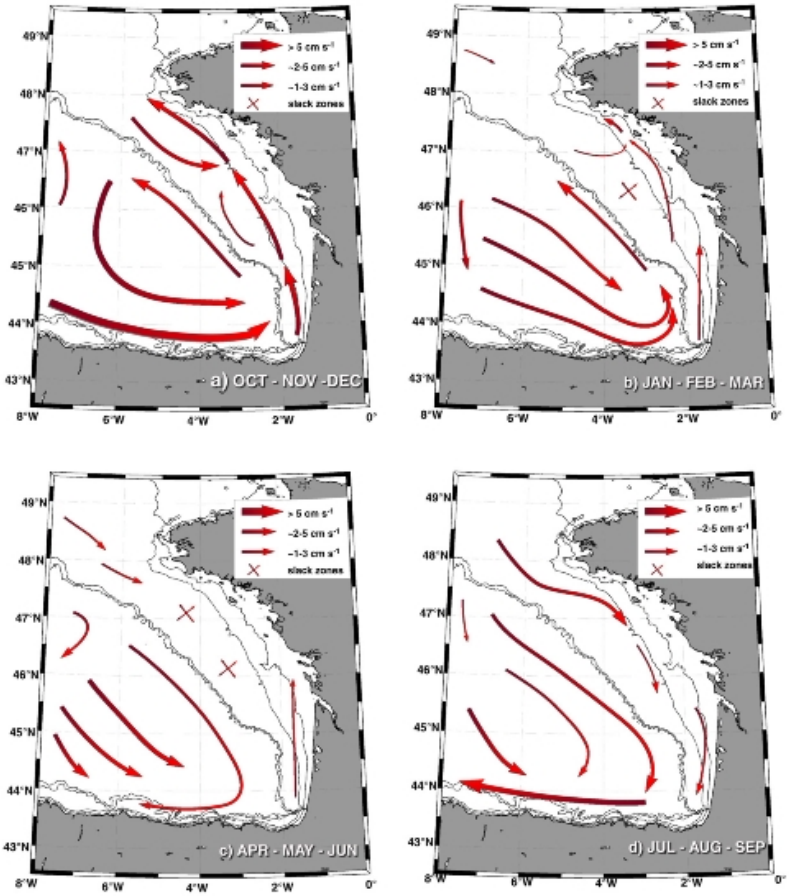

Figura 3: Circulación esquemática en el Golfo de Bizkaia. El ancho de las flechas es proporcional a la velocidad de la corriente (Charria et al., 2013).

La circulación de plataforma/talud está influenciada por diferentes forzamientos como: las irregularidades de la batimetría (Peliz *et al*., 2003), la marcada estacionalidad y variación espacial del viento (Pingree y Le Cann, 1989; Le Cann y Serpette, 2009; Le Boyer *et al*., 2013), variación de los flujos de calor (Somavilla *et al.,* 2013) o el efecto de la intrusión de aguas dulces (Lazure y Jegou, 1998; Lazure *et al*., 2008; Ferrer *et al*., 2009).

1.2.4.3. Variabilidad de mesoescala y remolinos

En el Golfo de Bizkaia, la IPC es la responsable de la generación de anticiclones persistentes (Peliz *et al*., 2003). Estos anticiclones llegan hasta los 1500 m de

profundidad y tienen diámetros medios de 100 km. Los remolinos más intensos se observan en invierno, generándose sobre el talud y disipándose más adelante, a lo largo del año en el Golfo de Bizkaia (van Aken, 2002; Pingree y Le Cann, 1990, 1992a, 1992b).

1.2.4.4. Afloramiento y hundimiento costero

Durante la primavera y verano, el proceso hidrodinámico más importante en el Golfo de Bizkaia y la costa Oeste de la Península Ibérica es el afloramiento costero. Se desarrolla durante los meses de abril a octubre y es la respuesta a los vientos persistentes y estables del norte (Wooster *et al*, 1976; Blanton *et al*., 1984). Durante el otoño e invierno, los vientos intensos del sur y oeste, aumentan la densidad de las aguas debido al enfriamiento. Además, estos vientos reactivan las corrientes hacia el este y norte con predominio al hundimiento en el SE del Golfo de Bizkaia (Valencia *et al*., 2004).

1.3. CONCLUSIONES Y OBJETIVOS DE LA TESIS

Los patrones de circulación del SE del Golfo de Bizkaia muestran una gran variabilidad espacial y temporal vinculado al efecto conjunto de varios forzamientos y procesos. La fuerte estacionalidad de los vientos, las corrientes de talud y la hidrografía, la actividad mesoescalar, el cambio de orientación de la costa y la abrupta batimetría, son algunos de los principales contribuyentes a la variabilidad observada.

Como se ha visto anteriormente, la mayor parte de la investigación realizada en el área de estudio, se ha realizado a partir de datos puntuales en el espacio y/o tiempo, por lo que no había descripciones completas de los patrones superficiales cuando se inició esta tesis. Por ello, desde el principio se esperó que los datos radar HF ayudasen en el conocimiento de los procesos físicos y su contribución a la circulación. Se han realizado dos estudios previos en el área utilizando datos radar HF (Rubio et al, 2011; Fontán et al, 2013). Ambos se centraron en escalas específicas y series de datos más cortos que la serie utilizada en esta tesis doctoral.

En este contexto, el objetivo general de esta tesis es profundizar en el conocimiento de las corrientes superficiales en SE del Golfo de Bizkaia con datos radar HF, de alta cobertura espacio-temporal. Se establecen los siguientes tres objetivos:

i. Evaluar el rendimiento del sistema radar HF y su potencialidad para el uso operativo en el cálculo de la deriva/trayectorias en el mar.
ii. Proporcionar una nueva visión de los patrones de circulación y la variabilidad de la circulación en el área de estudio a diferentes escalas temporales (desde la alta frecuencia hasta la interanual), utilizando datos espacio-temporales de alta resolución de radar HF.
iii. Estudiar las relaciones entre los patrones del viento y corrientes en la zona de estudio

La tesis se estructura de la siguiente manera: los capítulos I y II, ofrecen una introducción al estado del conocimiento sobre las corrientes superficiales en el área de estudio y de la tecnología Radar HF, respectivamente. En el capítulo III se describen las observaciones de radar HF y se comparan con otras medidas *in situ*. Las comparaciones eulerianas incluidas en este capítulo están publicadas parcialmente en Rubio *et al*. (2011) y en Solabarrieta *et al*. (2014); mientras que el análisis de la predictibilidad lagrangiana se incluye en Solabarrieta et al. (en preparación). El Capítulo IV estudia los patrones de circulación superficial del SE del Golfo de Bizkaia y es una adaptación de Solabarrieta *et al.* (2014). El Capítulo V incluye una descripción de los patrones del viento y circulación en el Golfo de Bizkaia y se analiza la interacción entre el viento y las corrientes, utilizando la técnica de clasificación k-medias (KMA). El contenido de este capítulo se han incluido en Solabarrieta *et al.* (enviado a Ocean Dynamics). Finalmente, el capítulo VI describe las conclusiones de la tesis y las futuras líneas de investigación que se deriven de ella.

CAPÍTULO II: TECNOLOGÍA RADAR HF

En los últimos años ha habido un aumento del uso de corrientes obtenidas mediante datos radar HF para el estudio de procesos de corrientes superficiales (Paduan y Rosenfeld, 1996; Kohut y Glenn, 2003; Gough *et al*., 2010; Schaeffer *et al*., 2011; Rubio *et al*., 2011; Paduan y Washburn 2013). Además, también se está aplicando esta tecnología en otros sectores como el medioambiente, la seguridad y la explotación de recursos marinos (Paduan y Washburn, 2013; Wyatt, 2014).

2.1. TECNOLOGÍA RADAR HF: ESTADO DEL CONOCIMIENTO

2.1.1. Descripción general

El radar HF, puede cubrir los huecos que tienen otras tecnologías remotas (los datos de satélite o datos *in-situ*, por ejemplo). Ofrece datos con gran cobertura espacial y alta resolución espacio-temporal. Además ofrece datos en tiempo real de valor inestimable en el campo de la oceanografía operacional, con múltiples aplicaciones en el sector marítimo: investigación, rescate, navegación, validación y calibración de modelos de predicción oceanográfica, especialmente cerca de la costa (Abascal *et al*., 2012; Paduan y Washburn, 2013; Wyatt, 2014).

Actualmente coexisten varios modelos de radar HF en el Mercado. Sin embargo, 2 son los más extendidos WERA (WavE Radar) y CODAR. Aunque ambos tienen los mismos principios de operación, difieren en el diseño de la antena receptora y por consiguiente, también en la determinación del ángulo de incidencia del eco de la señal. Esto también determina el número mínimo de antenas a instalar. CODAR sólo necesita 2 estaciones (cada una con una antena emisora y otra receptora). Para instalaciones de larga duración, las antenas CODAR necesitan calibraciones de las antenas receptoras, debido a que los patrones de respuesta pueden verse afectados por cambios en las cercanías de las antenas (Kohut y Glenn, 2003). Recientemente, se han realizado diferentes comparaciones entre los datos de WERA y CODAR (R. Wyatt, 2013 y Liu *et al*., 2014) donde se han observado resultados similares con ambos sistemas. De aquí en adelante la descripción de la tecnología se centrará en el sistema CODAR, al que pertenecen las antenas instaladas en la costa vasca.

2.1.2. Radares CODAR HF para la obtención de corrientes superficiales

El Sistema consiste en una antena emisora que envía señales de radio en una frecuencia de 3-300 MHz y una antera receptora que recibe la señal causada por la reflexión difusa de las olas (Crombie, 1955) (Figura 4). La medida de radar HF se basa en la retrodispersión de resonancia resultante de la reflexión de la onda transmitida por las olas cuya longitud de onda es ½ de la de la onda emitida. Este es el fenómeno de dispersión de Bragg y se observa en el pico de primer orden del espectro de la señal recibida (Paduan y Graber, 1997) (Figura 5). En ausencia de corrientes, la frecuencia del pico de primer orden tiene un desplazamiento Doppler causado por la velocidad de fase de las olas en la dirección radial. Esta velocidad (Vg) es la velocidad de propagación del

oleaje y viene dada por la relación de dispersión en aguas profundas $V_g = (g * L / 2\Pi)^{1/2} = (g/k)^{1/2}$ (Siendo: L: longitud de onda; g: gravedad; k: número de onda).

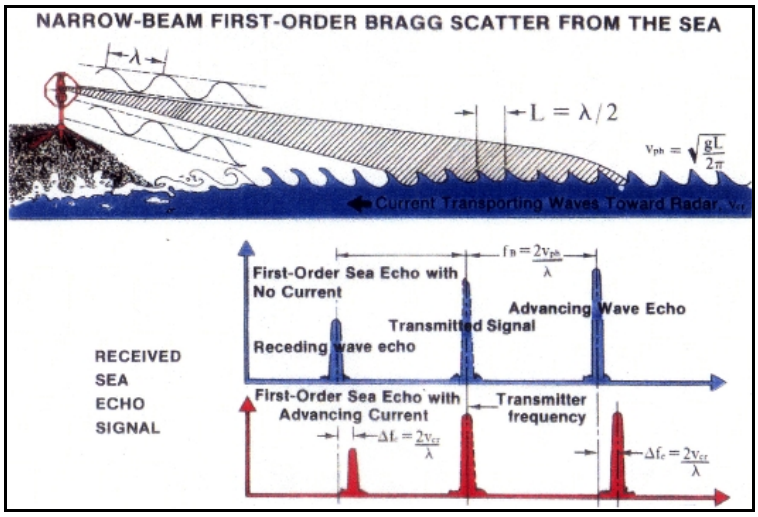

Figura 4: Esquema que muestra cómo mide las corrientes el radar HF. La antena de la costa emite una señal de longitud de onda λ y es reflejada por el oleaje superficial con una longitud de onda λ / 2. (Barrick et al., 1977)

El desplazamiento Doppler se presenta en los dos picos del espectro de la señal recibida (ondas que viajan hacia y desde la antena), situados simétricamente a ambos lados de la frecuencia, como se muestra en la Figura 5. La componente radial de la corriente, se puede calcular de la diferencia de velocidad entre la velocidad teórica del oleaje de Bragg y la velocidad observada en el espectro.

Para determinar el ángulo de la señal recibida, CODAR utiliza el método "direction finding". Este método se basa en normalizar la señal recibida por los bucles (loops) perpendiculares, de la antena receptora, llamada monopolo (Kohut y Glenn, 2003). En realidad, se utiliza un algoritmo mucho más complicado, llamado MUSIC (Multiple Signal Classification, Schmidt 1986). La correcta aplicación de este algoritmo requiere el perfecto conocimiento de la respuesta angular del patrón de cada antena. Hay 2 métodos para obtener estos patrones angulares: i) asumir los patrones teóricos o ideales basados en el diseño de la antena. ii) la medición de los patrones de las antenas (APM), después de su instalación. Esta medición se lleva a cabo moviendo un transponder en un círculo alrededor de la antena. Se recomienda calibrar las antenas CODAR una vez al año o cuando hay cambios alrededor de la mismas, que puedan distorsionar la señal (Kohut y Glenn, 2003).

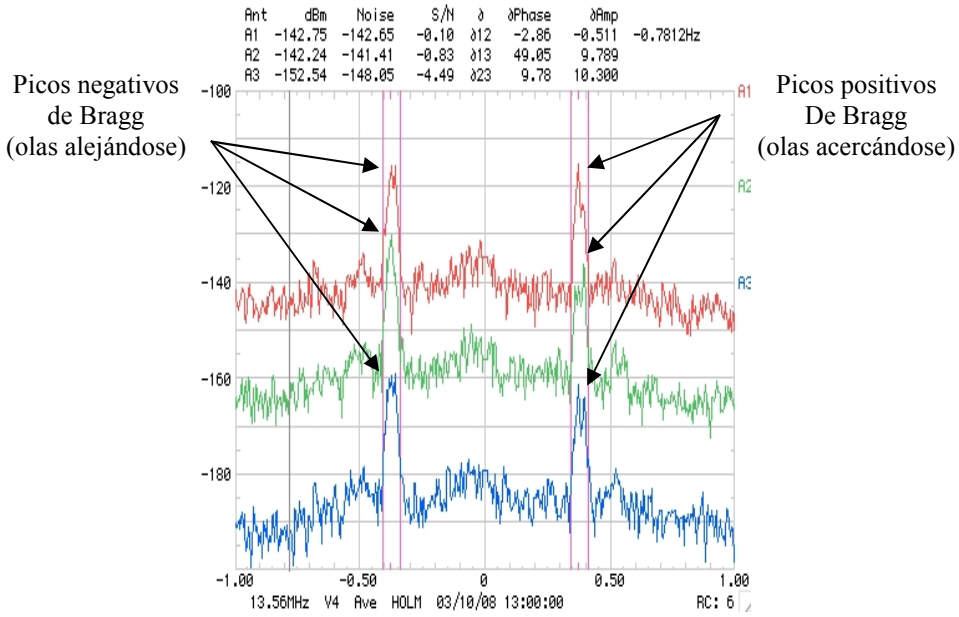

Figura 5: Ejemplo de un espectro real (cortesía de Qualitas Remos).

La disponibilidad de la información va desde minutos a pocas horas pero normalmente, se dispone de datos horarios. Para obtener esta información horaria, hay que procesar la señal bruta recibida para obtener los espectros (aplicando la transformada de Fourier FFT). A partir de la transformación y combinación de varios de estos espectros, se obtiene la información radial.

Como la información obtenida es radial, se requiere un mínimo de 2 estaciones con un área coincidente, para reconstruir la magnitud de las corrientes superficiales totales. La velocidad obtenida en cada nodo de estudio, es el ajuste por mínimos cuadrados de las velocidades radiales presentes en un círculo de radio dado, centrado en el nodo de estudio. En la siguiente sección se describe la configuración del sistema del País Vasco.

2.2. DESCRIPCIÓN DE SISTEMA RADAR HF DEL PAÍS VASCO

El Sistema radar HF del País Vasco consiste en 2 estaciones radar, uno en el cabo Higer y el otro en el cabo Matxitxako. Emiten en un ancho de banda de 40 kHz y a una frecuencia de 4,86 MHz. Este sistema ofrece datos de corrientes en una malla de 5,12 km de resolución espacial.

La configuración actual permite cubrir un área de aproximadamente 10000 km2. La precisión teórica de los datos es de 2 - 3 cm • s^{-1}, con una resolución espacial de 5º angulares. La Figura 6 presenta un ejemplo de las radiales de ambas antenas y las

corrientes totales obtenidas a partir de ellas. La información recibida se promedia en los nodos de una malla regular (Figura 7) de 5 km de separación entre nodos.

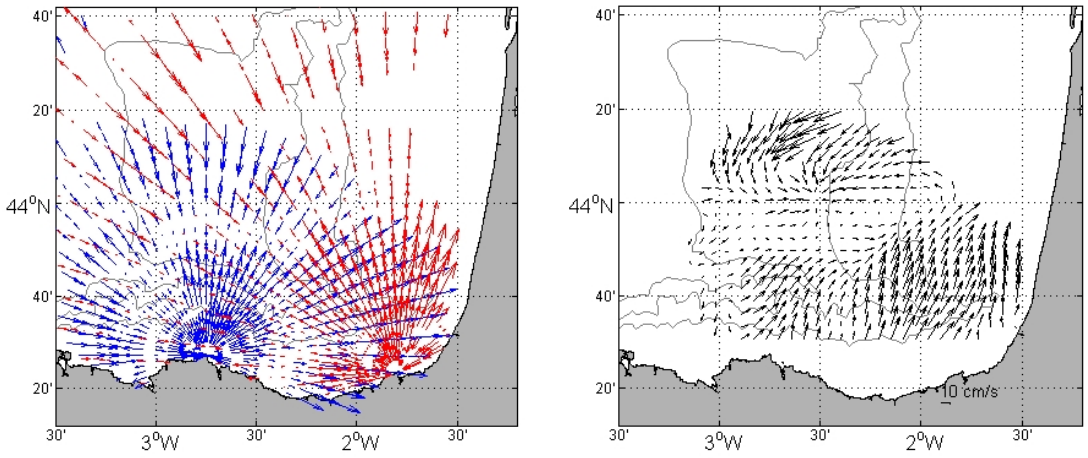

Figura 6: (Izquierda) Velocidades radiales de Matxitxako (azul) e Higer (rojo). (Derecha) Corrientes superficiales obtenidas de las radiales de la Figura 6 (izquierda), el día 22 de julio de 2009 a las 12:00.

Como criterio de calidad para garantizar suficiente información ortogonal, se ha estipulado que el ángulo entre radiales para obtener información de corrientes totales sea superior a 30º. Y se rechazan velocidades superiores a 100 cm • s^{-1}, ya que en la zona de estudio no se esperan velocidades superiores a este valor (Le Cann y Serpette, 2009; Rubio *et al*., 2013).

Como ya se ha dicho, los sistemas CODAR necesitan calibrar sus antenas regularmente. Desde la instalación del Sistema del País Vasco, se han hecho 3 campañas de calibración, para mejorar la calidad de las medidas del radar HF: el 21 de julio de 2009, el 10 de octubre de 2011 y el 30 de septiembre de 2014 (Figura 8). A pesar de ser aconsejable realizar una campaña anual, las consecutivas campañas y corrientes obtenidas desde éstas, han presentado diferencias muy pequeñas. Por ello se asume que las campañas realizadas han sido suficientes, para garantizar la calidad de los datos.

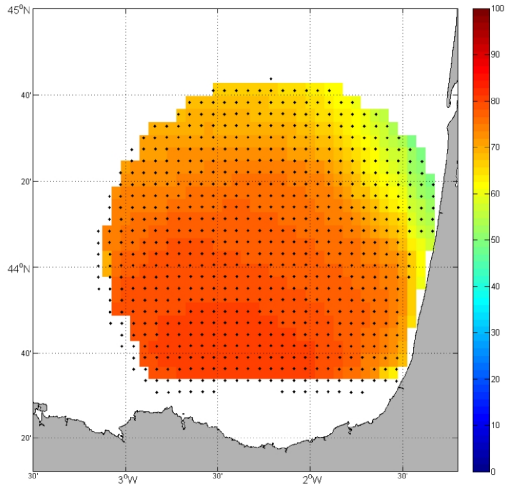

Figura 7: Posición espacial de los nodos del Sistema radar HF del País Vasco (puntos negros). Los colores representan la disponibilidad de datos totales, para el periodo 2009-13.

Pattern type	Matxitxako	Higer
Ideal	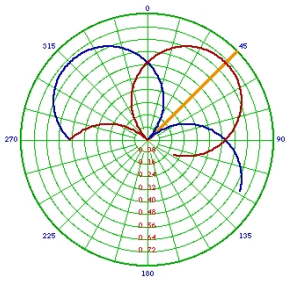	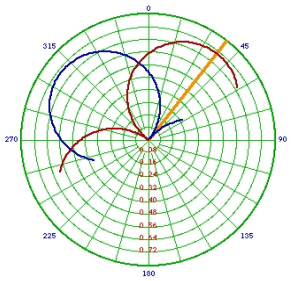
Measured (July 2009)	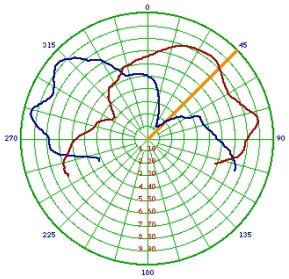	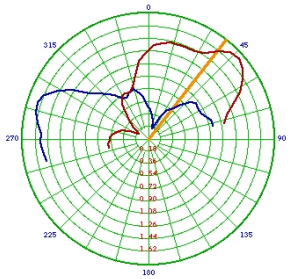

Figura 8: Patrones de calibración ideales y medidos para las antenas de Matxitxako e Higer.

2.2.1. Integración del radar HF en el Sistema oceanográfico *in-situ* del País Vasco

El radar HF se integró al sistema oceanográfico *in-situ* del País Vasco, perteneciente a la Dirección de Atención y Emergencias del Gobierno Vasco, a finales de 2008 y se obtuvieron las primeras corrientes a principios del 2009. Además del radar HF, el sistema tiene 6 estaciones costeras que ofrecen información cada 10' desde 2004 y 2

boyas situadas sobre el talud frente a Donostia-San Sebastián y el cabo Matxitxako (Figura 9).

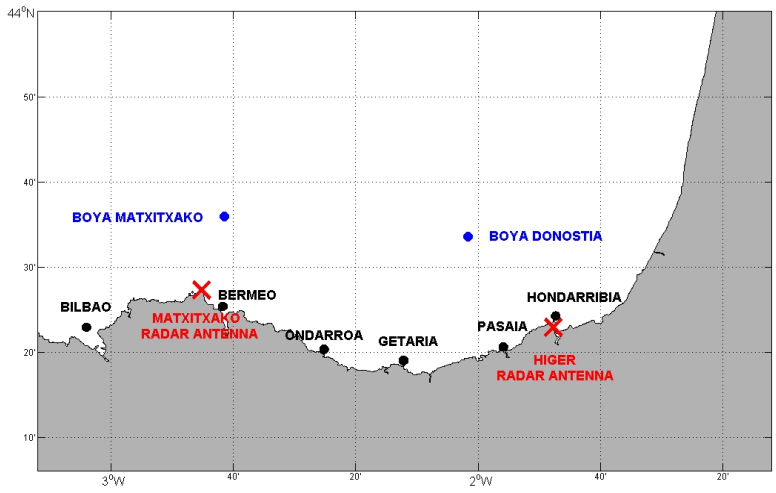

Figura 9: Localización de las (2) boyas océano-meteorológicas (azul), (6) estaciones costeras (negro) y (2) estaciones radar HF (rojo) de la Dirección de Atención y Emergencias del Gobierno Vasco.

2.2.2. Datos disponibles del Sistema radar HF del País Vasco.

En esta tesis se usarán datos radar HF de 2009 a 2013 (Figura 10). La disponibilidad de los datos no ha sido uniforme debido a paradas de mantenimiento, reparación de las antenas, errores debidos a condiciones atmosféricas…

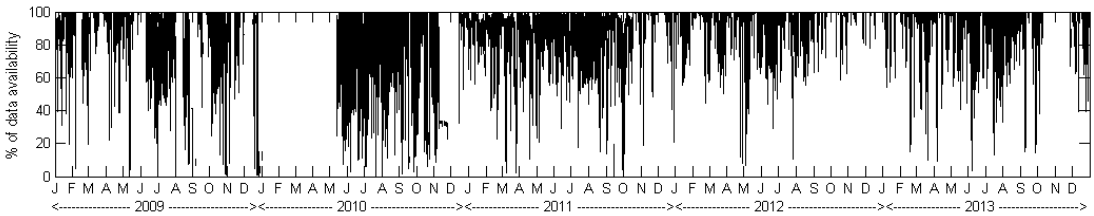

Figura 10: % de disponibilidad de datos radar HF, de los nodos de la Figura 7.

CAPÍTULO III: EVALUACIÓN DE LOS RESULTADOS RADAR HF Y PREDICTIBILIDAD LAGRANGIANA

Aunque la calidad de los datos radar HF sobre el talud de la zona de estudio ha sido previamente evaluado en Rubio et al. (2011), aquí se presentan comparaciones adicionales de datos radar-*in situ* con el fin de: (i) evaluar las prestaciones del sistema

radar HF; (ii) mostrar comparación cuantitativa y cualitativa con otras mediciones *in situ* de la zona; (iii) evaluar las capacidades del sistema para proporcionar estimaciones lagrangianas.

3.1. COMPARACIÓN DE DATOS RADAR CON OTROS DATOS COMPLEMENTARIOS EXISTENTES

Se han usado datos *in situ* de fuentes independientes para ver las capacidades del radar HF. Los diferentes datos y las comparaciones realizadas con ellos se detallan en los siguientes párrafos y se resumen en las Tabla 1 yTabla 2.

3.1.1. Datos

El procesamiento y análisis de datos radar HF para 2009-11, se ha realizado utilizando la librería de Matlab "HFR_Progs" (https://cencalarchive.org/ ~cocmpmb/COCMP-wiki/index.php/Main_Page). Para obtener velocidades totales, se combinan las velocidades radiales de cada antena en una malla regular mediante un ajuste de mínimos cuadrados (en lo sucesivo LS) de las velocidades radiales en un radio de 10 km alrededor de cada nodo. Después, se calculan y se controlan los valores de 2 indicadores de incertidumbre:

(i) Por un lado, al alejarse de las antenas, la distancia entre las radiales aumenta. Para evitar nodos donde las incertidumbres se vuelven importantes, se calcula la diferencia RMS entre la corriente radial medida y la corriente radial predicha por el modelo utilizado para el ajuste LS de radiales a totales. Se excluyen velocidades radiales donde las diferencias RMS son mayores de 18 cm • s^{-1} (valor elegido para un equilibrio adecuado entre la calidad de los datos y la pérdida de cobertura espacial y temporal).

(ii) Por otro lado, otro tema importante en el cálculo de las velocidades totales es la Dilución Geométrica de la Precisión (GDOP). Éste aumenta drásticamente cuando el ángulo entre las radiales llega a ser demasiado pequeña. Aunque todas las mediciones radiales disponibles se utilizan para conseguir las velocidades totales, para cada nodo se calcula una incertidumbre radial no uniforme y la componente de la incertidumbre radial medida. Cuando la incertidumbre es mayor que 8 cm • s^{-1} los datos obtenidos para ese nodo se descartan.

Finalmente y debido al procesado de los espectros, cada velocidad horaria radial, se obtiene haciendo la media móvil de 3 horas de datos.

DATOS	POSICIÓN	TIPO DE DATO	AÑOS	RESOLUCIÓN TEMPORAL (horas)	RESOLUCIÓN ESPACIAL (km)	PROFUNDIDAD DE LA MEDIDA (m)	FUENTE DE DATOS
Radar HF Costero	Matxitxako: 43º 27.3' N 02º 45.2' W Higer 43º 23.5' N 01º 47.7' W	Remoto	2009 2010 2011	1	5.12	2-3	Gobierno Vasco
Boyas fondeadas	Donostia: 43º 33.6' N 02º 1.8' W Matxitxako: 43º 36' N 02º 41.4' W	*In-situ*	2009	1	-	1.5	Gobierno Vasco
	Donostia: 43º 33.6' N 02º 1.8' W Matxitxako: 43º 36' N 02º 41.4' W		2009 2010 2011			12	
Boyas de deriva	43º 21' N – 44º 42' N 1-3º W	*In-situ*	2009	-	-	15	Ver Charria *et al.* 2013

Tabla 1: Breve descripción de los datos y sus características

Como se observa en la Tabla 1, se han utilizado las series de datos de las boyas de Donostia y Matxitxako. Estas boyas ofrecen desde 2007 series de datos de corrientes e hidrografía, adecuadas para la validación y observación de la variabilidad estacional e interanual.

También se han utilizado los datos de 20 boyas de deriva con vela a 15 m de profundidad y lanzados durante diferentes campañas en 2009, en el Golfo de Bizkaia (para más detalle véase Charria *et al*., 2013).

3.1.2. Resultados de comparaciones eulerianas

La comparación entre las corrientes de radar HF y los datos de corriente obtenidos de plataformas *in-situ* no es sencilla; esto es debido a las características e imprecisiones propias de los diferentes sistemas de medición (Paduan y Rosenfeld, 1996; Kohut y Glenn, 2003; Ohlmann *et al,* 2007; y Kohut *et al*, 2006). Se ha de señalar que a 4,86 MHz de frecuencia, el radar mide la corrientes integradas de los 2-3 primeros metros de la columna de agua (Laws, 2001). Las profundidades de los datos disponibles para las

comparaciones son puntuales, y varían en profundidad desde 1,5 hasta 15 m. Además, hay diferencias en las medias espaciales y temporales: el radar es un promedio de 3 horas, mientras que las boyas miden las corrientes cada hora. Por ello, las comparaciones presentadas en este capítulo deben ser analizadas teniendo en cuenta estos aspectos.

Comparaciones previas entre radar HF y las boyas de Matxitxako y Donostia a 1,5 m de profundidad para al año 2009 (Rubio *et al* 2011), mostraron (i) correlaciones superiores a 0,86 y RMSd menores a 9 cm • s^{-1} en Matxitxako (componente este-oeste); (ii) correlaciones cercanas a 0,5 (este-oeste) y RMSd superiores a 10 cm • s^{-1} (Tabla 2) en Donostia.

Para el periodo 2009-11, las comparaciones a 12 m de profundidad indican menores correlaciones y mayores RMSd (ver Tabla 2); las correlaciones más bajas que cuando se compara con boyas a 1,5 m, pueden ser debidas a que como se ha dicho anteriormente, el dato radar es un promedio de los primeros 2-3 m de agua.

Para los meses con condiciones de mezcla y una circulación hacia el este más fuerte, las correlaciones de la componente u son mayores que durante los periodos de estratificación.

Las comparaciones entre las boyas de deriva y radar HF también están resumidas en la Tabla 2. Teniendo en cuenta que la mayoría de estas boyas fueron lanzadas entre abril y octubre, los resultados son comparables a los obtenidos entre radar HF y boyas a 12 m durante los meses de estratificación. Con valores de RMSd ligeramente superiores y correlaciones similares, los resultados de las comparaciones de boyas de deriva-radar (para toda la zona) son del mismo orden que los observados con las boyas sobre el talud.

3.2. PREDICTIBILIDAD LAGRANGIANA

El objetivo de esta sección es comparar las trayectorias reales con las simuladas utilizando corrientes radar HF.

El principal problema a la hora de generar trayectorias son los huecos en los datos. Para evitar esto, se ha aplicado a los datos el análisis "Open-Boundary Modal Analysis" (OMA) (Lekien *et al.*, 2004 y Kaplan y Lekien 2007). Esta técnica genera modos físicos independientes, que después se utilizan para interpolar, extrapolar y filtrar las corrientes. Los modos se generan utilizando una malla triangular y no cambian con el tiempo

** Rubio et al., 2011*

Datos *In-Situ*	**Profundidad de medida (m)**	**Periodo de tiempo**	**RMS (cm·s^{-1})**				**Mean Speed**				**Corr-u *In-situ*- Datos radar**	**Corr-v *In-situ*- Datos radar**	**RMSd-u (cm·s^{-1}]) *In-situ*- Datos radar**	**RMSd-v (cm·s^{-1}]) *In-situ*- Datos radar**
			Datos *In-Situ*		**Nodo radar**		**Datos *In-Situ***		**Nodo radar**					
			u	**v**	**u**	**v**	**u**	**v**	**u**	**v**				
Matxitxako*	1.5	2009	0.16*	0.10*	0.13*	0.08*	-	-	-	-	0.86*	0.64*	8.09*	8.12*
Donostia*	1.5	2009	0.12*	0.11*	0.11*	0.12*	-	-	-	-	0.53*	0.34*	10.38*	12.88*
Matxitxako	12	01-Jan-2009 /07-Sep-2011	13.88	8.20	14.32	9.21	5.30	-2.28	4.09	0.22	0.66	0.50	11.12	8.97
Donostia	12	01-Jan-2009 /15-Oct-2010	9.72	6.84	12.40	13.07	2.75	-0.01	3.84	4.20	0.49	0.27	10.95	13.09
Matxitxako	12	Well mixed months	20.03	8.98	18.55	8.69	13.30	2.05	11.10	0.62	0.67	0.46	12.38	9.46
Donostia	12	Well mixed months	13.23	7.79	14.70	16.40	5.84	1.03	6.06	9.27	0.59	0.20	11.49	16.41
Matxitxako	12	Stratified months	9.03	8.58	11.84	9.73	1.14	2.57	0.31	0.31	0.51	0.57	10.70	8.89
Donostia	12	Stratified months	8.77	6.76	11.91	11.61	1.67	0.28	2.66	2.51	0.44	0.32	11.07	11.52
Drifters	15	May-Sep-2009	13.99	13.67	13.77	13.84	-0.88	-0.33	-1.49	-1.14	0.42	0.46	14.85	14.30

Tabla 2: Valores de RMS , velocidades medias, correlaciones y RMSd de las comparaciones de datos radar HF- datos in situ..

(Lekien *et al.*, 2004). Para generar las velocidades totales, se utilizan directamente las velocidades radiales (Kaplan y Lekien 2007) (Figura 11); por ello, es posible obtener velocidades totales, aunque con menor calidad, con los datos de una única antena. Las corrientes OMA se han generado utilizando la librería HFR_progs (descrito en el capítulo II) y utilizando un radio promedio de 10 km.

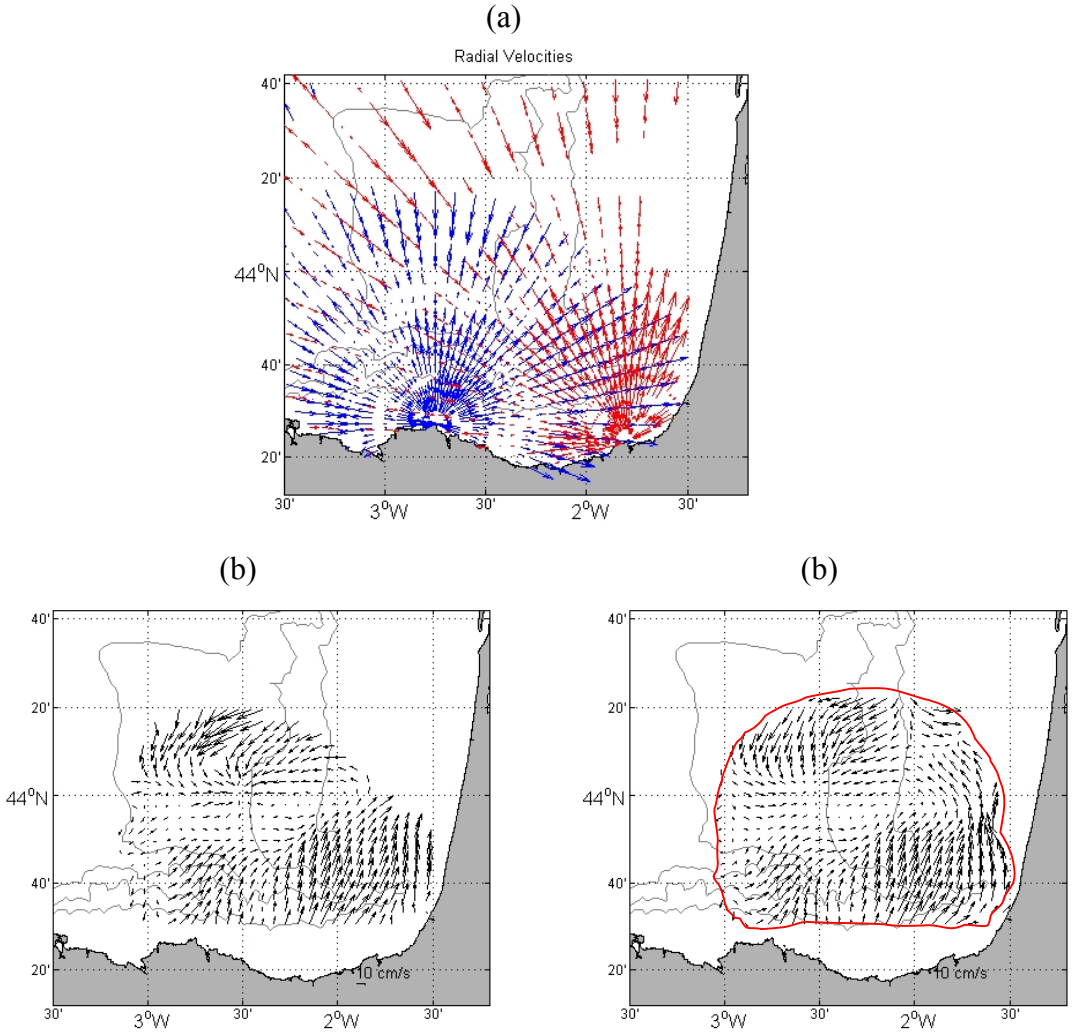

Figura 11: Mapas de corrientes superficiales del 12 de julio de 2009 a las 12:00. (a) Corrientes radiales. (b) Corrientes totales. (c) Corrientes OMA. La línea roja delimita el área utilizado para obtener velocidades OMA.

Una vez obtenida una serie sin huecos, se ha utilizado la nueva versión del modelo "lagrangian particle-tracking model" (LPTM), para generar trayectorias (Ferrer *et al.*, 2004). Para disponer de mayor número de trayectorias comparables, se han generado trayectorias cada 6 horas de las trayectorias reales, de 48 horas de duración (ver Figura 12).

La Figura 13 muestra las distancias de separación entre trayectorias reales y simuladas y la Tabla 3, resume los valores a las 6, 12 y 24 horas de simulación. La separación utilizando velocidades OMA es mayor, ya que la reconstrucción OMA es menos precisa que las velocidades totales observadas. Esta figura muestra también el progresivo aumento de la separación con el tiempo.

Después de 6 horas de simulación, la diferencia de distancias entre velocidades totales y OMA es de 0,75 km (33 % de la separación media entre trayectorias reales y simuladas con totales). Esta diferencia aumenta hasta 1,50 km (28%) y 2,81 km (34%) después de 24 y 48 horas de simulación, respectivamente. Esto significa que la distancia de separación relativa entre trayectorias obtenidas utilizando velocidades totales y OMA, respecto a las distancias entre trayectorias reales y simuladas con totales, no aumenta.

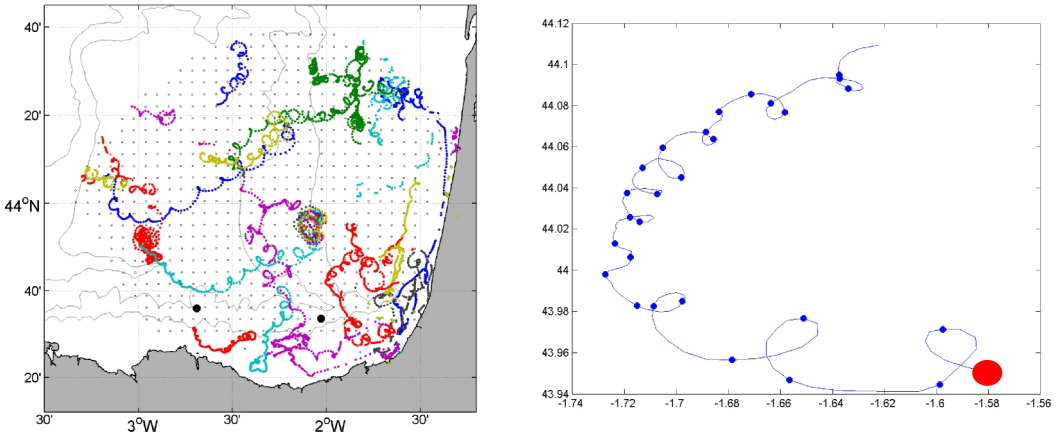

Figura 12: (Izquierda) Trayectorias reales de las boyas de deriva, entre abril y octubre de 2009. (Derecha) Trayectoria real (línea azul) de una boya de deriva de las de la figura izquierda. Los puntos azules son los puntos donde se han inicializado las trayectorias simuladas, cada 6 horas de la trayectoria real. La trayectoria empezó el 30 de mayo de 2009 a las 22:00 y acabó el 6 de junio de 2009 a las 21:00. El punto de inicio de la trayectoria real está indicado con un punto rojo.

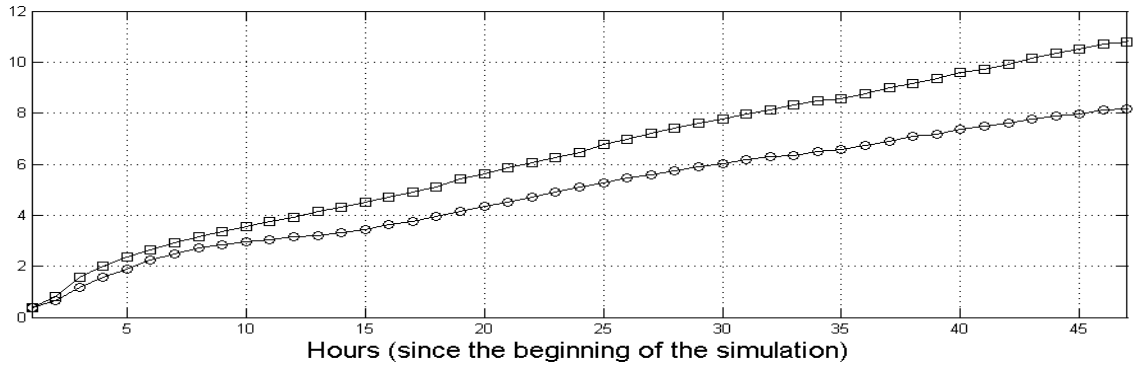

Figura 13: Media en km de la distancia de separación entre trayectorias reales y simuladas utilizando velocidades totales (círculos) y velocidades OMA (cuadrados).

Corrientes	Distancia de separación entre trayectorias reales y simuladas [km]		
	6 hours	12 hours	24 hours
Totales	2,25	3,25	5,23
OMA	3,00	4,14	6,73

Tabla 3: Valores de la distancia de separación entre trayectorias reales y simuladas.

3.2.1. Discusión de la predictibilidad lagrangiana

Las distancias de separación observadas en esta sección utilizando velocidades totales están de acuerdo con otros estudios realizados con modelos (Thompson *et al*., 2003) o datos radar (Ullman *et al* 2006, Frolov *et al*, 2012) para simular trayectorias. Las distancias a las 6, 12 y 24 horas de simulación están entre 2,25-3,00 y 5,23-6,73 km. Para permitir las comparaciones entre totales y OMA, sólo se han utilizado periodos donde había disponibilidad de datos totales. Por lo que este ejercicio de comparación, no es válido para la evaluación de las capacidades de las velocidades OMA, cuando sólo se utiliza la información radial de una de las 2 antenas, ya que se sabe que la reconstrucción es menos precisa. Los resultados muestran que la separación entre trayectorias reales y simuladas aumenta en un 30% si se utilizan velocidades OMA para las simulaciones.

Los radios de búsqueda utilizados actualmente por el servicio nacional de salvamento marítimo (SASEMAR) son significativamente mayores (comunicación personal) que las distancias de separación obtenidas entre trayectorias reales y simuladas con corrientes radar HF, obtenidas en este estudio. Los resultados sugieren que el uso de datos radar HF en el área de estudio, mejorarían considerablemente las operaciones actuales de búsqueda y rescate.

3.3. CONCLUSIONES

A pesar de las diferencias conocidas entre las diferentes medidas disponibles, los resultados de la comparación entre los datos *in-situ* y radar HF muestran valores razonables y coherentes con los descritos por otros autores (Paduan y Rosenfeld, 1996;. Kaplan et al, 2005). Esta observación refuerza la confianza en los resultados obtenidos

mediante el uso del radar HF del País Vasco para estudiar la circulación superficial en el SE del Golfo de Bizkaia.

Por otro lado, con los resultados del análisis de la predictibilidad lagrangiana, es posible concluir que el radar HF permite generar trayectorias en situaciones reales con razonable precisión.

Para usos operacionales, ambas corrientes, Totales y OMA ofrecen buenos resultados. Y aunque las corrientes OMA generan mayores errores, ofrecen campos de corrientes sin huecos, mucho más adecuados para la generación operacional de trayectorias y estimación de transporte.

CAPÍTULO IV: CIRCULACIÓN OCEÁNICA SUPERFICIAL EN EL SE DEL GOLFO DE BIZKAIA

Los principales objetivos de este capítulo son: (i) estudiar y describir los principales patrones de circulación superficial estacional, de mesoescala y la variabilidad en las bandas mareal e inercial. (ii) cuantificar la contribución de estos procesos a la variabilidad total observada en el SE del Golfo de Bizkaia.

4.1. DATOS Y ANÁLISIS DE DATOS

Para estudiar las corrientes a diferentes escalas temporales en el periodo 2009-11, se han aplicado diferentes filtros: medias mensuales para estudiar los patrones estacionales; filtro digital Butterworth de 10º orden (Emery y Thomson, 2001), para extraer la señal de T<48 horas (paso bajo) y 14<TL<20 (oscilaciones inerciales); análisis harmónico para extraer la señal de la marea.

Posteriormente se ha aplicado el análisis EOF (Empirical Orthogonal Function) a los datos filtrados de baja frecuencia e inercial, obteniendo los modos EOF con su varianza y su serie de amplitud temporal. Para estudiar la circulación, se han tenido en cuenta, los primeros 4 modos, aplicando el criterio de truncamiento de North et al. (1982).

4.2. CIRCULACIÓN A GRAN ESCALA Y MESOESCALA

En los campos horarios de radar son observables procesos desde escalas estacionales a mesoescalares. Pero la cantidad de datos disponibles, hace muy difícil resumir estas observaciones. Por ello, con el objetivo de representar algunos de los patrones usuales,

en la Figura 14. se han seleccionado ciertos campos horarios (campos de corrientes sobre imágenes satelitales de SST y Chl-a, cuando había disponibilidad). En las siguientes secciones se describe un análisis más detallado de los patrones y la variabilidad observados en la Figura 14.

4.2.1. Patrones mensuales y circulación a lo largo del talud

Las medias mensuales muestran una marcada estacionalidad con diferencias significativas durante verano e invierno (Figura 15). Para los meses de invierno se observa una circulación ciclónica con intensificación sobre el talud. También se observa una interanualidad, respecto al centro de esa circulación ciclónica y respecto a sus características. La circulación se invierte en verano y presenta una gran interanualidad y variabilidad. Como se observa en estas medias, las corrientes son más intensas en invierno, con intensificaciones sobre el talud y más débiles en verano con intensificaciones mar adentro. Finalmente, las medias del resto del año presentan una mayor variabilidad en espacio y en tiempo, con velocidades menores.

La mayor variabilidad se observa durante los meses de transición, cuando las elipses de varianza muestras valores altos, en comparación con las corrientes medias. Durante el verano, las elipses son similares o mayores, pero los valores de la corriente son también más fuertes, por lo que los patrones observados son más persistentes en verano que en los meses de transición. Los meses de invierno presentan las mayores elipses y mayores valores de las corrientes.

Para estudiar la variabilidad temporal de la circulación sobre el talud, se ha representado en un transecto frente al cabo Matxitxako, la componente este-oeste de la corriente medida por el radar (Figura 16 y Figura 17.arriba). También se ha dibujado la circulación de la boya de Matxitxako, en los primeros 150 m (Figura 17.abajo), bajo ese transecto. Durante los meses de invierno se observa una intensa circulación hacia el este, con velocidades que alcanzan los 70 cm • s^{-1} y una clara señal en la vertical. Durante los meses de verano, por el contrario, se observa una circulación superficial hacia el oeste, con menores velocidades.

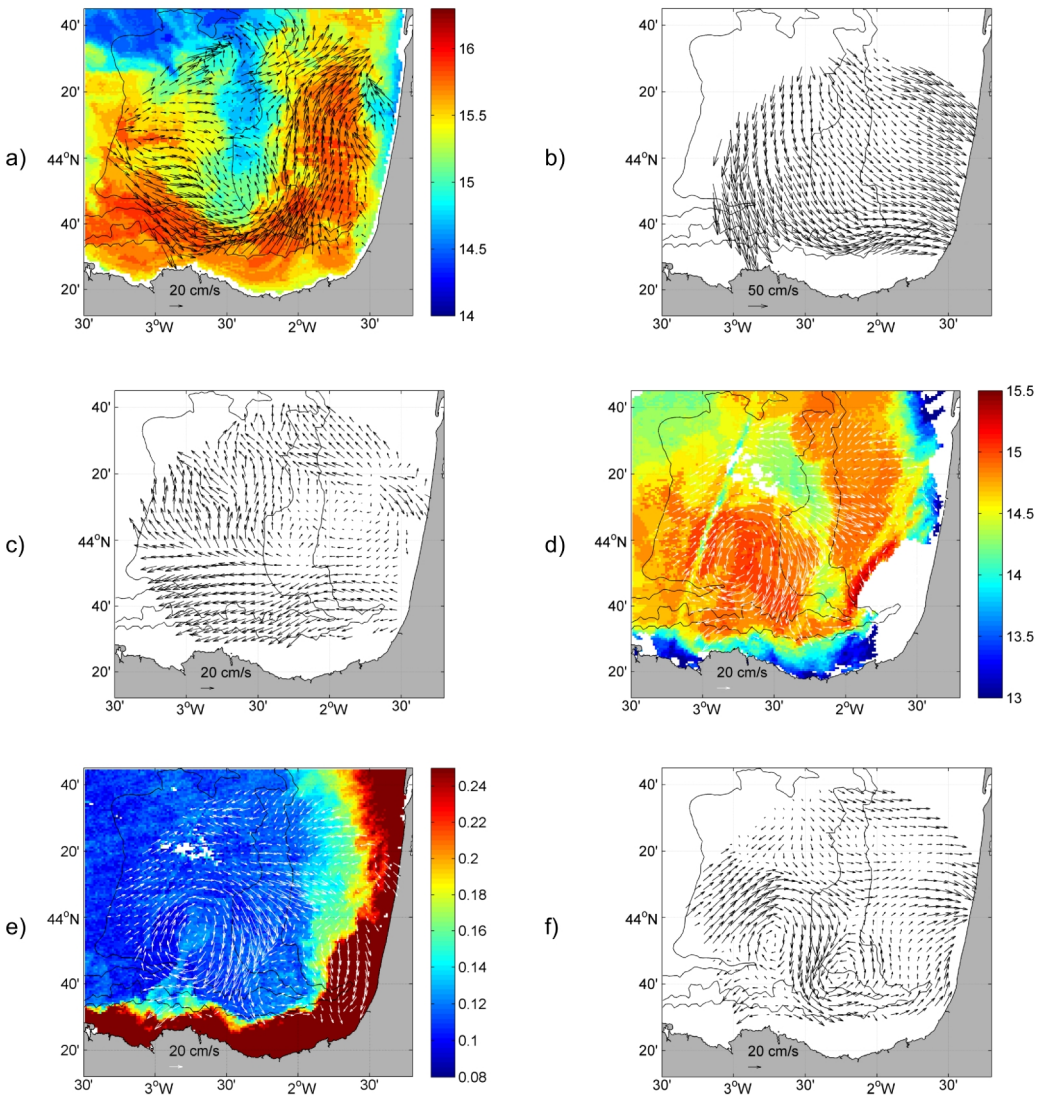

Figura 14: Mapas de corrientes radar HF de la zona de estudio. Las figuras se han elegido para ilustrar algunos patrones típicos de la zona de estudio: (a) circulación de invierno con señal superficial de la IPC sobre el talud, asociada a un flujo templado; (b) corrientes intensas hacia el sur como respuesta a vientos intensos del norte, asociados a la ciclogénesis explosiva Klaus durante el invierno de 2009; (c) circulación de verano, con corrientes intensificadas en la parte oeste sobre el talud español; (d, e, f) patrones asociados a un remolino anticiclónico. Su señal en datos de SST y Chl-a se muestra en (d) y (e) respectivamente; (f) su interacción con una estructura ciclónica más pequeña, unos días más tarde. Las fechas son (a) 24/11/2009 13:59 para SST y 24/11/2009 00:00 para datos radar HF; (b)24/01/2009 09:00; (c) 22/09/2010 09:00; (d, e) 27/12/2011 12:36 y 27/12/2011 12:50 para SST y Chl-a respectivamente y 29/12/2011 19:00 para radar HF; (f) 31/12/2011. Batimétricas: 200, 1000, 2000m.

4.2.2. Análisis EOF a los datos filtrados de baja frecuencia

Los resultados del análisis aplicados a la banda T>48 h se muestran en la Figura 18. Los 4 primeros modos EOF explican el 64% de la varianza.

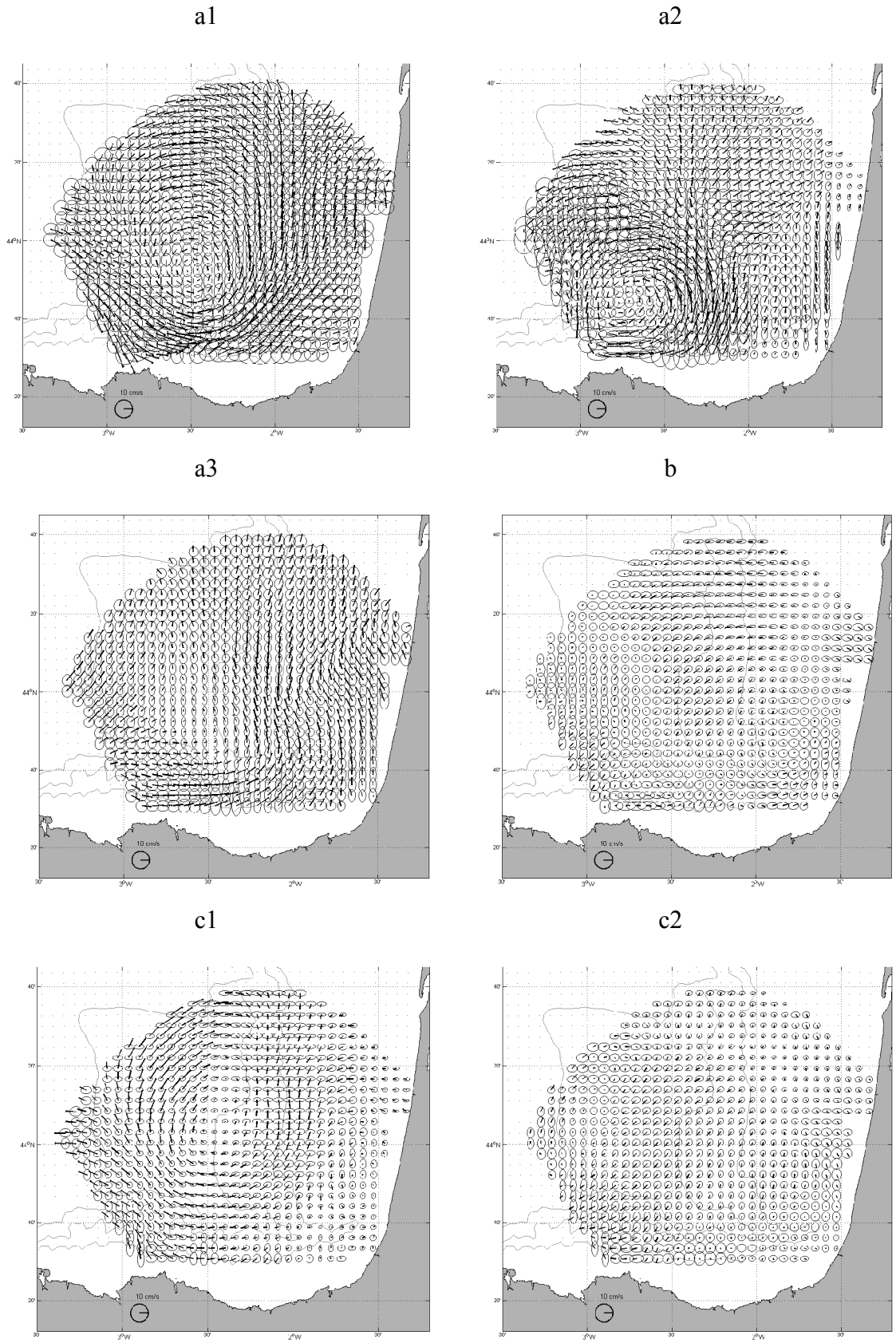

Figura 15: Corrientes medias y elipses de varianza de: (a) Invierno: (a1) Noviembre2009; (a2) Enero 2011; (a3) Noviembre 2011. (b) Meses intermedios: Mayo 2010. (c) Verano: (c1) Septiembre 2009; (c.2) Julio 2010. Batimétricas: 200, 1000, 2000m.

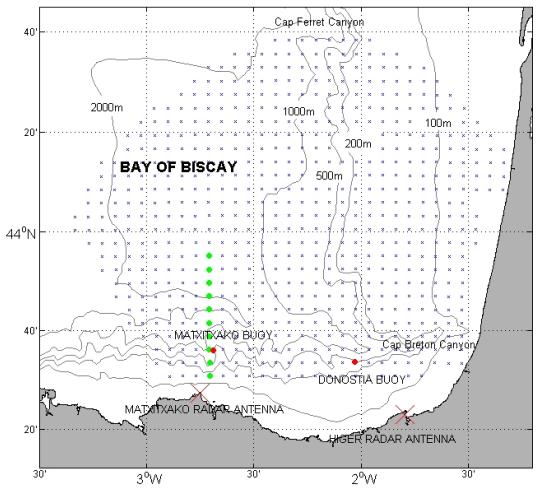

Figura 16: Área de estudio. Las cruces rojas son las posiciones de las antenas radar HF. .Los puntos azules son los nodos de la malla regular utilizada. Los puntos verdes señalan los nodos utilizados para el estudio del transecto frente al cabo Matxitxako. Batimétricas: 100, 200, 500, 1000, 2000m.

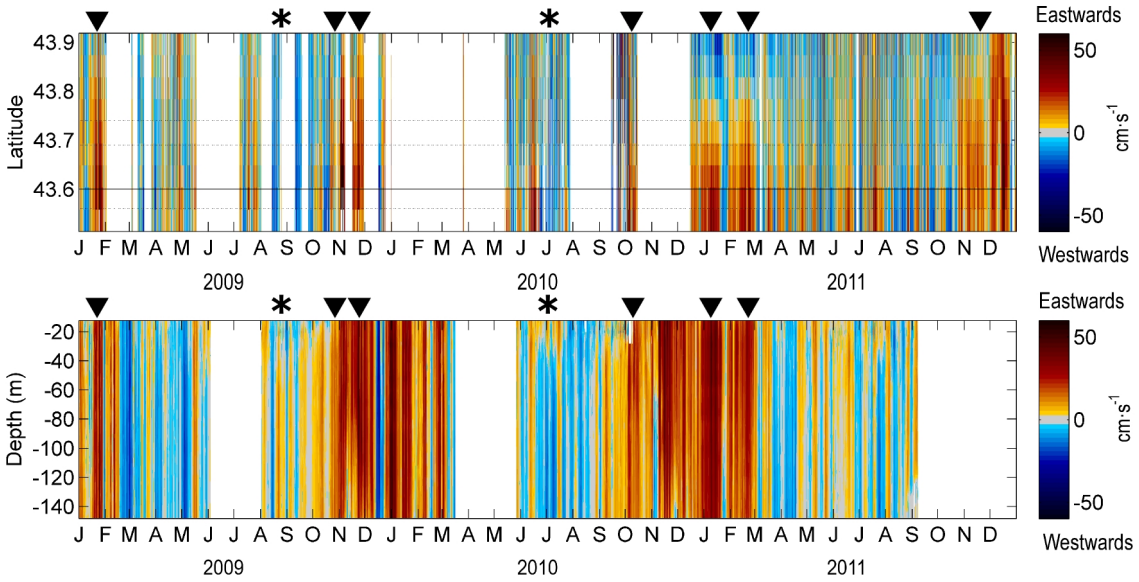

Figura 17: (Arriba) Corriente de talud hacia el Este (positivo) – Oeste (negativo) de los nodos del transecto de la Figura 16. Las líneas horizontales finas indican las batimétricas de 200m, 1000m y 2000m y la línea solida indica la posición de la boya de Matxitxako. (Abajo) Corriente de talud hacia el Este (positivo) – Oeste (negativo) en la columna de agua de la boya de Matxitxako Los huecos en blanco son periodos sin dato.

El modo 1 representa el 28% de la varianza y muestra un patrón ciclónico, con velocidades mínimas cerca de 2º 45'O y 44ºN. Las velocidades se intensifican sobre el talud. En términos temporales, durante el invierno se observan valores positivos

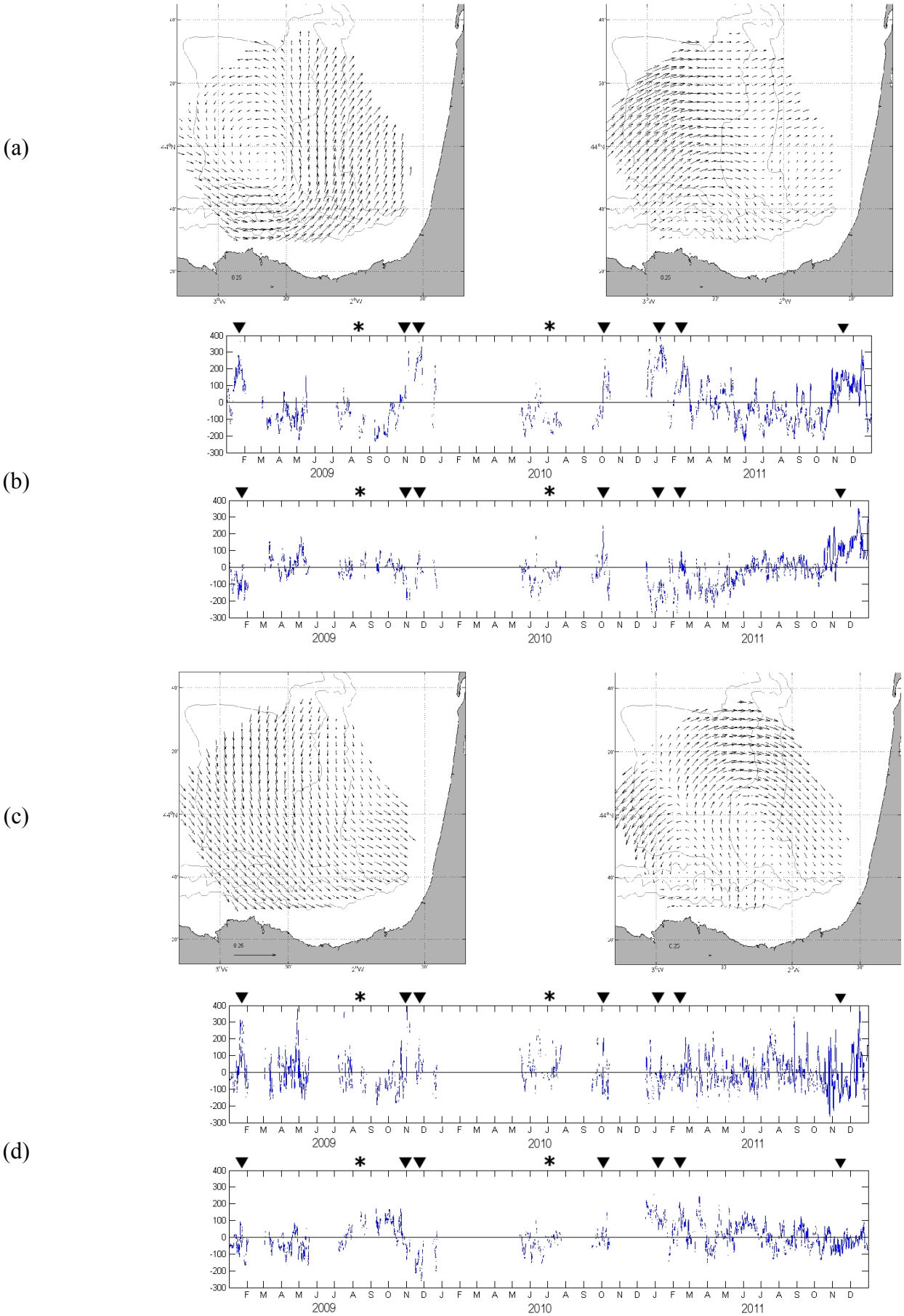

Figura 18: Resultados del análisis EOF aplicados a datos de baja frecuencia. (a) Modos espaciales 1 y 2; (b) Series temporales de los modos 1 y 2. (c) Modos espaciales 3 y 4; (d) Series temporales de los modos 3 y 4. Batimétricas: 200, 1000, 2000m

mientras que en verano predominan los negativos. Por lo que el modo 1 muestra una circulación ciclónica durante el invierno y anticiclónica durante el verano. Se observa una relación entre los eventos positivos del modo 1 y las corrientes persistentes hacia el este de la Figura 17. De forma parecida, los eventos negativos del modo 1 se corresponden con las corrientes persistentes hacia el oeste de la Figura 17. Esta observación está de acuerdo con diversos estudios previos (Le Cann y Serpette 2009; García-Soto, 2004; García-Soto *et al*., 2002; van Aken, 2002; Pingree y Le Cann, 1992a, 1992b; Rubio *et al*, 2011). La serie temporal del modo 1 también sugiere que durante el invierno las corrientes son 3 veces más intensas que durante el verano. El modo 2 explica el 16% de la varianza y presenta una circulación principalmente hacia el noreste, intensificado sobre la zona oeste y corrientes débiles sobre la plataforma. En la serie temporal se observa que los valores más intensos se observan durante los 3 últimos meses de 2011 y no presenta una clara estacionalidad. El modo 3 explica el 12% de la varianza y el flujo es hacia el sureste. Sobre el talud francés se observan corrientes débiles, con intensificación cerca de la costa española y sobre el talud. En este modo tampoco se observa ninguna estacionalidad. El modo 4 explica un 10% de la varianza y presenta dos áreas con patrones de circulación cerrada.

Globalmente, el modo 1 es el que está contribuyendo principalmente a la variabilidad estacional observada en el área de estudio, determinando la circulación ciclónica/anticiclónica. Los modos 2, 3 y 4 añaden complejidad a la circulación y contribuyen a la intensificación de la corriente sobre el talud y a la presencia de patrones de circulación cerrados. También contribuyen a la interanualidad observada y descrita previamente.

4.3. CORRIENTES DE MAREA E INERCIALES

4.3.1. Análisis EOF a las corrientes inerciales

Los primeros 4 modos de las corrientes en la banda inercial representan más del 70% de la varianza total (Figura 19).

El modo 1 explica el 35% de la varianza y presenta un campo de corrientes no uniforme, con vectores orientados N-S sobre la zona sur y sobre NE-SO en la zona noroeste. Se observan intensidades mayores sobre la parte más profunda del talud, con intensidades menores sobre la plataforma francesa y sobre el talud español. Similar a los

siguientes 3 modos, la serie temporal de amplitud cambia de signo a lo largo del periodo inercial (TL ~17.04 h). La amplitud de las oscilaciones presenta una clara estacionalidad, con mayores valores en verano que en invierno. El modo 2 presenta el 23% de la varianza. Este campo de vectores está orientado E-O; es bastante uniforme y unidireccional, para la mayor parte del área de estudio. Cabe destacar que en la mayoría de la zona de estudio, los vectores del modo 2 son perpendiculares a los del modo 1. El modo 3 explica el 11% de la varianza y muestra una distribución de corrientes más compleja con un área central de vectores más débiles. Los vectores se intensifican en el SE y son más débiles en el norte. La serie temporal sugiere que 2009 es el año con mayores oscilaciones de este modo. El modo 4 explica sólo el 6% de la varianza. De forma parecida al modo 3, hay una zona central donde los vectores son más débiles y en este caso, orientados perpendicularmente a los del modo 3.

Para interpretar los resultados, los modos 1 y 2 se analizan conjuntamente. Teniendo en cuenta que el desfase de la serie temporal de ambos modos es de ~TL/4, combinando los modos de dos en dos, se completa la oscilación inercial; esta oscilación está intensificada en el centro y noroeste de la zona de estudio. La combinación conjunta de los modos 3 y 4, vuelve a completar la oscilación inercial completa. Teniendo en cuenta los 4 modos, mientras que los modos 1 y 2 contribuyen fuertemente a la modulación estacional de las oscilaciones y la intensificación en la zona central, los modos 3 y 4 contribuyen a la intensificación o debilitamiento de las gradientes espaciales de la amplitud de las oscilaciones.

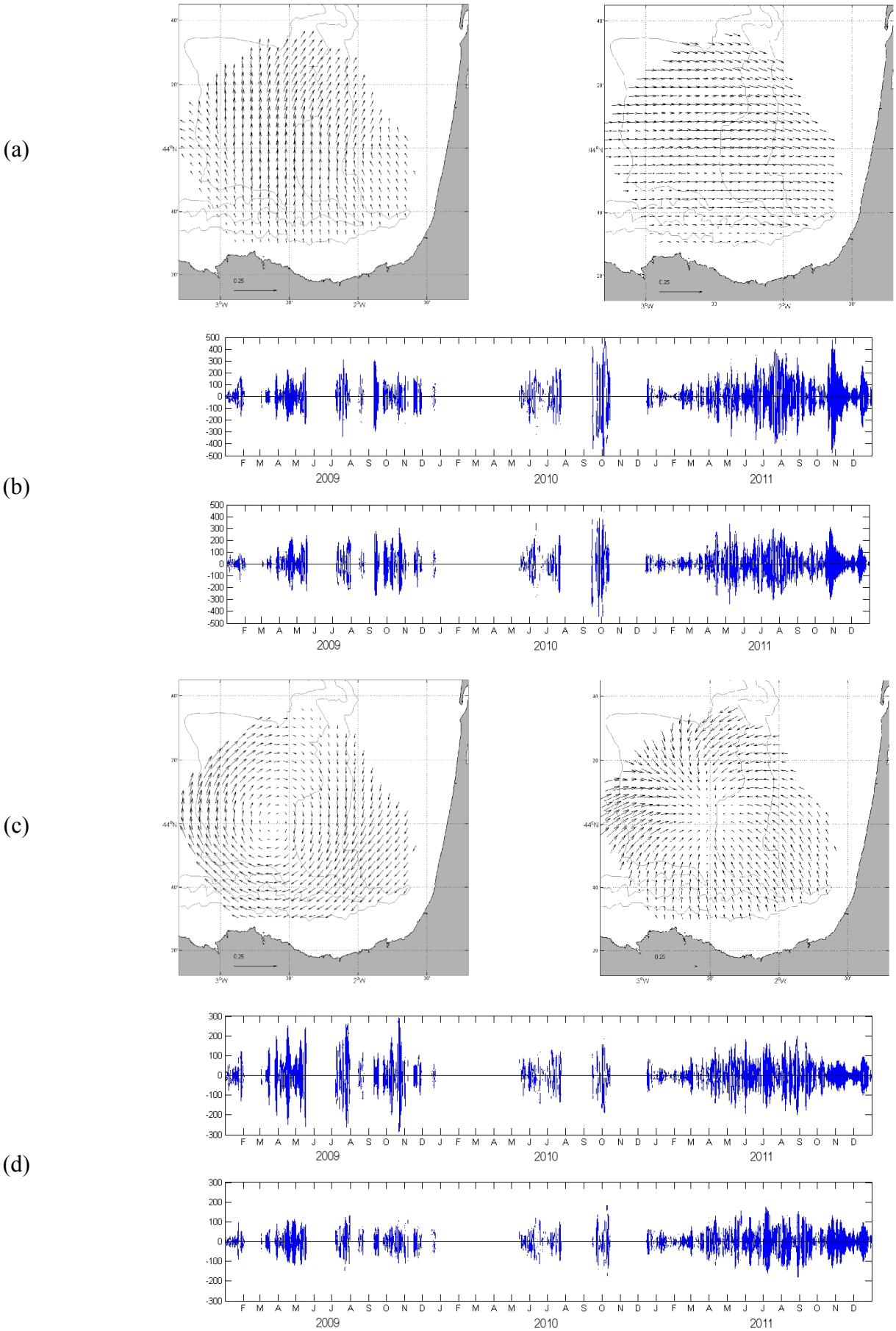

Figura 19: Resultados del análisis EOF aplicado a datos de la banda inercial. (a) Modos espaciales 1 y 2; (b) Series temporales de los modos 1 y 2. (c) Modos espaciales 3 y 4; (d) Series temporales de los modos 3 y 4. Batimétricas: 200, 1000, 2000m.

4.3.2. Contribución de la banda de alta frecuencia a las corrientes totales

La contribución cuantitativa de las corrientes de marea e inercia, a la energía cinética, se muestra en la Figura 20.

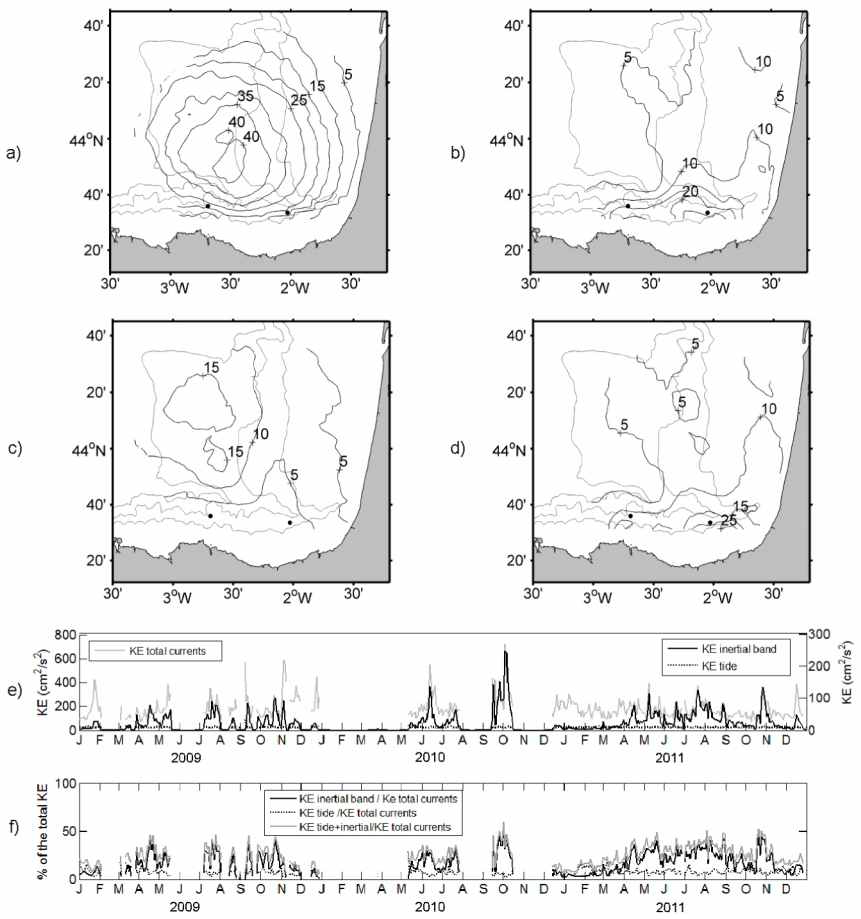

Figura 20: Contribución (porcentajes) a la energía total de la variabilidad contenida en las bandas inercial (a,c) y (mareal) (b,d). (a,b) meses de circulación de verano (media temporal de las distribuciones espaciales para julio, agosto y septiembre) y (c,d) meses con circulación de invierno (media temporal de las distribuciones espaciales para noviembre, diciembre y enero). Batimétricas: 200, 1000 y 2000m. (e) Evolución temporal de la energía cinética media de las corrientes totales (línea sólida gris, eje izquierdo) y corrientes inerciales (línea negra de puntos, eje derecho). (f) Evolución temporal de la contribución (porcentajes) a la energía cinética total de la variabilidad contenida en las bandas inercial (línea sólida negra) y mareal (línea negra de puntos) (la suma de ambas contribuciones está dibujada en una línea sólida gris).

La contribución relativa de ambos procesos es variable en el espacio y en el tiempo, siendo más importante en verano, cuando la intensidad total de las corrientes es más débil. En general, las corrientes inerciales representan entre un 10-40% de la variabilidad total. Espacialmente, su distribución presenta un máximo de energía sobre

la parte más profunda del talud en invierno y centrada cerca de 44ºN y 2º 30'O en verano. Por el contrario, la mayor contribución de la marea está entre 10-15% de la energía cinética total. Las corrientes inerciales presentan una fuerte estacionalidad. En general su contribución es máxima desde marzo a octubre. La contribución de la marea es menos fuerte, excepto en invierno, donde puede ser similar o incluso más fuerte que la de la inercia en las zonas más someras.

4.4. DISCUSIÓN Y CONCLUSIONES

La señal dominante de la zona, reflejada principalmente por el modo 1 del análisis EOF de las corrientes filtradas de paso bajo, muestra una circulación estacional sobre el talud. Este modo está intensificado sobre la parte alta del talud, por lo que se puede relacionar con la IPC y su estacionalidad, de acuerdo a diversos autores (Pingree y Le Cann, 1992a, 1992b; García-Soto *et al*., 2002; García-Soto, 2004; Le Cann y Serpette 2009). El análisis conjunto de radar HF y la boya de Matxitxako, muestra una corriente hacia el este y norte frente a las costas española y francesa respectivamente durante el invierno, alcanzando los 70 cm • s^{-1}. La buena correlación entre la corriente superficial y las corrientes más profundas, sugieren que a lo largo de gran parte del año, la señal superficial del talud afecta al menos a los primeros 100 m de la columna de agua; esto es más evidente en invierno, cuando la IPC se intensifica sobre el talud. En verano, la circulación se invierte y la intensidad de las corrientes es 3 veces más débil.

El modo 1 del análisis EOF de la serie de baja frecuencia, revela también, la presencia de un remolino ciclónico persistente durante el invierno y anticiclónico durante el verano. La actividad de mesoescala en el SE del Golfo de Bizkaia ha sido estudiado por muchos autores (Pingree y Le Cann, 1992a, 1992b; García-Soto *et al*. 2002; Serpete *et al*., 2006; Caballero *et al*., 2008; Caballero *et al.*, 2013) y éstos relacionan la generación de los remolinos a la interacción de la corriente de talud con la compleja batimetría. Los modos 2, 3 y 4, tienen menor señal estacional y añaden complejidad a la circulación descrita anteriormente. La uniformidad de las corrientes del modo 2 sugieren que éste puede estar relacionado con la señal dominante del viento local (de acuerdo con Fontán *et al*., 2013). El modo 3 será importante en procesos de afloramiento y hundimiento.

En las frecuencias entre varias horas y un día, las corrientes de marea e inerciales añaden complejidad a los patrones anteriores. Los modos EOF de las corrientes inerciales muestran 2 modos principales (1 y 2) relacionados con la modulación estacional de las oscilaciones inerciales en el área de estudio y su intensificación en la

zona central. La contribución relativa de estos procesos a la energía cinética total es variable en el espacio y en el tiempo. Globalmente, las corrientes inerciales representan entre un 10-40% de la variabilidad total, siendo su contribución mayor en verano.

El análisis realizado en este capítulo es el primer paso para mejorar el conocimiento de la circulación superficial multiescalar del SE del Golfo de Bizkaia. Aunque estos 3 años de datos han ofrecido una visión inestimable de la circulación, una serie de datos más larga permitirá el análisis de otros procesos como es el caso de la variabilidad interanual, ya observada en este estudio. Algunos estudios relacionan la circulación del talud del Golfo de Bizkaia a oscilaciones remotas como la NAO o el EA (Le Cann y Serpette, 2009 y García-Soto y Pingree, 2012). El análisis de estos procesos a partir de los datos radar HF es una línea de trabajo futura de especial interés.

CAPÍTULO V: CIRCULACIÓN SUPERFICIAL E INTERACCIÓN CON EL VIENTO UTILIZANDO ALGORITMOS DE CLASIFICACIÓN

Este capítulo analiza la relación entre las corrientes superficiales y los vientos, utilizando una técnica de clasificación de series de datos. En este contexto, se establecen 2 objetivos: (i) utilizar el algoritmo KMA (Hastie *et al*., 2001) para estudiar patrones de corriente y viento; (ii) estudiar la relación entre las corrientes y los vientos mediante probabilidades condicionadas. Al final se estudiará la relación entre la IPC y las corrientes, utilizando una serie de datos de IPC basada en imágenes SST (Esnaola *et al*., 2013).

5.1. DATOS

El filtro de paso bajo descrito en el capítulo IV, se ha aplicado a la serie de datos radar HF de 2009-2013, antes de aplicar la técnica de clasificación KMA. Para el mismo periodo de tiempo, se ha aplicado el mismo análisis KMA a los vientos del modelo WRF (Weather Research and Forecasting atmospheric numerical model) de MeteoGalicia (Skamarock *et al*., 2005), con una resolución de 12 km.

Para la estimación de la serie de IPC, se han utilizado imágenes SST con 4 km de resolución espacial, disponibles para 1981-2012 en http://www.nodc.noaa.gov. Estos

datos han sido preprocesados, extrayendo los datos del Golfo de Bizkaia y seleccionando sólo los datos con mejor calidad.

5.2. ALGORITMO DE CLASIFICACIÓN K-MEDIAS (KMA)

Los métodos de clasificación son una alternativa a los análisis lineales de series de datos, con la ventaja de manejar relaciones no lineales. En este estudio se ha elegido el método KMA, ya que permite clasificar la serie de datos cubriendo la mayor parte del espacio de datos (incluso datos cercanos a los extremos) (Camus *et al*., 2011). El algoritmo KMA divide el espacio de datos en un número reducido de grupos, representados por un prototipo que es el más similar a cada uno de los datos pertenecientes a ese grupo. Cabe destacar que el prototipo es un dato de la serie de datos.

En este estudio, se ha aplicado esta técnica a las corrientes radar HF del SE del Golfo de Bizkaia y a los vientos del Golfo de Bizkaia, para obtener 12 grupos representativos, para cada una de las series. El criterio de decisión del número de grupos está sin resolver todavía (Guanche *et al*., 2013). La recomendación es elegir el número de grupos que simplifican la interpretación, sin perder mucha variabilidad. En este caso, se han elegido 12 grupos de vientos y corrientes, después de hacer pruebas con diferentes números de grupos (9, 12, 16). Este número de grupos representa los patrones de vientos y corrientes conocidos en la zona de estudio (González *et al*., 2002, 2004; Solabarrieta *et al*., 2014) y ofrece una buena descripción de los mismos.

5.3. RELACIONES PROBABILÍSTICAS

Una vez obtenidos los grupos o patrones del predictor (viento) y predictando (corrientes) mediante la técnica KMA, es posible estudiar las probabilidades condicionadas entre ambas variables, P_{xy}. De este modo se estudiarán las probabilidades de ocurrencia de los grupos de corrientes (CG) para cada uno de los grupos de viento (WG).

5.4. OCURRENCIA DE SERIES DE TIEMPO DE IPC

Las series de datos diarios de ocurrencia de la IPC de los periodos de invierno (noviembre, diciembre, enero, febrero), para 1981-2010 se pueden encontrar en Esnaola *et al*. (2013). Esta serie temporal se genera a partir de datos SST reconstruidos del Golfo

de Bizkaia. Para este trabajo, se ha extendido esta serie de datos para cubrir el periodo de estudio, de la misma forma en la que se hizo en Esnaola *et al*. (2013).

5.5. RESULTADOS

5.5.1. Patrones de viento y corriente

En este capítulo, el periodo de invierno se refiere a los meses de noviembre a marzo y el periodo de verano se refiere a los meses de julio a septiembre (siguiendo la terminología de Solabarrieta *et al*. 2014).

La Figura 21 muestra una malla de resultados de 4 x 3 del análisis KMA aplicado a los vientos y sus características principales se resumen en la Tabla 4. Cerca del 44% de ellos son vientos del norte (WG-1-2-4-10-11) y cerca del 45% son vientos del sur (WG-3-5-6-7-8-12). El 10% restante (WG9) son vientos variables en espacio e intensidad, que representan, seguramente, periodos de calma.

Se ha calculado la probabilidad de ocurrencia de los grupos de viento durante verano e invierno y se ha observado una estacionalidad en los grupos WG-3-5-6-7-8-9-11-12, con probabilidades de ocurrencia superiores al 50% en verano o invierno (Tabla 4) (excluyendo WG-9-12, que predominan en una estación pero con probabilidad <50%). Todos ellos son vientos de invierno (excepto WG9) y confirman la estacionalidad conocida con vientos del nor-noroeste en verano y del sur en invierno). Cabe destacar que el 36% de los vientos no son estacionales, lo que significa que hay vientos del norte también en invierno. La Figura 22 también muestra que los vientos WG-1-2-4 del nor-noroeste tienen gran probabilidad de ocurrencia en verano aunque no presenten clara estacionalidad. WG-7-8-12 son vientos estacionales del sur que ocurren principalmente en invierno (

Tabla *5*), aunque aparezcan durante todo el año (Figura 22).

Se ha estudiado la probabilidad de ocurrencia de cada grupo de vientos para cada año (2009-2013), para ver si hay interanualidad (

Tabla *5*). Cuantitativamente y teniendo en cuenta el percentil 95 (30%), ningún grupo presenta una clara interanualidad. Pero una inspección cualitativa a la Figura 22, destaca que los grupos WG-3-5-7 tuvieron mayor probabilidad de ocurrencia durante los inviernos 2011-13.

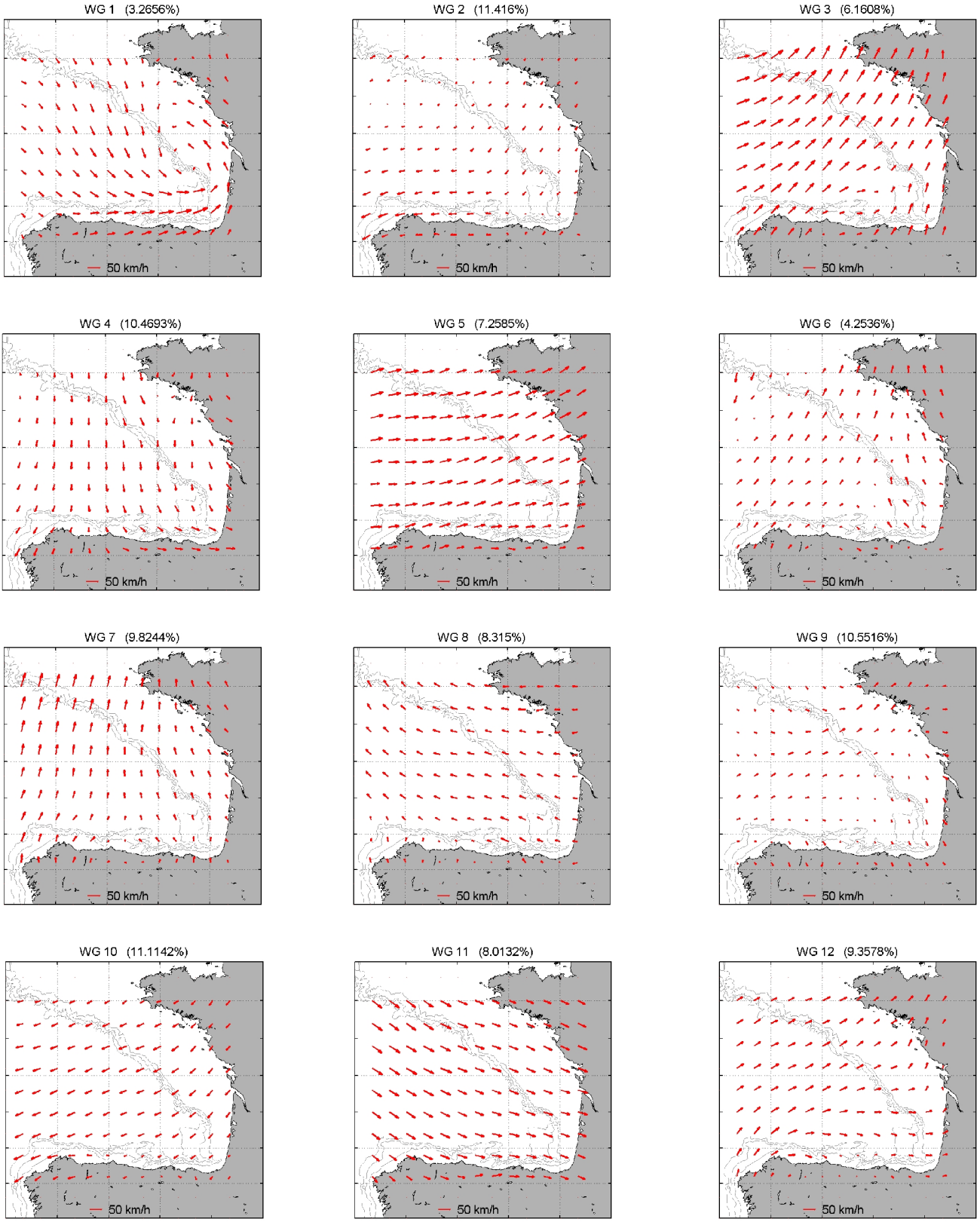

Figura 21: Patrones resultantes del análisis KMA aplicado a los vientos del modelo WRF.

Orientación		Grupo de Viento	Estaciona-lidad	% ocurrencia			Descripción		Velocid. max. [cm/s]	Velocid. media [cm/s]
							Golfo de Bizkaia	Área Radar HF		
N	E	WG2	no	11.41	22.52	44.25	Patrón anticiclónico cerrado centrado en 47,5ºN, 7ºO	Vientos muy débiles de noreste	39,85	15,51
		WG10	no	11.11			Vientos del noreste	Vientos más débiles del noreste	46,15	24,94
	O	WG1	no	3.26	21.73		Patrón ciclónico cerrado, centrado en 45º30' N and 3º O	Vientos del suroeste con velocidades máximas	64,08	28,90
		WG4	no	10.46			Vientos homogéneos del norte (giro ciclónico sobre la costa)	Vientos del noroeste y oeste	43,92	24,3
		WG11	i*	8.01			Vientos fuertes del noroeste	Vientos más débiles del noroeste	48,63	37,44
S	E	WG8	i*	8.31	8.31	45.14	Vientos del este, con una ligera tendencia al giro anticiclónico en la parte noreste	Vientos débiles del este	37,26	22,06
		WG6	i*	4.25	14.07		Vientos del sur, con gran variabilidad de velocidades	Vientos del sureste	39,92	20,23
		WG7	i*	9.82			Vientos intensos del sur, con dirección uniforme	Vientos del sureste	55,47	27,79
	O	WG3	i*	6.16	22.76		Patrón de vientos del suroeste. Tiene un giro paralelo a la costa en 5ºO.	Vientos del sur	57,31	42,69
		WG5	i*	7.25			Vientos fuertes y homogéneos del oeste	Vientos del oeste, fuertes y homogéneos	53,85	41,90
		W12	i	9.35			Vientos del suroeste (similar a WG3)	Vientos del oeste	41,54	24,84
-	-	WG9	v	10.55	10.55	10.55	Vientos débiles con gran variabilidad espacial	Vientos del noroeste	26,13	13,89

*Tabla 4: Las columnas contienen, de izquierda a derecha: (i) Dirección del viento. (ii) Número del grupo de viento. (iii) Estacionalidad. (i: mayor ocurrencia en invierno; v: mayor ocurrencia en verano. * la probabilidad de ocurrencia en ese periodo es > 50%). (iv) La probabilidad de ocurrencia de cada grupo de vientos. (v) Las principales características del viento. (vi-vii) velocidades máximas y medias del viento.*

	2009	2010	2011	2012	2013	∑ 2009-13	Invierno (I)	Verano (V)	∑ (I,V)
WG1	13,36	30,40	13,42	15,48	27,32	100	48,90	15,42	64,32
WG2	10,72	17,11	17,97	32,20	21,98	100	30,55	36,07	66,62
WG3	26,02	3,87	16,07	25,88	28,14	100	82,85	2,23	85,08
WG4	8,90	28,34	21,85	16,80	24,07	100	37,15	15,85	53
WG5	27,35	10,44	22,98	25,52	13,67	100	76,00	12,57	88,57
WG6	22,43	10,38	30,34	22,02	14,81	100	63,30	6,73	70,03
WG7	16,16	15,56	28,14	19,32	20,80	100	55,68	12,06	67,74
WG8	16,42	18,68	18,70	20,15	26,02	100	54,97	14,40	69,37
WG9	14,25	27,61	21,59	18,59	17,92	100	29,01	41,57	70,58
WG10	27,60	27,74	10,15	18,22	16,26	100	39,15	29,05	68,2
WG11	28,56	11,56	20,25	16,88	22,72	100	56,99	19,76	76,75
WG12	27,36	11,90	27,50	17,73	15,48	100	48,85	19,60	68,45

Tabla 5: Estos valores representan la variabilidad de cada grupo de viento, durante el periodo de estudio. Los valores son los % de ocurrencia de cada grupo, durante cada año o en verano (julio a septiembre) o invierno (noviembre a marzo).

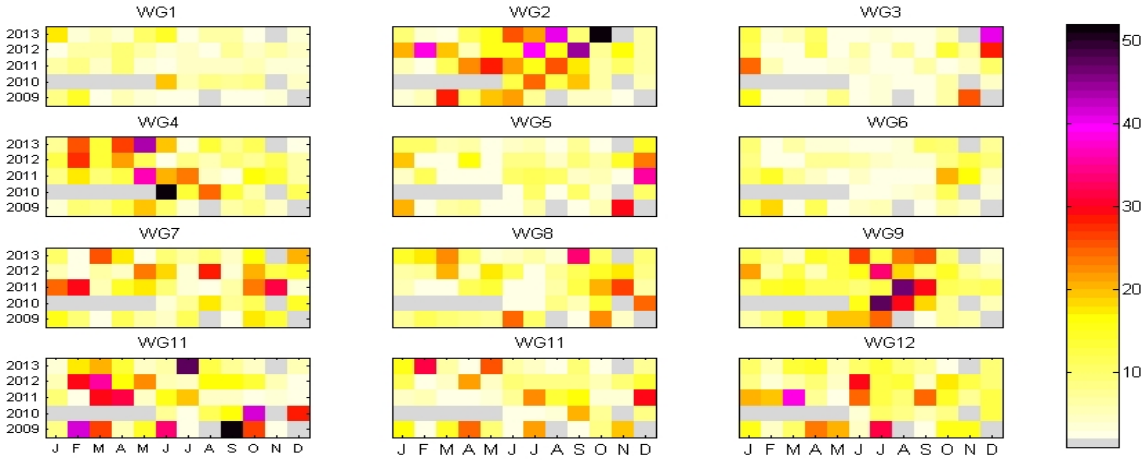

Figura 22: % de ocurrencia de cada grupo de vientos para cada uno de los meses de los 5 años de estudio. %. Los meses con menos del 50% de datos, están sombreados en gris y no se han tenido en cuenta.

La Figura 23 muestra una malla de resultados de 4 x 3 del análisis KMA aplicado a las corrientes y sus características principales se resumen en la Tabla 6. Los 12 CG descritos resumen el conocimiento previo de las corrientes de la zona de estudio. Cerca del 40% de las corrientes muestran corrientes hacia el norte (CG-3-5-6-12) y otro 25% son corrientes hacia el sur (CG-4-7-9). Dentro de las corrientes hacia el norte, los más intensos son los que presentan corrientes hacia el norte-este (CG3-6) con velocidades medias de 15 y 10 cm • s^{-1}, respectivamente. Los grupos con corrientes hacia el norte-oeste (CG-5-12) son similares y sólo varían en intensidad. Dentro de los grupos con corrientes hacia el sur, los CG4-9 (hacia el sur-este) son similares y el CG7 tiene un giro hacia el este sobre el talud español, con corrientes de ~ 7 cm • s^{-1}. El porcentaje restante (33%) lo componen los grupos ciclónicos CG-1-8-10-11 y anticiclónico CG2.

Se ha calculado la probabilidad de ocurrencia de los grupos en verano Tabla 7 y se ha identificado un carácter estacional en los grupos CG-1-2-3-4-6-8-11-12. La mayoría de estos grupos presentan patrones ciclónicos o anticiclónicos (CG-1-2-8-11), siendo el grupo CG10 el único con carácter ciclónico no estacional. CG-3-6-12 son también estacionales pero muestran patrones ciclónicos no cerrados. CG4 también muestra estacionalidad con mayor ocurrencia en invierno y corrientes hacia el sur-oeste. Dentro de los grupos estacionales, hay dos tendencias: anticiclónicos en verano (CG2) y ciclónicos en invierno (CG-1-3-6-8-11-12). CG-4-12 se han identificado como grupos estacionales de invierno pero hay que señalar que también ocurren durante los meses de verano (Figura 24).

Se ha calculado la probabilidad de ocurrencia de los grupos a lo largo de los 5 años del periodo de estudio para ver su interanualidad. El percentil 95 (40%) muestra que hay diferencias significativas en los CG-1-2-3-7-8-11 a lo largo de los 5 años, por lo que se consideran grupos con variación interanual. Aunque los grupos CG-3-6-12 no presentan valores superiores al umbral propuesto, tienen mayor presencia durante los inviernos de 2011-13, lo que sugiere su carácter interanual (Figura 24). CG7 también tiene mayor ocurrencia durante 2011-13. CG-1-2-11 aparecen más durante 2009-10 mientras que CG8 tiene probabilidad de ocurrencia del 98% durante 2011 (Figura 24).

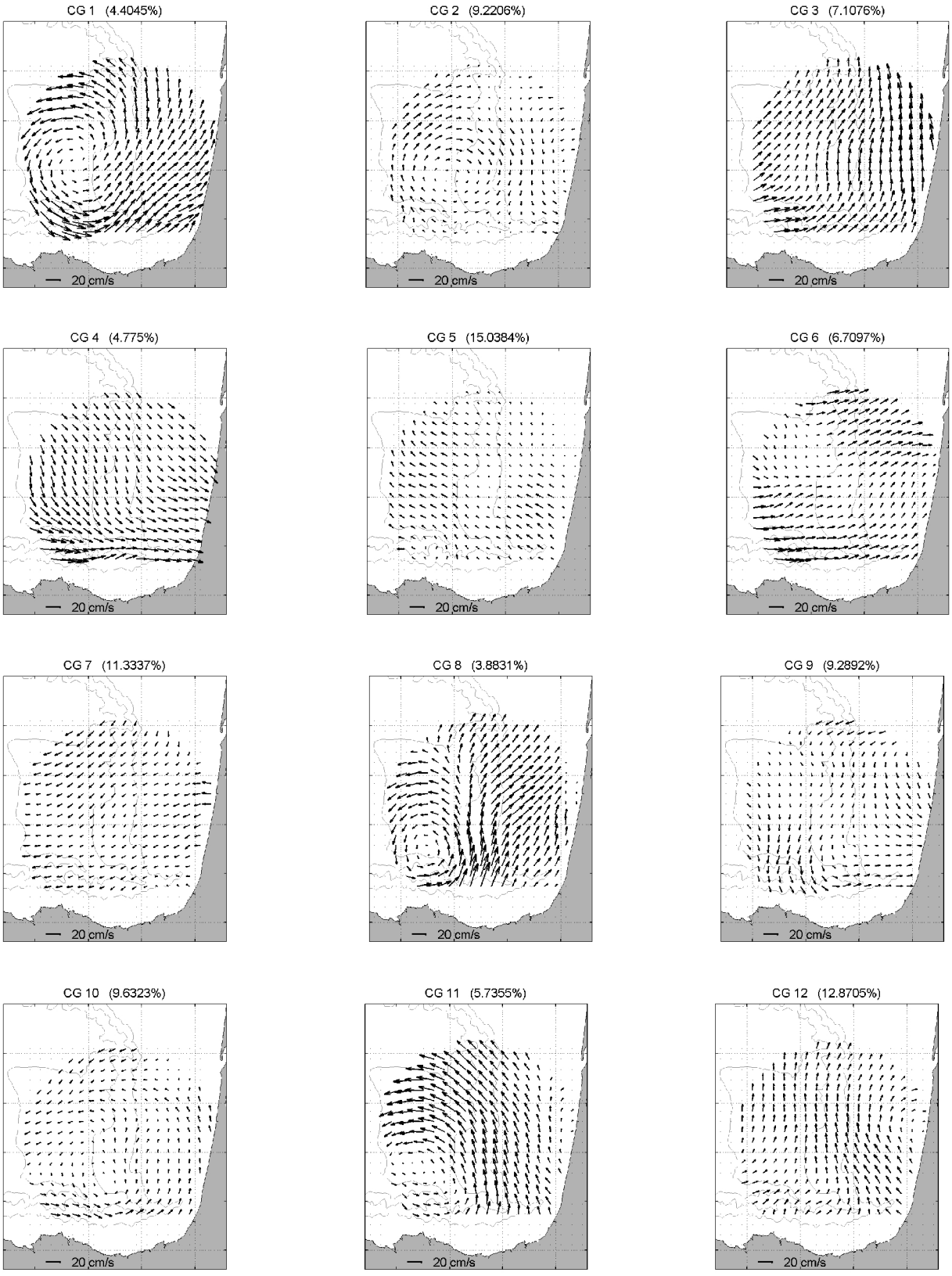

Figura 23: Patrones resultantes del análisis KMA aplicado a las corrientes radar HF.

Orientación		Grupo de Viento	Estaciona-lidad	Interanualidad (I)	% ocurrencia			Descripción	Velocidad máx. [cm/s]	Velocidad media [cm/s]
N	E	CG3	i*	I	7.10	13.8	41.7	Patrón de corrientes hacia el norte paralelos a la costa, con un giro ciclónico abierto sobre el cañón de Cap Bretón	24.26	14.88
		CG6	i*	I	6.70			Corrientes que vienen del oeste y giran hacia el norte en la esquina SE del Golfo de Bizkaia	35.44	10.57
	O	CG5	no		15.03	27.9		Corrientes débiles con gran variabilidad. Corrientes hacia el noroeste	11.59	5.42
		CG12	i*		12.87			Patrón de corrientes uniformes y hacia el norte	13.90	8.71
S	E	CG4	i*		4.77	14.05	25.38	Corrientes hacia el noroeste que generan hundimiento en la costa francesa.	37.37	12.67
		CG9	no		9.28			Corrientes débiles hacia el sur, con gran variabilidad especial y de velocidad	14.13	6.61
	O	CG7	no		11.33	11.33		Grupo de corrientes débiles hacia el suroeste	13.10	7.01
Giro cerrado ciclónico		CG1	i*	I	4.40	23.64	32.85	Patrón ciclónico cerrado, con corrientes fuertes centrado en 44ºN and 2º45'O	33.93	16.02
		CG8	i*	I	3.88			Corriente ciclónica cerrada centradas en 43º50'N y 2º45'O	36.14	14.19
		CG10			9.63			Patrón ciclónico cerrado , con corrientes débiles y velocidades homogéneas	13.60	5.81
		CG11	i*	I	5.73			Patrón centrado en 43º50'N y2º45'O, con altas velocidades (27 cm/s)	27.26	13.58
Giro cerrado anticiclónico		CG2	v*		9.22	9.22		Patrón débil anticiclónico y cerrado, centrado en 44ºN, 2º30'O	14.03	5.47

*Tabla 6: Las columnas contienen, de izquierda a derecha: (i) Orientación de la corriente. (ii) Número del grupo de corrientes. (iii) Estacionalidad. (i: mayor ocurrencia en invierno; v: mayor ocurrencia en verano. * la probabilidad de ocurrencia en ese periodo es > 50%). (iv) Interanualidad. (v) La probabilidad de ocurrencia de cada grupo de corrientes. (vi) Las principales características de la corriente. (vii-viii) velocidades máximas y medias de la corriente.*

	2009	2010	2011	2012	2013	∑ 2009-13	Invierno (I)	Verano (V)	∑ (I,V)
CG1	71,97	25,18	2,83	0	0	100	87,58	0,00	87,58
CG2	28,23	50,38	10,84	6,68	3,85	100	11,01	61,16	72,17
CG3	0	0	20,63	40,63	38,73	100	85,91	0,00	85,91
CG4	23,32	23,87	11,01	19,70	22,13	100	60,81	18,44	79,25
CG5	31,87	7,52	13,67	15,95	30,97	100	28,25	28,44	56,69
CG6	1,32	5,76	30,05	31,52	31,33	100	79,63	6,17	85,8
CG7	4,33	0,51	22,97	48,21	23,96	100	41,16	32,45	73,61
CG8	1,94	0	98,05	0	0	100	92,58	0,00	92,58
CG9	18,36	24,48	15,77	14,67	26,68	100	26,55	30,32	56,87
CG10	15,54	25,61	21,51	20,17	17,14	100	27,71	24,34	52,05
CG11	35,58	56,48	3,36	0	4,56	100	85,35	0,00	85,35
CG12	3,04	6,22	28,21	34,72	27,79	100	55,65	7,78	63,43

Tabla 7: Estos valores representan la variabilidad de cada grupo de corrientes, durante el periodo de estudio. Los valores son los % de ocurrencia de cada grupo, durante cada año y en verano (julio a septiembre) o invierno (noviembre a marzo).

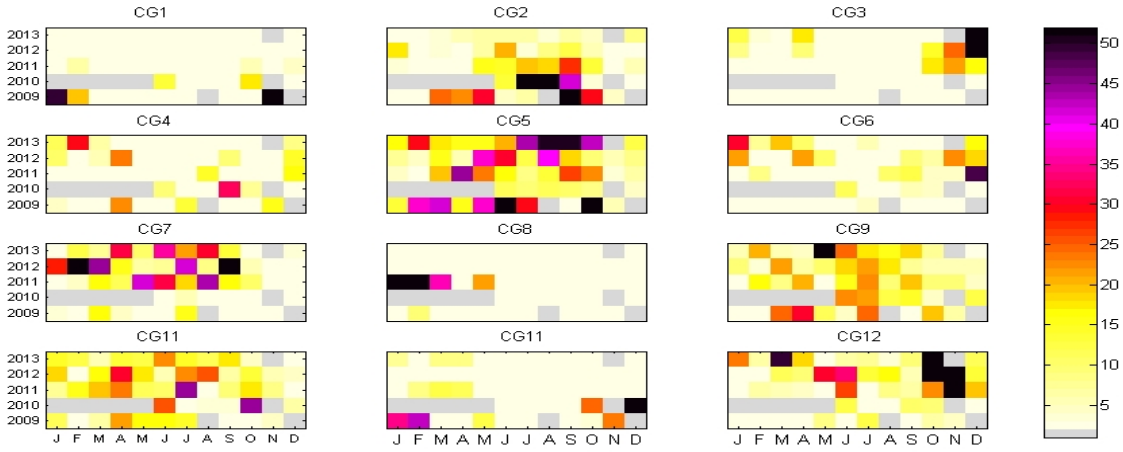

Figura 24: % de ocurrencia de cada grupo de corrientes para cada uno de los meses de los 5 años de estudio. %. Los meses con menos del 50% de datos, están sombreados en gris y no se han tenido en cuenta.

5.5.2. Relaciones probabilísticas entre patrones de viento y corriente

La Figura 25 establece las probabilidades de ocurrencia de cada uno de los 12 grupos de corrientes (12 CG) condicionada a los 12 grupos de viento (12 WG). En este apartado sólo se estudiarán las relaciones que presenten probabilidades de ocurrencia conjunta superiores al 25%.

WG2-10 son vientos del noreste y están relacionados con el grupo CG5 (corrientes hacia el norte-oste) y CG7 (corrientes hacia el sur-oeste).

En los grupos WG1-4-11 (vientos del norte-oeste) se observan altas probabilidades con CG9 (corrientes hacia el sur-oeste) (Figura 25). WG-1-11 están también relacionados con CG6 (corrientes paralelas a las costas española y francesa). WG11 también tiene altas probabilidades de ocurrencia con CG4, que es similar al CG9 pero más intenso. WG4 está principalmente relacionado con CG7, que son corrientes hacia el sur-oeste.

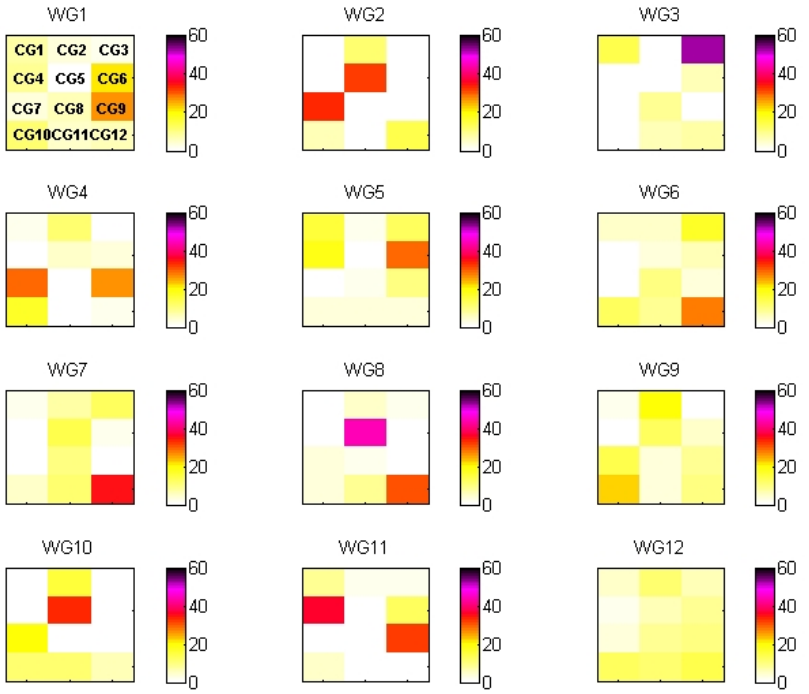

Figura 25: Probabilidades de ocurrencia de los 12 grupos de corrientes sobre cada uno de los grupo de viento.

WG8 presenta los vientos del sur-este más intensos y homogéneos y está estrechamente relacionado con CG5 (corrientes variables hacia el norte-oeste) y CG12 (corrientes hacia el norte). WG3 presenta los vientos más intensos del sur-oeste y está muy ligado al CG3 (corrientes hacia el norte-noreste, coincidiendo en dirección. WG5 es el segundo grupo más intenso de vientos del SO y está relacionado con CG6 (corrientes hacia el este frente a la costa española y hacia el noreste frente a la costa francesa).

Finalmente WG9 está relacionado con CG10, siendo ambos variables y poco intensos.

5.5.3. Patrones de corriente sin relación con los grupos de viento

Hay que destacar que los grupos CG-1-2-8-10-11 no están relacionados con ningún grupo de viento, que todos son grupos con circulaciones cerradas y que todos presentan una clara estacionalidad.

5.5.4. Series de tiempo de IPC y su relación con los grupos de corrientes

La Figura 26 muestra las probabilidades de los 12 CG sobre las series de eventos de IPC +1 y -1 (siendo los -1 eventos favorables a la IPC y los +1, eventos que no favorecen las fuertes corrientes de IPC). Los grupos de corrientes CG-1-5-11 presentan altas probabilidades de ocurrencia con los IPC negativos. CG-1-11 se han caracterizado como corrientes no relacionadas con los vientos y este resultado sugiere su relación con la corriente IPC. En el caso de IPC +1, los grupos CG-3-12 son los que presentan mayores probabilidades de ocurrencia. Los parecidos entre CG-3-12 y CG-1-11 son evidentes, ya que todos presentan corrientes ciclónicas. Sin embargo, mientras que los grupos CG-1-11 son patrones cerrados mesoescalares y no presentan relación destacada con ningún viento, los grupos CG3-12 están relacionados con vientos del sur-este (WG-3-5).

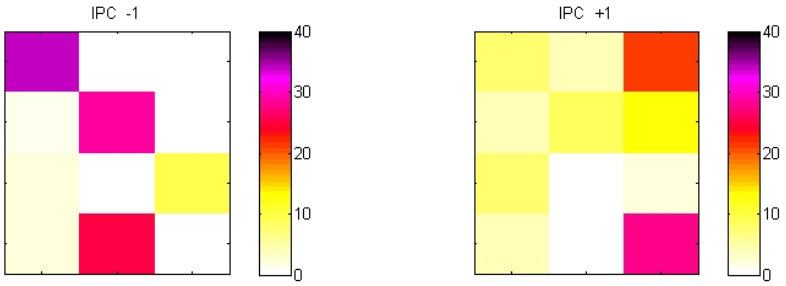

Figura 26: Probabilidades de ocurrencia de los 12 grupos de corrientes sobre las series de datos de IPC -1 e IPC +1

5.6. DISCUSIÓN Y CONCLUSIONES

La mayoría de los posibles escenarios de viento y corriente, se han descrito con los resultados del análisis KMA. Presentan vientos intensos del suroeste en otoño e invierno y más variables y del noreste en primavera y verano (González *et al*. 2004). Del mismo modo, se han observado corrientes conocidas en los 12 grupos de corrientes (CG) (Le Cann y Serpette 2009; Rubio *et al*. 2013; Solabarrieta *et al*. 2014) con corrientes hacia el este (norte) sobre el talud de la costa española (francesa) en invierno y corrientes en sentido opuesto y menor intensidad en verano.

El 44% de los vientos son del norte, el 45% del sur y el restante 10% son vientos variables. Se ha observado variabilidad estacional en algunos vientos del sur con ocurrencia en invierno. No se ha podido establecer interanualidad en los vientos, pero esto puede ser debido a que sólo se dispone de 5 años de datos.

Cerca del 40% de las corrientes tienen circulación hacia el norte y cerca del 25% hacia el sur. Dentro del primer grupo, los más intensos tienen circulación hacia el este (norte) sobre la plataforma-talud español (francesa). El 33% restante corresponde a grupos con corrientes más complejas y variables. Se ha observado variabilidad estacional en sólo 8 grupos de corrientes (55% de ocurrencia). En estos grupos se observan 2 tendencias: corrientes anticiclónicas en verano y ciclónicas en invierno. También se ha observado variabilidad interanual en los patrones ciclónicos y anticiclónicos. Los patrones ciclónicos no cerrados tienen mayor ocurrencia en 2011-13 mientras que los cerrados son más persistentes durante 2009-10. El patrón anticiclónico de verano es más recurrente en 2009-10.

Aunque la relación entre vientos y la dinámica superficial de las corrientes es conocida, esta relación no siempre es sencilla. La dispersión de las probabilidades de ocurrencia de las corrientes sobre los vientos refleja esta compleja relación entre ambos. Estrictamente, las relaciones probabilísticas entre vientos y corrientes, no significan causalidad. En este sentido, los resultados de este capítulo serán discutidos teniendo en cuenta estas limitaciones y fijándose sólo en altas probabilidades de ocurrencia conjuntas.

Analizando las probabilidades de ocurrencia de las corrientes sobre los vientos, se han observado relaciones entre grupos de vientos del norte y grupos de corrientes hacia el sur y también entre grupos de vientos del sur con grupos de corrientes hacia el norte, con variaciones direccionales y espaciales.

Los grupos de corriente con circulaciones cerradas ciclónicas, no presentan relaciones significativas con los grupos de viento. Estas corrientes tienen una marcada interanualidad, siendo más recurrentes durante 2009-11. Durante el verano, también se observan corrientes no relacionados con ningún grupo de vientos en concreto, siendo estas corrientes cerradas anticiclónicas y más recurrentes en 2009 y 2010.

La relación de los grupos de corrientes con la serie de IPC, presenta una relación de los patrones ciclónicos cerrados de corrientes de invierno y no relacionados con el viento, con eventos de marcada IPC. Estas relaciones también muestran eventos no tan fuertes

de IPC, relacionados con patrones de circulación ciclónica pero no cerrada y relacionadas con grupos de vientos.

La técnica KMA ha resultado adecuada para la extracción de grupos de viento y corrientes en la zona de estudio y para caracterizar sus principales características, ya que este estudio ha permitido realizar una descripción detallada de las corrientes superficiales oceánicas y su variabilidad en relación a algunos forzamientos. Esta técnica y resultados, son interesantes para la validación de modelos, evaluación de capacidades de predicción de modelos numéricos y el estudio de patrones de transporte. Pero se necesitan más estudios para entender las características 3D de la circulación del área; especialmente las estructuras de mesoescala observadas durante algunos inviernos y veranos.

CAPÍTULO VI: CONCLUSIONES Y FUTURAS LÍNEAS DE INVESTIGACIÓN

6.1. CONCLUSIONES

- La tecnología radar HF se está utilizando desde hace más de tres décadas y esta tesis es una evidencia más de las ventajas que esta tecnología ofrece a la mejora del conocimiento y monitoreo de las corrientes superficiales.

- La comparación entre los datos radar HF y diferentes medidas disponibles es buena y las comparaciones son similares a las descritas por otros autores. Estas comparaciones refuerzan la confianza en los datos radar HF para analizar la circulación superficial en el SE del Golfo de Bizkaia y dar una nueva visión de las corrientes y su variabilidad espacio-temporal.

- Se han aplicado diferentes metodologías a los datos radar HF (por ejemplo, EOF, KMA) y se ha demostrado que son herramientas de análisis útiles para extraer patrones superficiales de corrientes y para el estudio de las diferentes escalas espacio-temporales. Teniendo en cuenta las diferencias significativas entre ellos, el acuerdo en los resultados obtenidos por ambos métodos (teniendo en cuenta que la técnica EOF proporciona patrones matemáticos teóricos, mientras que la técnica KMA clasifica patrones reales) refuerza la confianza en la metodología utilizada en la tesis. También se ha demostrado que la estrategia de utilizar el análisis de agrupamiento KMA independientemente para predictor (viento) y

predictando (corrientes) y obtener posteriormente las relaciones probabilísticas entre ellos, es un enfoque interesante para estudiar la dinámica oceánica de superficie en la zona.

- Los resultados ponen de manifiesto la continuidad de la circulación superficial sobre el talud/plataforma del SE del Golfo de Bizkaia, con orientación este-oeste (norte-sur) frente a la costa española (francesa), con una marcada estacionalidad, de acuerdo a las observaciones anteriores. La corriente circula hacia el este (norte) sobre el talud de la costa española (francesa) en invierno, con velocidades que alcanzan hasta 70 cm • s^{-1}. En verano, la circulación se invierte con intensidades 3 veces más débiles que los observados en invierno, con las corrientes predominantes hacia el oeste sobre el talud de la costa española.

- Los buenos resultados de comparación entre el radar HF y los datos de ADCP, sugieren que durante gran parte del tiempo, las corrientes superficiales más intensas sobre el talud tienen una señal vertical que afecta, al menos, a los primeros 100 m de la columna de agua

- Se ha observado la presencia y persistencia de remolinos mesoescalares, con estructuras ciclónicas predominantes durante el invierno y anticiclónicas en verano.

- La mayoría de los patrones superficiales observados, están claramente relacionados con patrones de vientos específicos, recurrentes en el área de estudio. Sin embargo, hay una gran variabilidad entre los patrones superficiales de corrientes y las interacciones viento-corriente.

- Se han identificado varios patrones de corrientes, no claramente relacionados con vientos específicos. Estos patrones, muestran circulaciones ciclónicas cerradas, con mayor ocurrencia durante los meses de invierno. Estas corrientes de invierno, con intensificación de la corriente sobre el talud, son las corrientes de oeste más intensas observadas sobre el talud. La presencia de estos patrones, está relacionada con la señal superficial de la IPC y su marcada estacionalidad.

- Globalmente, las corrientes inerciales representan entre un 10 y un 40% de la variabilidad total, siendo su contribución mayor en verano. Espacialmente, presentan un máximo de energía sobre la parte más profunda del talud, durante el invierno y que está centrado en 44ºN y 2º 30’O durante el verano. La marea

contribuye mucho menos a la energía cinética total, aunque su aportación puede ser mayor que la de las oscilaciones inerciales en las zonas más someras, durante el invierno.

- Se ha observado una variabilidad interanual entre corrientes ciclónicas y anticiclónicas. Los patrones ciclónicos que no presentan estructuras mesoescalares, tienen mayor presencia durante 2011-13 mientras que los patrones mesoescales ciclónicos cerrados tienen más persistencia durante 2009-10. El patrón anticiclónico de verano, también ha sido más recurrente durante 2009-10 (es importante tener en cuenta que este estudio se basa sólo en datos de 5 años por lo que el estudio de interanualidad está limitado)

- Los resultados dan una visión espacio-temporal global de la complejidad de las corrientes y por tanto de la complejidad en la variabilidad del transporte en el área de estudio. El conocimiento del transporte es clave para una gestión mejorada de la costa relacionada con la seguridad y contaminación marítima. Teniendo en cuenta la complejidad de la circulación, es importante resaltar el potencial que tiene el radar HF en la gestión integrada de la costa. Además, los resultados sugieren mejoras sustanciales en la generación de trayectorias para la búsqueda y rescate, ya que mejoran considerablemente los radios actuales de búsqueda.

- La técnica de clasificación OMA se usa para rellenar huecos de radar HF para que estos datos sean mejores para la gestión costera. Como el rellenado se basa en modos físicos teóricos, los campos resultantes tienen mayores errores. Pero las pequeñas diferencias observadas en la predicción lagrangiana utilizando velocidades radar HF y velocidades OMA, sugieren que éstos últimos son más adecuados para las estimaciones de transporte y trayectorias en un uso operacional.

6.2. INVESTIGACIÓN FUTURA

El análisis llevado a cabo en esta tesis, se basa en la mejora del conocimiento de la circulación superficial en el SE del Golfo de Bizkaia. Además, los 5 años de datos disponibles, han ofrecido una visión inestimable de los patrones de esta área. El continuo aumento de los datos disponibles permitirá el análisis de más procesos, como la variabilidad interanual de las corrientes superficiales y reforzar la descripción

estadística de las corrientes. Concretamente, la serie extendida de datos permitirá el análisis de la relación de la variabilidad de las corrientes sobre el talud del SE del Golfo de Bizkaia con oscilaciones remotas.

Se necesita seguir investigando para entender los mecanismos físicos que generan los patrones de circulación descritos y también para evaluar su contribución a la variación de la circulación regional. Esta tesis ha analizado la variabilidad de las corrientes en un amplio rango de escalas. El uso de técnicas similares combinadas con filtros que permitan aislar escalas específicas, es una prometedora línea de investigación futura. Asimismo también se necesita más investigación para entender las características 3D de la circulación en la zona; en concreto, de las estructuras de mesoescala observadas durante algunos periodos de invierno y verano. Para este propósito, los datos de radar HF podrían ser analizados en conjunto con boyas a diferentes profundidades, con el fin de explorar la circulación 3D.

Aunque los datos totales y OMA a tiempo casi real son adecuados para su uso en fines operativos, los productos más adecuados para la búsqueda y rescate y situaciones relacionadas con la contaminación marina deben basarse en pronósticos. En este sentido, estamos actualmente trabajando en la metodología descrita por Frolov *et al*. (2012) para proporcionar la predicción a corto plazo (48 horas) de las corrientes superficiales basadas en el estudio de corrientes pasadas y corrientes de las últimas 48 horas. Los resultados obtenidos son prometedores, aunque este estudio no se ha incluido en este manuscrito ya que se requiere más análisis para su validación e implementación de la gestión integrada en el área de estudio.

Finalmente, la aplicación de modelos numéricos de circulación oceánica y costera es una práctica común para proporcionar previsiones operativas. En el Golfo de Bizkaia hay varios sistemas de modelización operacionales que proporcionan pronóstico diario de corrientes (entre otras variables) como entrada para los modelos de derrames, para el estudio de las plumas de los ríos, los modelos de calidad del agua, modelos biológicos, etc. Tener una base de datos larga confiable y de alta resolución de radar HF, representa una valiosa oportunidad para aumentar la calidad de estos productos a través de una mejor comprensión de los procesos de circulación oceánica y de la calibración y validación del modelo. Por último, la asimilación operacional de las corrientes superficiales en tiempo real en los modelos oceánicos costeros aplicados en la zona, es otro de los beneficios esperados de esta tecnología.

UNIVERSITY OF CANTABRIA

DEPARTMENT OF SCIENCES AND TECHNIQUES

OF WATER AND ENVIROMENT

PhD. THESIS

STUDY OF THE SURFACE OCEAN DYNAMICS IN THE BAY OF BISCAY, USING HF RADAR TECHNOLOGY

Presented by: LOHITZUNE SOLABARRIETA ODRIOZOLA

Supervisors: ANNA RUBIO COMPAÑY
SONIA CASTANEDO BÁRCENA
RAÚL MEDINA SANTAMARÍA

May 2015

Abstract

2 HF (High Frequency) radar stations work operationally in the southeastern Bay of Biscay since 2009, emitting at a bandwidth of 40 kHz and a frequency of 4.86 MHz. This system provides hourly surface currents with 5.12 km spatial resolution and radial coverage lying close to 180 km, covering 10,000 km2.

Because of their spatio-temporal coverage, HF radar data have improved the knowledge of the ocean circulation characteristics in coastal areas around the word. Moreover, since HF radar systems provide data in near real time, they have become invaluable tools in the field of operational oceanography, with multiple applications for the maritime sector: coastal marine environment, research, rescue, navigation….

The first step of this PhD Thesis, has been to assess the performances of the Basque HF radar system and its potential for operational calculation of trajectories at sea. The agreement between the different available measurements and HF radar data is reasonably good. Data comparison results are consistent with those described previously by several authors. These comparisons reinforce the confidence in HF radar data to analyse the surface circulation in the SE Bay of Biscay and to provide a new insight into the currents and their spatio-temporal variability (Chapter III).

Secondly, different methodologies have successfully been applied to HF radar data (e.g. EOF, KMA) to extract surface current patterns and to study the different spatio-temporal scales. The results reveal the continuity of the along shelf/slope surface circulation in the SE corner of the Bay of Biscay, with east-west (north-south) surface circulation in front of the Spanish (French) coast, with a marked seasonality, in accordance to the previous observations. The current circulates eastward (north) over the slope off the Spanish (French) coast in winter, with speeds reaching up to 70 cm·s-1. In summer, the water circulation is reversed and has intensities 3 times weaker than those observed in winter. Vertically, the good agreement between surface HF radar data and deeper ADCP data, suggests that, most of the time, the most intense surface currents over the slope have a clear vertical signal affecting, at least, the first 100 m of the water column. The presence and persistence of eddy mesoscale circulations within

the area has been observed, with cyclonic structures in winter and anticyclonic mesoscale eddies during summer. Globally, inertial currents represent from 10 to 40% of the total variability, being their contribution significantly higher in summer. Tides contribute much less to the total KE, mainly over the shelf, although their contribution can be higher than that of inertial oscillations during winter (Chapter IV).

Most of the surface current patterns observed are clearly related to specific wind patterns, recurrent in the study area. However, there is high variability in terms of surface current spatial patterns and of wind–current interactions. Several current patterns not as clearly related with specific wind conditions have also been identified. These are patterns showing closed cyclonic circulation features with higher occurrence during winter months. These winter currents, with an along-slope circulation clearly intensified over the upper part of the slope, are the strongest westerly currents observed over the slope. Their higher occurrence during periods of winter along-slope currents (IPC) intensification, is demonstrated. The presence of these patterns is, in consequence, related to the surface signature of the slope current (IPC) and its marked seasonality (Chapter V).

Contents

List of figures

List of tables

List of acronyms

ADC	Acoustic Doppler Currentmeter
ADCP	Acoustic Doppler Current Profiler
AMO	Atlantic Multidecadal Oscillation
AIS	Automatic Identification System
APM	Antenna Pattern Measurement
ARGOS	Advanced Research and Global Observation Satellite
CCA	Canonical Correlation Analysis
CG	Current Group
CODAR	Coastal Ocean Dynamics Application Radar
CSS	Averaged cross spectra
CSQ	Unaveraged cross spectra
ENACW	Eastern North Atlantic Central Water
EOF	Empirical Orthogonal Function
FFT	Fast Fourier Transform
GDOP	Geometric Dilution Of the Precision
GFS	Global Forecast System
HF	High Frequency
IPC	Iberian Poleward Current
KE	Kinetic Energy
KMA	K-means Classification Algorithm
LPTM	Lagrangian Particle-Tracking Model

MUSIC	Multiple Signal Classification,
MW	Mediterranean Water
NAC	North Atlantic Current
NACW	North Atlantic Central Water
NAO	North Atlantic Oscillation
NCEP	National Center for Environmental Prediction
NE	North-East
NW	North-West
NOFO	NOrwegian clean seas Association For Operating companies
OMA	Open-boundary Modal Analysis
RADAR	RAdio Detection And Ranging
RMS	Root Mean Square
SOM	Self-Organizing Map
SST	Sea Surface Temperature
SE	South-Eastern
SW	South-West
SWOODIES	Slope Water Oceanic edDIES
PCA	Principal Component Analysis
PhD	Philosophy Doctor
WERA	WavE RAdar
WG	Wind Group

CHAPTER I
INTRODUCTION

1.1. INTRODUCTION

1.1.1. Framework of the Thesis

This PhD thesis has been conducted at AZTI-Tecnalia Foundation in collaboration with the University of Cantabria, within the PhD program "Science and technology for the management of the coast". It has been co-supervised by Dr. Anna Rubio Compañy, from AZTI-Tecnalia, and Professor Raúl Medina Santamaría and Associate Professor Sonia Castanedo Bárcena, from the University of Cantabria.

The main focus of the PhD thesis is the study of surface ocean currents in the Bay of Biscay at different scales, using data from a High Frequency (hereinafter, HF) oceanic radar (Radio Detection and Ranging) system. This investigation has been conducted

under the funding of Iñaki Goenaga Technological Centers Foundation (Fundación de Centros Tecnológicos Iñaki Goenaga) PhD scholarship "Surface currents in the Bay of Biscay by HF Radar".

1.1.2. Deal of the thesis

A CODAR (Coastal Ocean Dynamics Application Radar) Seasonde HF radar network is operational since the beginning of 2009 for the oceanic region of the Basque Country (south-eastern (hereinafter, SE) Bay of Biscay) (Figure 1). It forms part of the operational data acquisition system established by the Directorate of Emergency Attention and Meteorology of the Basque Government. It is made up of two antennas, located at cape Higer (43º 23.554'N, 1º 47.745'W) and cape Matxitxako (43º 27.350'N, 2º 45.163'W), emitting at 4.86 MHz frequency. This system provides hourly surface currents with 5.12 km spatial resolution, covering 10,000 km^2.

HF Radar data, with high spatial and temporal resolution, contribute considerably to the study of surface current patterns and physical processes of the coastal ocean and to the development of operational oceanography tools (e.g. Paduan and Rosenfeld, 1996; Kohut and Glenn, 2003; Abascal *et al*., 2009; Gough *et al*., 2010; Schaeffer *et al*., 2011; Paduan and Washburn, 2013; Wyatt, 2014; Lorente *et al*., 2015). Taking advantage of the availability of these new data and the existing gaps in knowledge of sea surface currents in the study area, this PhD thesis will give a new insight to the surface ocean dynamics in the SE Bay of Biscay. The study area is indicated by a black square in Figure 1.

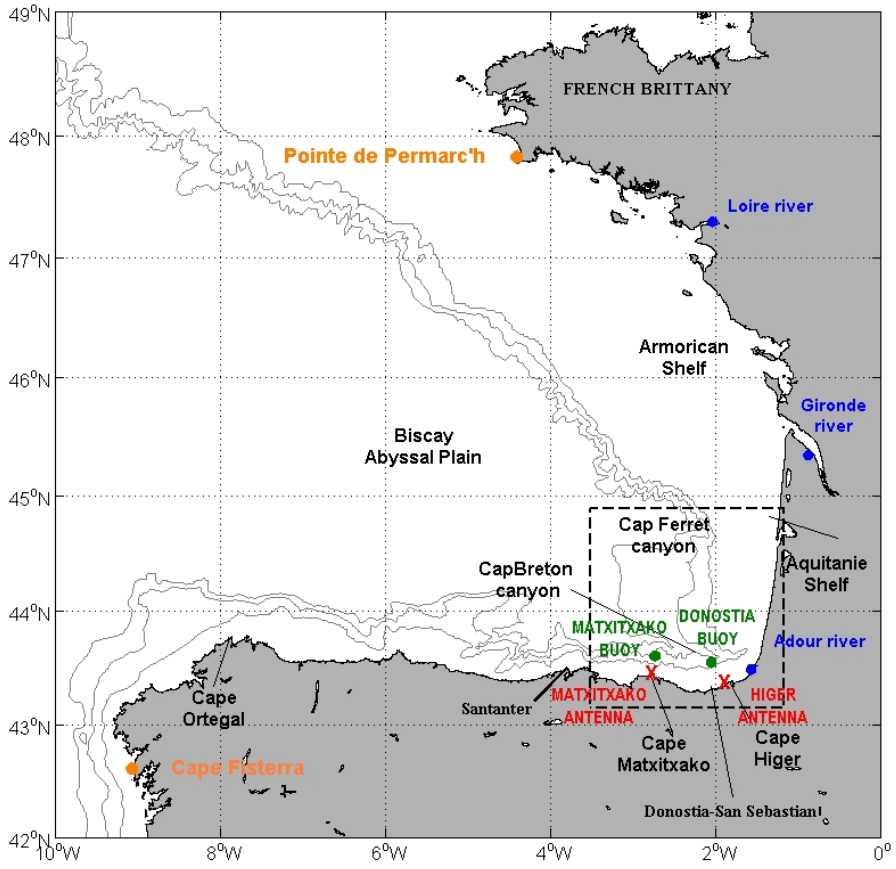

Figure 1: Geography of the Bay of Biscay, including the main characteristics referred in this manuscript. Matxitxako and Higer HF radar antennas (in red) and Matxitxako and Donostia Buoys (in green) complete the Basque operational data acquisition system, together with 3 coastal stations. Black square delimits the study area.

1.2. REVISION OF PREVIOUS KNOWLEDGE

The starting point of any research is the analysis and review of the studies and state of the art of the previous knowledge. Thus, it is possible to see what remains to be studied. In this section, the geography, the current state of knowledge of meteorology, hydrology and surface ocean currents in the Bay of Biscay and the study area is summarized.

1.2.1. Geography

The Bay of Biscay is a region of the North Atlantic Ocean. It is a transition sea between the cold northern and mild tropical seas and covers the area from Cape Finisterre (A Coruña, Spain), to the Point of Penmarc'h (Brittany, France) (Figure 1). Traditionally, it is considered that the western boundary is Cape Ortegal, in the NW of the Iberian Peninsula. However in this thesis the approach of some authors which extend the western boundary to Cape Finisterre is followed (e.g. Sánchez and Olaso, 2004). The Bay of Biscay is located between latitude 42º 30'N and 48ºN and longitude 1ºW and 9ºW approximately, as shown in Figure 1. The area covered by the Spanish platform was baptized by the Romans in the first century b.c. as Cantabricus Oceanus (Ocean of Cantabrian) and in older classic references elsewhere appears with the name of Britannicus Oceanus and Gallicus Oceanus (Valdés and Lavín, 2002).

The most important morphological feature of the Bay of Biscay is the strong discontinuity in the orientation of the coast; west-east along the Spanish coast and north-south along the French coast. The continental shelf off the Spanish coast is called Cantabrian shelf. It is oriented E-W and it is narrow and uniform (30-40 km). The width of the French shelf is extended with latitude. The French shelf is divided into the Aquitaine shelf (50-150 km) with N-S orientation and the Armorican shelf (180 km), oriented NW-SE. Dividing both shelves the Cap Ferret Canyon is located, which is bordered on the north by the Landes Plateau. Both shelves, the French and the Cantabrian, are indented by several submarine canyons, and divided by Cap Breton Canyon (Figure 2). The complex bathymetry of the region, largely affects the general circulation and the environmental and biological distributions in the Bay of Biscay (e.g. Bardey *et al*, 1999; Koutsikopoulos and Le Cann, 1996; Lavín *et al*., 2006).

1.2.2. Meteorology

In western Europe, the atmospheric circulation in the mid-latitudes of the North Atlantic is governed by the existence of two main centers of activity: the anticyclonic area under 40°N, centered near the Azores, and a low pressure area, centered about 60°N, near Iceland. Between these two areas, the prevailing winds are from the west to southwest,

being stronger in winter and weaker and less regular in summer. The wind tends to come from the south-west (SW) in winter and from the W-NW in summer (OSPAR, 2000). However, the average annual patterns show high interannual variability, especially during March and April (Lazure 1997; González *et al*., 2002, 2004; Lavín *et al*., 2006; Fontán *et al*. 2009, 2013).

1.2.3. Water masses

Most of the Bay of Biscay's water masses have their origin in the North Atlantic or they are the result of the interaction of water formed in the Atlantic with water of Mediterranean origin (OSPAR, 2000).

The Eastern North Atlantic Central Water (ENACW), which occupies the upper layers of the Bay of Biscay, is affected by the winter mixing and it is subject to seasonal variation of surface water. The core of ENACW has a potential density (σ_Θ) between 27.1 and 27.2 and is located in the Bay of Biscay at about 350 m, which corresponds to the depth of the permanent thermocline (Somavilla *et al*., 2009). According to their area of generation, two water groups have been identified: the first one is a subpolar branch formed in the southern area of the North Atlantic Current (NAC), which spreads south or southeast of the Bay of Biscay (Pollard *et al*., 1996). The second one is a subtropical branch formed in the northern part of the Azores current (approximately at the southern boundary of the convection area), moving to the north-east along the coast of the Iberian Peninsula (Pingree, 1997; Valencia *et al*, 2004).

Below the ENACW, the Mediterranean Water (MW) begins to influence the intermediate waters (Somavilla *et al*., 2009). MW has two maxima at 750 m and 1250 m water depth. The core of the MW is mixed with less saline waters along the Cantabrian slope and consequently, the maximum salinity of MW in the SE-Bay of Biscay is lower than the values observed in other areas (Valencia *et al*., 2004). The mixed layer in this area describes a marked seasonal cycle. Whilst the upper water column is mixed during winter months, during summer it shows a well-defined thermocline at mean water depths ranging from 30 to 50 m (Somavilla *et al*., 2013; Rubio *et al*., 2013a).

1.2.4. River runoff

During winter, the continental shelf off the mouth of the major rivers and estuaries (Loire, Gironde and Adour) is characterized by cold and low salinity waters. The rivers Loire and Gironde are the two main sources of continental water of the Atlantic French coast, and can induce density currents of about 10 cm • s-1 (Lazure and Jégou, 1998). Often, thermal inversions are observed over the shelf, near estuaries, linked to the saline stratification. The contribution of the water flow of the rivers is diluted throughout the water column. This action will regulate the salinity and temperature on the inner shelf and it will help to preserve the coast's perpendicular gradient between shelf water and offshore, which balances the slope current (Koutsikopoulos and Le Cann, 1996; Lavín *et al*., 2006). During the summer, low salinity water cover most of the continental shelf and its extension depends on the extent of river discharge and wind regime (Koutsikopoulos and Le Cann, 1996; Lavín *et al*., 2006, Reverdin *et al*. 2013). Notably, in the study area, the effect on the flow of the rivers draining the Basque valleys is not very significant and it is only punctual due to their torrential character; being the river Adour the main source of water of continental origin (Valencia *et al.*, 2004; Ferrer *et al*., 2009).

1.2.5. General aspects of the ocean circulation in the Bay of Biscay

The main characteristics of the ocean circulation in the Bay of Biscay are summarized in Figure 2.

1.2.5.1. General circulation in the abyssal plain

Several authors (Saunders, 1982; Maillard, 1986; Koutsikopoulos and Le Cann, 1996) have characterized the outer part of the Bay of Biscay by a variable weak anticyclonic circulation (1-2 cm • s-1) and by the presence of eddies both cyclonic and anticyclonic . These eddies have their origin in the slope current (Pingree and Le Cann, 1992a).

Pingree (1993) showed, using lagrangian buoy data, that ENACW (Eastern North Atlantic Central Water) penetrates into the southern Bay of Biscay following the anticyclonic circulation over the abyssal plain at 400 m water depth. Surface currents

obtained from measurements of lagrangian buoys, placed at about 15m water depth (van Aken, 2002), have confirmed the flow patterns. They also confirmed the seasonal variation of the flow, with an eastern component in autumn and southern component in spring and summer.

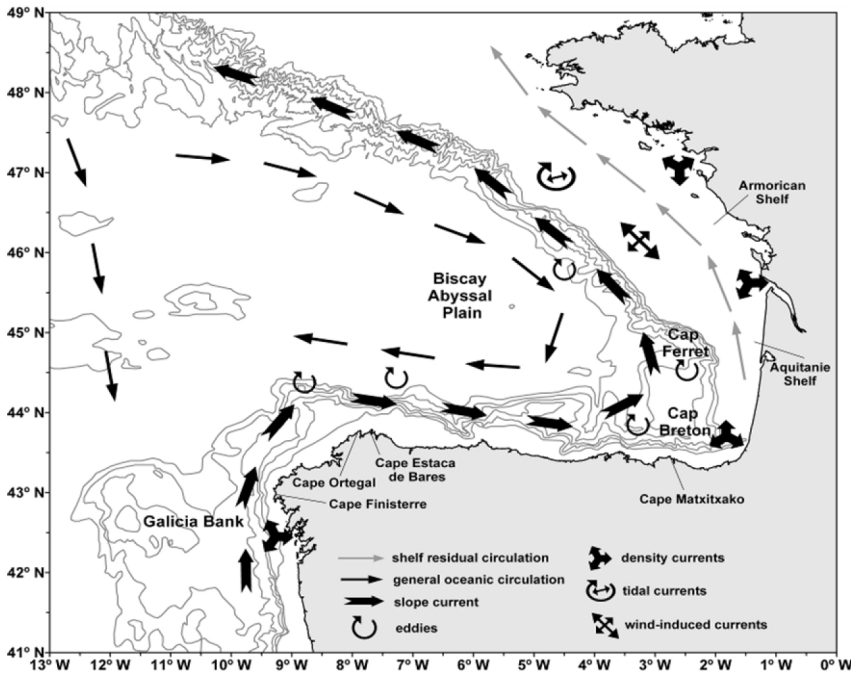

Figure 2: Main characteristics of the circulation in the Bay of Biscay (Ferrer et al., 2009).

1.2.5.2. Shelf / Slope currents

The ocean circulation over the slope is dominated by the seasonal Iberian Poleward Current (IPC). In the study area, the IPC travels east along the northern Iberian Peninsula, until it meets the continental contours of the French coast and thus forced to turn northwards (Frouin *et al*, 1990; Haynes and Barton, 1990, Pingree and Le Cann, 1990, 1992a, 1992b; Charria *et al*., 2013).

During winter, a warm and saline intrusion on the coast it is often observed, associated with the IPC (Le Cann and Serpette, 2009; Esnaola *et al*., 2013). Figure 3, shows this warm intrusion, isolated by the first EOF (49% of the variance) of the PCA analysis in the 1981-2010 reconstructed Sea Surface Temperature (SST) dataset of Esnaola *et al.* (2013). It consists of a positive anomaly, with main values between 0.6 and 0.9 ºC,

showing highest values off the western Iberian coast. To the north and east this current follows the 1000 m isobath as the coast changes its orientation. East of 7ºW it follows the 200 m isobath until it weakens and finally it is reinforced in the SE corner of the Bay of Biscay and to the North along the French coast (Esnaola *et al*., 2013).

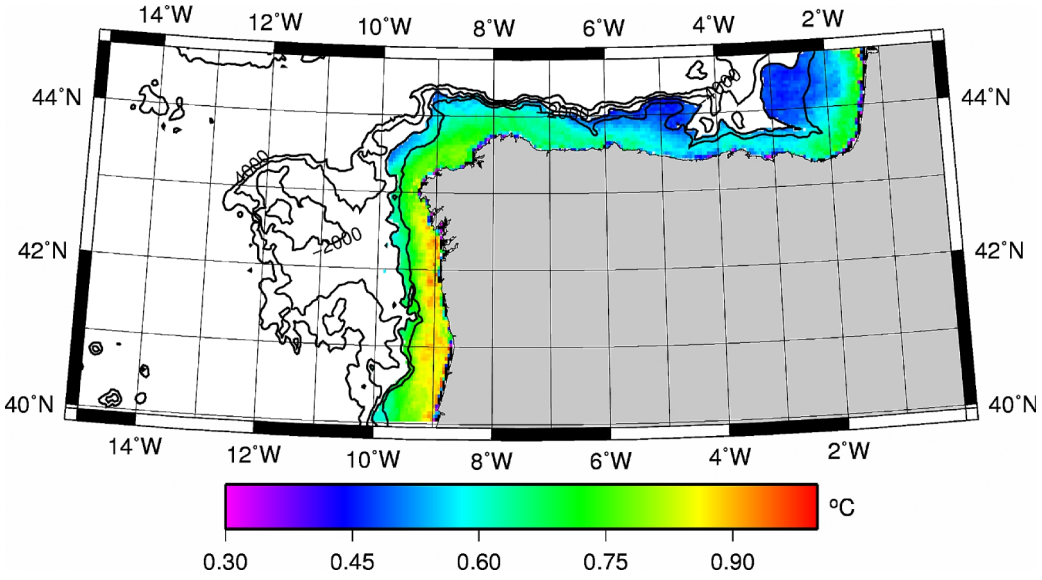

Figure 3: First EOF of the PCA analysis of the 1981-2010 reconstructed SST dataset when only pixels with a related depth of less than 2000 m are taken into account. (Esnaola et al., 2013).

This phenomenon of intensification of the slope current and its surface signal is also known as "Navidad Current" since it reaches the slope of the Cantabrian coastline at this time of the year (Pingree and Le Cann, 1992b).

The presence of the IPC in the study area is linked to the weakening of the Azores anticyclone. This weakening allows the current travelling northward along the Portuguese slope, to reach the western part of the Cantabrian coast (Pingree, 1993). At this point, it turns almost at a right angle to preserve its potential vorticity. It continues along the Cantabrian coast, moving with average speeds of 20-30 cm • s^{-1} and increasing its speed in the flow direction (Frouin *et al*. 1990; Haynes and Barton, 1990). The flow is markedly baroclinic with a highly water depth depending current field and with a velocity shear, which shows variability with depth and along the axis of the current (Gil and Sánchez, 2001).

In a recent study, Le Boyer *et al*. (2013) provided an overview of the shelf and slope circulation throughout the entire water column over a large range of spatial and time scales. The average circulation over the continental shelf and upper slope of the Bay of Biscay was poleward following the topography. This average circulation had marked seasonal variability. Indeed, several other studies have shown that the water circulation over the slope in the area is reversed and has intensities markedly weaker than those observed in winter, with predominant westerly currents over the Spanish slope (Pingree and Le Cann, 1990; Rubio *et al*. 2013b; Charria *et al*., 2013).

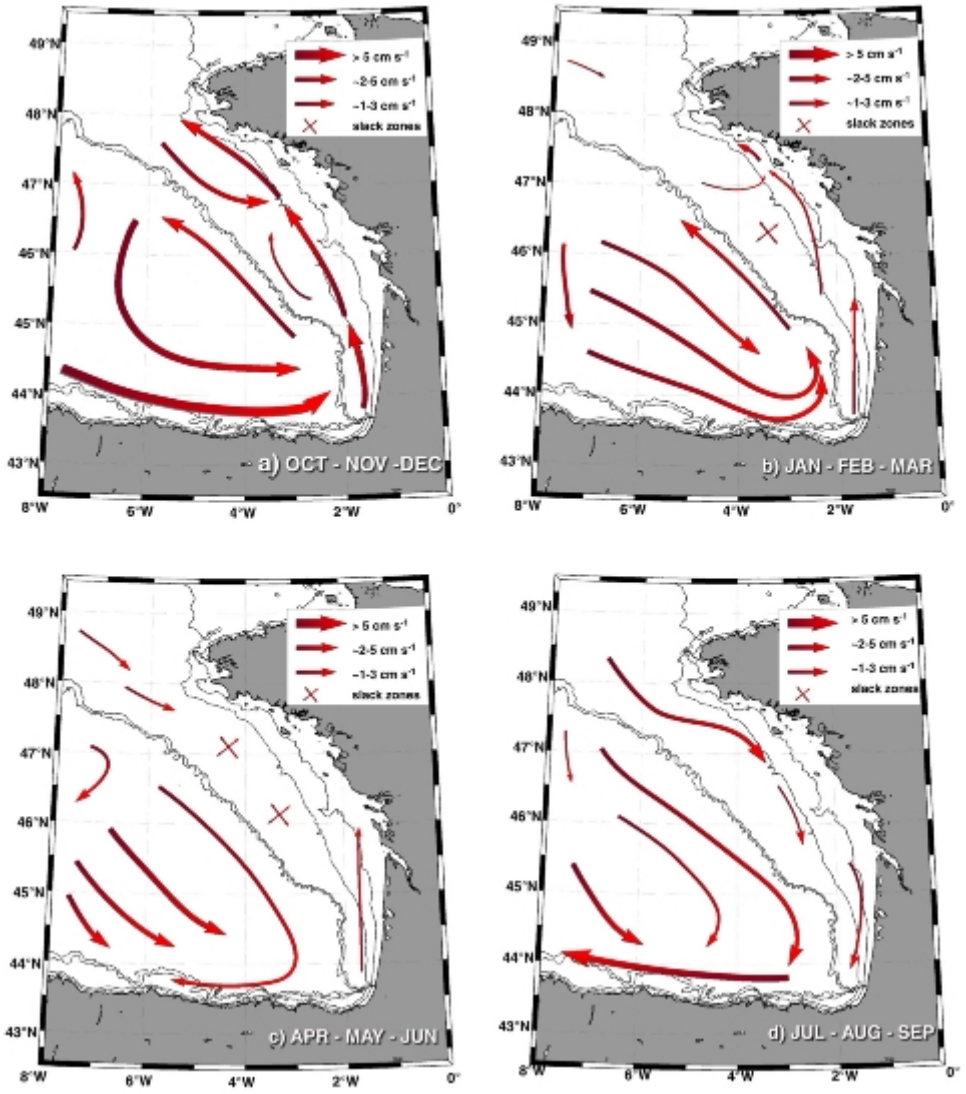

Figure 4: Schematic representation of the seasonal circulation in the Bay of Biscay. The arrow thickness is proportional to current speed (Charria et al., 2013).

Charria *et al*. (2013) showed, from drifter data, a schematic circulation in the Bay of Biscay where the seasonal alternation of the slope and abyssal plain surface circulation can be clearly observed (Figure 4).

The shelf/slope ocean circulation in the Bay of Biscay is influenced by different forcing factors as: bathymetric irregularities (Peliz *et al*., 2003), marked seasonality and spatial variability of wind forcing (Pingree and Le Cann, 1990; Le Cann and Serpette, 2009; Le Boyer *et al*., 2013), variation in heat fluxes (Somavilla *et al.,* 2013) or the effect of fresh water inflows (Lazure and Jegou, 1998; Ferrer *et al*., 2009). Concerning the IPC, different studies have related the intensification of the current with south-westerly (Haynes and Barton, 1990; González-Pola *et al*. 2005; García-Soto and Pingree, 2012) and northern (Álvarez *et al*., 2014) winds and to different North Atlantic atmospheric teleconnection patterns (García-Soto *et al.,* 2002; García-Soto, 2004; Le Cann and Serpette 2009; García-Soto and Pingree, 2012; Esnaola *et al*. 2013). Interanual variability in the SST surface signature of this current has been also reported: satellite images show a trend towards increasing SSTs during the last three decades as a result of the combined positive phase of the Atlantic Multidecadal Oscillation (AMO) and global warming (García-Soto and Pingree, 2012).

1.2.5.3. Mesoscale variability and eddies

In the Bay of Biscay, the IPC is responsible for the generation of persistent anticyclones that remain trapped in the lee of topographic features (Peliz *et al*., 2003). These eddies are feed by the slope current and their influence can reach 1,500 m water depth, presenting average diameters of about 100 km. After being generated, they tend to drift westward in the Bay of Biscay, with speeds of about 2 km • day^{-1}. They are responsible for increased shelf – open sea exchanges, modifying local circulation and transport and favoring mixing processes. The most energetic eddies are observed in winter, generating in the slope and dissipating later throughout the year within the Bay of Biscay (van Aken, 2002; Pingree and Le Cann, 1990, 1992a, 1992b). Pingree and Le Cann (1992a) refer to them as SWODDIES (Slope Water Oceanic Eddies). Besides, the presence of quasi-stationary eddies has been reported for different years near the same position, around 44.5ºN-4ºW, west of the study area (Pingree and Le Cann, 1992a; Pingree and Le Cann, 1992b; García-Soto *et al*., 2002; Serpette *et al*., 2006, Caballero *et al*., 2008,

2014). These eddies have been observed to remain stationary for a long time, in some cases up to 7 months (Pingree and Le Cann, 1992b). East of 5ºW, the major change of the coast and slope orientations, together with the presence of the steep bathymetric irregularities, can be expected to significantly affect the shelf/slope circulation by adding complexity to the regional ocean circulation (Caballero, 2014). Indeed, the area between Cap Breton and Cap Ferret canyons is known for its intense mesoscale activity (Le Cann and Serpette, 2009).

1.2.5.4.Coastal upwelling and downwelling

Coastal upwelling is the most significant hydrodynamic process during spring and summer in the Bay of Biscay and the west coast of the Iberian Peninsula. It typically develops between the months of April and October in response to persistent and stable northerly winds (Wooster *et al*, 1976; Blanton *et al*., 1984).

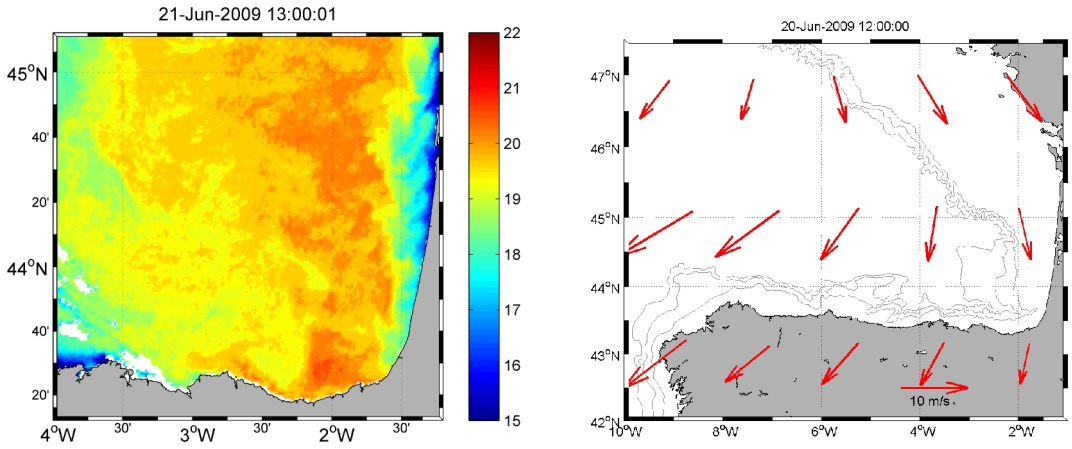

Figure 5: Sea Surface temperature plot (http://ers.cmima.csic.es/saidin/sst.html) and the winds during 21 and 20 June 2009 respectively (the wind did not have significant variation during the previous and next day). (Source for the image http://www.nco.ncep.noaa.gov/pmb/ nwprod/analysis/).

During an upwelling event, the surface layer of water moves seawards due to the combined effect of wind and the Coriolis force. Continuity requires that the water transported offshore to be replaced by coastal water from deeper levels. This phenomenon occurs within a narrow band whose width is about 10 km and depends on

the stratification of the water column. As the emerging water is colder than the surrounding surface water, it can be easily detected by images obtained with surface temperature remote sensing (see example in Figure 5).

In most upwelling systems, the circulation pattern induced by favorable wind episodes is characterized by shelf currents along the coast that are stronger than the transverse currents (Smith, 1981). In the Cantabrian Coast, near Santander, upwelling events have been described (Lavín *et al*, 1998) in June. For example the event of June 1995 was particularly notable as seen in the sections of Figure 6.

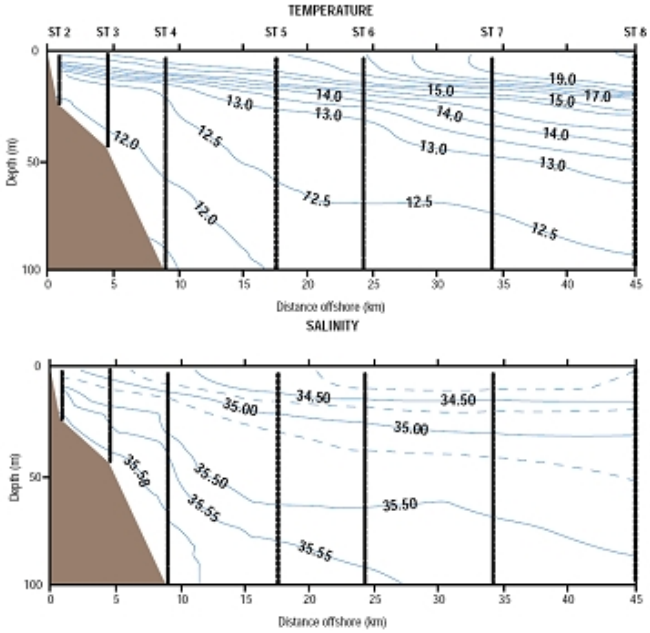

Figure 6: Temperature and salinity cross sections at Santander's shelf (3° 47' O, July 1995), (Lavín et al. 1998).

At the French coast of the Bay of Biscay, upwelling processes have also been described by Puillat *et al*. (2004, 2006). These authors describe repeated processes of upwelling in the southern coast of the French Brittany, associated with winds from the north-northwest.

During fall and winter, intense cold winds from the south and west, increase the density of surface waters. In addition, these winds also reactivate eastward and northward

currents together with the predominance of the downwelling in the SE area of the Bay of Biscay (Valencia *et al*., 2004).

1.2.6. Particularities of the shelf/slope circulation in the study area

1.2.6.1. Slope currents

In a recent study (Rubio *et al*., 2013a), the variability of currents, temperature and salinity on the continental slope of the study area was studied, using data from the two moored buoys over the upper slope showed in Figure 1. The slope dynamics within the first 200m confirmed the above mentioned seasonal variability: (i) switching between stratified and homogeneous regimes dominates the distribution of temperature and salinity; and, (ii) E-NE oriented net flow was observed during winter, whilst weaker S-SW currents were observed during summer (Figure 7). Overall, the flow in the first 200m was markedly barotropic although vertical gradients of the currents showed significant vertical shear values in the first tens of meters of the water column.

One striking result of this study was the difference observed in the current measurements at each of the buoys. Indeed, in terms of transport and variability at seasonal and intermediate scales, Donostia and Matxitxako buoys represented two different regimes. A slope regime was observed at Matxitxako where there was a clear transport along the slope, with higher intensity mesoscale variability. However, at Donostia, the influence of slope current appeared to be less significant and it was observed stronger stratification. The results suggested that, apart from the variability observed at different time scales, significant spatial variability characterizes the study area hydrography and currents.

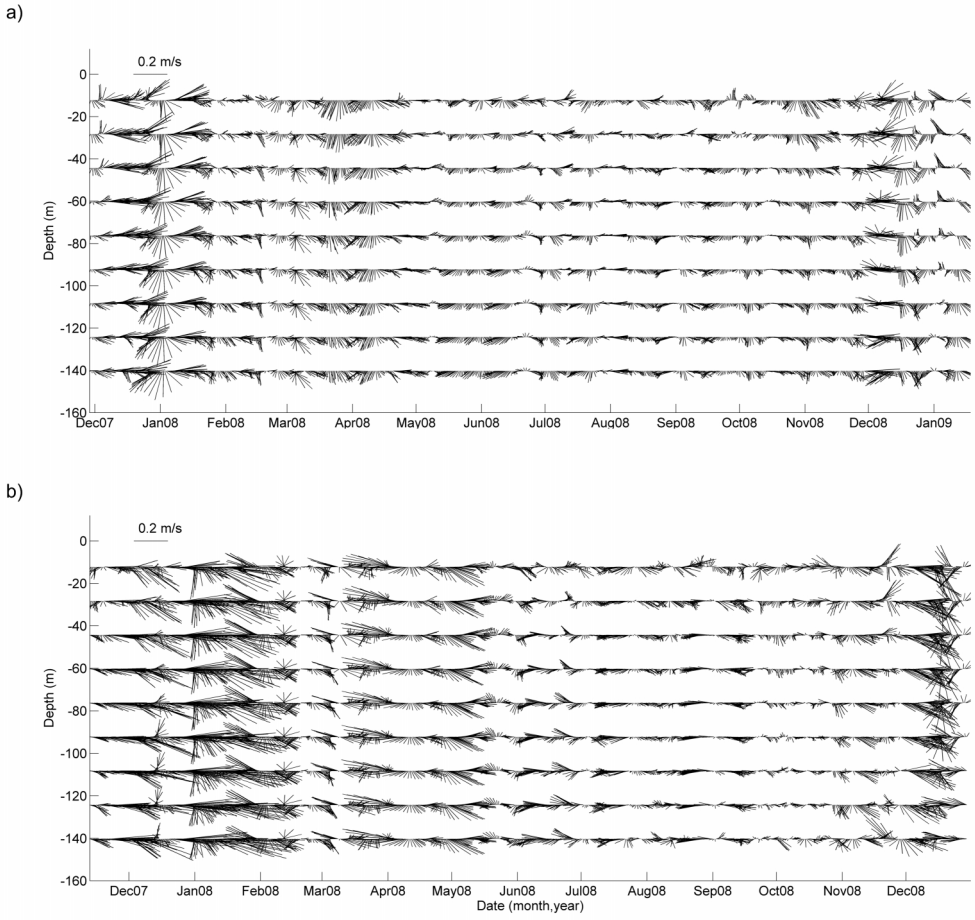

Figure 7: (a) Donostia buoy and (b) Matxitxako buoy 48 h-averaged current velocity stick plots from ADCP data, from surface to 150 m (Rubio et al., 2013a).

1.2.6.2. Shelf currents

Shelf circulation in the study area is mainly driven by wind, since over the narrow shelf tidal currents are weak, and there are no rivers that generate large density variations (Ibañez, 1979; González *et al*., 2004).

Early studies of current patterns of the SE Bay of Biscay (Ibáñez, 1979) revealed the existence of an eastward circulation off the Cantabrian Coast and northward currents near the French coast during intense autumn and winter winds. Since the winds present a marked seasonality, wind induced currents present also a marked seasonal variability. Predominantly, southwestern autumn and winter winds generate eastward and northward currents. Northwest spring winds cause southern currents on the French coast

and western-southwestern currents on the Spanish coast. The situation is similar during spring and summer; however, in summer, weak and high variable winds produce more variable currents (Lazure, 1997; González *et al*., 2004).

In the period 2000-2002 several moorings where deployed in shallow depths along the coast in the study area (González *et al*., 2002) (Figure 8). In autumn and winter, winds blowing predominantly from the SW gave rise to surface currents that, on average, caused drifting towards the N and E (González *et al*., 2002, 2004). During spring, winds blowing towards the NE, caused currents towards the W-SW in the deeper stations. The summer situation was similar to the spring one, however, with weaker and more variable wind, that resulted in high variable currents (González *et al*., 2002, 2004). Although the area covered in this study is out of the Basque HF radar footprint, it is interesting to note how differences between the surface layers and deeper layers are described. In summer, the vertical pattern of the current has less variability than in winter. Nevertheless, both seasons seem to confirm the existence of a surface layer (up to about 4 m deep) directly influenced by the wind. An intermediate transition layer and a deep layer with more moderate speeds and in which the current is practically parallel to the bathymetric lines, it is also observed.

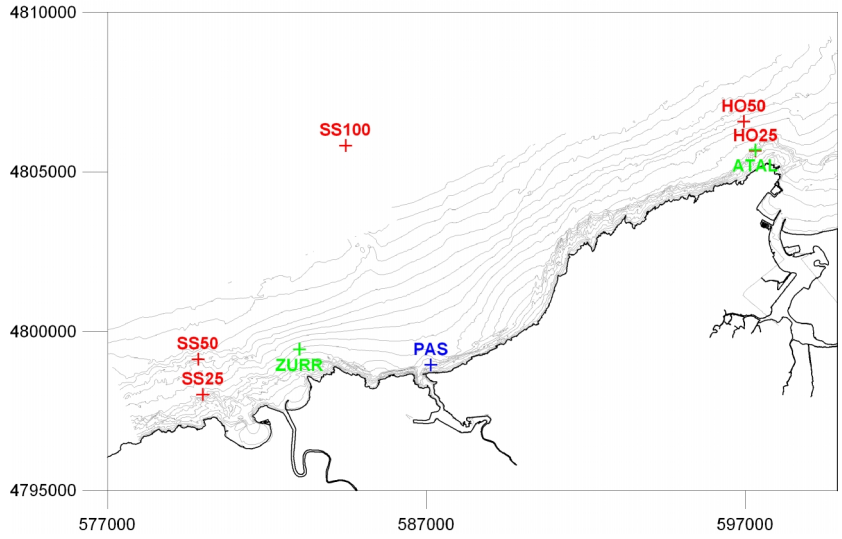

Figure 8: Map with the positions of the measurement points. Red stations are from 2000-2002 at 25, 50 and 100 m depth. Green stations are from 1998 y 1999. The blue one is the ocean-meteorologyc station of Pasaia (González et al., 2002).

The physical processes responsible for the temporal and spatial (horizontal and vertical) variability of the ocean circulation in the study area, were further analyzed in the studies developed by Fontán (2009) and Fontán *et al*. (2009). To do this, different data series were analyzed from moorings and stations at different depths on the shelf. In this study, the complexity of the circulation in the study area was underlined (due to the coexistence of different simultaneous processes on a great range of spatial and temporal scales). Likewise, significant differences in terms of circulation and processes between coastal waters and the deeper waters of the continental shelf, were also highlighted.

Finally, Fontán *et al*., (2013), showed using HF radar data, that the local winds play an important role in driving the upper water circulation. In this study, the wind-current interaction timescales were mainly related to diurnal breezes and synoptic variability. In particular, the breezes forced diurnal currents in waters of the continental shelf and slope of the SE Bay. They also related north-westerly winds to southeastward currents in a synoptic scale.

1.2.6.3. Astronomical tide and inertial currents

On the Cantabrian coast, the tidal range is of 3.5 m on average (González *et al*., 2004). The astronomical tide is semidiurnal, penetrating from the southwest into the Bay of Biscay. In this area, the effect of the tides on the oscillations of the sea surface is higher compared to the fluctuations due to atmospheric pressure, which is of the order of centimeters. Despite the importance of level fluctuations due to the tide, the tidal contribution to surface currents is small in general (except in estuaries). Indeed, in the study area the magnitude of the tidal currents is <15 cm • s-1, which is significantly weaker than the tidal currents observed in other areas within the Bay of Biscay (González *et al.*, 2002; Le Cann, 1990; Rubio *et al*., 2011).

A previous study using HF radar showed a strong seasonal inertial variability in the study area (Rubio *et al*., 2011). They observed a peak in the inertial kinetic energy (KE) closer to the shelf-break in summer, whereas winter surface maximum inertial KE is weaker and located further to the north-west.

1.3. CONCLUSIONS, OBJETIVES AND OVERVIEW OF THE THESIS

The circulation in the SE corner of the Bay of Biscay shows high spatial and temporal variability linked to the joint effect of several forcing factors and processes. The strong seasonality of winds, the slope current and hydrography, the mesoscale activity, the change of orientation of the coast and the abrupt bathymetry of the SE corner of the Bay of Biscay, are some of the main contributors to the observed variability.

As seen previously, most of the research in the study area has been done using data limited in space and/or time, thus no comprehensive descriptions of surface current patterns in the area was available when this PhD thesis began. For this reason, the newly available high spatio-temporal resolution HF radar observations are expected to help significantly in the understanding of the physical processes contributing to the complex water circulation in the study area. Two previous specific studies have been undertaken using Basque HF radar data in the study area (Rubio *et al.,* 2011; Fontán *et al*., 2013). Both focused on specific current scales and shorter datasets (2009 and 2009-10, respectively), than the one used within this PhD thesis.

In this way, the overall objective of this PhD thesis is to deepen in the knowledge of surface currents in the SE Bay of Biscay using data from HF radar, with high spatio-temporal coverage. Specifically, the following two objectives are established:

i. Assess the performance of the HF radar system and potentiality for its operational use in the calculation of drifting trajectories at sea.
ii. Provide a new insight to the circulation patterns and current variability in the study area at different time scales (from high frequency to interannual), using high temporal and spatial resolution HF radar data.
iii. Study the relationships between wind and currents patterns in the study area.

Following this purpose, the thesis is structured as follows: Chapters I and II, offer an introduction to the state of the art of oceanographic processes in the study area and the HF radar technology, respectively. In Chapter III, HF radar observations are described and analyzed in comparison with other in situ measurements. Eulerian comparisons

included in this chapter are partially published in Rubio *et al*. (2011) and in Solabarrieta *et al*. (2014), whilst the lagrangian predictability analysis is included in Solabarrieta *et al*. (in preparation). Chapter IV studies the surface ocean patterns in the SE Bay of Biscay and has been adapted from Solabarrieta *et al*. (2014). Chapter V includes a description of the wind and current patterns in the Bay of Biscay and SE Bay of Biscay, and analyzes the interaction between wind and currents, using k-means classification algorithm. The contents of this chapter have been included in Solabarrieta *et al*. (submitted to Ocean Dynamics). Finally, Chapter VI offers the main conclusions of this thesis and future research lines.

CHAPTER II
HF RADAR TECHNOLOGY

In the last decades, there has been a growing number of studies about coastal ocean dynamics using HF radar surface current data (e.g. Paduan and Rosenfeld, 1996; Kohut and Glenn, 2003; Gough *et al*., 2010; Schaeffer *et al*., 2011; Rubio *et al*., 2011; Paduan and Washburn 2013). All these studies support the use of this technology as a tool for understanding coastal surface current processes. Moreover, recent publications provide examples of the application of HF radar technology to different sectors in relation with the marine environment, safety and exploitation (Paduan and Washburn, 2013; Wyatt, 2014). The use of HF radar to measure currents and sea state has been increasing and

today HF radar systems are being operated by several countries worldwide. USA offers one of the few examples of integrated HF radar networks providing real-time surface currents and key information for scientific and societal needs along extended coastal areas (http://cordc.ucsd.edu/projects/mapping/maps/, http://www.ioos.noaa.gov/globalhfr).

2.1. HF RADAR TECHNOLOGY: STATE OF THE ART

2.1.1. General description

HF radar systems are able to cover the gaps that other remote (as is the case for satellite altimetry) or *in-situ* (e.g. moorings) technologies have in these areas. They provide measurements of currents with a relatively wide spatial coverage and high spatio-temporal resolution. They also provide data in near real time (there are systems with lags of only 20 minutes, after acquisition), so they have become invaluable tools in the field of operational oceanography, with multiple applications for the maritime sector: coastal marine environment, research, rescue, navigation…. (Abascal *et al*., 2012; Paduan and Washburn, 2013; Wyatt, 2014) Moreover, these data also have a great interest for the validation and calibration of numerical ocean forecasting models, especially near the coast.

Since no *in-situ* operations are required in a regular basis and the access to the on-land installations in case of maintenance procedures is easy, the measurements from HF radars in the short and long terms, are relatively inexpensive to obtain, compared to those from other in situ and remote measuring systems. Indeed, the resulting cost per data collected from any other conventional technology (current meters, drifters) is one order of magnitude more expensive, with the additional advantage associated with getting surface current data in real-time. However, the initial investment for the installation of the antennas is important.

Currently, several HF radar systems coexist on the market, nevertheless two are the most extended: WERA (WavE Radar) and CODAR. Although they share the same basic principles of operation, these two systems differ in the design of the receiver antenna and, thus, how the angle of incidence of the echo signal is determined. This

determines as well the minimum number of antennas needed to be placed at each site. WERA systems use a setting of antennas at every station (minimum of 4 if uses direction finding and minimum of 8 if uses beam forming (Gurgel *et al*., 2001; Helzel *et al*., 2006)) and applies "Direction Finding" and "Beam Forming" techniques to measure the angle of incidence of the echo (Figure 9). CODAR systems require only two antenna-stations (each station consists of a transmitter and a receiver antenna, which may be incorporated into a single antenna). It uses the "Direction Finding" system to measure the angle of incidence of the echo (Figure 10).For long term deployments, CODAR antennas need regular calibration of the directional receiver antenna, since the antenna response pattern can be affected by changes in the environment close of the installation (Kohut and Glenn, 2003). Recently, comparisons between the measurements of both systems have been done by L. R. Wyatt (2013) and Liu *et al*. (2014), where they observed similar measurements of the currents, using both systems.

The data used in this PhD thesis are obtained from a CODAR Seasonde HF radar. Further descriptions of the technology and operation will, in consequence, focus on these particular systems.

Figure 9: Example of WERA system's antenna installation (courtesy of T. Helzel)

The typical range of the HF radars is 70 km with a spatial resolution of 3 km (transmitting at 25 MHz). The spatial resolution depends on the angular distance between the radials and it decreases with the distance from the antenna. Some versions of these antennas (whose frequency is between 4.4 and 6 MHz) allow a range up to 220 km with the same temporal resolution and a spatial resolution of 6 km (see Table 1).

Figure 10: HF radar antennas (CODAR system) at Point Sur in California; transmitter (left) and receiver (right)

Each unit is designed to operate autonomously, almost without maintenance (but with surveillance) and indefinitely as long as the conditions of energy and security exist. Data can be obtained remotely via telephone by direct connection to the computer. In case of power failure, is possible to re-initialize the system by telephone. The raw data are then processed in order to obtain hourly maps of surface current vector.

The treatment, quality control, management and operational use of data obtained by HF radar is not trivial and requires the development of a number of specific tools.

Radar Frequency (MHz)	Radar Wavelength (m)	Ocean Wavelength (m)	Ocean Wave Period (s)	Depth of current[1] (m)	Typical Range[2] (km)	Typical Resolution[3] (km)	Typical Bandwidth (kHz)	Upper $H_{1/3}$ Limit[4] (m)
5	60	30	4.5	2	175-220	6-12	15-30	25
12	25	12.5	2.5	1-1.5	60-75	2-5	25-100	13
25	12.5	6	2	0.5-1	35-50	1-3	50-300	7
48	6	3	1.5	<0.5	15-20	0.25-1	150-600	3

1. Depth averaged current.
2. Range based on 40W averaged power output. Salinity, wave climate and RF noise may affect this.
3. Based on bandwidth approval only -no system limitations- higher resolution will cause some range loss
4. Significant Waveheight al which 2nd order spectra saturates 1st order and no current measurements possible

Table 1: Different characteristics of the HF radar systems and data according to the frequency of the emitted signal. (courtesy of Qualitas Remos (Technological solutions and services for a safe and sustainable marine environment)).

In recent years, the radar technology has spread worldwide and consequently, the market is developing rapidly due to the current high demand. The following developments are an example of this:

- Rapid deployment HF Radar Systems: The Norwegian company CodarNor A/S, with funding from the Norwegian Clean Seas Association for Operating Companies (NOFO) and from Innovation Norway through an industrial research and development contract, is developing a self-contained rapid deployment HF radar. This system can be deployed by helicopter or other means to remote and rugged locations along the coast and operate autonomously, communicating surface current data in real time back to operators and drift modelers (Whelan *et al*., 2010).

- Antenna calibration patterns from vessels: A method is presented for obtaining antenna pattern measurements (APM) for direction-finding HF radars from ships of opportunity. Positions obtained from the Automatic Identification System (AIS) are used to identify signals backscattered from ships in ocean current radar data. These signals and ship position data are then combined to determine the

HF radar APM (Emery *et al*., 2014). This calibration completes the conventional Antenna Calibration Patterns with a transponder, however it does not replace it. In one year, AIS is expected to auto control the APM of the system.

- Low consumption/autonomous systems: Low power systems are available nowadays. Their consumption is 250 watts and they work at external temperatures lower than 36ºC.

2.1.2. CODAR HF Radar System Operation to obtain surface ocean currents

The system consists of an omni-directional transmitter antenna which sends radio signals in the frequency range of 3-30 MHz (controllable by software) and an additional receiving antenna which receives the signal that is generated by the diffused reflection caused by waves on the sea surface (Crombie, 1955). The received signal has a half of the wavelength of the emitted signal's wavelength (Figure 11).

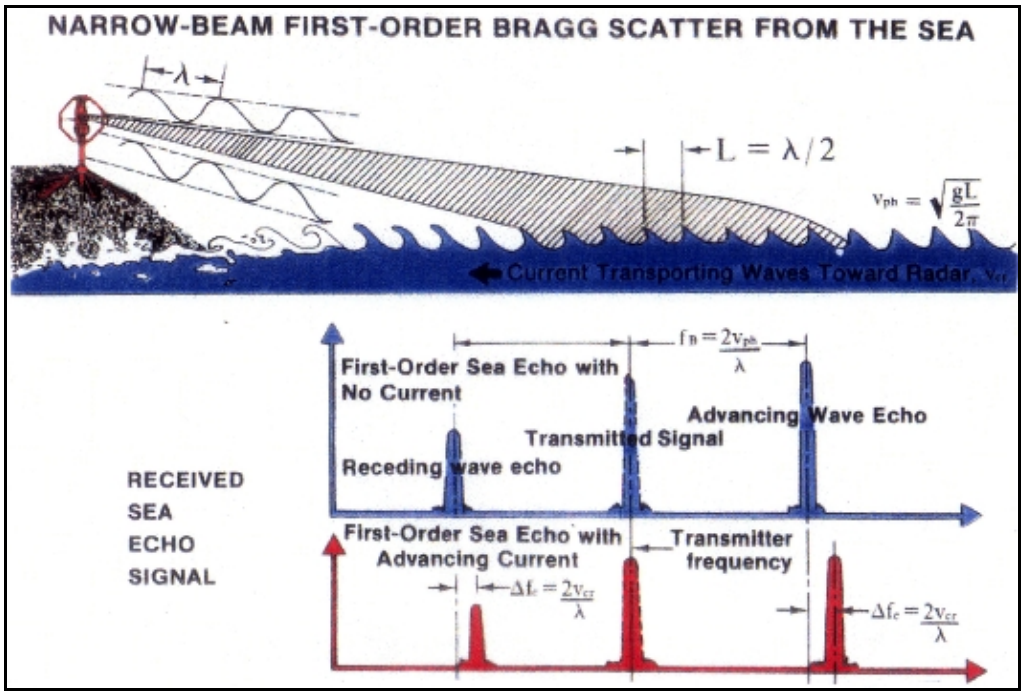

Figure 11: Scheme showing how the HF radar measure currents. The antenna on the coast outputs a signal with wavelength λ (depending on the frequency of the system) which is reflected by the surface waves whose wavelength is λ / 2. (Barrick et al., 1977)

Indeed, HF radar relies on resonant backscatter resulting from coherent reflection of the transmitted wave by the ocean waves whose wavelength is ½ of that of the transmitted wave. The energy reflected at one wave crest is in phase with the emitted wave. This is the Brags scattering phenomena and it results in the 1st order peak of the received (backscattered) spectrum (Paduan and Graber, 1997). In the absence of currents, the frequency of the 1st order peak has a Doppler shift caused by the phase velocity (speed) of the waves in the radial direction of the transmitting antenna. This speed (Vg) is known since it is the wave propagation speed (for waves with ½ wavelength of the emitted wave) and it is given by the dispersion relation in deep waters:

$$V_g = (g * L / 2\Pi)^{1/2} = (g/k)^{1/2}$$

Where: L = wavelength
g = gravity
k= wave number

The Doppler shift is presented in the two peaks of the spectrum of the received signal (associated with the waves traveling towards and away from the radar), symmetrically situated on either sides of the frequency, as shown in Figure 12.

If gravitational waves are propagated over a current field, the peaks are shifted in the frequency domain and an asymmetric spectrum is obtained (see Figure 12). The radial component of the current, which is the current in the same direction than the signal, can be directly calculated from the speed difference between the theoretical speed of the waves, for the given wavelength, and the velocity observed through the spectrum; the difference in speed is the speed of the current.

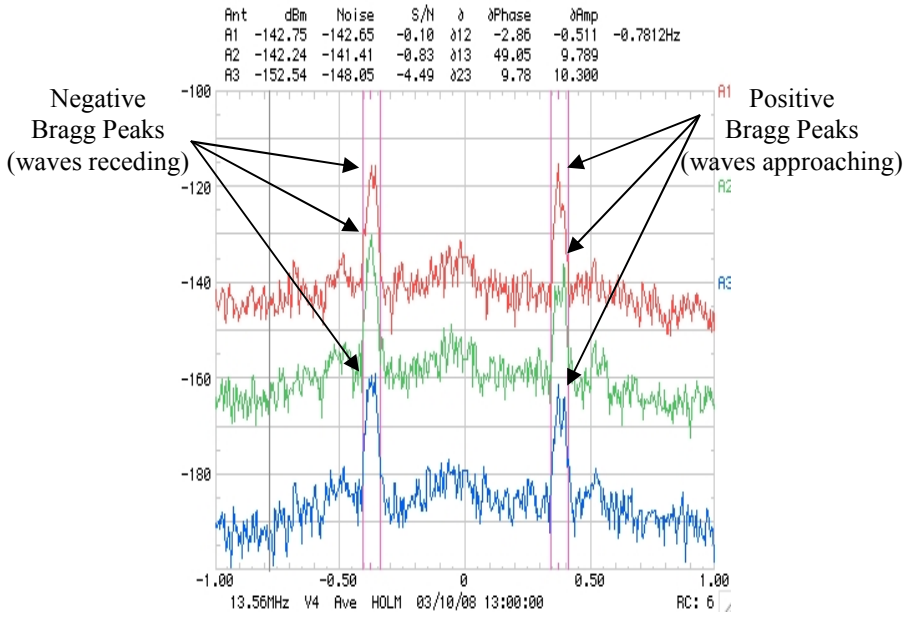

Figure 12: Example of a real received signal spectrum after the second FFT (courtesy of Qualitas Remos).

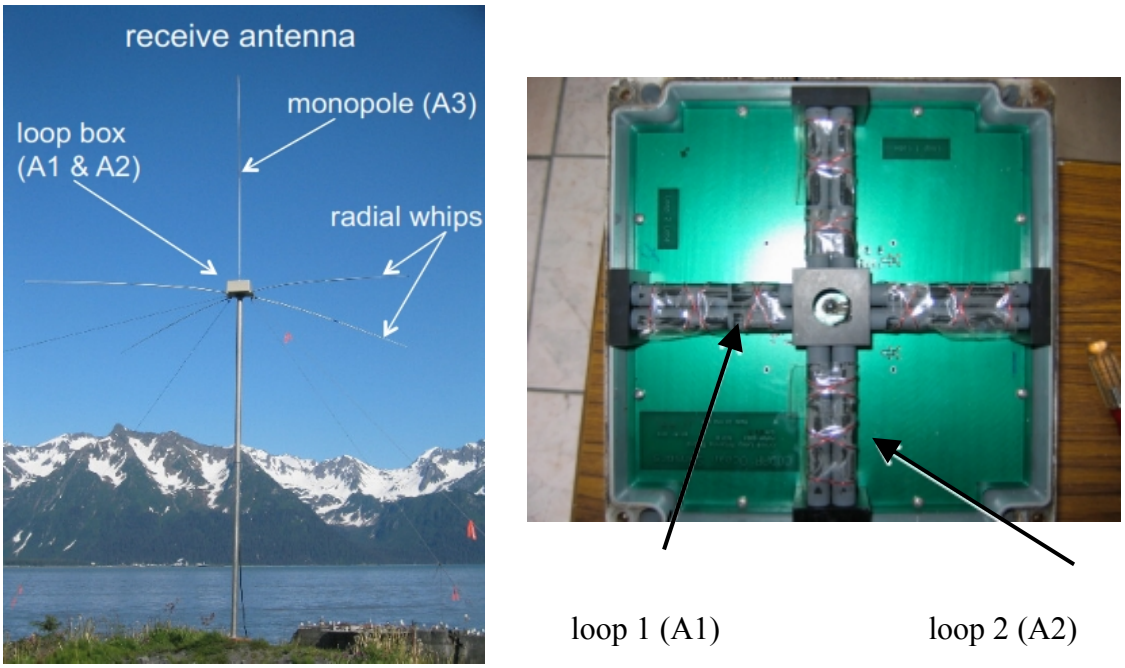

Figure 13: (Left) A Seasonde CODAR receiver antenna. (Right) Loop box (courtesy of Qualitas Remos).

To determine the angle from which a return signal is coming, CODAR systems use direction finding. Direction finding method uses the signal received by three different antennas (two loop antennae oriented ninety degrees to each other and a monopole to determine the angle (Figure 13)). The signal received by the two loop antennas is normalized with the monopole signal. After that, the arctangent of two crossed-loop signal ratio is used to determine the direction of the signal (Kohut and Glenn, 2003). A much more robust algorithm is used in practice to determine bearing and it is called MUSIC (Multiple Signal Classification, Schmidt 1986). MUSIC algorithm permits to resolve more complex ocean surface current fields. The correct application of this algorithm needs perfect knowledge of the angular response pattern of each antenna element. If there are errors in antenna patterns, these are translated into errors in angular placement of radial current values around a given range cell. There are two methods to ascertain the angular beam patterns: 1) assume the patterns theoretical (known as ideal patterns) which are based on the antenna design or 2) APM: measure the antenna patterns (known as measured patterns) after its installation. The ideal patterns of the two cross-loop antennae are cosine-dependent and oriented orthogonal to each other. The measured patterns of the receive antenna elements can be obtained by moving a small battery-operated transponder around the shore site on a boat. Figure 14 shows an example of the trajectory of the boat with the transponder on board to calibrate the receiver antenna.

The antenna patterns are sensitive to electromagnetic interference from the surrounding environment. If differences between the real and used or assumed beam patterns are not taken into account, there can be angular bias as large as 35 degrees (Barrick and Lipa, 1986). Kohut and Glenn (2003) also showed that system accuracy depends on the distortion of the measured pattern. It is recommended to calibrate CODAR antennas each year or when there are changes around the antennas that could distort the signal (Kohut and Glenn, 2003). More detail on the calibration operations of the HF radar system used in this thesis is provided in the next section.

Figure 14: Trajectory (in green) of the boat with the transponder on board to calibrate the antenna of Matxitxako in September 2014. Yellow marker shows the position of the receiving antenna (courtesy of Qualitas Remos).

The average time interval and availability of information ranges from minutes to few hours, however usually is of 1 hour. To obtain hourly information of currents, a received signal is processed following different steps starting from processing the received raw signal time series into spectral data (applying a FFT: Fast Fourier Transform). Then, different averages within defined time windows, which depend on the frequency of the emitted signal, are performed to obtain radial currents. The details of the processing of the raw data into radials used in this thesis are provided in next section.

Since currents from individual radar sites are obtained only in the radial direction of the transmitted signal, a minimum of two HF radar sites are needed with a common footprint to reconstruct the magnitude and direction of surface currents. Figure 15 shows this reconstruction. The velocity information at each node is a least square fit of the radial velocities that are within a given radius circle centered on that node. The radial components within that radius are combined to generate a single total vector for the study node. The total velocity vector is defined by U and V components (about x and y axes) that are determined by minimizing the sum of deviations.

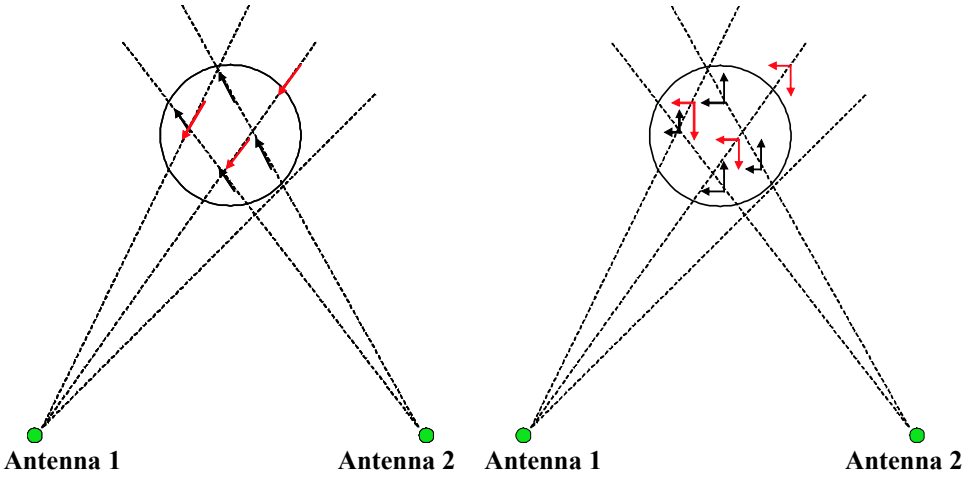

Figure 15: Surface direction generating scheme from each radial information (courtesy of Qualitas Remos).

2.2. DESCRIPTION OF THE BASQUE COUNTRY HF RADAR SYSTEM

The HF radar coastal system of the Basque Country is operational since the beginning of 2009. It consists of two radar stations, one located in cape Higer and the second one in cape Matxitxako (Figure 1), emitting at a bandwidth of 40 KHz, a frequency of 4.86 MHz and an average radiated power of 40W (see photographs in Figure 16 and Figure 17). This system provides long range hourly surface current data with a 5.12 km spatial resolution (width of the range cell). This dataset is a powerful tool for the regional operational oceanography, specifically, for the validation and improvement of numerical systems and monitoring and the forecasting of ocean currents and drifting objects or contaminants. These data have been already used in previous studies (Rubio *et al*., 2011, Fontán *et al*., 2013, Rubio *et al*., 2013b) on several aspects of the marked temporal and spatial variability of surface currents within the radar footprint.

Figure 16: Higer station antennae: (Left) receiver antenna. (Right) transmitter antenna (courtesy of Valentín Urgoiti).

As explained in the previous section, Basque HF radar system offers hourly information of currents. To obtain these currents, a received signal is processed following different steps, starting from processing the received raw signal time series into spectral data. In this process, first, an unaveraged cross spectrum, CSQ, is obtained, processing a received raw signal time series of 17 minutes into spectral data (applying a FFT: Fast Fourier Transform). Then, applying a running average (which removes eventual echoes from ships and smooths the results) to three consecutive CSQs, one averaged cross spectra, CSS, is obtained (which is an average of 51 minutes) every 30 minutes. Finally, the average of five CSS spectra is done, obtaining the radial information of the central time, being this an average of, approximately 3 hours (Figure 18 shows an example to obtain a radial file at 15:00 hours using 5 CSS files).

Figure 17: Matxitxako station antennae: (Up) transmitter antenna to the left and the receiver antenna to the right-down. (Down) receiver antenna (courtesy of Valentín Urgoiti).

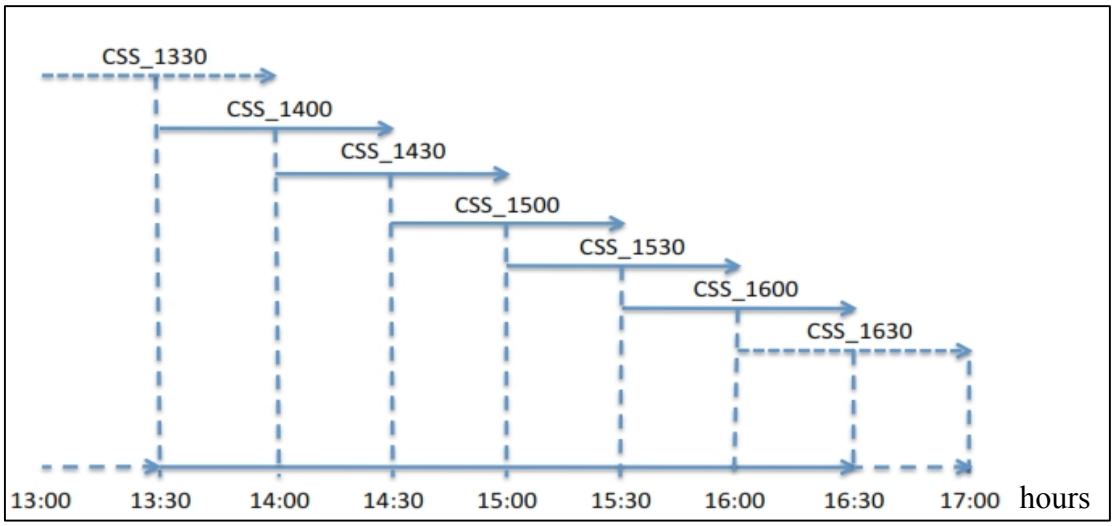

Figure 18: An example to obtain a radial file at 15:00 hours, using the 5 CSS files (14:00-14:30-15:00-15:30-16:00 hours). The final file is an average from 13:30 to 16:30 (3 hours) (courtesy of Qualitas Remos).

The current configuration permits to cover an area of approximately 10,000 km^2 of the sea surface (with a stable coverage radius of 100 km from the coast). The theoretical precision of the current data is between 2 - 3 cm • s^{-1}, with an hourly time resolution and spatial resolution of 5 angular degrees. Figure 19 shows an example of the radials for each antenna. A map of surface total currents is shown in Figure 20, which is obtained combining the radial data in Figure 19.

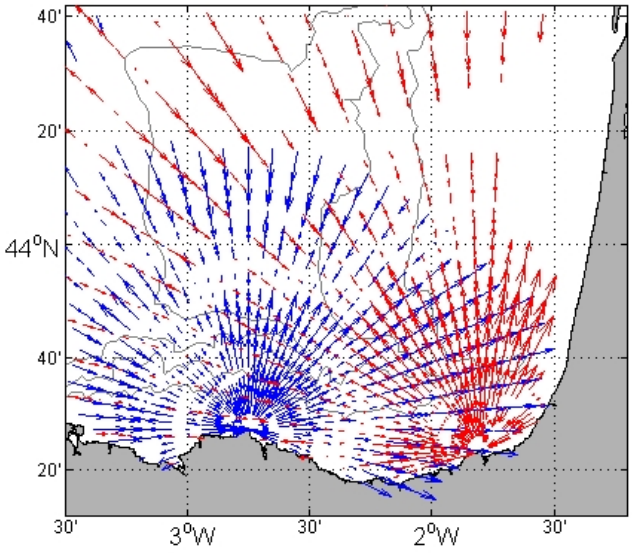

Figure 19: Radial velocity images of Matxitxako (left and blue) and Higer (right and red) antennas. Date: 22nd of July, 2009 at 12:00.

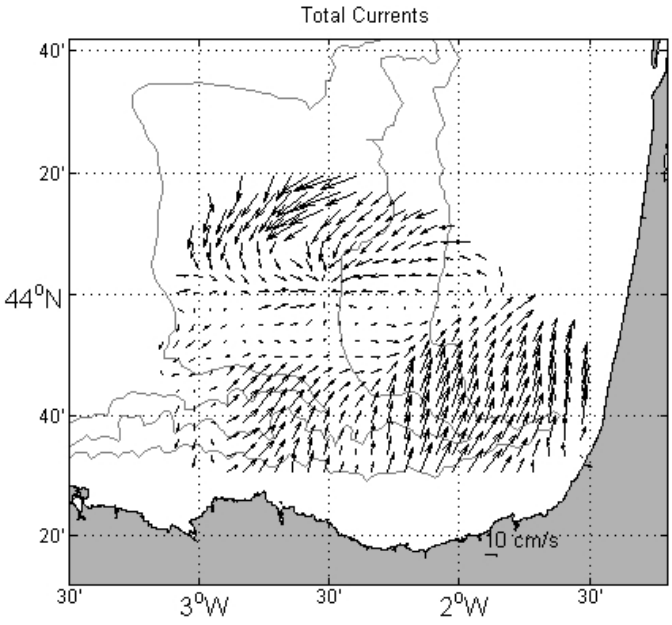

Figure 20: Map of the surface currents obtained from the radial data of Figure 19, using Basque HF radar system. Date: 22nd of July, 2009 at 12:00.

The received information is averaged and plotted on the nodes of a regular grid (shown in Figure 21). The Basque radar grid is orthogonal with a mean separation between nodes of 5 km.

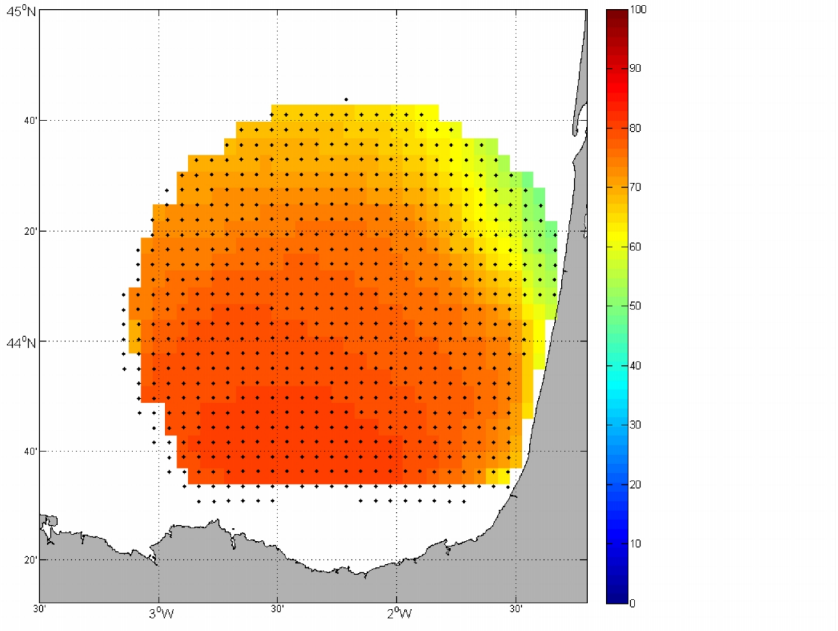

Figure 21: Spatial position of the nodes of the Basque HF radar system (black dots). Colours represent the % of available data, for 2009-2013 of the nodes which have passed the quality criteria.

The nodes that are closer to the antennas have more information since, while the angular separation remains constant, as we move away from the antennae, the spacing between the radials increases, remaining constant the radius used for selecting the averaging radial velocities. Therefore, the information has lower quality in the nodes located at higher distances from the antennae.

As basic quality criteria, applied to ensure that the data has enough orthogonal information, the angle between the radials used to compute total velocities has to be higher than 30º. Besides, a threshold for maximum total speeds is set to 100 cm • s^{-1}, since in the study area it is not expected that the total speed exceeds 70 cm • s^{-1} (Le Cann and Serpette, 2009; Rubio *et al*., 2013). Using these conditions the number of data nodes decreases. However, assures the quality of the data (see Figure 21).

As mentioned in previous paragraphs, CODAR systems need regular antenna patterns calibration campaigns. Since the installation of the Basque HF radar, 3 antenna calibrations have been done in order to improve the quality of the HF radar measurements: 21th July 2009, 10th October 2011 and 30th September 2014. In the last campaign a problem with the transponder avoided the calibration of the Higer antenna, which is pending. Figure 22 shows the ideal and measured patterns for both antennas and Figure 23 shows 2 of these calibration patterns over a Google Earth map. As said in previous paragraphs, annually calibration is recommended to each radar system. However, in this case, the campaign results showed minor differences between consecutive campaigns (Figure 22) and also between ideal and measured patterns (Figure 24 shows 2 pair of total current maps at the same time step using ideal and measured pattern). Comparisons between *in-situ* data and HF radar data also showed minor differences when using ideal or measured patterns So, although in this case the calibration frequencies have been lower than the recommended ones, the results show that this is not affecting significantly to the quality of the data. However, the smallest differences where obtained using measured patterns. Thus, since the measured patterns offer better results, after each of the three calibration campaigns, the measured patterns have been analyzed, validated and used in the data processing of subsequent radial velocities within the shortest delays.

Pattern type	Matxitxako	Higer
Ideal	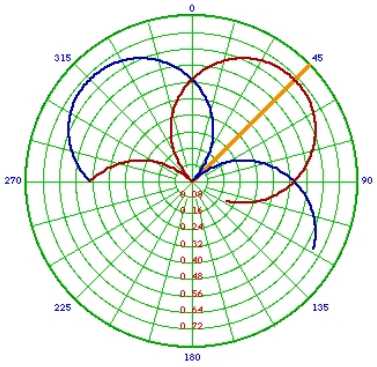	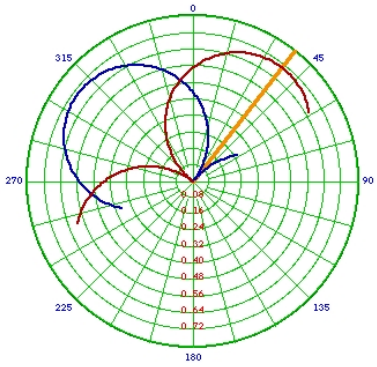
Measured (July 2009)	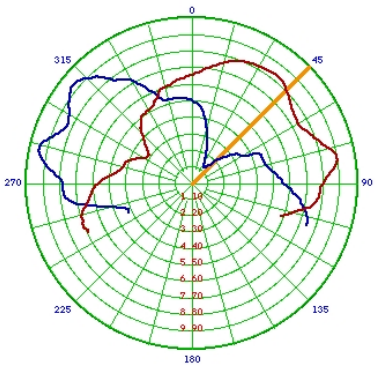	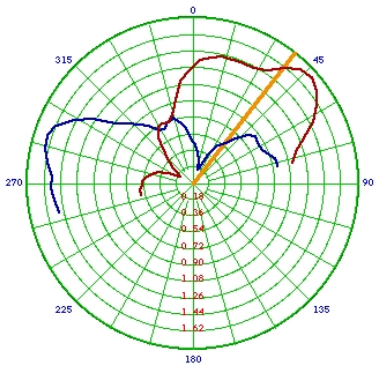
Measured (October 2011)	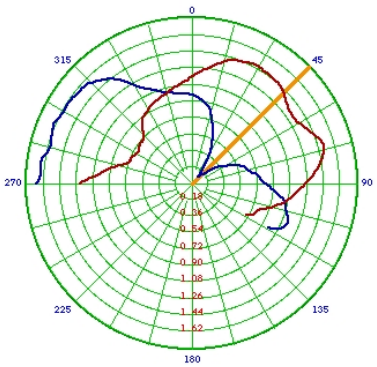	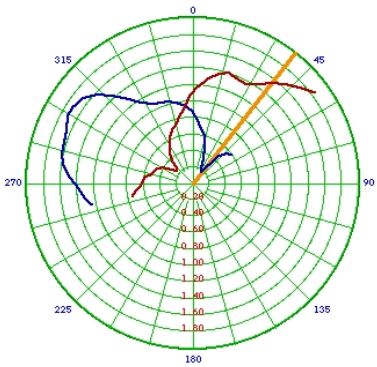
Measured (September 2014)	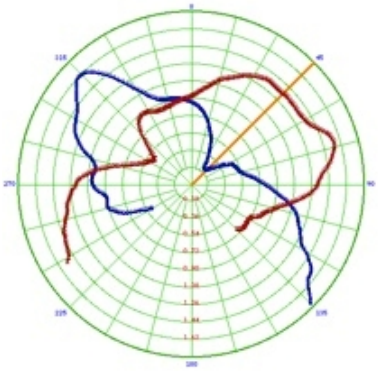	-

Figure 22: Ideal and measured HF radar antenna patterns of Matxitxako and Higer Sites.

Matxitxako 2014 **Higer 2011**

Figure 23: Measured HF radar antenna patterns of Matxitxako (2014) and Higer (2011) Sites over Google Earth maps.

(a)

(b)

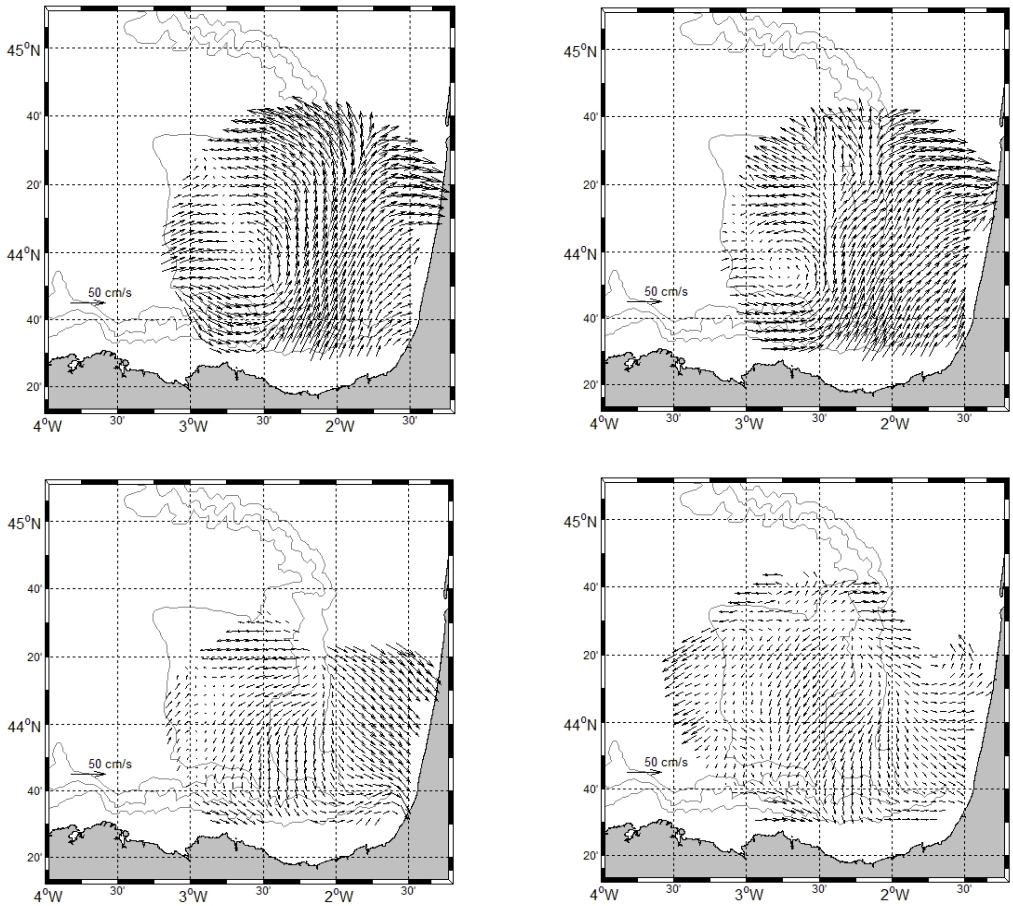

Figure 24: Total current snapshots using ideal (left) and measured (right) calibration patterns, for (a) 20th –November-2009 (b) 14th-May-2010 at 12:00.

2.2.1. Integration of HF radar in the Basque *in-situ* oceanography system

The HF radar data was integrated to the Basque country's *in-situ* Operational Oceanography observational network, owned by the Directorate of Emergency Attention and Meteorology of the Basque Government, in late 2008, providing the first surface current maps in January 2009. In addition to the HF radar system the Operational network consists of:

- Six coastal stations (water depths <30 m) that provide, since 2004, 10-minute data of temperature, currents, tides and waves at six strategic points of the Basque coast.
- Two buoys located over the slope in front of Donostia-San Sebastián (Donostia Buoy) and Cape Matxitxako (Matxitxako Buoy), over 550 and 450 m isobaths, respectively, which provide, since 2007, hourly data of meteorological and oceanographic variables at the sea surface. In addition to the surface sensors, a downward looking ADCP measures currentsat the upper 200 m of the water column, whilst a chain of CTs provide temperature and conductivity data at 10, 20, 30, 50, 75, 100 and 200 m.

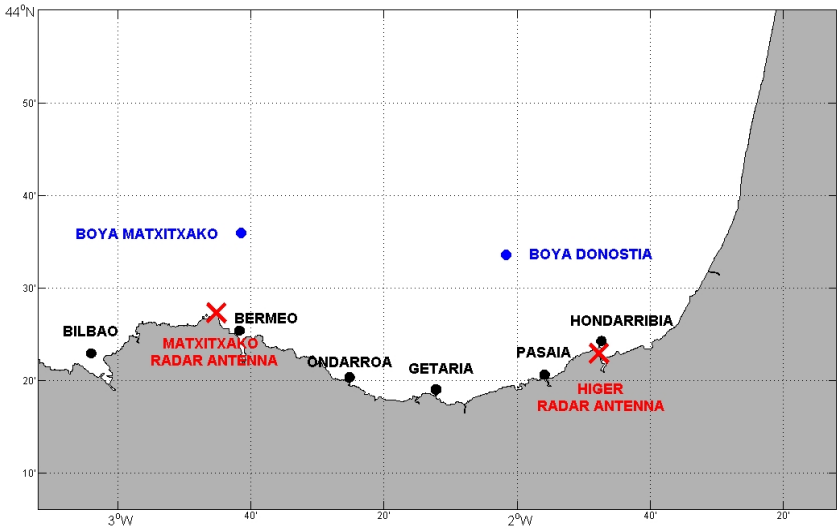

Figure 25: Locations of the (2) oceano-meteorological buoys (blue), (6) coastal stations (black) and (2) radar sites (red) of the Operational Oceanography System, established for the Basque Country region.

In the case of the Operational Oceanographic System of the Basque Country, the operational HF radar data are of particular interest with applications in various areas associated with the active management of the marine environment. Measures of surface currents from the HF radar system in combination with measurements of other integrated operational observing platforms are invaluable for the study and monitoring of coastal dynamics.

The combination of measurements of the HF radar with those of *in-situ* systems (mainly the slope buoys) has also offered the opportunity of extended validation and intercomparison exercises that will be detailed in the next chapter.

2.2.2. Available data from the Basque HF radar System.

In this thesis, HF radar data from 2009 to 2013 will be used in combination with other data from complementary observing and modelling systems (Figure 21). Data availability has not been uniform for all this period (see Figure 26, for the time series of data availability in the 655 nodes of HF radar footprint central part) due to several maintenance stops, troubleshooting of the antennas and errors due to atmospheric conditions; although the global coverage is good, several data gaps can be highlighted.

The first big failure of the system during 2009 to 2013 occurred in January of 2010. The problem lasted until early may. After the reparation it worked properly until the end of the same year, when it failed again. The technical stop at this time was for a month and the system worked properly, until the end of 2013 when it failed again for a month and a half. The most part of the problems have been due to hardware failures. Nevertheless, bad climatology has also caused problems in the antennas. It is also usual to have reception problems, which are solved just resetting the sites, which is done by DAEM (Directorate of Emergency Attention and Meteorology of the Basque Government) and/or Euskalmet group. The major problems of each antenna (Matxitako and Higer) are summarized in Table 2 and Table 3, respectively. Overall the system worked properly most of the time providing satisfactory current maps through the 5 years of data analyzed.

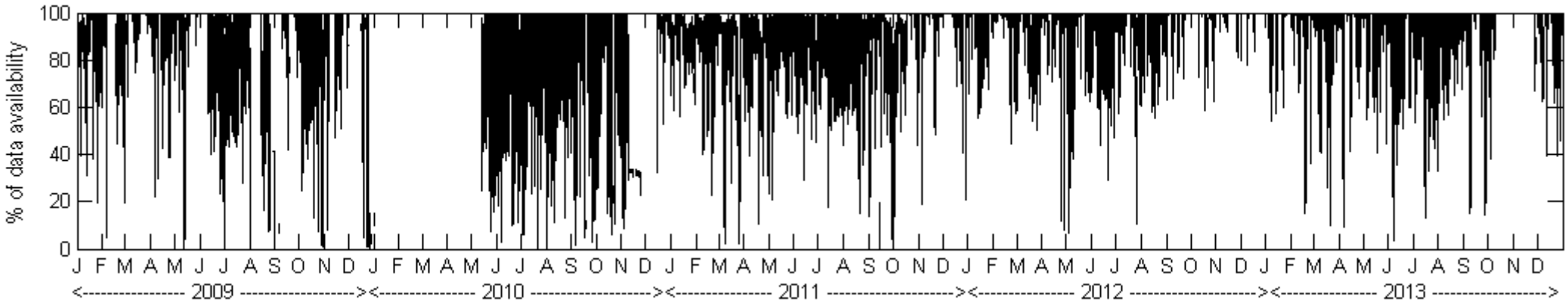

Figure 26: % of the data availability of the central 655 nodes, which had more than 50% of the coverage for the 5 years of data used in this thesis.

FAILURE DATA/PERIOD	FAILURE REASON
2010/Jan-May	High reflected power. Check and complete review of the system. Replacement of the damaged items.
2009/03/04-2009/03/10	Reduced range due to a heavy storm.
2010/11/26-2010/Dec	Failure of the receiving antenna.
2011/04/07	Increase of the temperature and reflected power of the transmitter antenna.
2012 May	Strong winds broke the rods.
2013/03/07	High reflected power.
2013/Oct-Nov	No data due to works in the lighthouse.

Table 2: Summary of the major failures of Matxitxako antenna

FAILURE DATA/PERIOD	FAILURE REASON
2010/Jan-May	High reflected power. Check and complete review of the system. Replacement of the damaged items.
2011/03/09	High reflected power. Humidity of the antenna base connector.
2011/12/26	Replacing deteriorated GPS antenna.
2013 November	Few days with no data produced by errors of an update of the system.

Table 3: Summary of the major failures of Higer antenna

CHAPTER III

ASSESMENT OF HF RADAR PERFORMANCES AND LAGRANGIAN PREDICTABILITY

Worldwide use and application of HF radar have been presented in previous chapters. Although the quality of the SE Basque Country HF radar data over the slope of the study area has been assessed in Rubio *et al*. (2011), additional radar –*in-situ* data comparison are presented here in order to: (i) assess the performances of the Basque HF radar system used in this thesis; (ii) show quantitative and qualitative comparison with other *in-situ* measurements in the area; (iii) evaluate the skills of the system to provide accurate lagrangian estimations.

3.1. COMPARISON OF THE HF RADAR DATA WITH EXISTING COMPLEMENTARY DATA

In situ data from independent sources are used for assessing the performances of the Basque HF radar system and to complete the information given by the radar, when suitable. The different data sets used for 2009-2011, as well as the details of the analyses performed on them, are described in the next paragraphs and summarised in Table 4.

DATA	POSITION	TYPE OF DATA	YEARS	TEMPORAL RESOLUTION (hours)	SPATIAL RESOLUTION (km)	DEPTH OF MESUREMENT (m)	DATA SOURCE
HF Coastal radar	Matxitxako: 43º 27.3' N 02º 45.2' W Higer 43º 23.5' N 01º 47.7' W	Remote	2009 2010 2011	1	5.12	2-3	Basque government
Offshore buoys	Donostia: 43º 33.6' N 02º 1.8' W	*In-situ*	2009	1	-	1.5	Basque government
	Matxitxako: 43º 36' N 02º 41.4' W						
	Donostia: 43º 33.6' N 02º 1.8' W		2009 2010 2011			12	
	Matxitxako: 43º 36' N 02º 41.4' W						
Drifters	43º 21' N – 44º 42' N 1-3º W	*In-situ*	2009	-	-	15	See Charria *et al.* 2013

Table 4: Brief description of the data and their characteristics.

3.1.1. Radar data

The processing and analysis of HF radar data have been done using the matlab toolbox "HFR_Progs" (https://cencalarchive.org/~cocmpmb/COCMP-wiki/index.php/Main_Page). To obtain total surface velocities, radial velocities from each antenna are combined in a regular grid through a least squares (hereinafter LS) fit of all radial velocities falling within a circle of 10 km radius around each node. For data quality control, a velocity threshold of 100 $cm \cdot s^{-1}$ is applied to the radial data (radial speeds over this value are disregarded). Then, the values of 2 uncertainty indicators are calculated and controlled when deriving total velocities from radials:

(i) On the one hand, it has to be taken into account that, with constant separation between radials and radial resolution, the spacing between radials increases as we move in the radial direction away from the antenna. Consequently, since the radius for the least square fitting (hereinafter LS fitting) to calculate total velocities is set constant to 10 km, further away the nodes are from the antennas, less information on the nodes there is. To avoid nodes where uncertainties become important, the RMS difference between the measured radial current and the radial current predicted by the model used for the LS fitting of radials to totals is calculated. Finding the right balance between optimal data quality and not losing too much spatial and temporal coverage, radial velocities where these RMS differences are over 18 $cm \bullet s^{-1}$ are excluded.

(ii) On the other hand, another major issue in the calculation of total velocities from radials is the Geometric Dilution of the Precision (GDOP) which increases drastically when the angles between radials become too small. Although all radial measurements available are used for getting the total velocities at each node, a non-uniform radial uncertainty is calculated for each node and component from the measured radial uncertainty. When uncertainty is over 8 $cm \bullet s^{-1}$ the data obtained for that node are disregarded.

Finally, regarding temporal resolution of radials and corresponding total vectors, due to cross spectra processing and averaging, each hourly radial velocity is a running average of 3 hours (as it has been explained in the previous chapter).

For this comparison, total hourly velocity radar data for the period from 2009 to 2011 are used. The availability of these data is not homogeneous during the 3-years study

period. Data gaps from few hours to several weeks exist in the data, with the year 2011 being the one with the most continuous data series (Figure 26). The main periods with no data are: January to middle May 2010, August to middle September 2010 and a large part of December 2010. Spatially, data availability decreases with the distance from the antennas, being the area enclosed by a radius of 100 km from the coast the one with highest data availability.

3.1.2. Buoy data

As observed in Table 4, data series from the two moored buoys (described in section 2.2.1) have been used (Figure 25). They provide, since 2007, long data series invaluable for validation purposes and also for observing seasonal and interannual variability of large scale processes.

Donostia and Matxitxako buoys are located over the upper part of the slope (Figure 25) (see Ferrer *et al*. 2009, Rubio *et al*. 2013a, for more details on the data). They are equipped with a surface Acoustic Doppler Currentmeter (ADC, working at 2MHz) which measures hourly current speed and direction at 1.5 m water depth. In addition to the surface sensors, a downward looking Acoustic Doppler Current Profiler (ADCP, working at 150 kHz) measures hourly currents, within 8 m vertical bins, over the upper 200 m of the water column (Figure 27). The periods of the maintenance stops of these 2 buoys for 2009-2011 are summarized in Table 5.

Matxitxako Buoy Failure/Stop date	**Donostia buoy Failure/Stop date**
Jun-Aug 2009	Jan 2009
Feb-May 2010	Jan-Feb 2010
Apr-May 2011	Dec 2010
Sep-Nov 2011	Jan-Feb 2011

Table 5: Matxitxako and Donostia buoy's maintenance/failure stops.

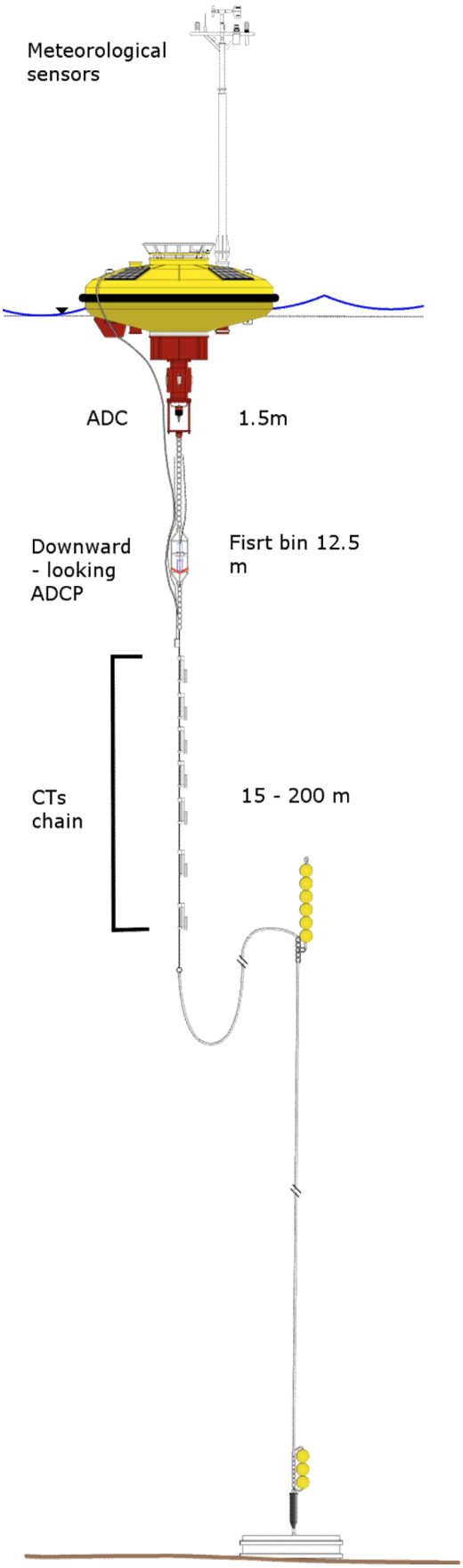

Figure 27: Donostia and Matxitxako moored buoys scheme (courtesy of C. Hernandez. AZTI-TECNALIA).

3.1.3. Drifter data

Data from 20 drifter buoys launched during several field cruises within the Bay of Biscay have been also used here (Charria *et al*., 2013). All the buoys had similar characteristics, with a surface float linked to a long (~10 m long×~1 m wide) holey sock drogue by a thin (~5 mm) cable and centred at 15 m depth. The position was transferred by an ARGOS localization system every hour. The drifter trajectories – HF radar data pairs used for comparisons in 2009, between 1ºW - 3ºW and 43º 21'N – 44º 42'N are represented in Figure 28-up, whilst temporal coverage of the data pairs is shown in Figure 28-down. Note that drifters were deployed during different cruises covering the period April – October 2009, mostly within a stratified water column.

3.1.4. Eulerian comparison results

As discussed previously by several authors (Paduan and Rosenfeld, 1996; Kohut and Glenn, 2003; Ohlmann *et al*., 2007; and Kohut *et al*., 2006) the comparison between HF radar-derived currents and current data obtained from *in-situ* platforms is not straightforward; this is due to the specificities and own inaccuracies of the different measuring systems. It has to be noted that at 4.86 MHz frequency, the measurements made by the radar integrate currents vertically within the upper 2-3 m of the water column (Laws, 2001). The nominal depths of the available data for comparisons are punctual, ranging in depth from 1.5 m to more than 10 m. Thus, it might be expected that vertical or horizontal shear in currents contribute also to the differences observed between the measurements. Moreover, there are differences in spatial and temporal averages: radar velocities are running averages of 3 hours, whilst buoys measure currents hourly. Comparisons presented in this chapter need to be analysed taking into account these differences.

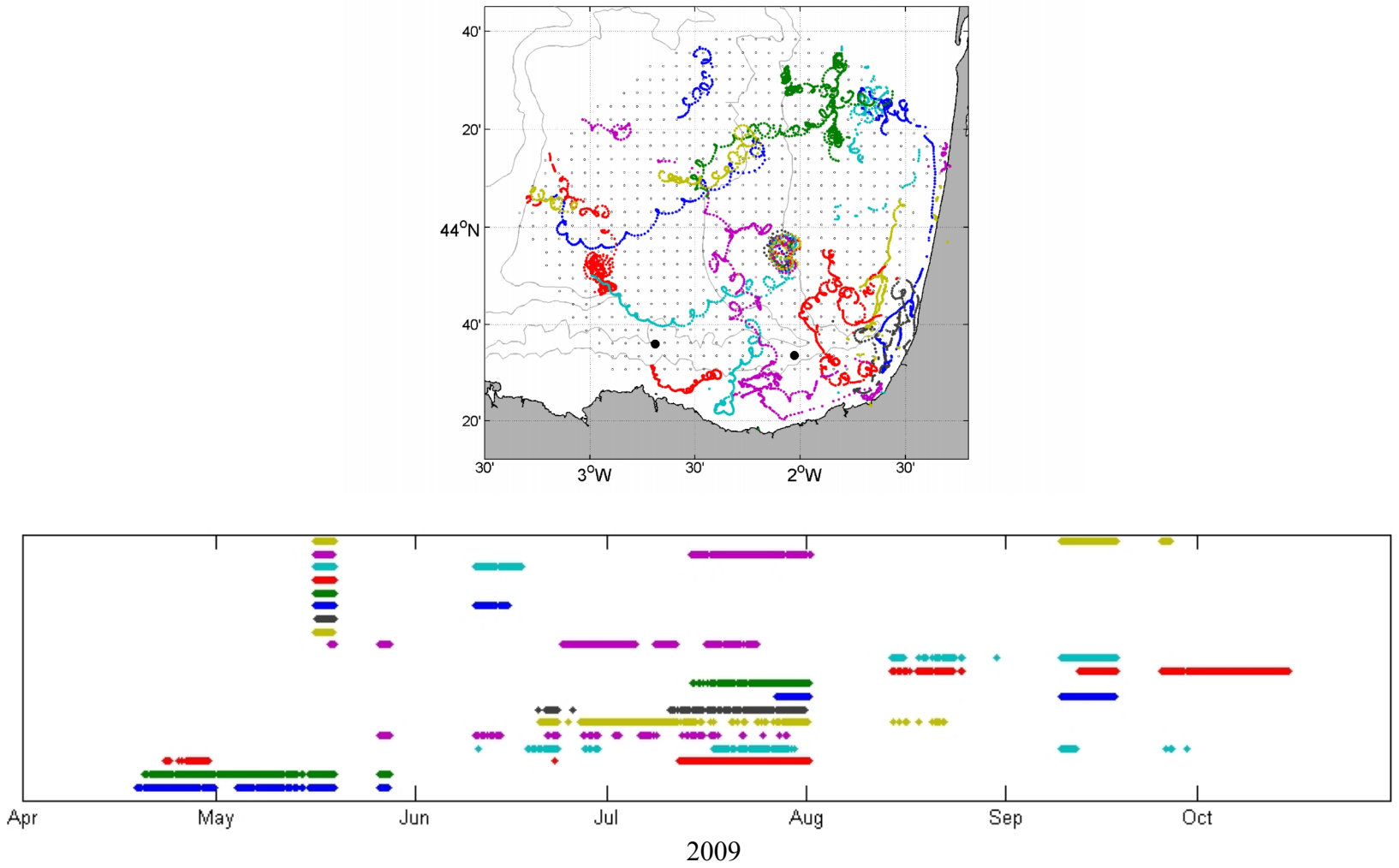

Figure 28: (Up) Spatial position of the joint drifter/radar information. Matxitxako and, Donostia buoys are represented by black points). Isobaths: 200, 1000, 2000m. (Down) Hours with radar and drifter/radar jointly information, for each of the 20 drifters, during 2009 (colours are just to difference the trajectories).

Previous, comparison between HF radar data and measurements from the Matxitxako and Donostia buoys at 1.5 m depth and for 2009 (Rubio *et al* 2011), showed: (i) correlation > 0.86 at Matxitxako buoy in the East-West component, u, with Root Mean Square differences (RMSd) values lower than 9 $cm \cdot s^{-1}$; and (ii) a correlation for the Donostia buoy lying close to 0.5 in the same direction, with RMSd values > 10 $cm \cdot s^{-1}$ (Table 6). The spatial differences in the correlations have been discussed in Rubio *et al*. (2011), in terms of the higher vertical shear and the higher variability of the current regime observed offshore at Donostia.

For 2009-2011 and *in-situ* data depth from the moored buoys at 12 m, lower correlations and higher RMSd are observed (see Table 6); this is consistent with the results of Rubio *et al*. 2011. At 12 m depth, the best correlation value for the U component is 0.67 at Matxitxako buoy and 0.57 at Donostia buoy. These lower values, compared with the values obtained when using data from the moored buoys at 1.5 m, can be related to the different measuring depth of both systems. As explained previously, the HF radar velocity corresponds to the integrated velocity over the upper 2-3 m of the water column. Thus, it can be expected that the measurement lies nearer to that of the moored buoy current-meter at 1.5 m.

Moored buoy velocities at 12 m and HF radar-derived velocities comparison have been performed also for the well-mixed and stratified months separately (Table 6). In this case, during months corresponding to mixed conditions (December to March) and a stronger eastward circulation over the Spanish slope (associated with the winter IPC), the correlation is higher in the u component of the velocity than during months corresponding to stratified conditions (June to October). This pattern is observed for both of the moored buoys (Figure 29).

** Rubio et al., 2011*

***In-Situ* Data**	**Measu-rement depth (m)**	**Time period**	**RMS ($cm \cdot s^{-1}$)**				**Mean Speed**				**Corr-u *In-situ*-Radar data**	**Corr-v *In-situ*-Radar data**	**RMSd-u ($cm \cdot s^{-1}$]) *In-situ*-Radar data**	**RMSd-v ($cm \cdot s^{-1}$]) *In-situ*-Radar data**
			***In-Situ* data**		**Radar node**		***In-Situ* data**		**Radar node**					
			u	**v**	**u**	**v**	**u**	**v**	**u**	**v**				
Matxitxako*	1.5	2009	0.16*	0.10*	0.13*	0.08*	-	-	-	-	0.86*	0.64*	8.09*	8.12*
Donostia*	1.5	2009	0.12*	0.11*	0.11*	0.12*	-	-	-	-	0.53*	0.34*	10.38*	12.88*
Matxitxako	12	01-Jan-2009 /07-Sep-2011	13.88	8.20	14.32	9.21	5.30	-2.28	4.09	0.22	0.66	0.50	11.12	8.97
Donostia	12	01-Jan-2009 /15-Oct-2010	9.72	6.84	12.40	13.07	2.75	-0.01	3.84	4.20	0.49	0.27	10.95	13.09
Matxitxako	12	Well mixed months	20.03	8.98	18.55	8.69	13.30	2.05	11.10	0.62	0.67	0.46	12.38	9.46
Donostia	12	Well mixed months	13.23	7.79	14.70	16.40	5.84	1.03	6.06	9.27	0.59	0.20	11.49	16.41
Matxitxako	12	Stratified months	9.03	8.58	11.84	9.73	1.14	2.57	0.31	0.31	0.51	0.57	10.70	8.89
Donostia	12	Stratified months	8.77	6.76	11.91	11.61	1.67	0.28	2.66	2.51	0.44	0.32	11.07	11.52
Drifters	15	May-Sep-2009 (See Figure 28)	13.99	13.67	13.77	13.84	-0.88	-0.33	-1.49	-1.14	0.42	0.46	14.85	14.30

Table 6: RMS values of in-situ data and radar data. mean speed of in-situ and radar data. Correlation of u and v velocity components between in-situ and radar data. RMSd values between in-situ and radar data.

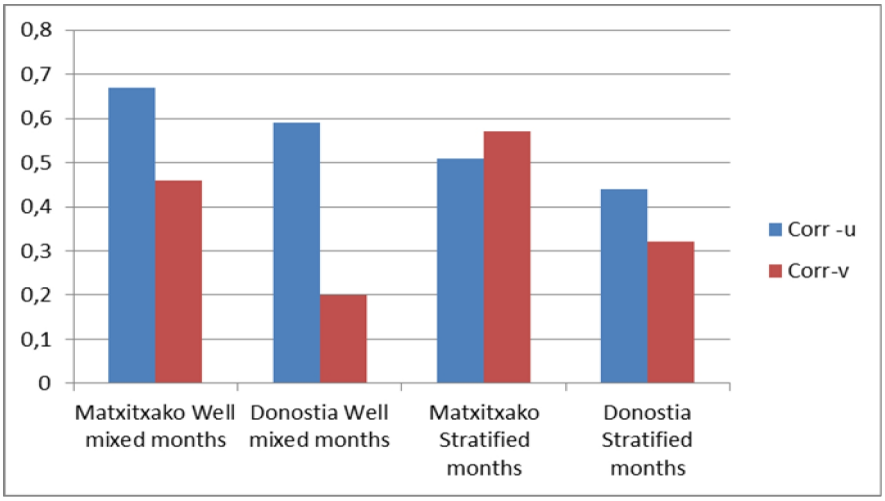

Figure 29: Correlation coefficient values between radar and Matxitxako and Donostia buoys, summarized in Table 6

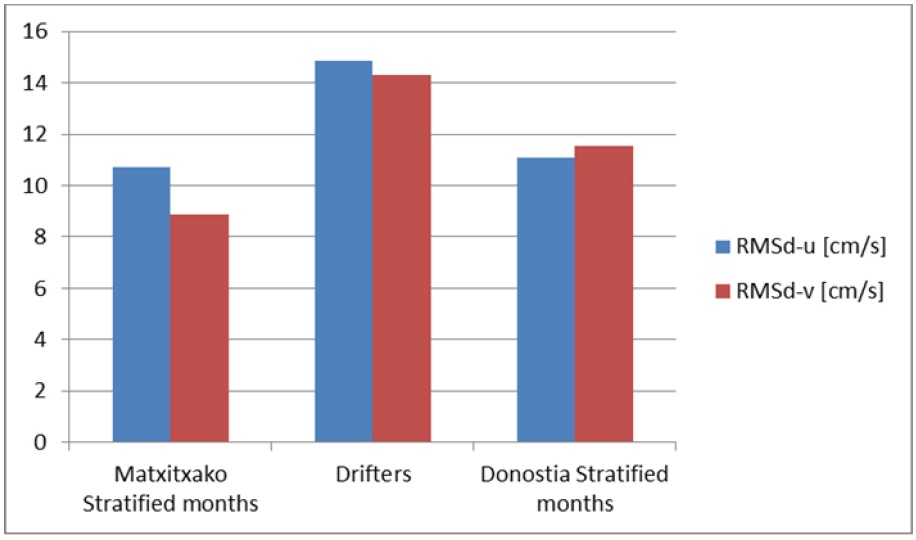

Figure 30: RMSd between radar and Matxitxako buoy (12 m depth), Drifters and Donostia buoy (12 m depth), summarized in Table 6.

The comparisons between drifting buoy's pseudo-Eulerian velocities (i.e. vector velocities at the consecutive positions of the buoys calculated from the discrete distances covered by the buoy in a given time step) and HF radar velocities are also summarised in Table 6. Taking into account that most of these drifters were deployed between April and October (Figure 28), the results have to be compared with those obtained between radar and moored buoys at 12 m during months of stratified conditions. With slightly higher RMSd (Figure 30), and similar coefficient of correlation

(Figure 31), the results of the drifter-HF radar data comparisons for the whole of the study area are in agreement with those obtained over the slope.

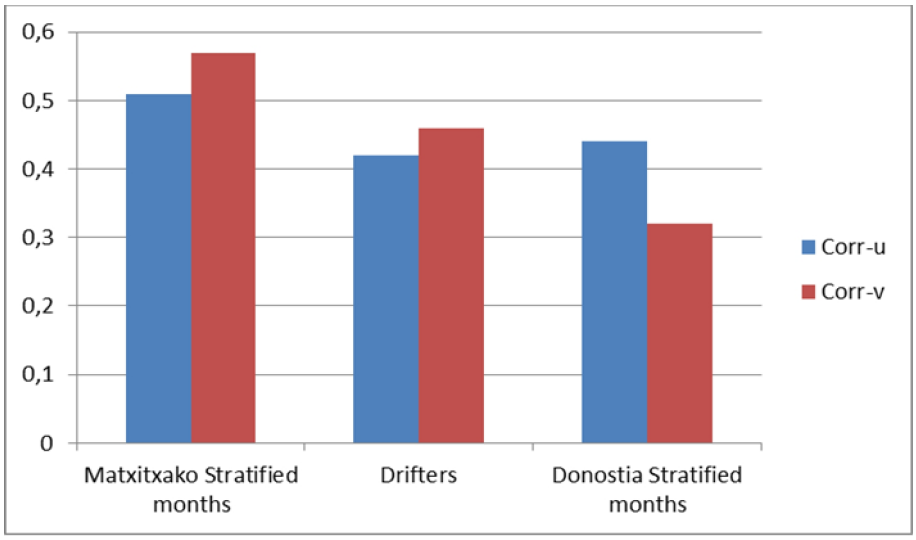

Figure 31: Correlation coefficient values between radar and Matxitxako buoy (12 m depth), Drifters and Donostia buoy (12 m depth), summarized in Table 6.

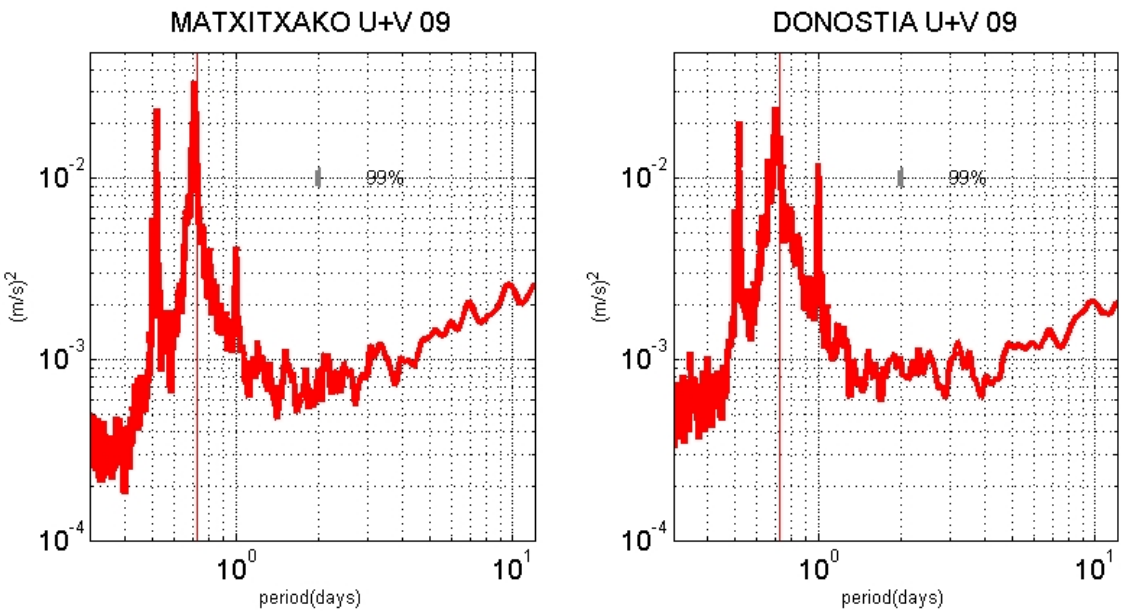

Figure 32: Matxitxako and Donostia power spectra inferred from HF radar (red line) for 2009-2011 data.

Finally, to complete the comparison made by Rubio *et al*. (2011), a spectral analysis was applied to HF radar data (nearest nodes to Matxitxako and Donostia buoy locations) for the period 2009-2011. In order to check whether the variability content of the HF Radar series is correct also for this period, the frequency energy content of the surface velocity records obtained was analyzed. For this purpose the corresponding frequency spectra were calculated, using the Lomb-Scargle method (Lomb, 1976; Scargle, 1982), as done in Rubio *et al*. (2011) to obtain comparable results (Figure 32).

If we observe the total KE content by frequency band of the HF radar data series, in general the energetic content of the spectra is very similar to the obtained in Rubio *et al*. (2011). The most important variability peaks are also correctly represented. It is observed that the energy is distributed in three main peaks [diurnal peak (due to the tide and breezes, 1 day), semi-diurnal peak (12.4 hours) and local inertial peak (17.04 hours)]. It is worth to highlight that in Donostia, the inertial band contains more energy than the diurnal tidal peak and this behavior is not observed in Matxitxako. This behavior, already observed in previous analysis of the *in-situ* buoy data, is confirmed in HF radar data, which shows the ability of the radar system to measure two-dimensional velocity fields with enough accuracy to detect differences in the spatial distribution of high frequency processes.

Consequently, it can be concluded that the spectra of the HF radar reproduce well the phenomena observed in the spectra of the two buoys, so the validation at these scales was successful.

3.2. LAGRANGIAN PREDICTABILITY

The temporal resolution of the HF radar derived surface currents (hourly data) allows to simulate surface drifter trajectories with the same time step as that of real drifters (described in section 3.1.3). In this way, the main goal of this section is to compare real drifter trajectories with simulated trajectories computed from HF radar derived currents and see the capability of the Basque HF radar system to simulate trajectories.

The major problem to generate trajectories using HF radar current maps, are the spatio-temporal gaps that usually contain the data. To solve this problem, data gaps in space and time are filled applying Open-Boundary Modal Analysis (hereinafter OMA), based on Lekien *et al.*, 2004 and Kaplan and Lekien (2007). The technique is two-dimensional so it has an advantage of not requiring any knowledge of the full three-dimensional circulation pattern. The end result of the OMA analysis is a set of time and data linearly independent eigenfunctions or modes (boundary, incompressible or irrotational) that can be used to interpolate, extrapolate and filter flows on an arbitrary domain with or without flow through segments of the boundary. The composition of the modes is generated using a triangular mesh and the generated physical modes depend only on the geometry and do not change in time (Lekien *et al.*, 2004). In this case, 85 OMA modes (some of these modes can be observed in Figure 33) have been generated to create gap-filled velocity maps (hereinafter OMA velocities or OMA currents).

For real-time applications, the velocity modes can be stored, and OMA only requires solving a linear system of N equations (N is of the order of 10 to 100) at each time step (Lekien *et al*., 2004). In this case radial velocities given by the HF radar are used to generate final OMA velocity fields, fitting these radial current measurements to the previously generated modes (as explained in Kaplan and Lekien 2007).

OMA currents used in this chapter have been generated with the HFR_progs library (described in Chapter II), using a 10 km average radius. The generated OMA velocities are based on two dimensional radial velocities. And this is one of the major advantages of this method: it is possible to have OMA velocity fields, with just one antenna radial velocities. The quality of the generated velocities is better using the two radial data. However it is possible to have data to use in operational way if it is necessary (rescue, oil spill…). Figure 34 represents the snapshots of the currents of the 22nd of July, with total and OMA currents. Figure 34.a shows radial velocities given by HF radar, for each of the two antennas. Figure 34.b shows total currents, and Figure 34.c shows currents with OMA analysis. This figure shows how OMA currents fill the data gaps in the selected area, using the available radial information.

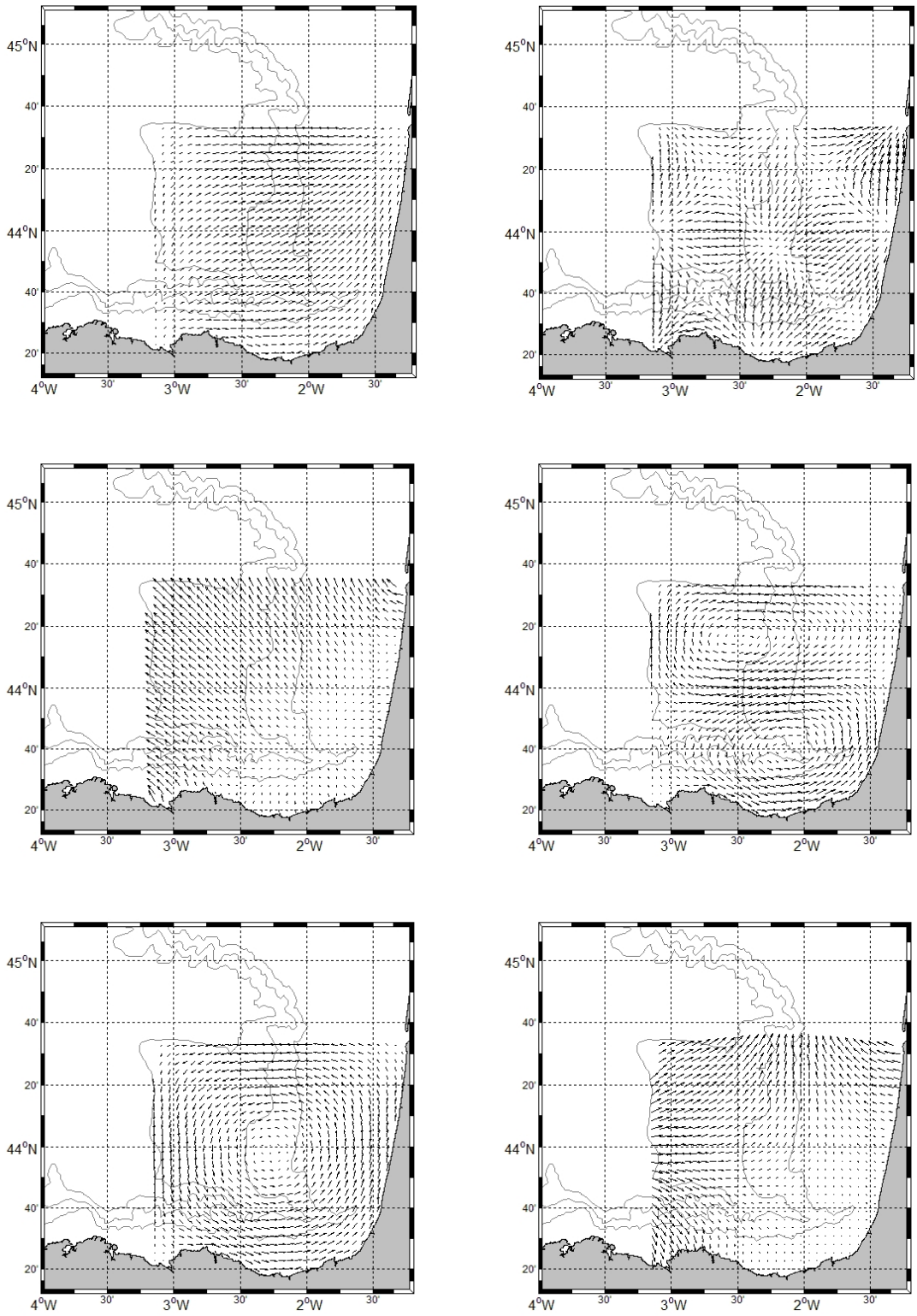

Figure 33: Some of the time and data independent eigenfuncions of the OMA analysis.

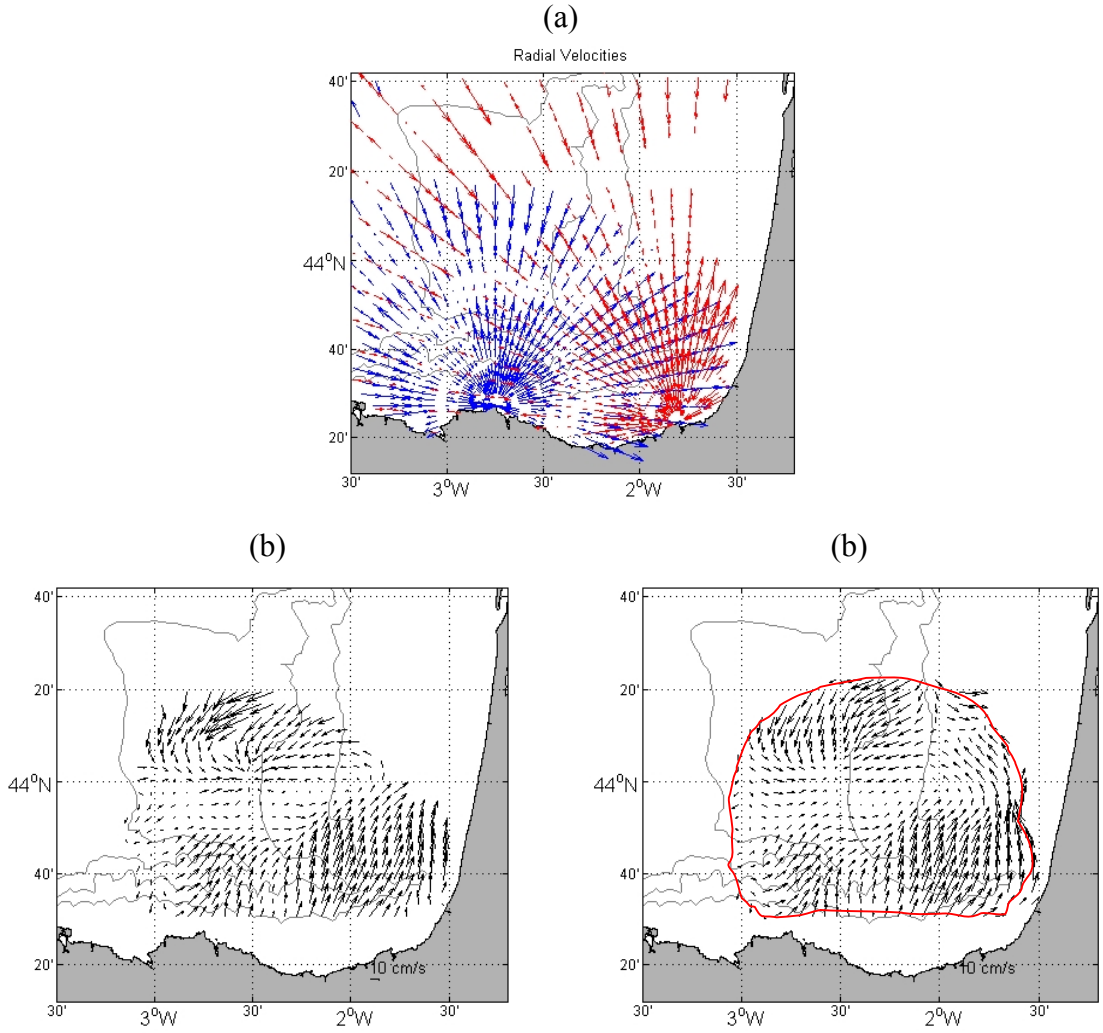

Figure 34: Snapshots of the surface currents of the 22nd of July at 12:00.(a) radial currents from the 2 radar sites. (b) total currents, generated from radial currents. (c) currents generated by OMA analysis. Red line limits the area used to obtain OMA velocities.

Once obtained a without-gap dataset, a lagrangian particle-tracking model (LPTM) has been used on total and OMA current datasets to reproduce the observed trajectory tracks. Using a new (2D) version of the LPTM previously used by (Ferrer *et al*., 2004) on numerical simulations of currents, particles have been released within the HF radar domain The method used for the particle movement in this LPTM, at a low computational cost, is based upon the 4th order Runge–Kutta scheme (Benson, 1992).

In order to have more than one comparison trajectory for each real drifter track (20 drifters in total), one trajectory has been generated every 6 hours at the corresponding

position along every real trajectory available in the study area and advected during 48 hours. In this way, the comparison tracks have increased substantially (see Figure 35.a as an example), from 20 real trajectories to 4543 possible comparison trajectories.. To allow comparison between OMA and total currents, only periods and locations when total data (i.e. data from the two radial stations) is available have been selected.

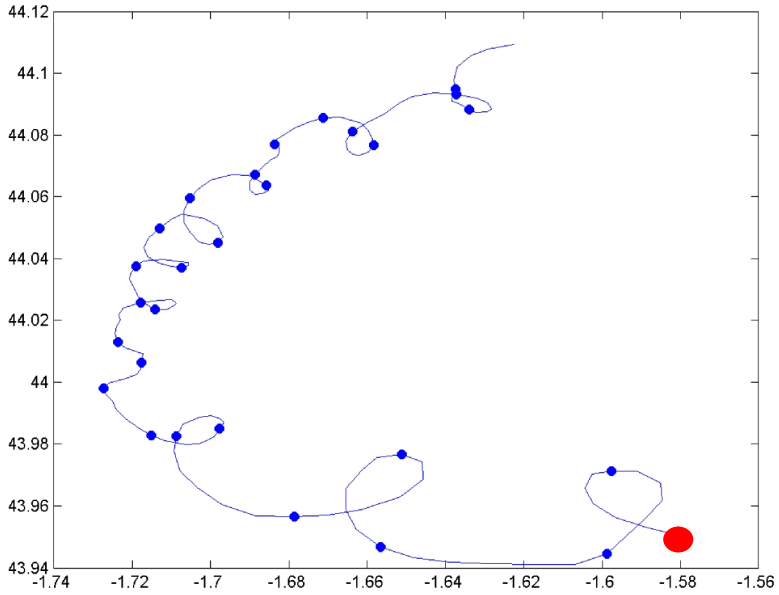

Figure 35: Blue line is the trajectory of a real drifter and blue points are the positions where a simulated trajectory has been initialized, each 6 hours of the real trajectory. The trajectory started on 30th May of 2009, at 22:00 and ended on 6th June of 2009, at 21:00. The starting point of the real trajectory is marked with a red dot.

Different comparisons exercises have been done to study the differences between real and simulated trajectories. First of all, separation distances between real and simulated tracks along the time have been calculated (Figure 36). After that, probability density function of distances between real buoys and simulated buoys after 6, 12 and 24 hours of simulations have been plotted (Figure 37). And finally, percentage of separation distances respect the total trajectory longitude have also been calculated (Figure 38)

Figure 36 shows a graph of the accumulative mean separation distances between real and simulated trajectories. The separation distance using the OMA currents are higher, since OMA reconstruction is always less accurate than total observed fields (even when 2 sites radial data is available). Figure 37 shows the progressive increase of distances

between simulated and real trajectories with time. Values of the separation at fixed intervals (6, 12 and 24 hours) have been estimated using probability density functions and a lognormal function fit. In Figure 37, probability density functions of distances between real buoys and simulated buoys (bars) after 6, 12 and 24 hours of simulations have been plotted. The lognormal function fitted to each distribution is given by the red continuous line, whilst dashed lines represent the limits of the 95% confidence interval. Parameters of the lognormal functions are given in Table 7. After 6 hours, the separation distance is between 2.25 and 3.00 km and these values increase until 5.23 and 6.73 km after 24 hours of simulation, reaching separation distances of 8.18-10.99 km after 48 hours of simulation, with total and OMA velocities, respectively. The standard deviation also increases with the simulation time steps, as observed in Table 7.

After 6 hour of simulation, the separation difference between total and OMA currents is 0.75 km (33% of the mean separation distance between real and simulated (with total) trajectories). However, it increases up to 1.50 (28%) and 2.81 km (34%) after 24 and 48 hour of simulation, respectively. This means that the relative separation distance between trajectories obtained using total and OMA currents respect to the distances between simulated and real trajectories does not increase with time.

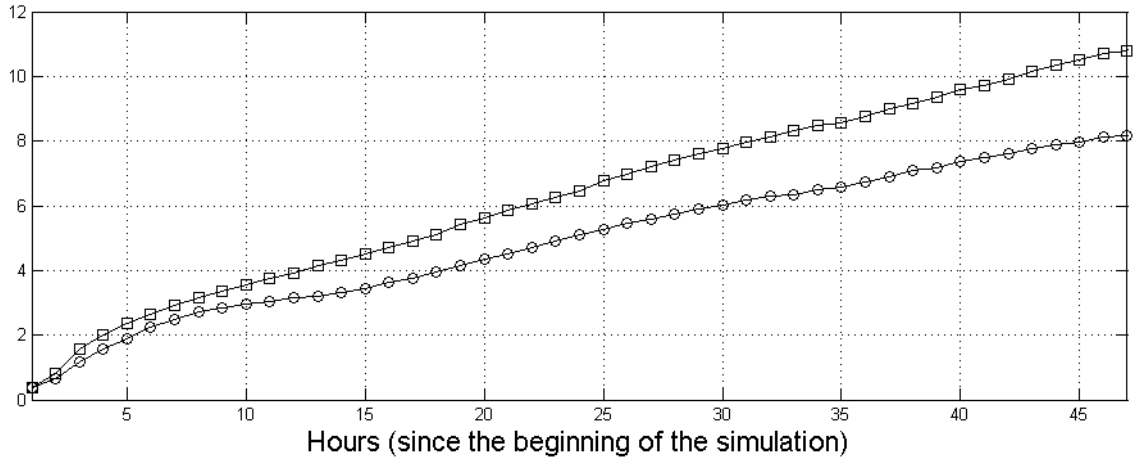

Figure 36: Separation distance average in km between real drifter trajectories and their simulated trajectories using Total (circles) and OMA (Squares) currents.

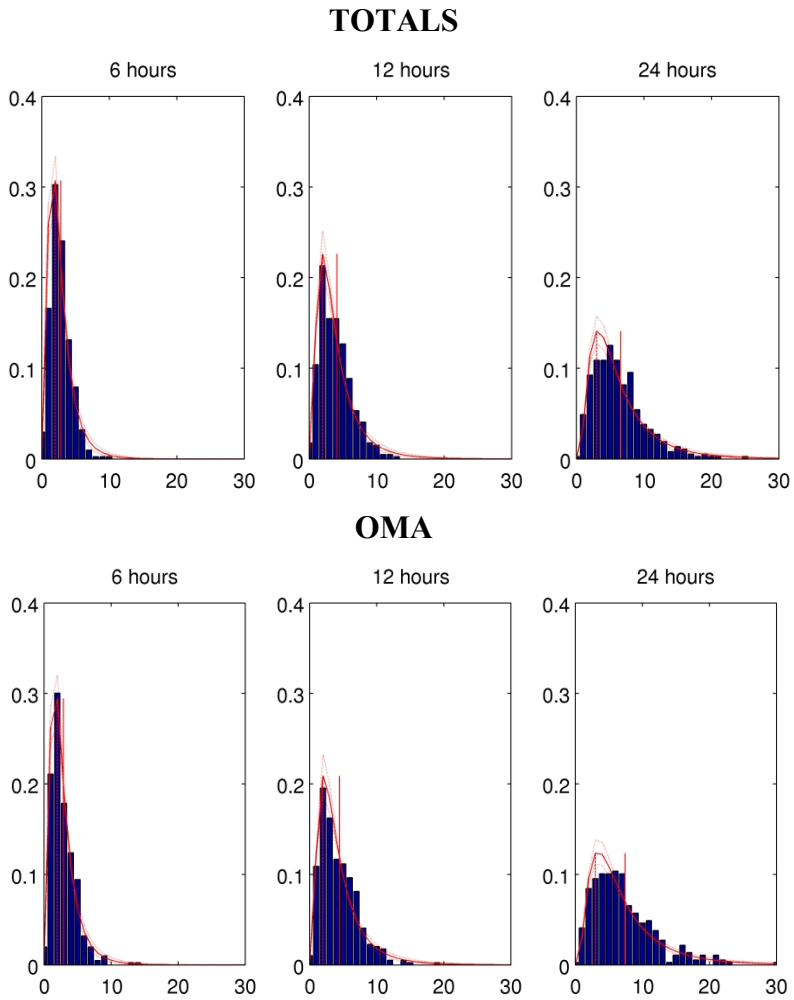

Figure 37: Probability density function of distances [km] between real buoys and simulated buoys (bars) after 6, 12 and 24 hours of simulations with (a) total currents (b) OMA currents.

Time (hours)	Main statistical parameters [km]			
	(a) TOTALS		*(b) OMA*	
	Mean	***Standard deviation***	***Mean***	***Standard deviation***
6	2.25 [2.32, 2.41]	1.76 [1.66, 1.88]	3.00 [2.89, 3.12]	2.68 [2.50, 2.88]
12	3.25 [3.14, 3.37]	2.58 [2.42, 2.77]	4.14 [4.00, 4.33]	3.36 [3.15, 3.60]
24	5.23 [5.06, 5.43]	3.86 [3.62, 4.13]	6.73 [6.49,6.99]	5.34 [4.99, 5.73]

Table 7: Statistical parameters for lognormal distributions of distances between real and simulated trajectories in figure 5, after 6, 12 and 24 hours of simulations with (a) total currents (b) OMA currents.

Figure 38 shows a similar plot where separation error % respect the total real trajectories' length is represented and Table 8 indicate the values after 6, 12 and 24 hours. This percentage is less than 20% with the 2 currents for 12 hours of simulation and increases until 32.66% with OMA currents for 24 hours of simulation. After 48 hours of simulation, both have near 55% of separation distance respect total trajectory length.

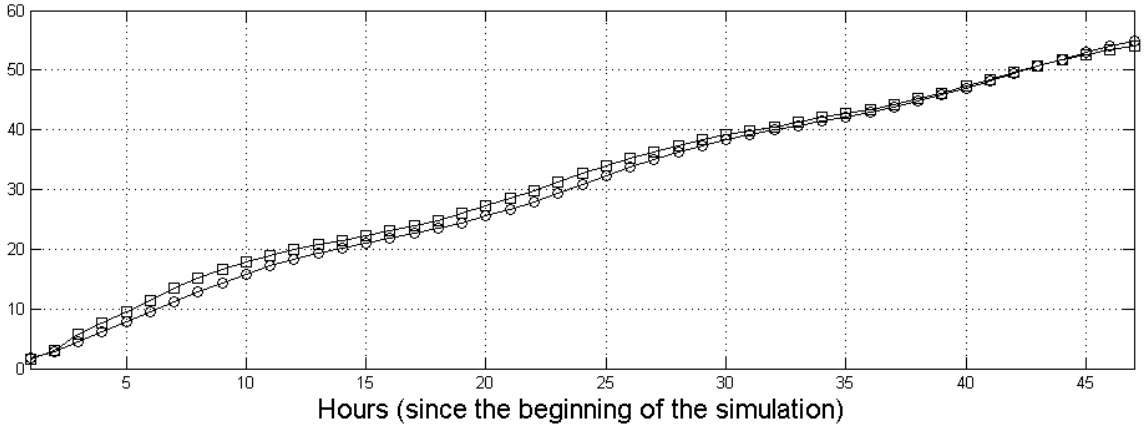

Figure 38: Percentage of separation distance respect the total real trajectory longitude, using Total (circles) and OMA (squares) currents.

Currents with:	% of separation distance respect total trajectory length after:			
	6 hours	12 hours	24 hours	48 hours
Totals	9.51	18.30	30.78	54.80
OMA	11.49	19.98	32.66	54.10

Table 8: Values of percentage of separation distance respect the total trajectory length, plotted in Figure 38)

3.2.1. Discussion of the lagrangian predictability

As written in previous section, the separation distance between real and simulated trajectories increases using OMA velocity currents instead of using total HF radar velocity currents for the trajectory simulations. The separation distances using OMA are 30% (approximately) higher than the separation between the real trajectories and simulated trajectories using total velocities. The separation distances observed in this section using total velocities agree with the results obtained in previous studies, using models (Thompson *et al*., 2003) or HF radar data (Ullman *et al.* 2006, Frolov *et al.*,

2012) to simulate trajectories. In order to allow comparison between OMA and total currents, only periods when total data (i.e. data from the two radial stations) is available have been analyzed. Consequently, this exercise does not account for an evaluation of the performances of the OMA analysis when radial information is lacking and reconstruction of total currents is done using only one radial component and/or temporal information from nearby time steps. In these cases OMA currents are known to be less accurate. However it can be expected that, although the use of OMA velocities will increase the separation distances, it will still be useful from operational purposes since it can guarantee no-gap current maps, which is an advantage when computing operational trajectories.

The search radius currently used by the national Marine Security governmental organization in Spain (SASEMAR) are significantly higher (SASEMAR, personal communication) than the separation distances between real and simulated trajectories obtained using HF radar data observed in this study. Because of confidentiality issues, it is not possible to offer real values in this thesis. However, results obtained suggest that the use of HF radar currents in the study area will greatly improve the actual search and rescue operations. This finding is in line with the growing use of HF radar data in all around the world for this and other purposes related to Marine Safety and Marine Pollution (i.e. http://www.cordc.ucsd.edu/projects/mapping/, Breivik *et al*., 2013).

3.3. CONCLUSION

Despite the known differences between the different available measurements, the results from the comparison between *in-situ* and HF radar show reasonable values, consistent with those described by other authors (Paduan and Rosenfeld, 1996; Kaplan *et al*., 2005). This observation reinforces the confidence in the results obtained by using the Basque Country HF radar to study and monitor the surface circulation in the SE Bay of Biscay. The comparison in terms of spectral energy contents at the tidal and inertial bands are similar to those observed in previous analysis of the data (Rubio *et al*., 2011) for a shorter time period. They confirm the ability of the Basque HF radar to measure two-dimensional velocity fields with enough accuracy to detect differences in the spatial distribution of high frequency processes.

On the other hand, with the results of the analysis of lagrangian predictability, it is possible to conclude that HF radar data are useful to generate trajectories for real situations, since they considerably improve the actual real values used in search and rescue operations in the study area.

For operational uses, both Total and OMA currents are useful. And although OMA currents generate higher inaccuracies, they provide no-gap surface current fields, more suited to operational trajectory and transport estimations.

CHAPTER IV

SURFACE OCEAN CIRCULATION IN THE SE BAY OF BISCAY

As summarised previously, several studies have been undertaken in the past, to describe the main characteristics of the surface water circulation over the shelf and slope of the study area. However, since these studies were mainly based upon punctual *in-situ* measurements, both in space and/or in time, there are still significant gaps in the knowledge. Indeed, a detailed description of the dominant surface current patterns related to different time-scales and incorporating both slope and open sea regions, has not been undertaken.

Within the above context, the main objectives of this chapter are to: (i) study and describe the main water surface circulation patterns in the area, in relation to seasonal, mesoscale and high-frequency variability, such as inertial and tidal bands; and (ii) quantify the contribution of the processes at different scales to the observed current variability in the SE Bay of Biscay.

4.1. DATA AND DATA ANALYSIS

4.1.1. Radar data

The processing and analysis of HF radar data has been undertaken using the Matlab toolbox "HFR_Progs" as explained in Chapter II For the present chapter, hourly total velocity radar data for the period 2009 to 2011 are used. As observed in Figure 26, existing data gaps within this period extend from a few hours to several weeks. Spatially, data availability decreases with the distance from the antennae. The area enclosed by a radius of 100 km from the coast is that with the highest data availability.

4.1.2. Data analysis

In order to analyse the surface current patterns at different time scales in the study area, different filters have been applied to the radar data. Monthly averages are used to provide a description of the main seasonal patterns. Then, a 10^{th} order digital Butterworth filter (Emery and Thomson, 2001) has been applied, to each velocity component of the time-series at each node: a low-pass filter (filtering out T<48 hour signals) to isolate low frequency signals; and a band-pass (maintaining $14<T_L<20$ hour signals), to isolate the inertial oscillations. Harmonic analysis, performed through a least squares method by using the Singular Value Decomposition approach (Press *et al*., 1989), has been applied to determine the contribution of the tidal band to the total KE.

Empirical Orthogonal Function (EOF, hereinafter) analysis, using singular value decomposition, has been applied to low-pass and band-pass filtered data for the period 2009-2011, in order to study large-scale, mesoscale and inertial currents. The EOF analysis technique is effective in reducing large correlated data sets, into a smaller number of orthogonal patterns ordered by their relative variance. Many authors have applied this technique to radar data (Kaihatu *et al*., 1998; Kosro, 2005; Liu *et al*., 2006). EOF analysis requires the input data to be continuous and the HF radar dataset used to

have few gaps. Thus, in order to apply this particular technique, the radar nodes with less than 50% of data have been omitted. The time-steps that had gaps at any node have been also withdrawn. With these restrictions, a data matrix with 507 radar nodes and 330 days has been obtained to undertake the EOF analysis, which has been applied to the HF current data, considering the both velocity components (U and V) as independent variables. Subsequently, the EOF analysis spatial modes were obtained with their associated variance and temporal amplitude series for the whole of the given temporal matrix. To analyse the temporal variation of the whole period (2009-2011), the time-gaps have been reintroduced, at their initial positions, reconstructing the original time axis. To study water circulation in the area, four EOF modes have been analysed, applying a truncation criterion in accordance to North *et al*. (1982).

4.2. LARGE AND MESOSCALE CIRCULATION

Processes ranging from mesoscale to seasonal scales are observable in a visual examination of hourly current fields in the study area. However, the large number of available hurly current maps makes difficult to resume these observations using few figures. For this reason, with the objective of representing some of the commonly-observed surface current patterns over the area, some selected "snapshots" of hourly fields (superimposed upon SST and Chl-a fields, when possible or suitable) are shown in Figure 39.

A main feature observed around winter-time is the surface signal of the IPC over the slope. In this area, other authors and previous study provide estimates for the intensity and direction of the IPC from *in-situ* moorings along the slope; they suggest the continuity of the flow between the Spanish and French shelf/slope from SST imagery (Le Cann and Serpette 2009; García-Soto *et al*., 2002; van Aken, 2002; and Pingree and Le Cann, 1992a, 1992b). The maximum radar-derived velocities observed for this flow reach up to 70 $cm \cdot s^{-1}$; they are in accordance with values presented recently by other authors (Rubio *et al*., 2013a; Le Cann and Serpette, 2009). In the example given in Figure 39.a, for winter 2009, the surface flow associated with the slope circulation is connected clearly with a marked warm SST anomaly (+2ºC, with respect to waters overlying deeper floors), in accordance with what is described in the literature. A

different situation is plotted in Figure 39.b which gives an example of wind-driven flow, with uniform vectors oriented in the same direction. In this case, 30 cm • s^{-1} surface speeds were measured, in response to the strong northwestern winds of 23 and 24 January (the KLAUS storm (González *et al*., 2009)).

In summer, the flow is much more variable, with mainly westward-oriented and weaker currents, the presence of strong inertial oscillations and complex spatial patterns. Figure 39.c provides an example where the surface current off the Spanish coast is intensified over the upper slope, flowing westwards with velocities around 35 cm • s^{-1}. In the northern part of the domain, the flow is towards the north and northwest over deeper floors and much less intense over the French shelf and slope. Other common feature observed in summer is a more homogeneous wind-driven westerly flow, which induces upwelling in the French coastal area (not shown).

Finally, at intermediate scales, the observation of the surface signature of mesoscale cyclonic and anticyclonic eddies (between 50 and 80 km in diameter) is common over the area. The surface signature of these structures is not always persistent, lasting only for some hours or days; from the visual (non-exhaustive) examination of satellite imagery, they do not have always a clear or persistent signature in SST and Chl-a. In the examples provided in Figure 39.d and Figure 39.e, an anticyclone is observed by the HF radar. Velocities were 20-30 cm • s^{-1} over several days, associated with a warm anomaly. The images suggest that the warm core eddy is incorporating into its centre, nutrient-rich (upwelled) cold waters, originating from the coastal area (see Figure 39.e). Some days later (unfortunately, no more cloud-free images were available) the eddy is observed to interact with a smaller cyclone in the area (Figure 39.f).

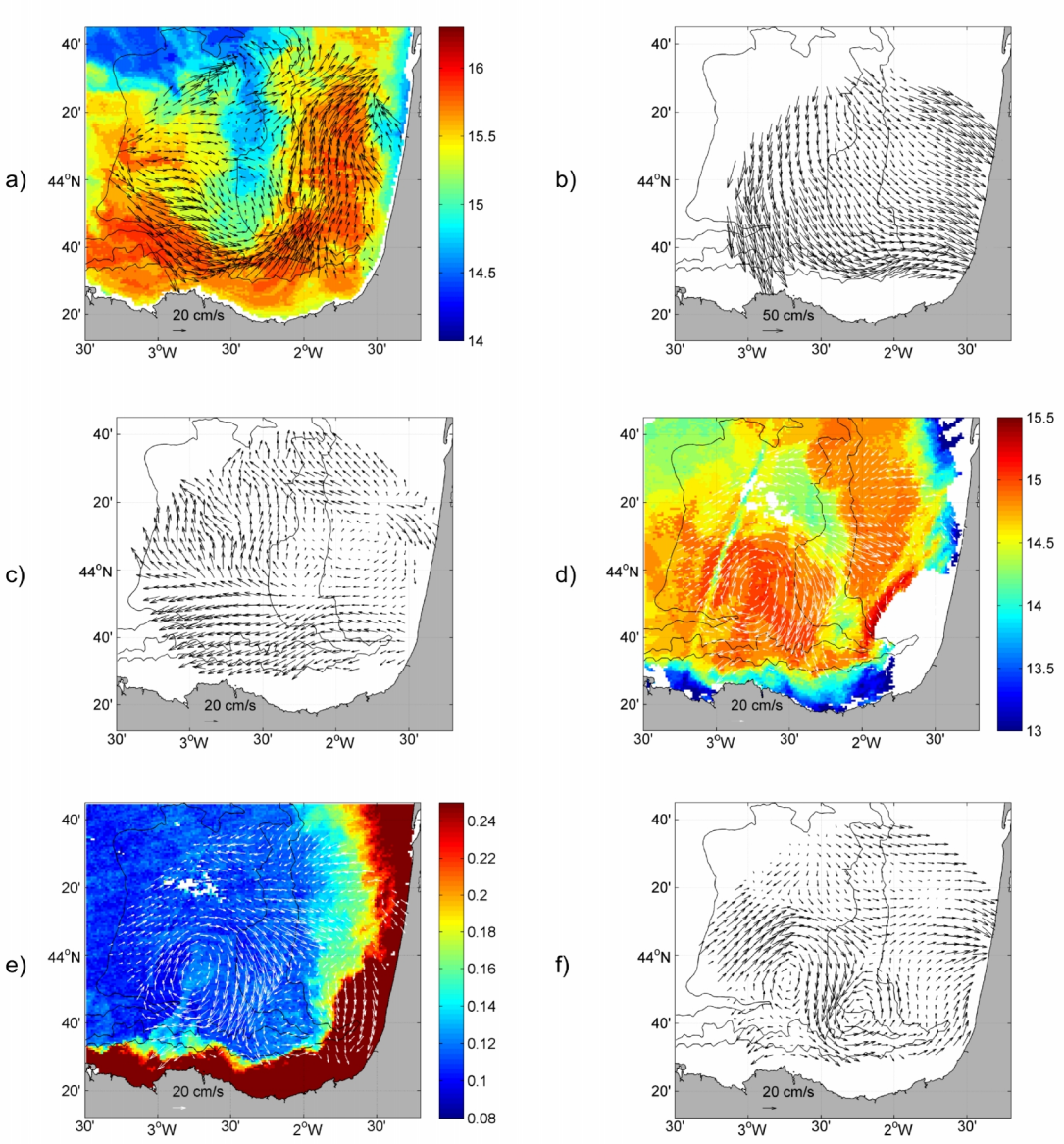

Figure 39: Snapshots of hourly radar-derived sea surface current fields for the study area. The time slots plotted have been chosen in order to give an illustration of some of the most commonly-observed patterns throughout the study period: (a) winter-time circulation with the surface signal of the along slope IPC and the associated warm surface flow; (b) intense southeastward currents in response to intense northwest winds associated with the passage of Klaus explosive cyclogenesis storm in winter 2009; (c) summer-time circulation, with intensified westerly currents over the Spanish slope, and (d,e,f) surface patterns associated with a well-defined anticyclonic mesoscale eddy. Its signal on SST and Chl-a satellite data is shown in (d) and (e), respectively; the interaction of this anticyclone with a smaller cyclone in the area, some days later, is shown in (f). Dates used are: (a) 24/11/2009 13:59 for SST satellite data and 24/11/2009 00:00 HF radar data; (b)24/01/2009 09:00; (c) 22/09/2010 09:00; (d, e) 27/12/2011 12:36 and 27/12/2011 12:50 for SST and Chl-a concentration, respectively, and 29/12/2011 19:00 for HF radar data; and (f) 31/12/2011. Isobaths: 200, 1000, 2000m

With the objective of giving a more detailed and quantitative analysis of the observed patterns in the study area and at different time scales, different analysis have been done in this chapter. Sections 4.2.1 and 4.2.2 show large and mesoscale circulation characteristics. In section 4.3, tidal and inertial currents of the study area are analysed. And finally, discussion and conclusions are shown in section 4.4.

4.2.1. Monthly patterns and along slope circulation

The monthly means calculated for the low-pass filtered HF radar currents, when data availability was sufficient, show a marked seasonality with significant surface current differences between summer and winter months (November is included in winter months, since the typical circulation during this month is very similar to that of the winter months). Figure 40 shows November 2009, January 2011, November 2011, September 2009, July 2010 and May 2010 monthly current means and variance ellipses, associated with each current vector. For the winter means (Figure 40.a1-a3), a cyclonic circulation with stronger currents over the slope characterises the three winter periods analysed. Interannual variability is observed, in terms of the position of the centre and characteristics of the cyclonic circulation. In winter 2009 (Figure 40.a1), the cyclonic circulation shows a closed pattern, with a central area with weaker currents near 2º 30'W and 43º 50'N, and a diameter around 60 km. Once again, a closed circulation appears in the monthly mean of January 2011, nevertheless centred farther to the southwest (around 2º 45'W, 43º 42'N) and with a smaller diameter, of around 50 km. In November 2011, the cyclonic circulation does not present a closed pattern. However the location of the area of weaker currents coincides with that of November 2009. As observed in Figure 40.c1-c2, this circulation reverses in summer and presents strong interannual and monthly variability. For September 2009, the centre of the closed anticyclonic circulation is located around 2º30´W and 44ºN; it has a diameter of around 100 km. In July 2010, there is (once again) an anticyclonic circulation, however centred near 3ºW and 44º10'N. As shown in the monthly means, the currents are stronger in winter and weaker in summer months, with intensification over the slope in winter and offshore in summer. Finally, the monthly means during the rest of the year, show much more variable currents in space and time, weaker speeds and no persistent clear structures. An example of the mean circulation observed in one of the transition months is provided for May 2010 (Figure 40.b).

The highest variability in the currents is observed during the transition months, when variance ellipses show large values, in comparison with the mean currents. Figure 40.b shows the average of May 2010: in most of the nodes, the variance is higher than the mean current value. During the summer months, the variance is similar and higher than during transition months. However the values of the currents are also stronger. Thus, the observed mean patterns are more persistent during summer, than in the transition months. The winter period months (Figure 40.a) show the highest variance ellipses and the highest mean currents values. Hence, the winter months have the most persistent and intense mean current patterns.

Focusing on the time variability of the circulation over the slope, the U component of the current in front of Cape Matxitxako (in a transect perpendicular to the coast spanning 10 radar nodes from the shelf break to depths of more than 2000 m over the slope (Figure 41)) is shown in Figure 42.a. The analyses of the data along this transect permits to study the along-slope component of the circulation. Then, to examine the vertical extension of the currents observed by HF radar over the slope the along-slope currents, measured by the Matxitxako buoy, over the upper 150 m of the water column, and for the same period, are shown in Figure 42.b. During winter months, several periods show an intense along slope eastwards circulation off Matxitxako: end of January-February, November and December 2009, October 2010, with U speeds up to 70 cm • s^{-1}; and January- February and November-December 2011, with U speeds over 60 cm • s^{-1}. From HF radar data, the meridional extension of the surface eastward currents in the strongest events is variable (where eastwards currents are observed in all of the vertical levels measured by the ADCP, except at the end of December 2011 since there is no buoy data available). During some episodes, the extension of the surface westwards flow is reduced and the maximum values are located closer to the coast (maximum in areas over the shelf and the upper slope, until 1000 m, as observed in January and February-March 2011). On other occasions, it extends farther to the north, involving all the nodes in the selected transect (as observed in December 2011). Two periods of clear and persistent westerly currents are also identified (Figure 42), in August-September 2009 and June-August 2010.

a1

a2

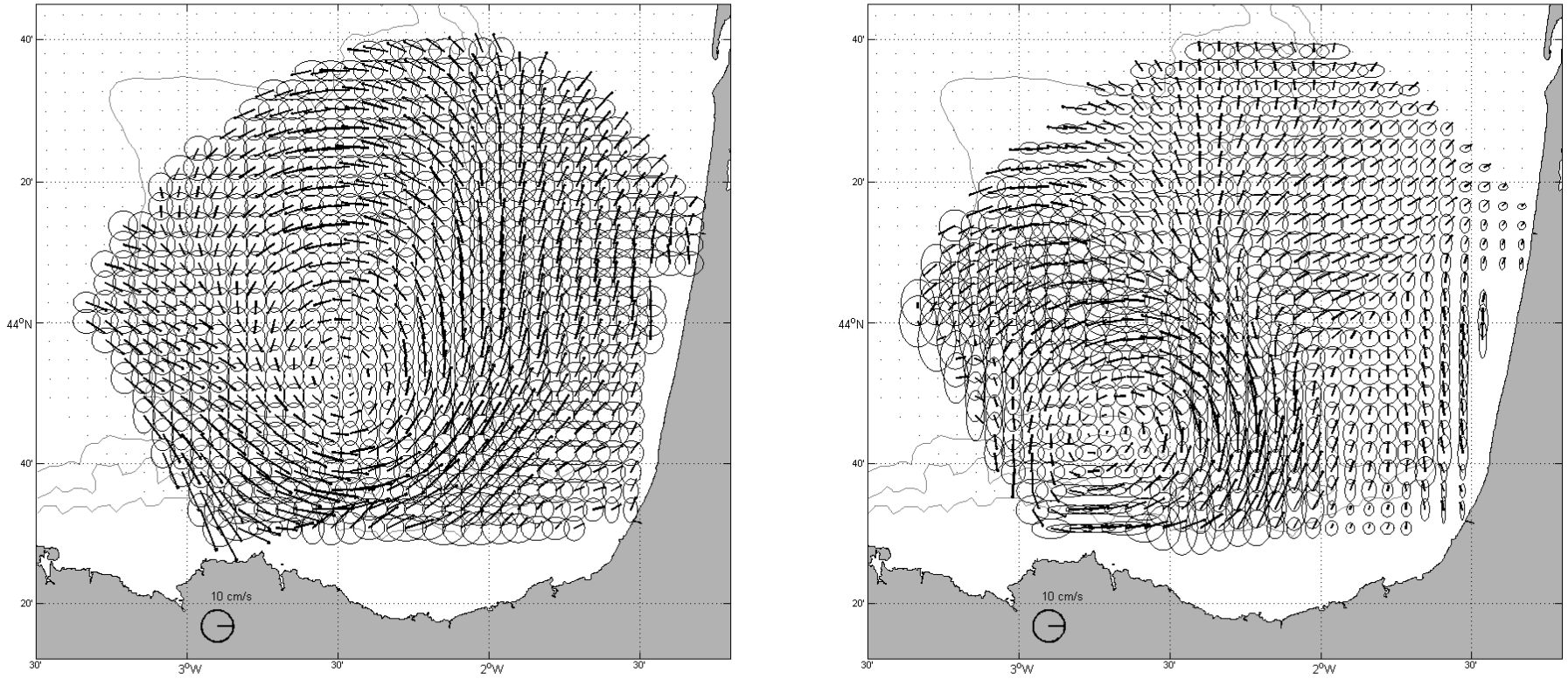

Figure 40 (1 of 3): Current mean and variance ellipses of: (a) Winter time: (a1) November 2009; (a2) January 2011; (a3) November 2011. (b) Intermediate time: May 2010. (c) Summer time (c1) September 2009; (c2) July 2010. Isobaths: 200, 1000, 2000m.

a3

b

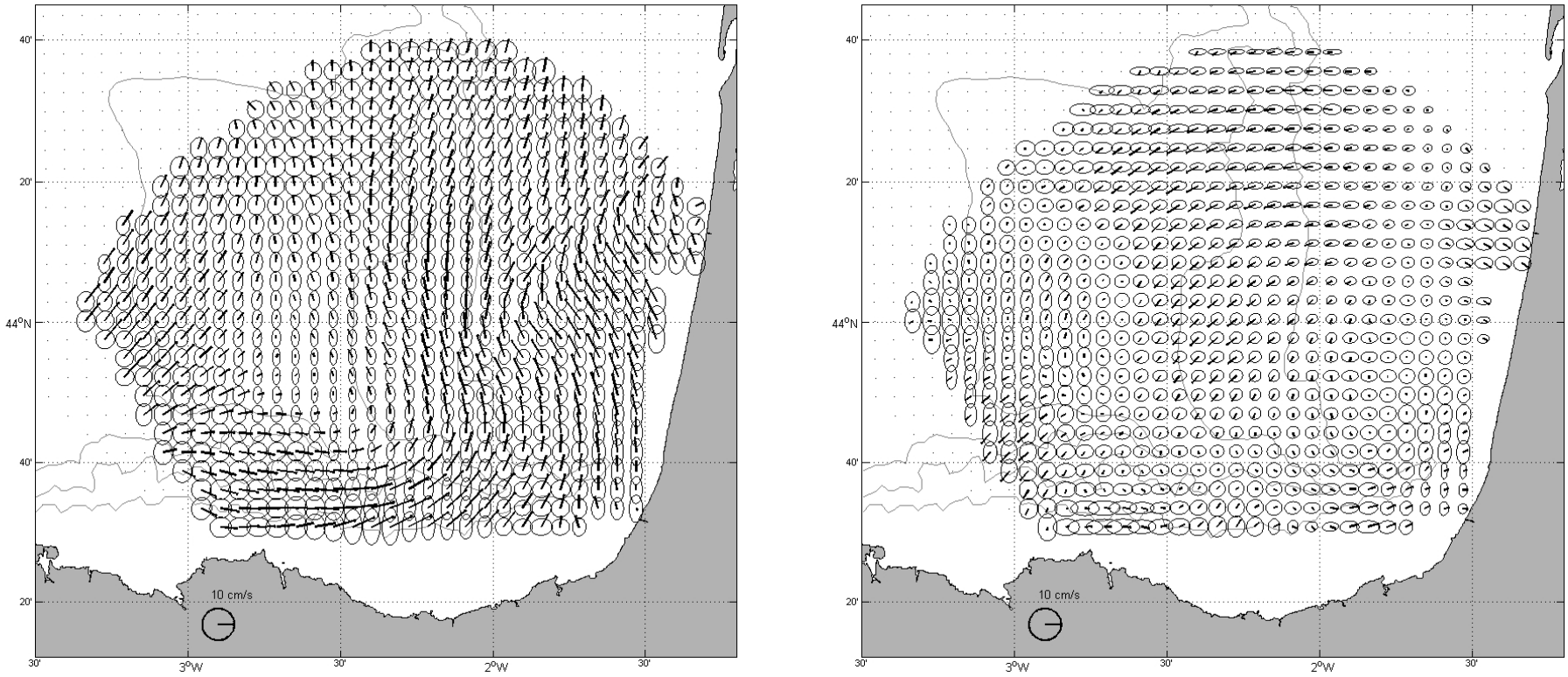

Figure 40 (2 of 3): Current mean and variance ellipses of: (a) Winter time: (a1) November 2009; (a2) January 2011; (a3) November 2011. (b) Intermediate time: May 2010. (c) Summer time (c1) September 2009; (c2) July 2010. Isobaths: 200, 1000, 2000m.

c1

c2

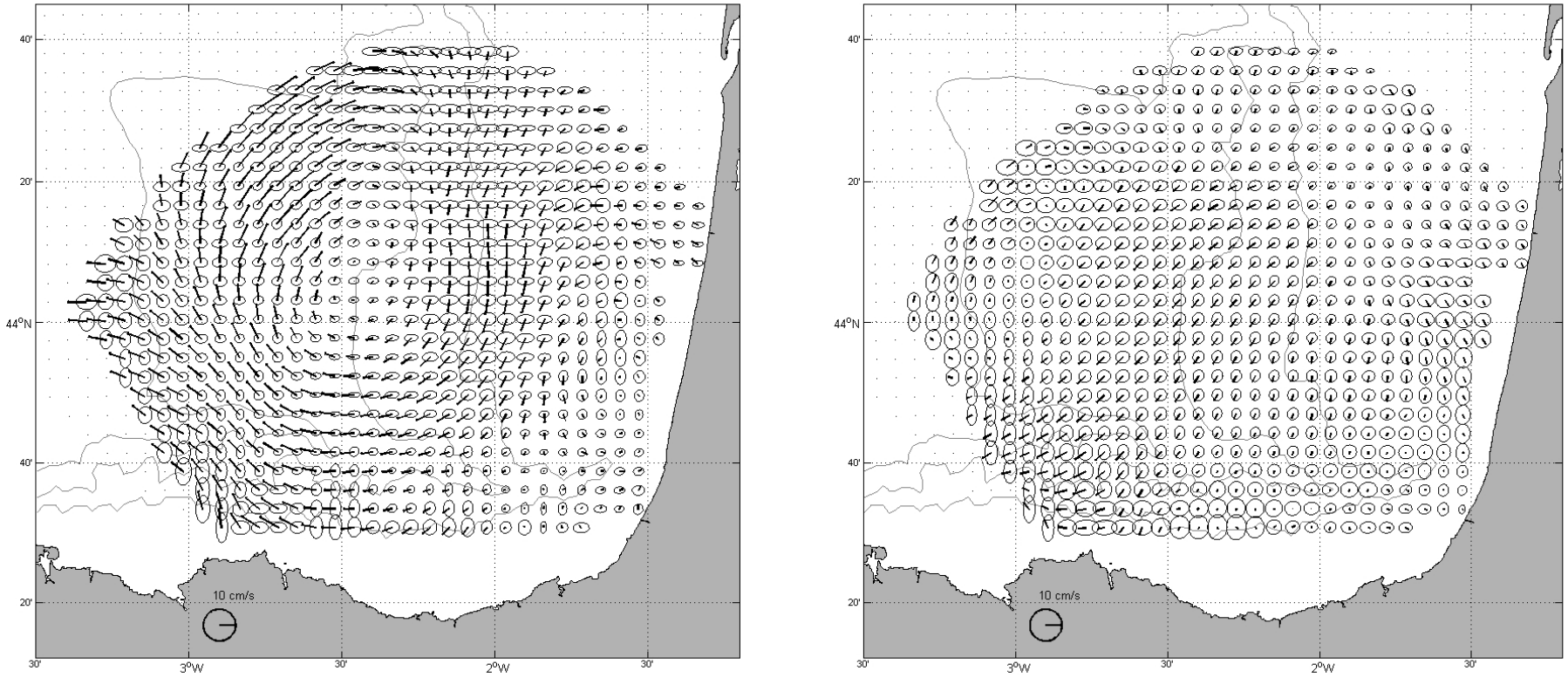

Figure 40 (3 of 3): Current mean and variance ellipses of: (a) Winter time: (a1) November 2009; (a2) January 2011; (a3) November 2011. (b) Intermediate time: May 2010. (c) Summer time (c1) September 2009; (c2) July 2010. Isobaths: 200, 1000, 2000m.

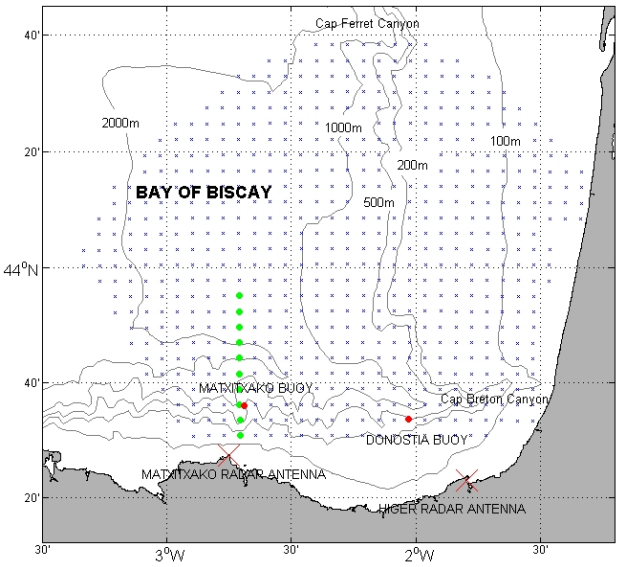

Figure 41: Study area. Red crosses show the position of the HF radar antennas at Higer and Matxitxako Capes. Blue points correspond to the nodes of the regular grid used to build radar-derived total current fields. Green points, highlight the nodes at which HF radar currents are used to compare with Matxitxako buoy data . Isobaths: 100, 200, 500, 1000, 2000m.

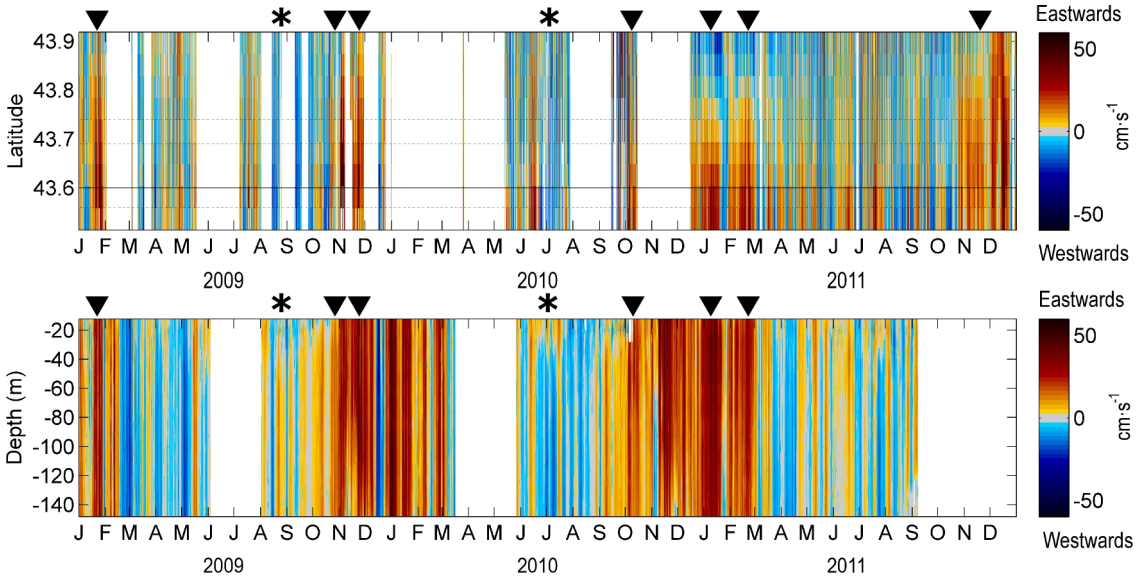

Figure 42: (a) Eastward (positive) – westward (negative) along-slope currents at the HF radar nodes, within the transect shown in Figure 41. Horizontal lines indicate the position in latitude at the longitude of the transect of the 200m, 1000m and 2000m isobaths (dashed lines) and Matxitxako buoy (solid line). (b) Eastward (positive) – westward (negative) along-slope currents at Matxitxako buoy, with depth. White spaces correspond to data gaps. Triangles and stars indicate some events during winter and summer periods, respectively, described in the text.

4.2.2. EOF analysis to low-pass filtered data

The results of the EOF analysis applied on the T>48 h band are shown in Figure 43. The first 4 EOFs explain 64% of the variance of the low-pass filtered surface circulation.

Mode 1 accounts for 28% of the variance; it shows a cyclonic pattern, with minimum velocities of around 2º 45'W and 44ºN. The velocities are intensified over the slope. In terms of the temporal variability, positive values are observed during winter, whilst negative values predominate in the summer months. The strongest positive events last for periods of several weeks (see, for instance, the period November- December 2009 or the peaks in the period December 2010 to March 2011). Mode 1 accounts for a cyclonic circulation during winter, whilst this circulation turns to anticyclonic during summer, revealing a clear seasonality. Note the good agreement between the positive events in the amplitude of Mode 1, with the periods of stronger and more persistent eastward currents identified in Figure 42. Similarly, negative values of Mode 1 correspond to the most persistent westerly currents in Figure 42. This observation is in agreement with the description given in the preceding Section, for the slope and shelf currents in the area, and with what has been identified in previous studies (Le Cann and Serpette 2009; García-Soto, 2004; García-Soto *et al*., 2002; van Aken, 2002; Pingree and Le Cann, 1992a, 1992b; Rubio *et al*, 2011). The time-series of the amplitude for Mode 1 suggests also that winter currents are 3 times more intense than summer currents. All of the winter strong intensification events have similar duration, of several weeks, with current reversals between the strongest poleward currents (see for example, the winter period of 2010-2011). In terms of temporal variability, the summer-type circulation periods are similar in duration throughout the 3 years analysed, occurring from May-June to the end of September (in summer 2009, there is a data gap from June to July). The winter of 2010-2011 is the only one with no large data gaps: the winter-type circulation period extends from November to April. This pattern contrasts with winter 2009, when the regime changes to westward predominant currents in March; this suggest a marked interannual variability, in accordance with the results of previous investigations (Le Cann and Serpette, 2009; García–Soto and Pingree, 2012).

(a)

(b)

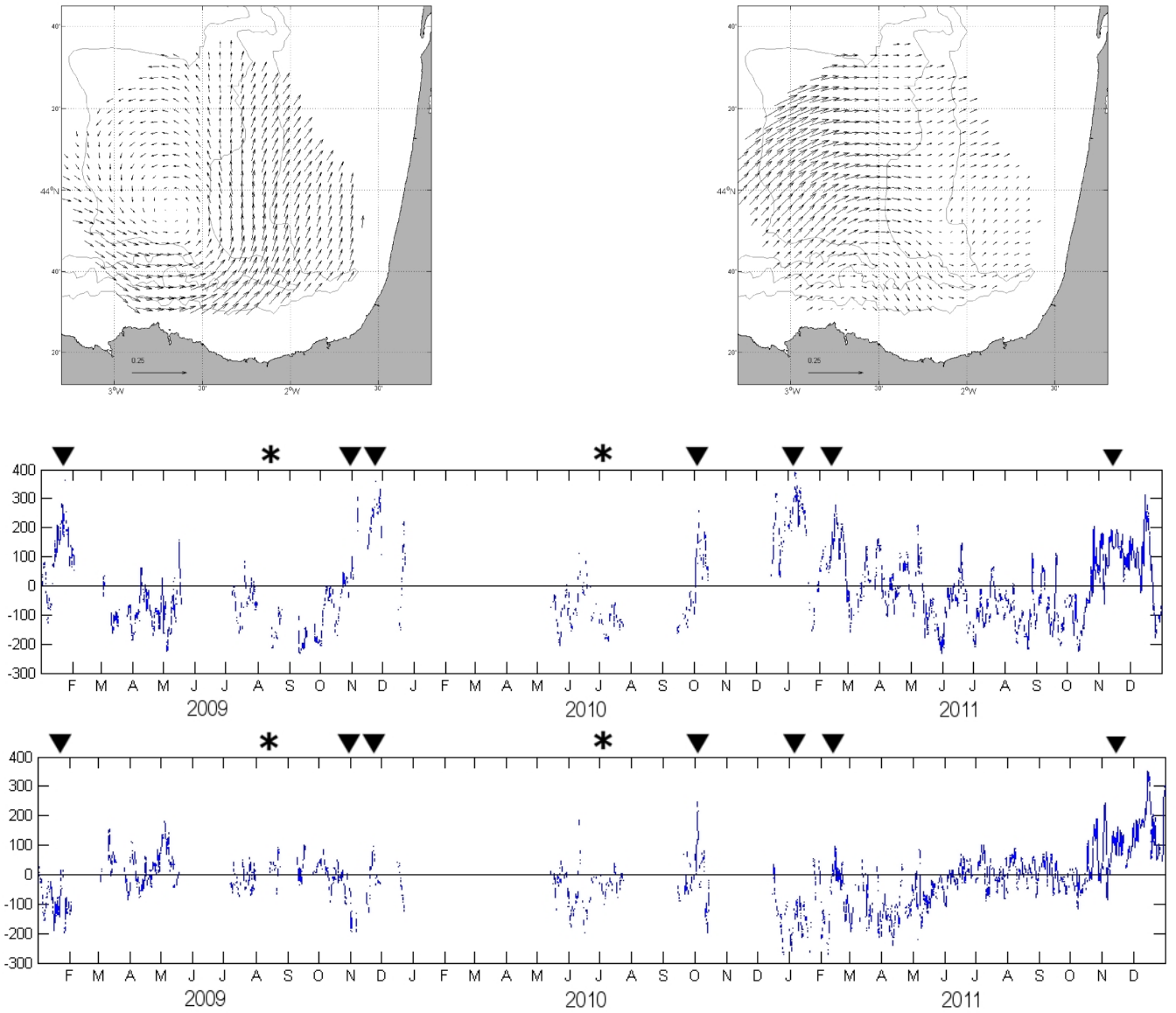

Figure 43 (1 of 2): Results of the EOF analysis applied to low-pass filtered data. (a) Modes 1(left) and 2 (right) spatial maps and (b) Modes 1 (upper) and 2 (lower) amplitude time-series. Triangles and stars mark summer and winter periods/events, explained during this paper. Isobaths: 200, 1000, 2000m.

(c)

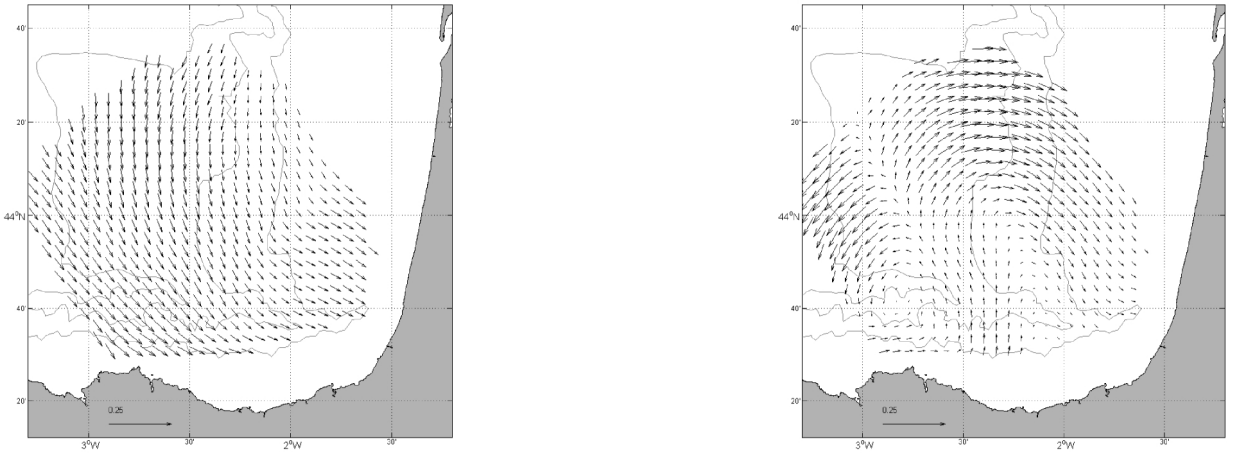

(d)

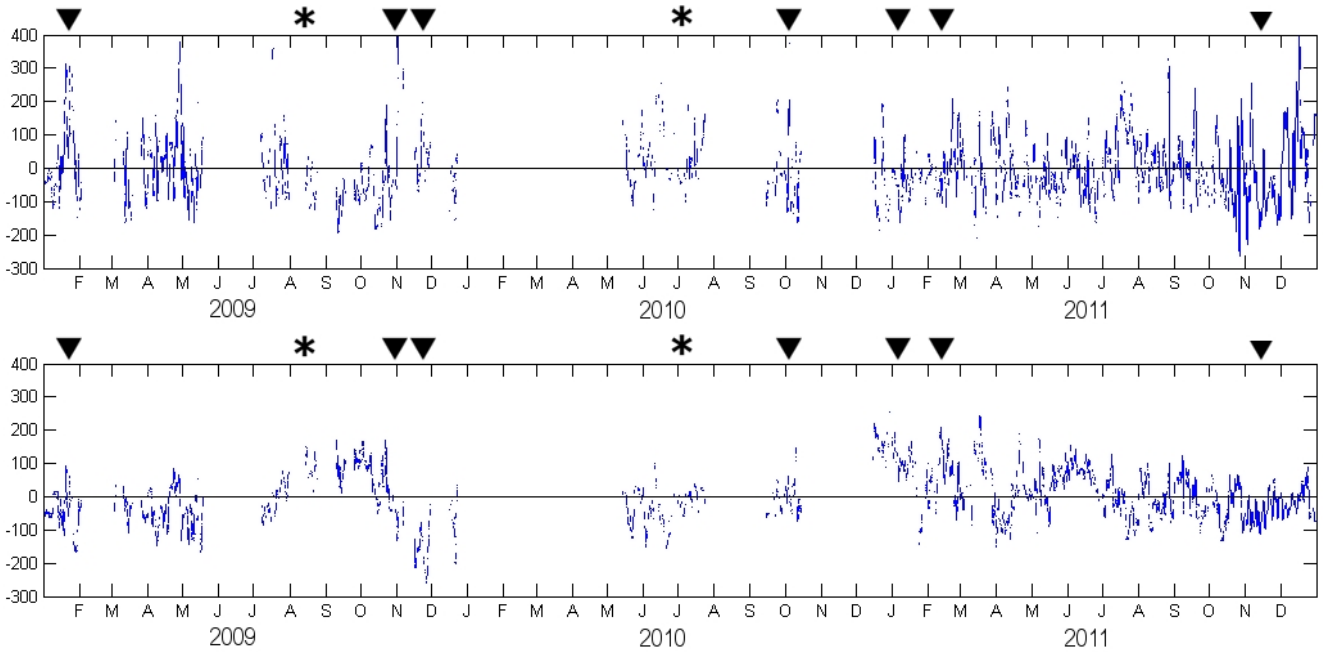

Figure 43 (2 of 2): Results of the EOF analysis applied to low-pass filtered data. (c) Modes 3 (left) and 4 (right) spatial maps and (d) Modes 3 (upper) and 4 (lower) amplitude time-series. Triangles and stars mark summer and winter periods/events, explained during this paper. Isobaths: 200, 1000, 2000m.

Mode 2 explains 16% of the variance; it presents a mostly unidirectional northeasterly surface current, intensified over the western part of the study area (i.e. over deeper water areas), with weak currents over the shelf. In terms of the temporal variability of the amplitude associated with this mode, it can be observed the highest positive values occurred during the last 3 months of 2011. The amplitude sign changes from negative to positive during the remainder of the period analysed, with a less clear seasonality than Mode 1. For example, negative values are observed during the winter 2010-2011; and from midway in 2011, to the end of the time-series, positive values are observed over most of the time, with a positive trend.

Mode 3 explains ~12% of the variance. The flow is southeastward (Figure 43.c,). Weaker currents are observed over the French slope, with more intense currents near the Spanish coast and over the slope. This southwesterly flow reverses depending upon the sign of the amplitude; this occurs repeatedly, throughout the year. In this mode, once again, there is not any clear seasonality; this contrasts with what is observed for Mode 1.

Mode 4 explains ~ 10% of the variance. The spatial map for this mode (Figure 43.c) presents two areas with closed circulation patterns: one with cyclonic polarization centred at 2º 45'W, 43º 40'N; and a second, anticyclonic at 2º 12'W and 43º 45'N. The flow is more intense over the northern and the western part of the study area; it is weaker over the remainder of the area. The amplitude time-series shows positive values in July-October 2009 and December 2010 to April 2011. The individual contribution of the subsequent EOFs (not shown), to the total variance, is much less significant (< 5 %). The derived spatial patterns and amplitudes present highly variable spatial-temporal distributions.

On the basis of the monthly averages (Figure 40), the results of the EOF analysis can be interpreted more easily; also, it is possible to relate them with the along-slope circulation observed at the Matxitxako location, for the study period (Figure 42).

Mode 1 is that contributing the most to the seasonal variability observed in the area, determining the cyclonic/anticyclonic polarization of the circulation. Modes 2, 3 and 4 add complexity to the circulation; contribute to the intensification of the along-slope current and the presence of regional closed circulation patterns. For example, the patterns observed in November 2009 and January 2011 result from the positive

amplitudes of Mode 1, and negative and positive amplitudes for Modes 2 and 3, respectively. This combination of the modes contribute to close the pattern over the northwest of the domain and to intensify the along-slope current along the Matxitxako transect. A different situation occurs in November 2011, where positive and negative amplitudes for Modes 2 and 3, respectively, added to the positive amplitudes of Mode 1, generate a cyclonic (but not closed) circulation. Finally, the strength and sign of Mode 4 displaces the location of the centre of the cyclonic circulation. This is the case for the winter of 2010-2011, where the amplitude of Mode 4 is positive, reinforcing the anticyclonic pattern of Mode 1. Likewise, positive values of mode 4 contribute to a closed cyclonic structure centred at 2º 45'W and 43º 43'N, as observed in the monthly mean for January 2011 (Figure 40.a2). It contributes as well to the intensification of the westward current over the slope, when maximum values appear closer to the coast, than that for the remaining winter periods Figure 42.a).

During the summer period, Mode 1 is again very important. Negative values of the amplitude for Mode 1 are observed during summer months, which contribute to an anticyclonic tendency over the area. Interpreting the contribution of the subsequent modes in summer is less straightforward than in winter, since there is much stronger variability. During August-October 2009, for example, there is an anticyclonic closed circulation; this results from negative values for Modes 1 and 3 and positive values for Modes 2 and 4. However, the contribution of the different modes to the mean circulation observed in July 2010, is less clear.

Similarly, during the months where monthly means do not show any clear patterns, the way the main modes combine to reproduce the highly variable observed circulation is difficult to interpret. Analysis of more years of data is needed, to study if there is any additional systematically repeated pattern during the transition months.

Globally, whilst Mode 1 is responsible mainly for the seasonal variability observed in the mean patterns, Modes 2 to 4 contribute to the observed interannual variability described previously.

4.3. TIDAL AND INERTIAL CURRENTS

4.3.1. EOF analysis of the inertial currents

With the objective of studying quantitatively the spatial and temporal patterns associated with these frequency bands, band pass-filters and EOF analysis have been applied to the data. Finally, the contribution of these processes, to the total currents in space and time, is evaluated quantitatively.

For studying inertial oscillations and their distribution within the study area, EOF analysis has been applied to the inertial band-pass filtered data. Here, the first 4 modes explain more than the 70% of the variance (Figure 44), with the first 2 modes being responsible for almost 60%

Mode 1 explains the 35% of the variance; it presents: a non-uniform current field with the vectors oriented along a north/south axis over the south of the study area and along a NE-SW axis in the northwest. Higher intensity is observed over the deeper part of the slope, with less intense currents over the French shelf and over the upper part of the slope off the Spanish coast. Similar to what is observed for the other three modes, the amplitude time-series of the first mode shows an oscillating behaviour, with values changing sign with the local inertial period (TL ~17.04 h); this has been determined quantitatively on the basis of the spectral analysis of the series (not shown). The amplitude of the oscillations shows a clear seasonal signal, with significantly higher values in summer months, than in winter. Some individual events can be highlighted from the amplitude series of Mode 1, which can be identified also at the subsequent modes. An example is the peak in September-October 2010, which is observed within the 4 modes (with strong signal in Modes 1 and 2); likewise that at the end of October 2011, present in Modes 1 and 2.

(a)

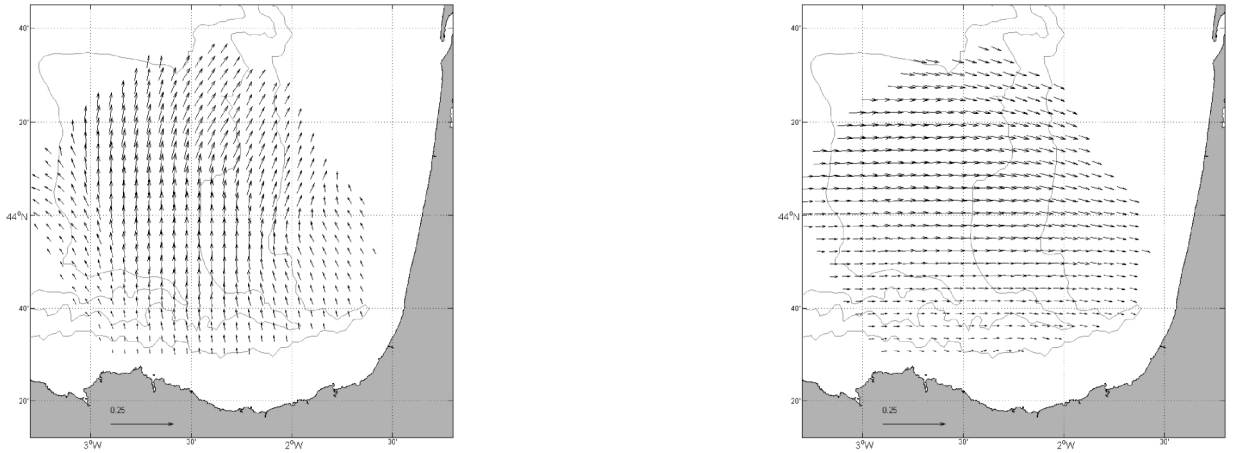

(b)

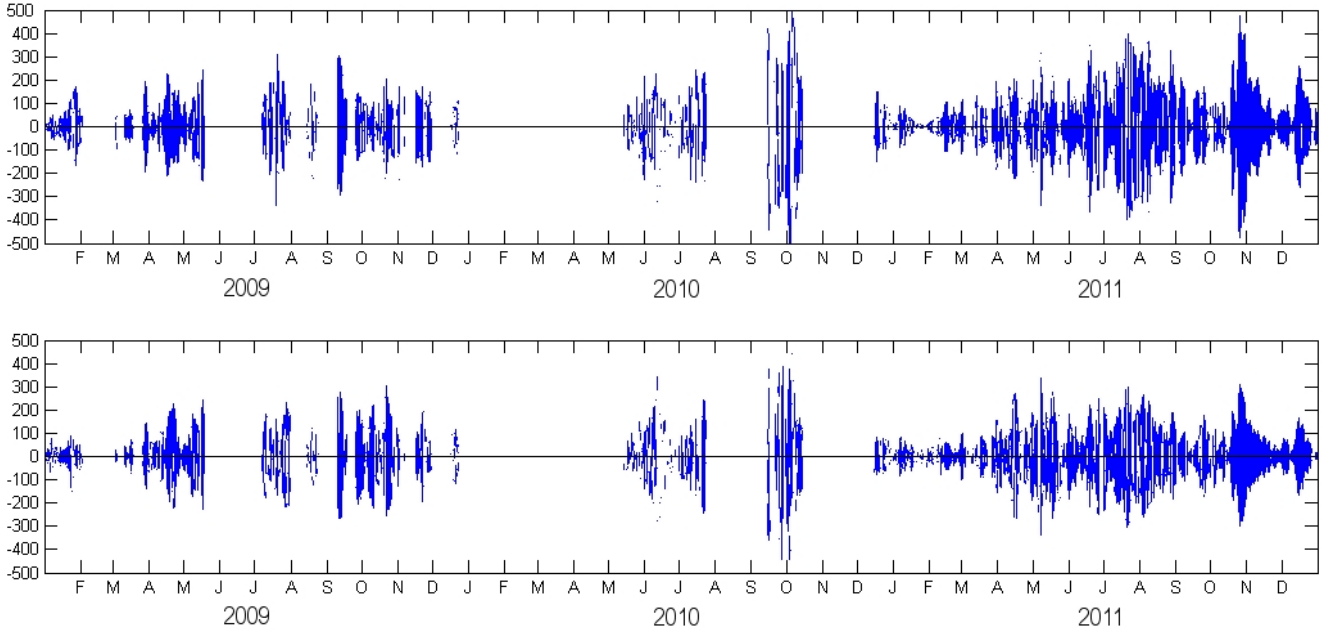

Figure 44 (1 of 2): Results of the EOF analysis applied to inertial band pass filtered data. (a) Modes 1(left) and 2 (right) spatial maps and (b) Modes 1 (upper) and 2 (lower) amplitude time-series.

(c)

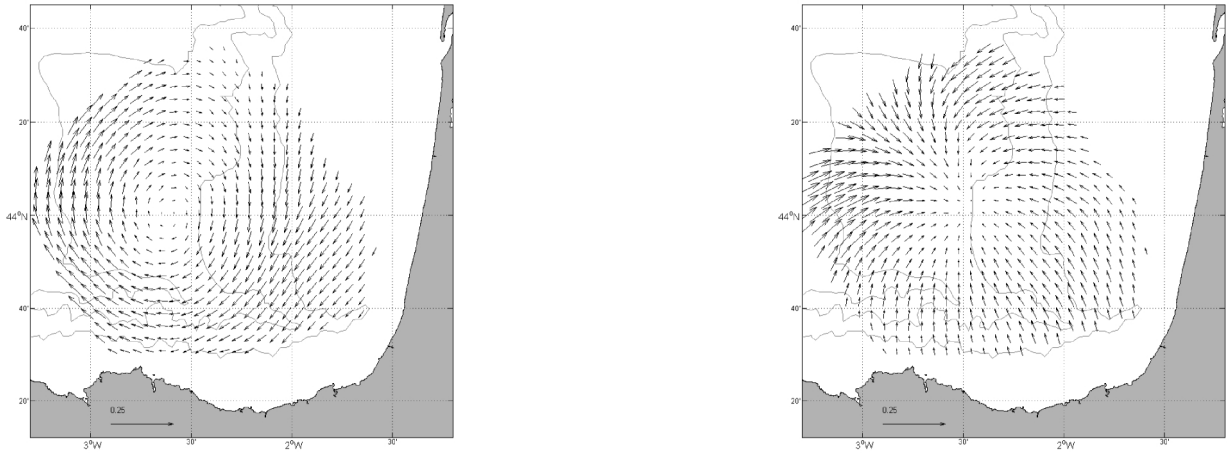

(d)

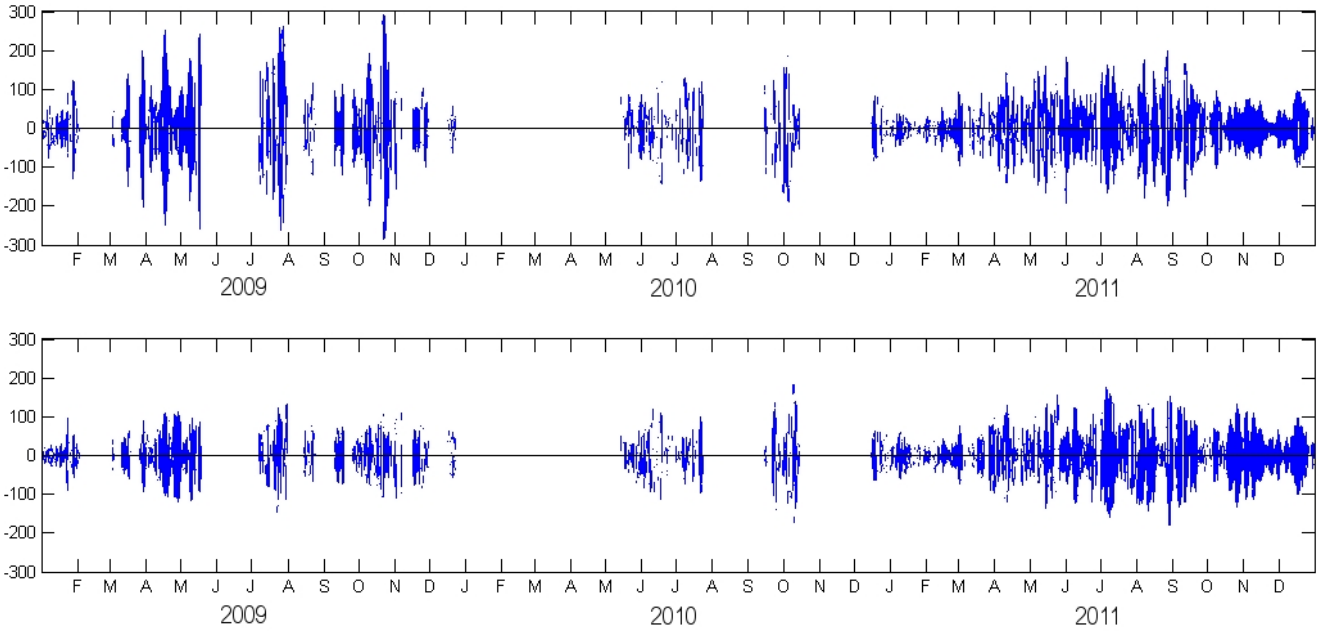

Figure 44 (2 of 2): Results of the EOF analysis applied to inertial band pass filtered data. (c) Modes 3 (left) and 4 (right) spatial maps and (d) Modes 3 (upper) and 4 (lower) amplitude time-series.

The Mode 2 accounts for some 23% of the variance. The vector field is oriented along the East/West axis; it is quite uniform and nearly unidirectional, for all of the study area except for the shallowest shelf areas of the Spanish and French coasts; here, the field is weaker. Note that vectors in the spatial pattern of Mode 2 are directed, for the most of the domain, in a perpendicular direction to those in Mode 1. The Mode 3 explains some 11% of the variance; it shows a more complex distribution of current vectors, with a central area where vectors are weaker (around 2º 36'W and 44ºN). Furthermore, vectors are intensified in the SE part of the domain and are weaker at the northern border. The amplitude time-series suggests that 2009 is the year with stronger oscillations associated with this mode. The Mode 4 (Figure 44.c-d) explains only 6% of the variance. Similar to Mode 3, there is a central area where the vectors are weaker and, in this case, they are oriented in a perpendicular direction to those in the Mode 3. Weaker vectors are found near 2º 30'W and 44ºN, with intensification of the current at the periphery of the study area. Each of the subsequent modes accounts for less than 4% of the variability and present more complex distributions (not shown).

In order to interpret the results obtained, Modes 1 and 2, with a higher contribution to the total variability, more uniform spatial patterns and vectors oriented in perpendicular directions, are analysed jointly. Taking into account that the phase lag between the amplitudes series of Modes 1 and 2 is $\sim T_L/4$, these two patterns combined reconstruct complete inertial oscillations; these are intensified slightly in the centre and northwest of the study area. In a similar way, Modes 3 and 4, with lower contributions to the total variability, higher spatial gradients in terms of vectors intensity and a phase lag between them of $\sim T_L/4$, will combine to reproduce a stronger oscillation in the outer part of the domain and low amplitude oscillations over the central part. Considering all the modes, whilst Modes 1 and 2 contribute strongly to the seasonal modulation of the oscillations over the study area and the intensification of the oscillations over the central part, Modes 3 and 4 will contribute to the enhancement or weakening of the spatial gradients of the amplitude of oscillations. As will be discussed below, this pattern is in agreement with the seasonal distribution of the KE at this frequency band shown in Section 5.3; likewise, observed by Rubio *et al*. (2011) for this data set, in 2009.

4.3.2. Contribution of the high-frequency band to the total currents

The quantitative contribution in terms of KE of the tidal and inertial currents to the total variability observed in the area is shown in Figure 45. The relative contribution of these 2 processes is variable, both in space and time; it tends to be more significant in summer, when the intensity of the total currents is lower. In general terms, it can be observed that the inertial currents are the main responsible for the variability in the spectral band, from 12 to 24 hours. Overall, inertial currents represent from 10 to 40% of the total variability with their contribution being significantly higher in summer, when these oscillations are intensified at the surface by a stronger stratification (Rubio *et al*., 2011).

Spatially, their distribution presents a maximum in energy over the deeper part of the slope in winter, nevertheless centred around 44ºN and 2º 30'W in summer (in accordance with the analysis presented in Rubio *et al*. (2011), using data for 2009). Conversely, the major contribution of tides is globally between 10 and 15 % of the total KE which occurs over the shelf, as expected, with intensification in the SE part of the domain. Over the shelf, in both summer and winter, the tides are the high frequency processes that contribute most to the observed total KE. Over time, inertial currents present strong seasonality in terms of spatial averaged contribution to the total KE. In general, their contribution is at a maximum from March to October, depending upon the year. The contribution of tides (semidiurnal band) to the spatially-integrated KE budget is much less significant than that of the inertial currents, except for winter periods. At this time, their contribution can be similar to that of the inertial currents, or greater (as happens for January-February 2009 and January-February 2011).

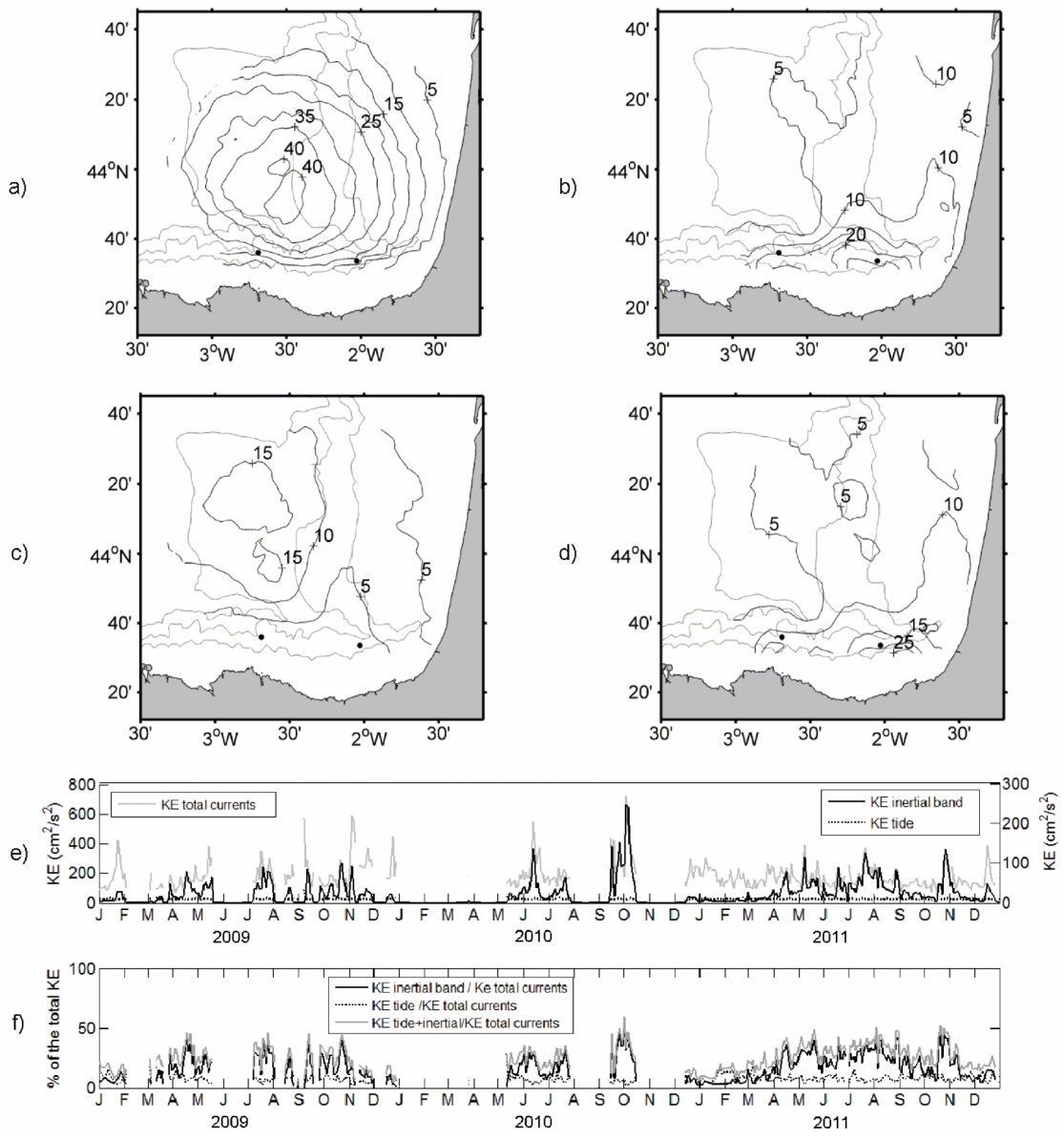

Figure 45: Contribution (percentages) to the total KE of the variability contained in the (a,c) inertial and (b,d) tidal bands, for (a,b) summer-type circulation months (temporal mean of spatial distributions for July, August and September) and (c,d) winter-type circulation months (temporal mean of spatial distributions for November, December and January). Isobaths (grey lines): 200, 1000 and 2000m. (e) Time evolution of the spatial average (for all the nodes) of the KE contained in the total currents (solid grey line, left y axis) and inertial (solid black line, right y axis) and tidal (dotted black line, right y axis) bands. (f) Time evolution of the contribution (percentages) to the total KE of the variability contained in the (solid black line) inertial and (dotted black line) tidal bands (the sum of both contributions is plotted using a solid grey line).

4.4. DISCUSSION AND CONCLUSIONS

The dominant signal over the area, indicated mostly by the first EOF mode (28 % of the variance) of the low-pass filtered currents, reveals an along-slope circulation with a marked seasonality. Clearly intensified over the upper part of the slope (Figure 43.a) and strongly related with the most persistent and strong westerly currents observed over the slope (Figure 42), Mode 1 can be related to the surface signature of the slope current IPC and its marked seasonality; this is in accordance with other descriptions of this current presented in the literature (Pingree and Le Cann, 1992a, 1992b; García-Soto *et al*., 2002; García-Soto, 2004; Le Cann and Serpette 2009, to cite a few). The analysis of hourly HF radar data and data from ADCP over the slope shows that, for the period analyzed, the current circulates eastward over the slope off the Spanish coast and northward over the slope off the French coast, in winter, with speeds reaching up to 70 cm • s^{-1}. An analysis of the forcing mechanism driving the slope current in the area is out of the scope of this chapter. However is worth noting that several authors relate the variability of the IPC to different forcings (buoyancy, the occurrence of south-westerly winds, JEBAR effect and topography) and to different North Atlantic atmospheric teleconnection patterns (Pingree and Le Cann, 1992a, 1992b; García-Soto *et al*., 2002; García-Soto, 2004; Le Cann and Serpette 2009; van Aken, 2002; García-Soto and Pingree, 2012; Esnaola *et al*. 2013). The strongest and more persistent easterly flows (in December 2009, January-February 2010, November-December 2010 and January 2011) coincide with periods of negative NAO index (not shown, source: http://www.cpc.ncep.noaa.gov/products/precip/CWlink/pna/norm.nao.monthly.b5001.current.ascii.table). Many authors relate this coincidence with SST positive anomalies, resulting from the advection of warmer surface waters by the IPC into the Bay of Biscay (as shown in Figure 39.a). Vertically, the good agreement between Figure 42.a and Figure 42.b, suggests that, most of the time, the surface observed patterns over the slope have a clear vertical signal affecting, at least, the first 100 m of the water column. This pattern is especially clear during the winter months, in periods when an intense IPC is observed over the slope, along the Matxitxako transect.

In summer, the water circulation over the slope in the area is reversed and has intensities 3 times weaker than those observed in winter, with predominant westward currents over

the Spanish slope. Mode 1 reveals, as well, the presence and persistence of eddy mesoscale circulation within the area. As shown by the monthly means of November 2009 and January 2011, persistent cyclonic structures are observed in winter, whilst persistent anticyclonic mesoscale eddies have been observed in summer (e.g. September 2009). Moreover, mesoscale and sub-mesoscale coherent structures developing in or drifting into the study area, such as those shown in Figure 39.d-e-f are observed on several occasions. The mesoscale activity in the SE Bay of Biscay, mainly between the Cap Ferret and Cap Breton canyons, has been studied by several authors (Pingree and Le Cann, 1992a, 1992b; García-Soto *et al*. 2002; Serpete *et al*., 2006; Caballero *et al*., 2008; Caballero *et al*, 2014), who relate eddy generation to the interactions of the slope current with the complex bathymetry. Further, recent research relates the presence of an anticyclonic surface circulation in the area, to the influence of NE winds (more frequent in summer); likewise, a cyclonic surface circulation to SW winds in winter (Fontán *et al*., 2013). Further research is needed: (i) to understand the physical mechanisms driving these circulation patterns; and (ii) to evaluate their contribution to the total variance of the regional circulation.

Modes 2, 3 and 4, with a weaker seasonal signal, add complexity to the circulation; they contribute to the intensification of the along-slope current and modify the mesoscale closed circulation patterns. Modes 2 and 3 show almost uniform currents, intensified slightly over at the deeper part of the study area, oriented northeastwards for Mode 2 and southeastwards for Mode 3. The more uniform distribution of the currents in Mode 2, in terms of speed and direction, suggest that this variability is related to the dominant (and seasonal) local wind regime in the area (in agreement with the findings of Fontán *et al*., 2013). In any case, Mode 3, with cross-shelf oriented currents over the Spanish and French shelf would be an important contributor to upwelling and downwelling conditions in the coastal areas.

At frequencies ranging from several hours to one day, tidal and inertial currents add complexity to these patterns. Concerning inertial currents, the EOF analysis applied to the inertial band filtered data shows 2 main modes (Modes 1 and 2; these account for 60% of the variance), related to the seasonal modulation of the oscillations in the study area and as well to their intensification in the central part. The latter observation is in agreement with the seasonal behaviour of the KE in the near-inertial band shown in section 4.3.2 and discussed already in Rubio *et al*. (2011). Modes 3 and 4, with

oscillations less intense over the central part, combine with modes 1 and 2 to modulate the enhancement or weakening of the spatial gradients observed in the amplitude of the oscillations.

The relative contribution of these processes to the total KE is variable both in space and time (Figure 45). Globally inertial currents represent from 10 to 40% of the total variability, being their contribution significantly higher in summer when these oscillations are intensified at the surface by a stronger stratification (Rubio *et al*. 2011). Spatially, their distribution presents an energy maximum over the deeper part of the slope in winter and centred around 44ºN and 2º 30'W in summer (in accordance with the analysis presented in Rubio *et al*. (2011), using data for 2009). Tides contribute much less to the total KE, mainly over the shelf, although their contribution can be higher than that of inertial oscillations during winter.

The analysis carried out in this study is the first attempt to improve the understanding of multiscale surface water circulation at the SE Bay of Biscay. Although the 3 years of available data have provided invaluable information to gain an insight into the surface circulation patterns in the study area, the continuous addition of HF radar data to this data set (during the coming years) will permit: the analysis of processes, such as the observed interannual variability of surface currents; and to obtain enhanced statistical description of the currents (i.e. long-term and extreme value distributions). Several studies relate the variability of currents over the Bay of Biscay slope circulation to remote oscillations (NAO, EA see, for instance, Le Cann and Serpette, 2009 and García-Soto and Pingree, 2012). An extended data series covering more years will permit analysis of this process, with HF radar data.

CHAPTER V

SURFACE WATER CIRCULATION AND WIND INTERACTION USING CLASSIFICATION ALGORITHMS

Surface circulation patterns have been analyzed in the previous chapter. In this chapter the relationships between currents and winds will be analyzed, using a clustering classification technique.

Within the above context, two objectives are proposed: (i) to use the k-means classification algorithm (hereinafter KMA) (Hastie *et al*., 2001). KMA is used to make a comprehensive description of the wind and current patterns in the Bay of Biscay and in the study area, taking into account a wide range of scales, from several days to interanual variability; (ii) to analyse the probabilistic relationships between wind and

current patterns by means of conditional probabilities. Finally, an extended time series of the occurrence of the IPC based on SST imagery (Esnaola *et al*., 2013), used together with HF radar surface current data for shared periods, offers the chance to explore the potential influence of the IPC on surface currents.

5.1. DATA

Surface current data used in this study cover the period 2009-2013. More detail on the HF radar data processing is provided in Chapter II. A 10^{th} order digital Butterworth low-pass filter (Emery and Thomson, 2001) has been applied to each HF radar velocity component of the time series at each node (filtering out T<48 hour signals), to isolate low frequency before KMA analysis.

A major disadvantage of the KMA technique is that it does not accept any gaps in the time series under analysis. To solve this problem, pre-processing of the data was needed, before starting with KMA. First, the 660 HF radar nodes that contained at least a 50% of non-missing data during the analysed period were selected. Then, the time steps containing gaps were also removed to obtain a continuous dataset without gaps, (getting finally a dataset with 7,288 time-steps). After applying these modifications, the temporal, interannual and seasonal coverage of the data is homogeneous during the study period.

For the same period, 2009-2013, hourly wind data were provided by MeteoGalicia (meteorological agency of Galicia Spanish region) and were obtained using the Weather Research and Forecasting atmospheric numerical model (WRF). A detailed description of this model can be found in Skamarock *et al*. (2005). WRF is run routinely by MeteoGalicia in operational mode since 2008. In its operational system, two one-way nested domains are used: the parent domain covers part of the North Atlantic Ocean and southwestern Europe, with a 36 km horizontal resolution, whilst the nested domain covers the Iberian Peninsula and the Bay of Biscay, with a 12 km horizontal resolution. The initial and boundary conditions for the WRF parent domain are provided by the National Center for Environmental Prediction (NCEP). These data (three-hourly and 0.5º horizontal resolution analysis/forecasts) are obtained using the Global Forecast

System (GFS). For the WRF nested domain, these conditions are obtained from the parent domain simulation. In 2009, WRF model results were compared with available observations of six ocean-meteorological stations located in the area of interest. The results showed that the WRF model was able to reproduce the time evolution of the offshore wind fields with a reasonable accuracy (Ferrer *et al*., 2010). For the study developed in this chapter, , 805 WRF grid points were used, covering from 43º to 48ºN and from 1º to 9ºW. In order to have two comparable data series, the same time steps removed from the HF radar dataset were also removed from the wind dataset.

For the estimation of the IPC occurrence series, 4 km spatial resolution Pathfinder v5.2 winter-time (November, December, January, February) SST images, available in the 1981-2012 period, were downloaded from http://www.nodc.noaa.gov. SST images were pre-processed by: (i) Extracting data for the Bay of Biscay area (15W-0E, 40N-44.75N); (ii) selecting only best quality data (flag7 data only) and; iii) selecting images with at least a 5% of available data. This pre-processing left a total of 1,356 high resolution SST images with a total of 83.5% of missing data.

5.2. K-MEANS CLUSTERING ALGORITHM (KMA)

Clustering methods provide an alternative to the most frequently used linear time-series analysis methods, with the main advantage of handling nonlinear relationships. Patterns of ocean current variability were extracted from a joint HF radar and ADCP dataset using Self-Organizing Map (SOM) clustering method (Liu *et al*., 2006). Although the topological connections of SOM are an advantage in identifying transitions between patterns, in this study KMA has been selected. The major objective of this study is the analysis of the probabilistic relationships between wind and current patterns so it is more important to cover all the data space than to obtain the transitions between them. KMA exploration of the data space is more suitable in this case since it takes in account the data close to the edges of the data space (Camus *et al*., 2011).

The KMA clustering algorithm divides the high-dimensional data space into a number of clusters or groups. Each one is defined by a prototype and formed by the data for which the prototype is the most similar (Hastie *et al*., 2001). A given database is composed by n-dimensional vectors $X=\{x_1, x_2, \ldots, x_N\}$, where N is the total amount of

data. In this case N=7,288 hours of the analysed 5 years. The dimension of each vector $x_k = \{x_{1k}, \ldots, x_{nk}\}$ is n=660 nodes for HF radar data and n=805 nodes for wind data. KMA has been applied to both two-dimensional hourly current and wind datasets, to obtain M=12 groups in each case, defined by a prototype or centroid $v_k = \{v_{1k}, \ldots, v_{nk}\}$ of the same n dimension of the original data.

The number of groups selected to obtain the classification of spatial patterns using KMA is set subjectively. As discussed in Guanche *et al*. (2013), the criteria for the selection of the appropriate number of groups are not solved yet. So, the major recommendation is to select a number of groups that simplifies the interpretation of the results, without losing too much variability in the resulting fields. Following this recommendation, in this study, the selected number of groups has been M=12 for the analysis of both, winds and currents, after careful observation of the differences obtained from using several approximations (i.e 9, 12, and 16 groups). The results obtained cover the previously known wind and current patterns in the study area (González *et al*., 2002, 2004; Solabarrieta *et al*., 2014) and offer a wide description of the characteristics and variability of winds and currents in the area.

The strategy chosen for the present chapter is to apply KMA analysis separately to both datasets (currents and winds) to be able to analyze variability and patterns of both dataset separately (and specifically those corresponding to currents not related to the wind). Then, joint occurrence probabilities have been calculated to study the probabilistic relationships amongst current and wind fields.

5.3. PROBABILISTIC RELATIONSHIP

The problem of analyzing the relationship between a multivariate predictor X (wind fields) and a multivariate predictand Y (current fields) is usually addressed by means of a linear model such as Principal Component Analysis (PCA) and/or Canonical Correlation Analysis (CCA) (von Storch and Zwiers, 2004).

A different approach consist in splitting up, both the predictor X and the predictand Y, in a number of patterns using different non-linear data mining classification algorithms such as SOM or KMA. Once obtained these M_x and M_y patterns for the predictor and

for the predictand, respectively, it is possible to explore the connections between X and Y obtaining the conditioned probabilities. In this case the patterns of X are named Wind Groups (hereinafter WG) and the patterns of Y are named Current Groups (hereinafter CG), therefore obtaining a set of patterns $\{WG_i, i=1, N_x\}$ and $\{CG_j, j=1,N_y)\}$. As an example, the probabilities of having the patterns CG_j for a given WG (say WG_3) are $\{P_{31}, P_{32}, \ldots P_{3Ny}\}$. In this way, the connections or probabilistic relationships between the predictor and the predictand are explored. A similar approach applied for atmospheric circulation (X) and wave directional spectra (Y) can be found in Espejo *et al* (2014).

5.4. IPC OCCURRENCE TIME-SERIES

A daily-frequency winter-time (November-December-January-February) time-series of the occurrence of the IPC over the 1981-2010 period can be found in Esnaola *et al*. (2013). This time-series is deduced from reconstructed satellite SST images of the Bay of Biscay area. Unfortunately, the time series by Esnaola *et al*. (2013) only shares a single winter with the HF radar dataset considered here. To overcome this limitation, the IPC time-series has been extended in this study to cover the 1981-2012 period, which by the time the deduction was made, was the full period covered by the SST dataset in which the analysis is based. Provided that the time-period covered by the IPC time-series is extended, the rest of the analysis is described in Esnaola *et al*. (2013).

The Data Interpolating EOFs, or DINEOF, methodology was then applied to pre-processed SST images to reconstruct the missing data. Detailed information on this technique can be found in Beckers and Rixen (2003) and Alvera-Azcárate *et al*. (2005, 2009). Some examples of reconstructions in the Bay of Biscay can be found in Ganzedo *et al*. (2011) and Esnaola *et al*. (2012). Here, DINEOF was applied with the time covariance smoothing (3 iterations) activated and using a cross-validation mask of a 5% of the available data. The data series was built masking the less cloudy images with real clouds taken from other images (see Alvera-Azcárate *et al*., 2009, for details on these configuration options). The quality indicators of the reconstruction were in the range of those shown in Esnaola *et al*. (2012, 2013).

Once reconstructed, the SST images were masked out with a bathymetry mask in order to retain only pixels with related depths below 2000 m. Then anomalies of those SST images were deduced by subtracting a smoothed (15 day running-mean) daily climatology to individual SST images. Finally, a Principal Component Analysis, PCA, (von Storch and Zwiers, 2004; Wilks, 2006) is applied to the anomalies. The first Principal Component obtained from that analysis can then be considered as a time series of the surface signal related to the IPC, as shown in Esnaola *et al*. (2013). In the case of this work, this principal component was deduced from the 1981-2012 period, although values for the 2009-2012 have been used. This was done to keep consistency with previous results in terms of the deduced PCs and EOFs. Such consistency was confirmed by the fact that the values in our 1981-2012 time-series and those found for the 1981-2010 period in Esnaola *et al*. (2013) were almost identical.

5.5. RESULTS

5.5.1. Wind and current patterns

The following results are shown in this section: (i) results of the KMA of the hourly wind and surface currents; (ii) monthly occurrence probabilities of the WG and the CG; (iii) occurrence probabilities of the CG projected into the wind lattice; and (iv) the surface currents and SST composites related to the IPC time series for the 2009-2012 time period. The period from November to March will be referred in this chapter as winter months and July to September as summer months (according to the assumption made in Solabarrieta *et al*. 2014).

Figure 46 displays the 4 x 3 lattice of the KMA applied to the previously described WRF winds and the main characteristics of the resulting WG are summarized in Table 9. Around 44% of them are prominently northern winds (WG-1-2-4-10-11) and around other 45% of the winds are prominently southern (WG-3-5-6-7-8-12). The remaining 10% of occurrence probability (WG9) is related to winds very variable in space and in intensity. WG9 winds with a large variability over the Bay of Biscay domain, probably represent wind-calm periods.

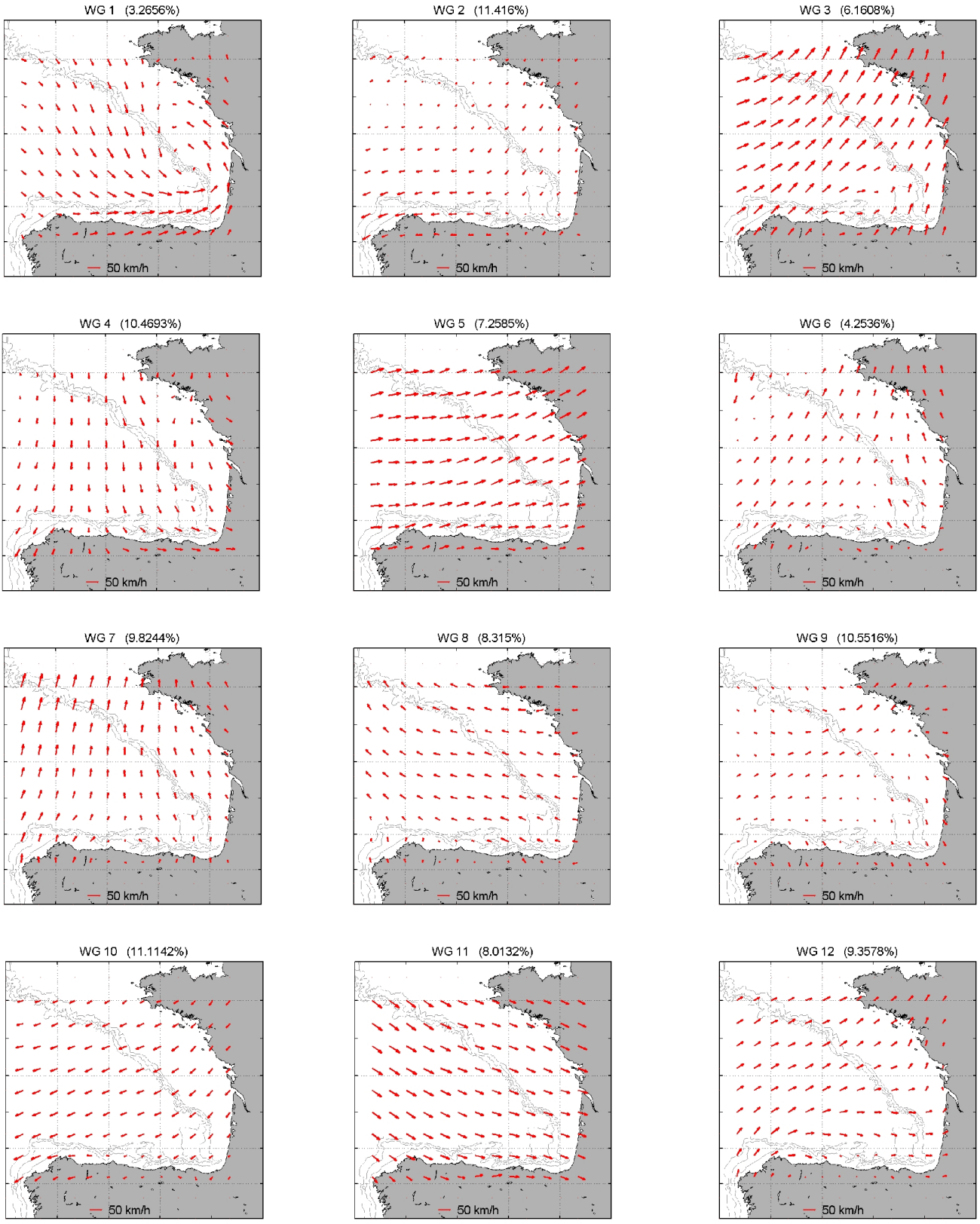

Figure 46: 4 x 3 lattice of the k-means analysis applied to the winds obtained using WRF model.

Orientation		Wind Group	Seasonality	% occurrence			Description		Max. velocity [cm/s]	Mean velocity [cm/s]
							Bay of Biscay	Radar Area (in comparison to Bay of Biscay)		
N	E	WG2	none	11.41	22.52	44.25	Anticyclonic closed pattern centred at 47,5ºN, 7ºW	Northeastern very weak winds	39,85	15,51
		WG10	none	11.11			North-eastern winds	Northeastern weaker winds	46,15	24,94
	W	WG1	none	3.26	21.73		Cyclonic closed pattern, centred at 45º30' N and 3º W	Southwestern winds with maximum velocities	64,08	28,90
		WG4	none	10.46			Northern homogeneous wind (cyclonic turn over the coast)	Northwestern and western winds	43,92	24,3
		WG11	w*	8.01			A strong northwesterly wind group	Waker northwestern wind	48,63	37,44
S	E	WG8	w*	8.31	8.31	45.14	Eastern winds with little tendency to turn to the right at the northwest part	Eastern weaker winds	37,26	22,06
		WG6	w*	4.25	14.07		Southern winds, with a great velocity variation	SE winds	39,92	20,23
		WG7	w*	9.82			Southern intense winds and uniform in direction	SE winds	55,47	27,79
	W	WG3	w*	6.16	22.76		Southwestern wind pattern. It turns parallel to the coast at 5ºW.	Southern winds	57,31	42,69
		WG5	w*	7.25			Western homogeneous and strong wind	Western homogeneous and strong wind	53,85	41,90
		W12	w	9.35			Southwestern wind pattern (similar to WG3)	Western winds	41,54	24,84
-	-	WG9	s	10.55	10.55	10.55	Weak winds with a great spatial variation	Northwestern winds	26,13	13,89

*Table 9: The columns content from left to right: (i) Orientation of the wind. (ii) Wind group number. (iii) Seasonality (w: higher occurrence in winter; s: higher occurrence in summer. * the probability of occurrence in that period is over 50%). (iv) The occurrence probability of each wind group or each group of wind groups, during the whole study period. (v) The description of the principal characteristics of the winds. (vi-vii) maximum and mean velocities of the wind.*

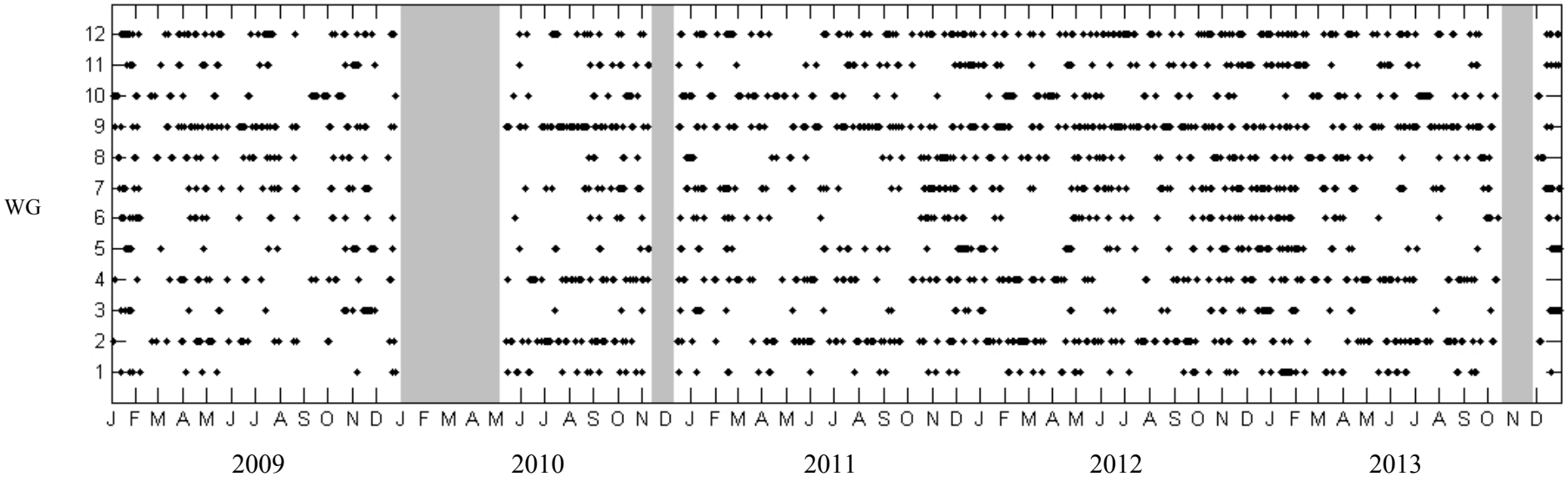

Figure 47: Time-step of appearance of each Wind Group (WG), during 2009-2013. The months are marked by the first letter.

Figure 47, shows the temporal occurrence of each group during the study period. The temporal distribution of the dots, shows the complexity of the wind-regime of the Bay of Biscay. Some wind groups appear evenly throughout the 5 analysed years and others however appear more in certain periods of the year. The occurrence probability of the wind groups during summer and winter periods has been calculated in order to analyse seasonality. Seasonal variability has been identified in WG-3-5-6-7-8-9-11-12 with occurrences in winter or summer periods over 50%, as observed in Table 9 (excluding WG-9-12, which predominate clearly in one season, but with occurrences under 50%). All of them are winter winds (except WG9). Amongst the winter patterns, only WG11 is a northwesterly wind group. The remaining winter wind groups are southerlies. WG9 (which shows very variable and very weak westerly winds) occurs during or around summer months. All these groups confirm the known seasonal main patterns of the wind fields in the Bay of Biscay (north-northwesterly winds in summer and southerly winds in winter). However, it is worth noting that 36% of the wind groups are not seasonal (WG-1-2-4-10) showing all of them northerly component. This means that significant occurrence of northerly winds also exists in winter. Figure 48 also shows that northern and north-western WG-1-2-4 have high occurrence probability during summer months although they do not present a clear seasonality. WG-7-8-12 are seasonal and southerly wind groups and occur mostly during winter months (Table 10). However it is worth noting that these groups also occur (with lower probability) during all the year (Figure 48), which adds variability to seasonal known winds.

The occurrence probability of the wind groups during each year of the study period (2009-2013) has been calculated in order to analyse the interannuality of each wind group (the occurrence is calculated in Table 10, as the percent of the observation related to the elements of each group per year, weighted by the number of observations available for that year). Quantitatively, according to the 95th percentile of the data (30%), any of the wind groups present clear interannual variability. However, from the qualitative inspection of Figure 48, it is worth noting the high occurrences of WG-3-5-7 during 2011-13 winters.

	2009	2010	2011	2012	2013	∑ 2009-13	Winter (W)	Summer (S)	∑ W-S
WG1	13,36	30,40	13,42	15,48	27,32	100	48,90	15,42	64,32
WG2	10,72	17,11	17,97	32,20	21,98	100	30,55	36,07	66,62
WG3	26,02	3,87	16,07	25,88	28,14	100	82,85	2,23	85,08
WG4	8,90	28,34	21,85	16,80	24,07	100	37,15	15,85	53
WG5	27,35	10,44	22,98	25,52	13,67	100	76,00	12,57	88,57
WG6	22,43	10,38	30,34	22,02	14,81	100	63,30	6,73	70,03
WG7	16,16	15,56	28,14	19,32	20,80	100	55,68	12,06	67,74
WG8	16,42	18,68	18,70	20,15	26,02	100	54,97	14,40	69,37
WG9	14,25	27,61	21,59	18,59	17,92	100	29,01	41,57	70,58
WG10	27,60	27,74	10,15	18,22	16,26	100	39,15	29,05	68,2
WG11	28,56	11,56	20,25	16,88	22,72	100	56,99	19,76	76,75
WG12	27,36	11,90	27,50	17,73	15,48	100	48,85	19,60	68,45

Table 10: These values represent the variability of each wind group, during the study period. The values are the % of occurrence of each group during the year, winter or summer periods, considering winter months, November to March, and summer months, July to September.

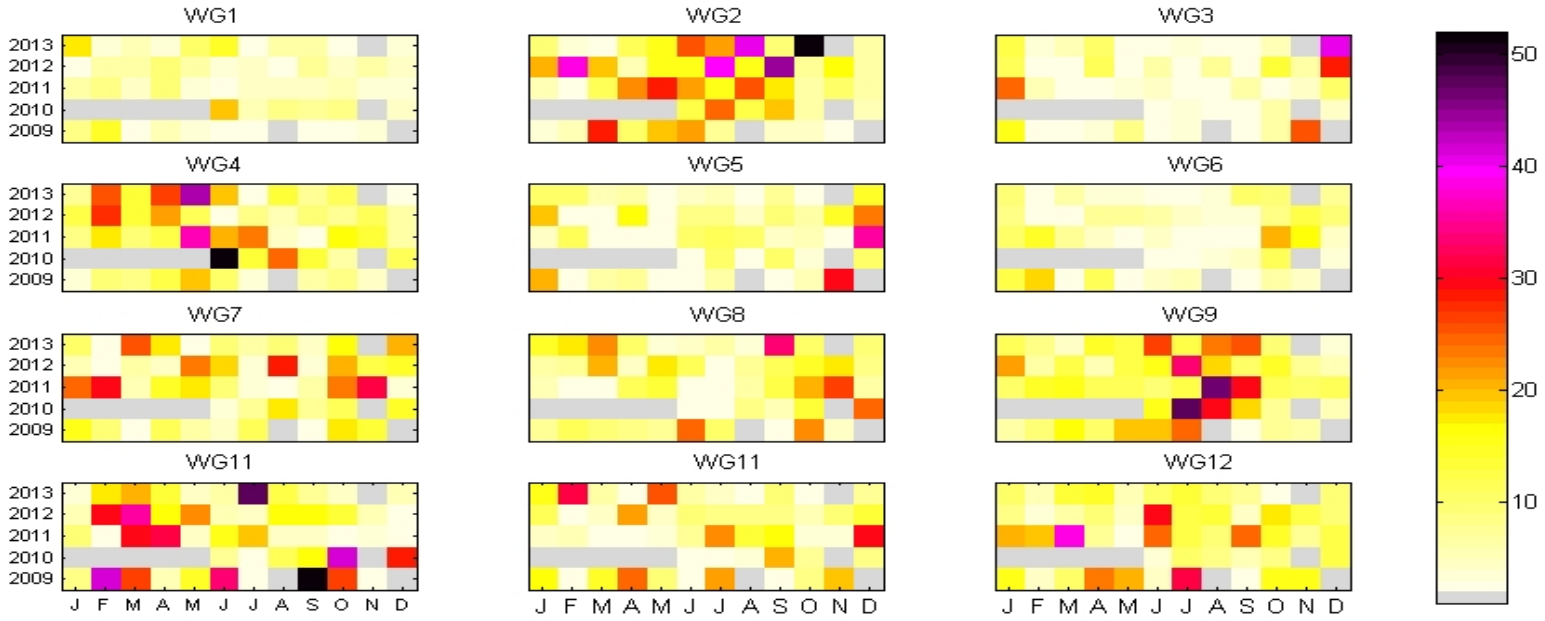

Figure 48: % of occurrence of each wind group for the months of the 5 analyzed years. The months with available data <50 time steps, have not been used to compute % of occurrence and they are shaded grey.

The resulting 4 x 3 lattice of results for the KMA analysis of HF radar currents is displayed in Figure 49. Figure 50 shows the temporal occurrence of each group during the study period. These 12 groups represent most of the previously known characteristics of the surface circulation in the study area. Table 11 summarizes the main CG characteristics. Around 40% of the surface currents in the area are mainly represented by current groups with mean northward velocities (CG-3-5-6-12) and around 25% are classified into groups where southward surface currents prevail (CG-4-7-9). Amongst the groups with mean northwards velocities the ones with predominant north-eastwards currents (CG3-6), and with currents oriented to the east (north) in the Spanish (French) shelf/slope, are the most intense (mean velocities of 15 and 10 cm • s^{-1}, respectively). The two groups with mean north-westwards currents (CG-5-12) show similar orientation and differ mainly in the intensity. CG12 is the one with higher mean velocities. CG5 currents are more probable, however, weaker than the previous ones.

Regarding the CG with prevailing southwards currents, the groups CG4-9 (south-eastwards currents) are quite similar; with currents mainly oriented towards the east and southeast in the Spanish and French shelf/slope. For CG9, southward currents are observed in the western shelf/slope area of the Basque Country. Their main difference is that GC4 presents mean velocities twice as high as CG9. CG7 is the only CG with mean south-westward currents (of ~ 7 cm • s^{-1}), which switch to eastwards over the Spanish shelf/slope.

The remaining (33%) of surface currents registered by the HF radar are classed into 5 groups with much more complex surface current patterns and showing cyclonic (CG-1-8-10-11) and anticyclonic (CG2) features. Three of the cyclonic groups (CG-1-8-11) are amongst the most intense CG with mean velocities ranging from 13.5 to 16 cm • s^{-1}). CG 10 shows much weaker velocities (< 6 cm • s^{-1}) and a weak cyclonic circulation. CG2 surface current velocities are also weak.

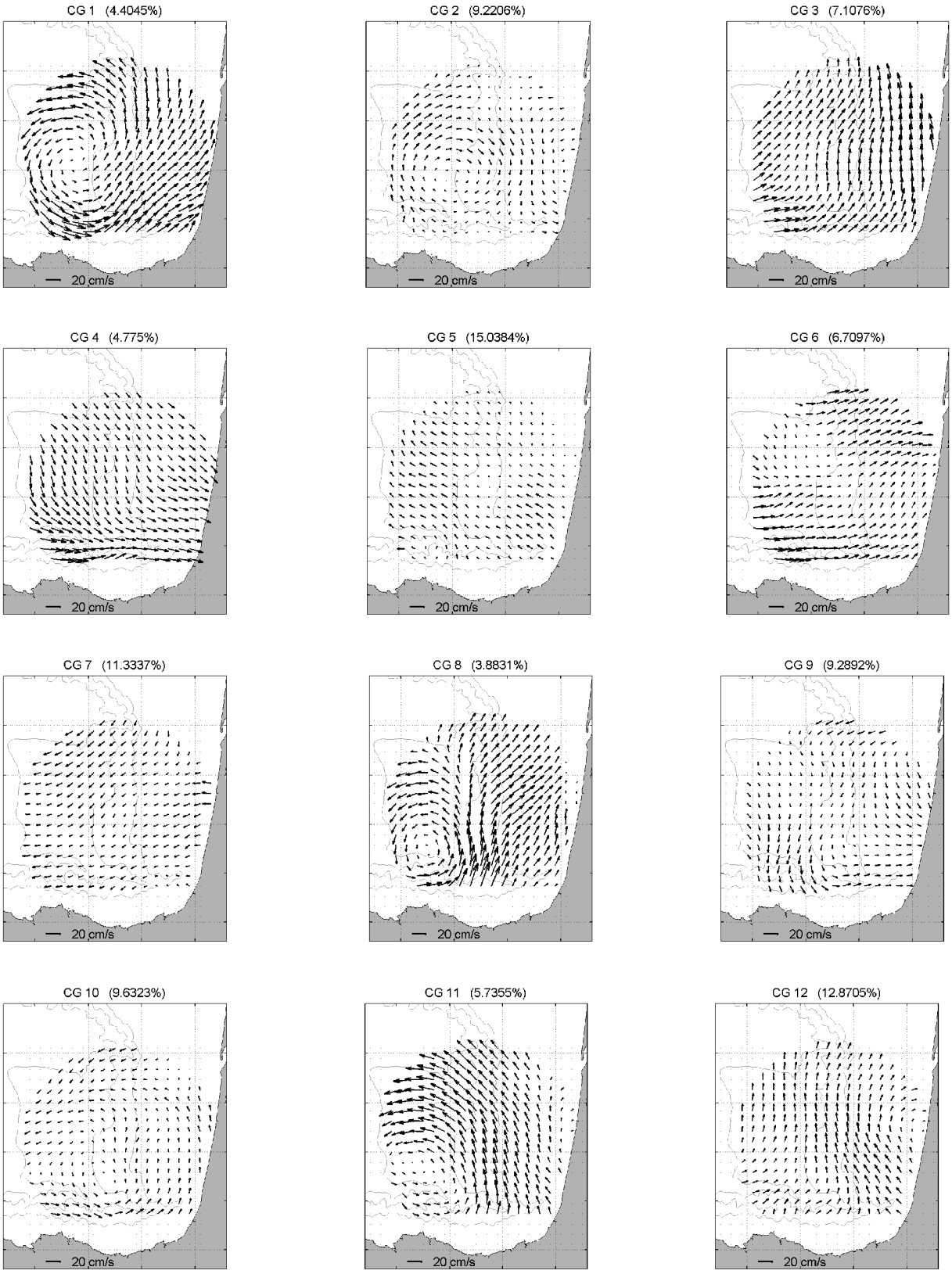

Figure 49: 4 x 3 lattice of the k-means analysis applied to the HF radar surface current data

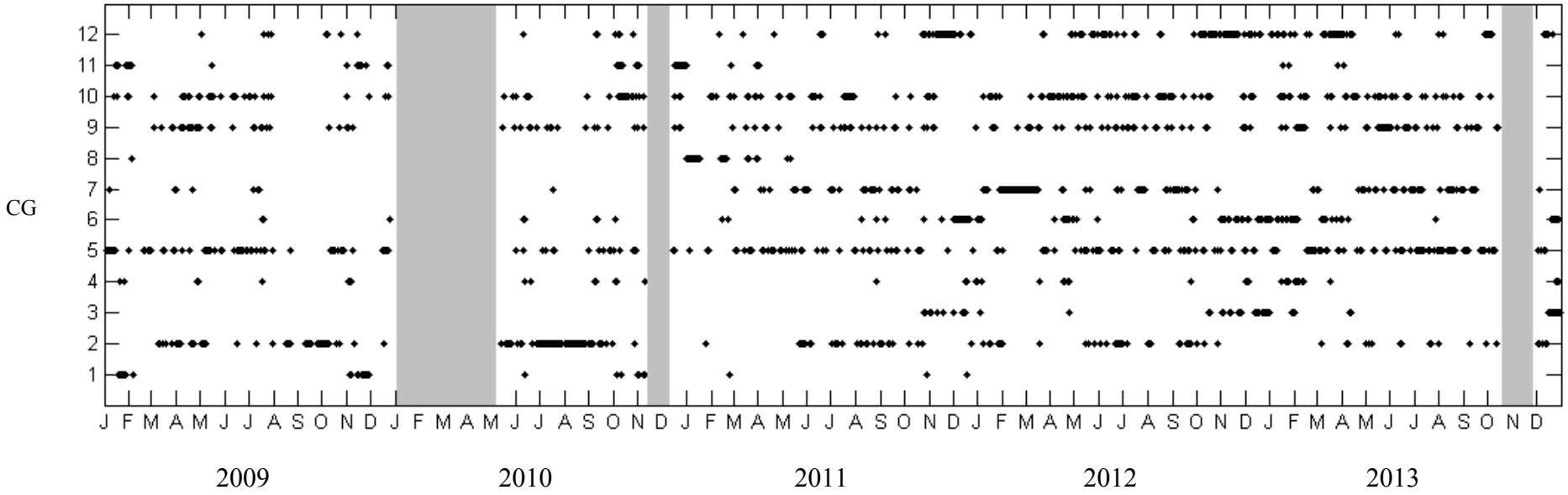

Figure 50: Time-step of appearance of each Current Group (CG), during 2009-2013. The months are marked by the first letter.

Orientation		Current Group	Seasonality	Interannuality (I)	% occurrence			Description	Max. velocity [cm/s]	Mean velocity [cm/s]
N	E	CG3	w*	I	7.10	13.8	41.7	A cost parallel northward pattern with a not closed cyclonic turn over the Cap Breton Canyon	24.26	14.88
		CG6	w*	I	6.70			Current comes from the west and turns in the SE corner ongoing to the northeast	35.44	10.57
	W	CG5	none		15.03	27.9		A weak currents group with a high variability. Currents are northwestward	11.59	5.42
		CG12	w*		12.87			A uniform and northward current pattern	13.90	8.71
S	E	CG4	w*		4.77	14.05	25.38	North-western currents that generate downwelling in the French coast.	37.37	12.67
		CG9	none		9.28			Southward current's group, with weak currents and high variability (speed and space)	14.13	6.61
	W	CG7	none		11.33	11.33		A homogeneous weak southwestward current group	13.10	7.01
Cyclonic closed turn		CG1	w*	I	4.40	23.64	32.85	Strong cyclonic closed current pattern, centred at 44ºN and 2º45'W	33.93	16.02
		CG8	w*	I	3.88			Closed surface current centred at 43º50'N and 2º45'W	36.14	14.19
		CG10			9.63			Cyclonic closed weak currents pattern, with homogeneous velocities	13.60	5.81
		CG11	w*	I	5.73			Pattern centered at 43º50'N and 2º45'W, with high velocities (27 cm/s)	27.26	13.58
Anticyclonic closed turn		CG2	s*		9.22	9.22		Weak antycyclonic closed current pattern, centred at 44ºN, 2º30'W	14.03	5.47

*Table 11: The columns content from left to right: (i) Orientation of the currents. (ii) Current group number (iii) Seasonality (w: higher occurrence in winter; s: higher occurrence in summer. * the probability of occurrence in that period is over 50%). (iv) Interannuality. (v)The occurrence probability of each current group or each group of current groups, during the whole study period. (vi) The description of the principal characteristics of the winds. (vii-viii) maximum and mean velocities of the currents.*

The occurrence probability of summer and winter periods has been also calculated for current groups (Table 12). Seasonal variability has been identified in CG-1-2-3-4-6-8-11-12 with occurrences in winter or summer periods over 50%, whilst the remaining groups do not present clear seasonality. Most of the seasonal patterns show cyclonic or anticyclonic circulations (CG-1-2-8-11), being CG10 the only group with cyclonic not seasonal currents. CG-3-6-12 are also current patterns affected by a seasonal variability. They show not closed cyclonic circulation with a prevailing east-northward orientation. CG 4 with south-westwards prevailing currents shows also a seasonal behaviour, with higher occurrences during winter. In the seasonal groups two clear tendencies are observed, anticyclonic during the summer (CG2) and cyclonic during winter months (CG-1-3-6-8-11-12). CG4-12 have been identified as winter seasonal groups. However, it is worth noting, that they also occur during summer months, as observed in Figure 51.

	2009	**2010**	**2011**	**2012**	**2013**	**∑ 2009-13**	**Winter (W)**	**Summer (S)**	**∑ W-S**
CG1	71,97	25,18	2,83	0	0	100	87,58	0,00	87,58
CG2	28,23	50,38	10,84	6,68	3,85	100	11,01	61,16	72,17
CG3	0	0	20,63	40,63	38,73	100	85,91	0,00	85,91
CG4	23,32	23,87	11,01	19,70	22,13	100	60,81	18,44	79,25
CG5	31,87	7,52	13,67	15,95	30,97	100	28,25	28,44	56,69
CG6	1,32	5,76	30,05	31,52	31,33	100	79,63	6,17	85,8
CG7	4,33	0,51	22,97	48,21	23,96	100	41,16	32,45	73,61
CG8	1,94	0	98,05	0	0	100	92,58	0,00	92,58
CG9	18,36	24,48	15,77	14,67	26,68	100	26,55	30,32	56,87
CG10	15,54	25,61	21,51	20,17	17,14	100	27,71	24,34	52,05
CG11	35,58	56,48	3,36	0	4,56	100	85,35	0,00	85,35
CG12	3,04	6,22	28,21	34,72	27,79	100	55,65	7,78	63,43

Table 12: These values represent the variability of each current group, during the study period. The values are the % of occurrence of each group during each year, winter or summer periods, considering winter months, November to March, and summer months, July to September.

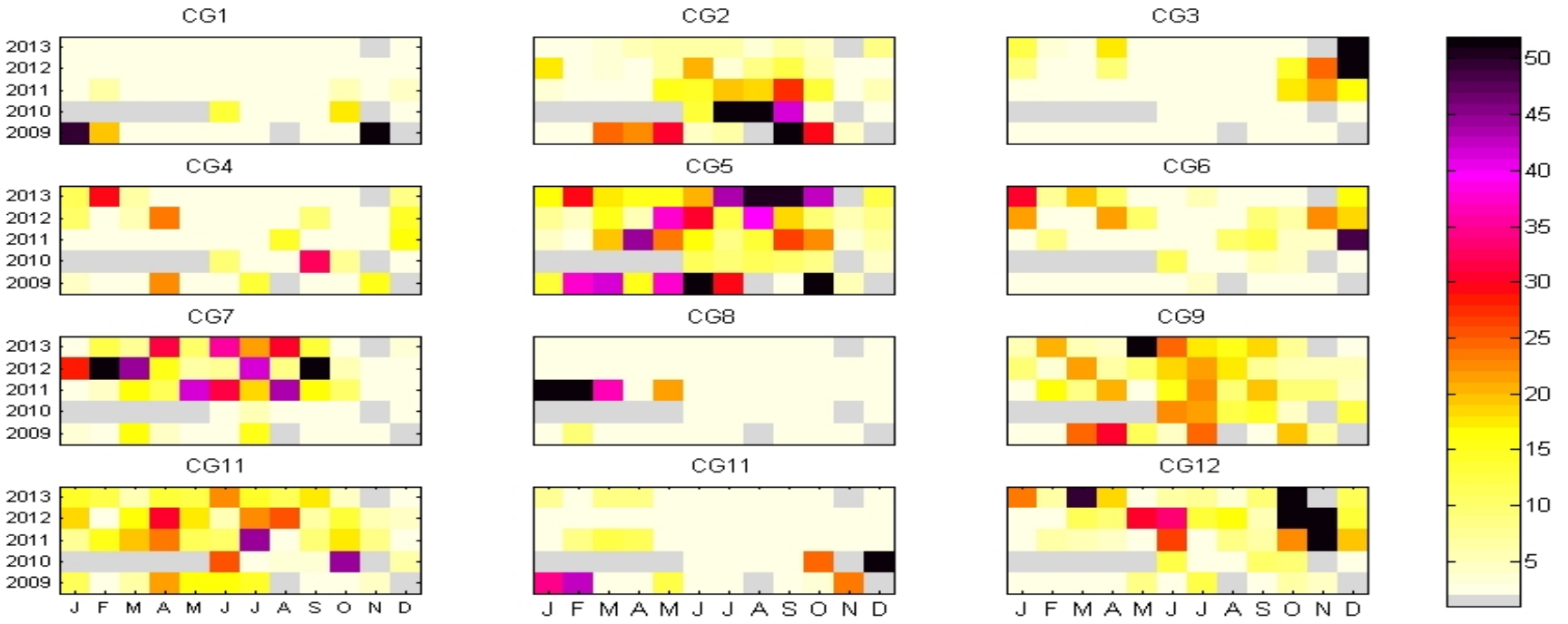

Figure 51: % of occurrence of each HF radar group for the months of the 5 analyzed years. The months with available data <50 time steps, have not been used to compute % of occurrence and they are shaded grey.

The occurrence probability of the current groups during each year of the study period (2009-2013) has been calculated in order to see the interannuality of each current group (Table 12). The 95th percentile of the data (40%) has shown that there are significant differences along the 5 years analysed in CG1-2-3-7-8-11, considering them as interannual current groups. Although CG-3-6-12 have not values of % of occurrence over the 90^{th} percentile, the major presence during 2011-2013 winter months suggests also that they present interannual variability (Figure 51). CG7 has also higher occurrence probabilities during 2011-2013. CG1-2-11 present higher occurrence probability during 2009-10, whilst CG8 has occurrence probabilities over 98% during 2011 (1.94% occurs in winter 2009) (Figure 51). The rest of the groups (CG4-5-9-10) do not present any significant interannual variability.

5.5.2. Probabilistic relationships between wind and current patterns

Figure 52 establishes the probabilistic relationships between the 12 WG and the 12 CG probabilities. For each WG_i, the occurrence probability of each CG_j is determined, P_{ij}, obtaining a multi-lattice as shown in Figure 52. Each subgrid represents the occurrence probability of each CG into each WG (e.g. WG3 is expected to produce (P=55%) the CG3). These connections are described here, following the classification of wind patterns used in Table 9 and only focusing on groups presenting joint occurrence probability over 25% (i.e. values over the 90th percentile). Joint occurrence over 25% is observed for 40% of the all possible combinations between the 12 WG and the 12 CG (Table 13).

WG2-10 are north-eastern wind groups with similar mean direction and occurrence probabilities excepting that WG2 has weaker velocity values. However, both of them seem to be related by occurrences over 25% to CG5. CG5 shows north-westward currents and has high occurrence probability during the whole study time period (15%). High joint occurrence probability is also observed between WG2 and CG7, which shows south-westward currents in agreement with the main wind's direction. Although the occurrence probability is less than 25%, WG10 and CG7 are also related with near 20% of occurrence probability.

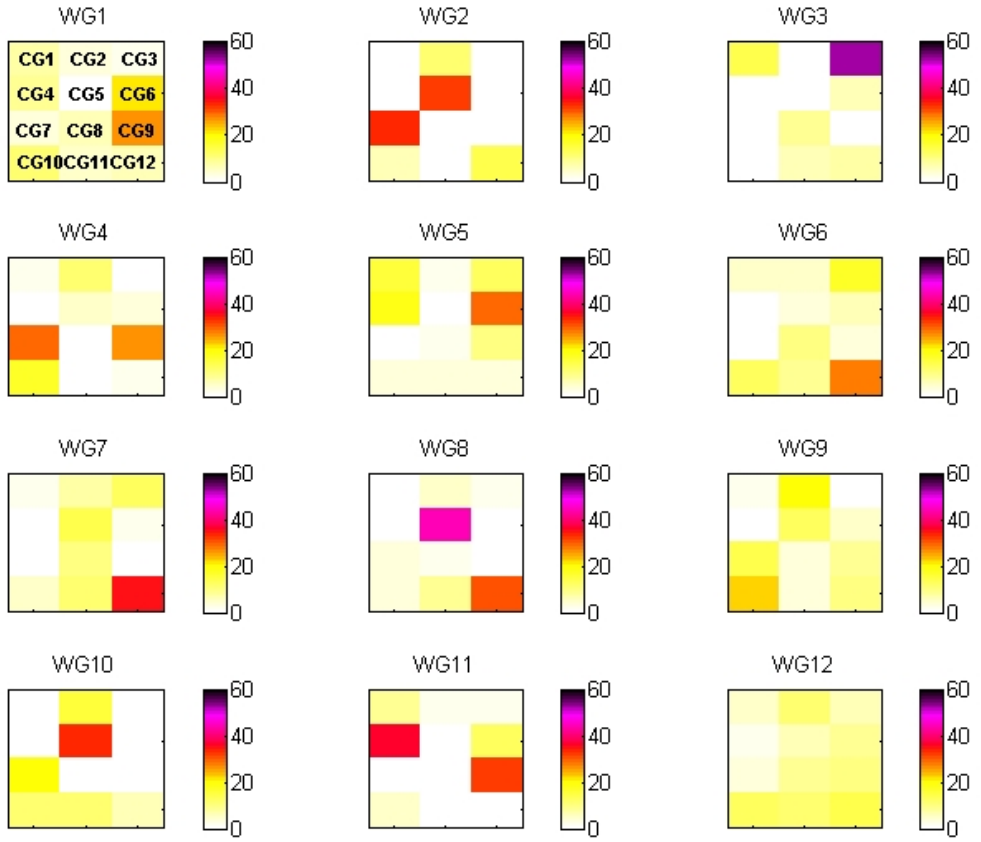

Figure 52: Occurrence probabilities of the 12 HF radar current groups (CG) projected into the wind lattice.

	(a)	(b)
WIND GROUP	Total expected % in each wind	Total expected %
WG1	26,05	0,85
WG2	65,50	7,47
WG3	52,78	3,25
WG4	55,70	5,83
WG5	28,73	2,08
WG6	27,74	1,18
WG7	34,92	3,43
WG8	74,09	6,16
WG9	0,00	0,00
WG10	33,21	3,69
WG11	68,32	5,47
WG12	0,00	0,00
TOTAL		39,41

Table 13: (a) Total expected % of the current groups into the wind groups for the WG-CG combinations presenting more than 25% of joint occurrence probability. (b) % of total expected current groups (with more than 25% of occurrence % in each wind group), respect to all the analyzed time steps [column (a) % of occurrence of each WG].*

Amongst the predominantly north-western wind groups, WG1-4-11, high occurrence probabilities are obtained for the CG9, with south-eastward currents over the French shelf indicating net transport towards the coast and southwards (eastwards) currents in the western (eastern) Basque Country coasts (surface currents which will favour downwelling conditions along French and Spanish coasts). CG9 is the only current group which is common to the three wind situations. Then the differences between the WGs, explain that other CG present high probabilities in relation to each of them in the joint occurrence lattice (Figure 52). WG1 are predominantly north-western winds, with a cyclonic turn to the north of the study area and westerly intense winds over the Spanish shelf/slope and southerly intense winds over the French shelf/slope. WG11 has intense more homogeneous north-western winds. In both cases, WG1-11, CG6 is also expected, however, with much lower occurrence probability (around 25%). CG6 currents vectors are oriented parallel to the Spanish and French coasts, with surface waters mainly directed to the east at the Spanish shelf/slope and to the north at the French shelf/slope and changing direction in agreement with the main orientation of the coast. Over the northern part of the French self within the HF radar footprint main currents are north-eastwards in agreement with the main wind direction of WG1. For WG11, the CG4 is the group with most occurrence probability. CG4 is similar to CG9, nevertheless with more intense and homogeneous currents over the whole domain, mainly oriented south-eastwards and intensified eastward along the Spanish shelf/slope. Finally, for WG4, the most probable current pattern is represented by CG7. Although WG4 shows north-westward winds over the Spanish shelf/slope area, for the Bay of Biscay northern winds predominate which result in south-westward surface currents on the HF radar footprint area.

The most intense and homogeneous situation with prevailing south-easterly winds over the Bay of Biscay is given by WG8. This is strongly related to CG5 (a group with variable north-westward currents). These winds are also highly concurrent with the northward currents pattern represented by CG12, which is also related to WG 6-7 more variable southern winds, with a SE component within the HF radar footprint area. Amongst the WG with prevailing south-westerly winds WG3 is strongly concurrent (52.78 % of probability) with north-northestward currents of the CG3. Both wind and currents agree in direction; WG3 is represented by the most energetic wind field (mean velocities ~43 km • h^{-1}) and CG3 represents the second most intense current pattern

(mean velocities ~15 cm • s^{-1}). WG5 is the second most intense wind pattern. It is oriented predominantly to the SW, with a stronger western component (specially, in the HF radar area) and it is related to CG6. The currents in this group are eastward along the Spanish coast and they switch to the north-east in the east and north-east regions of the study area. With similar orientation to WG5, and with weaker velocities and higher occurrence probability, WG12, does not show joint occurrence probabilities over 25% with any of the CGs.

Finally, WG9 group represents the weakest wind field, with high spatial variability. WG9 is concurrent with CG10 (weak and very variable cyclonic circulation) with a value on the limit of the 90th percentile (22.3 %). It does not show any joint occurrence probability over 25% with any of the remaining CGs.

5.5.3. Current patterns with no connection to any wind group

Again, considering the limit of the 90th percentile, CG-1-2-8-10-11 current groups are not related to any wind group. All of them contain closed circulation patterns, with cyclonic polarity for CG-1-8-10-11 and anticyclonic polarity for CG2. CG-1-2-8-11 are markedly seasonal (cyclonic patterns are recurrent in winter and CG2 is observed more recurrently in the summer months), whilst CG 10, with a much weaker cyclonic pattern, does not show seasonal variability. Moreover, three of the four CG present a marked interannual variability. CG1-2-11 occur with more frequency during the first 2 years (2009-2010). CG8 has significant occurrence only during the winter months (January to March) of 2011 (Figure 51). Only CG10 appears recurrently over all the analyzed years.

5.5.4. IPC time series and connection to current groups

In the following section, the results of the KMA of surface currents in relation to the IPC time-series are presented. The IPC time series for the 2009-2012 period is shown in Figure 53. Individual daily estimations are characterized by red dots whilst monthly means of the corresponding red dots are characterized by the grey bars. Vertical dashed lines indicate February to November jumps within a year. Horizontal dashed lines are the 80th and 20th percentiles of the time series (deduced from the whole 1981-2012 time

series). Results in the 2009-2010 period are almost identical to those found in Esnaola *et al*. (2013), whilst those for the 2011-2012 are new. Negative phases of the IPC series (hereinafter IPC-1) represent favourable IPC conditions, while positive phases (IPC +1) indicate conditions not favouring strong IPC events. The time series suggests a strong negative phase of the IPC during the beginning of 2009, and a moderately positive one to the end of the same year. Two positive to negative transitions are observed both by the beginning and end of 2010. At the beginning of 2011 two positive phases together with some negative values are observed. Strong positive phase is observed to the end of 2011 and it remains during January 2012. It reverses toward negative values in February 2012. Finally, by the end of 2012 the series suggests two positive phases. However, due to a very cloudy period the number of estimations during this month is low.

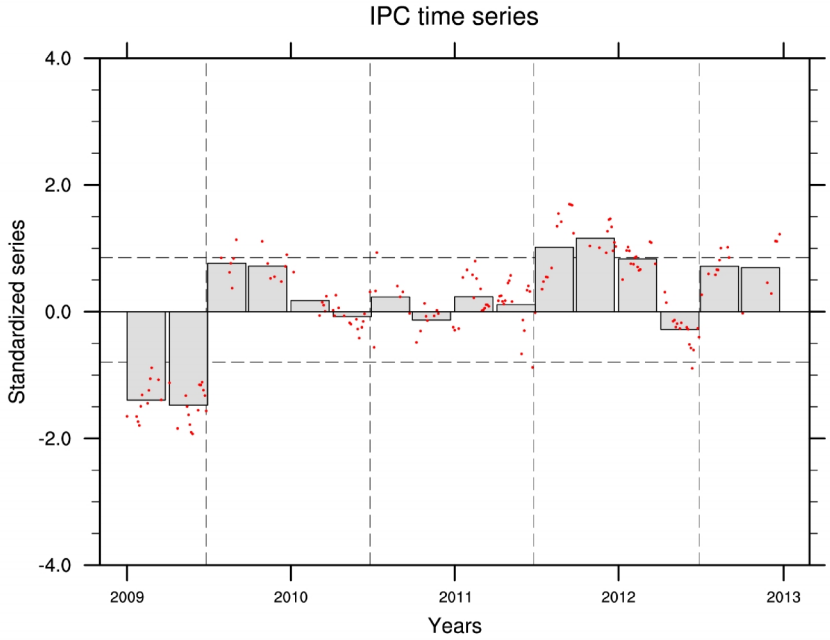

Figure 53: Time series of the surface signal of the IPC for the 2009-2012 period. Daily estimations are shown by the red dots whilst monthly averages are given the grey bars. Vertical dashed lies indicate the February to November transitions within a given year. The horizontal dashed lines indicate the 80th and 20th percentile of the IPC time series, computed over the whole 1981-2012 period.

Figure 54 shows the occurrence probabilities of the 12 current groups projected into the IPC –1 and +1 time step series. In the case of IPC -1 and representing IPC favourable conditions, CG1-5-11 show occurrence probabilities over 25%, whilst the remaining groups have low occurrence probabilities. CG1-11, have been characterized as current groups with no relation to wind groups and these results suggest their relation to the

IPC. CG5 also present stronger occurrences amongst the IPC -1 time steps. In the case for IPC +1 or conditions not indicating strong IPC, CG3-12 are the groups presenting higher occurrence probabilities. The similarities amongst CG-3-12 and CG1-11 are evident, since all these current groups represent cyclonic conditions in the study area. CG1-3 have much more intense currents oriented following the coast. Whilst CG1-11 depict closed mesoscale features and do not show any significant relation with any of the analysed wind groups, CG3 and 12 are related to south-easterly winter winds (WG 3-5).

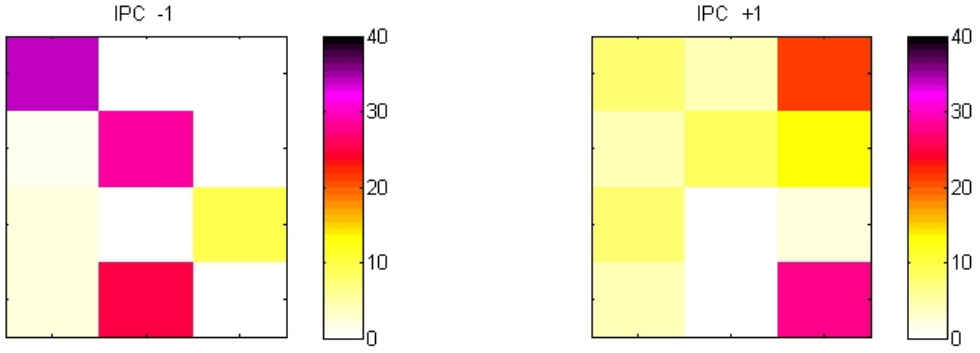

Figure 54: Occurrence probabilities of the 12 HF radar current groups (CG) projected into the IPC -1 and +1 time step series.

5.6. DISCUSSION

As summarized in Table 9, most of the possible wind scenarios in the study area are described in the 4 x 3 lattice of the KMA wind analysis (González *et al*., 2002, 2004). They agree with the seasonal winds described in previous works (González *et al*. 2004), with the most intense and south-westerly winds during autumn and winter and more variable north-easterly winds during spring and summer. In the same way, some of the previously known characteristics of the surface currents in the area (Le Cann and Serpette 2009; Rubio *et al*. 2013a; Solabarrieta *et al*. 2014) are described by the 12 current groups isolated by the KMA analysis. They show predominant eastwards currents in the Spanish shelf/slope and northwards current in the French shelf/slope in winter and much more variable westwards and southwestwards currents during summer.

Around 44% of the wind groups are prominently northern winds and around other 45% are prominently southern winds. The remaining 10% of occurrence is related to winds which are very variable in space and values, with a large variability over the Bay of Biscay domain.

Seasonal variability has been identified in several winter wind groups, being most of them predominantly southerly winds, with significant east-west variation. Variable westerly winds occur during or around summer months with a great presence of north winds (with east and west variation) with no apparent seasonality. The significant occurrence of northerly winds together with situation of southerly winds, during all the year, adds variability to the previously known seasonal patterns.

Analysing the interannual variability of the observed wind groups, there are no significant differences between the years to establish any interanuality. This lack of interannual variation could be related to the fact that the study is based in only 5 years data. It is worth noting that winter south-westerly intense winds situations, have higher occurrence during 2011-13.

Around 40% of the surface currents in the area are mainly represented by current groups with mean northward velocities and around 25% are classified into groups where southward surface currents prevail. Amongst the groups with mean northwards velocities, the ones with predominant north-eastwards currents and with currents oriented to the east (north) in the Spanish (French) shelf/slope, are the most intense (mean velocities of 15 and 10 cm • s^{-1}, respectively). The 2 groups with mean north-westwards currents show similar orientation and differ mainly in their intensity. The remaining (33%) surface currents registered by the HF radar system correspond to much more complex surface current patterns, showing cyclonic and anticyclonic features. The most intense currents are associated to one of these current groups presenting an intense cyclonic mesoscale circulation centred around 2.75ºW and 44ºN, and mean velocities ranging from 13.5 to 16 cm • s^{-1}.

Seasonal variability has been identified in 8 current groups with 55% of occurrence probability, whilst the remaining 4 groups with 45% of occurrence probability do not present clear seasonality. In the seasonal groups, two clear trends are observed,

anticyclonic currents around summer and cyclonic ones during winter months. Four of the five current groups showing closed circulation are affected by a seasonal variability. This result is coherent with the results of the EOF analysis applied to the same HF radar data set (period 2009-2011) in Solabarrieta *et al*. (2014), where the first mode of low-pass currents showed closed patterns with strong positive amplitude values (cyclonic circulation) in winter periods and negative amplitude values (anticyclonic circulation) in summer periods.

Interannual variability has been observed in cyclonic and anticyclonic currents. Cyclonic patterns, which do not show mesoscale cyclonic structures, have higher occurrences during 2011-13, whilst the current groups with closed cyclonic mesoscale structures have been more persistent during the first 2 years of the study period (2009-10). The anticyclonic summer pattern has also been more recurrent during 2009-10.

Although, it is known that the surface layer dynamics are strongly related to atmospheric forcing, the relation between spatially varying wind fields and observed surface ocean circulation is not always straightforward. The dispersion on the distribution of the joint occurrence probabilities of the current groups projected into the wind, highlight the complex relationships that can be established between the spatial patterns of these two variables in the study area. Strictly speaking, the probability of occurrence of winds and currents does not mean causality. For this reason, quantitative evaluation of the surface ocean response to the wind forcing cannot be derived from this analysis. In this sense, the results hereinafter are discussed on the light of these limitations and again only focusing on the strongest joint occurrences encountered between wind and current groups (values over the 90^{th} percentile).

Concerning the groups of north-eastern winds (all of them with similar mean direction and different mean intensity), they seem to be related to south-westward currents in agreement with the main wind's direction.

Amongst the predominantly north-western wind groups, high occurrences are obtained for different groups of prevailing south-eastward currents. From this analysis, a strong variability is encountered in the response to north-westerly prevailing winds depending on the spatial variability of the wind directions and intensity. For the most intense north-

western wind group, with highly homogeneous directions over the whole Bay of Biscay, the most probable current pattern shows south-eastwards currents over the French shelf. This situation indicates net transport towards the coast and southwards (eastwards) currents in the western (eastern) Basque Country coasts (surface currents which will favour downwelling conditions along French and Spanish coasts). Similar relation was observed by Fontán *et al*. (2013), for currents and winds over the study area. Then, for the most probable northwesterly wind pattern, represented by northerly wind, over the Bay of Biscay that switches to north-westerly winds over the HF radar footprint area two different responses in the surface currents are expected. On one hand, mainly oriented south-eastwards currents (in agreement with mean wind direction) and intensified eastward currents along the Spanish shelf/slope, are observed. On the other hand, the most probable current pattern results in south-westward surface currents indicating a larger scale response to wind forcing. This is in agreement with the expected orientation for vertically integrated currents within the Ekman layer. The most intense and homogeneous situation with prevailing south-easterly winds over the Bay of Biscay are related to variable north-westward currents and also to northward currents over the northwest area of the HF radar footprint. Northward currents are also expected with more variable southern winds. Prevailing south-westerly winds are strongly related to north-northeastward intense currents which agree in mean direction. However they present eastward (northward) orientation over the Spanish (French) shelf/slope. South-westerly winds that switch to western wind in the HF radar area are related to eastward currents along the Spanish coast. These currents switch to the north in the study area and are less intense than the previous north-northeastward currents. Finally, weak winds with high spatial variability are concurrent with weak very variable cyclonic circulation.

The observed winter current patterns showing cyclonic mesoscale features present no significant occurrence with the wind groups. These winter current groups present, moreover a marked interannual variability, being recurrent during the first 3 years of the analysed study period (2009-11) (i.e winters 2009-2010 and 2010-2011).

Also unrelated to any particular wind group, anticyclonic closed currents are recurrently observed in summer, and mostly during 2009 and 2010. Similar patterns where isolated by means of EOF analysis in Solabarrieta *et al*. (2014), for the period 2009-2011, and related to independent velocity measurements over the slope that showed coherent

currents affecting, at least, the first 100 m of the water column. This was especially clear during the winter months, when an intense circulation was observed over the slope.

The occurrence probabilities of the 12 current groups projected into the IPC –1 (strongest IPC favourable conditions) and +1 (weakest) time step series show a relation between the strongest IPC events with closed cyclonic currents which are not related to the wind. This result is in agreement with the interpretation made in Solabarrieta *et al*. (2014). It suggests that current groups showing the strongest closed cyclonic mesoscale structures in the study area (with eastwards currents in the Spanish shelf/slope and northward currents in the French shelf/slope), are related with favourable IPC conditions.

The occurrence probabilities of current groups into the IPC series, also relate the IPC +1 time steps (indicating weak IPC conditions), with cyclonic and not closed surface current circulation. Indeed, during the last 2 years, the two most probable winter current groups are related to prevailing intense south-western winds. These groups are the ones that show high occurrences with IPC+1 time steps. These wind groups are also characterized by strong cyclonic circulation, with no closed mesoscale features. It is worth noting that during this period (2012-2013) south-westerly winds, also present higher occurrences and intensity during winter months than in the period 2009-2011.

From the visual inspection of surface currents and their response to wind forcing, it is not uncommon to observe how any persistent mesoscale signal observed during calm conditions is quickly masked out after few hours of strong persistent local winds. For this reason, less frequent occurrences for current groups with closed circulation features during winters with higher occurrence probability of strong south-westerly winds, could be expected. These winds would favour more occurrence probability for not closed cyclonic current in CG3. However it is stirring that no occurrence of any of those groups is observed for 2012 and that only 4.5 % of occurrence is observed for group CG11 in 2013. The presence of mesoscale features in the area could be related to several forcing mechanisms (generation of mesoscale features has already been observed after strong wind-induced coastal jets in the area). The higher occurrences of the groups showing presence of mesoscale features in the radar footprint during the

years with positive IPC signal suggests that their formation could be favoured by strong slope current conditions. More analysis is needed to characterize these mesoscale patterns, their vertical extent, and duration and generation mechanisms. Their persistence in the study area, of several weeks for most of the observed events, suggests that they could have significant effects on the transport patterns in the area and on the vertical exchanges. Future research should focus on gathering more observational 3D data in the area to better understand the vertical structure and to provide evidences about their origin. Numerical modelling experiments could also help to elucidate the principal possible formation mechanisms.

Indeed, the KMA technique applied to HF radar hourly velocity fields has proved to be an interesting and useful technique to characterize the main ocean surface circulation and transport patterns in the area. The application of KMA to wind fields and the computation of joint occurrences of wind and current fields has provided an insight to the relationships between ocean surface currents and transport and wind fields. This technique and results are of special interest for model validation and to evaluate forecast skills wind forced numerical models.

The high variability in terms of surface current spatial patterns and of wind-current interactions suggests that the evaluation of transport processes in the area is not straightforward. Although, some mean conditions have been identified, which favour offshore or along shore coastal transport convergence situations. Future work, combining the use of lagrangian techniques with clustering methods will be of highest interest to provide a more deep insight into transport processes and connectivity in the area.

5.7. CONCLUSIONS

In this chapter it has been demonstrated that KMA clustering analysis for both, a multivariate predictor and predictand, and obtaining its probabilistic relationships is a useful classification technique tool. It has been used to extract winds and surface currents patterns in the Bay of Biscay, since the results obtained applying the technique agree with the previous knowledge of both wind and currents.

Most of the surface current groups or patterns (66%) obtained by means of KMA clustering are clearly related to specific wind patterns recurrent in the study area However, there are some current patterns, which are not clearly related to the winds. These are closed patterns occurring during winter months, whose generation can be also related or favored by other mechanisms

During summer months, the typical current pattern is an antyciclonic closed pattern without any relation to the prevailing winds. During winter months cyclonic circulation prevails. Nevertheless, significant internal variability in the surface circulation patterns can be observed. During winters 2011-2013, with strong south-southwestern winds, cyclonic surface circulation is observed. During the winters 2009-2011, characterized by less intense southwesterlies, the winter circulation patterns are similar. However, they present closed cyclonic mesoscale structures, in accordance to observations in previous studies by Solabarrieta (2011) and Solabarrieta *et al*. (2014).

More studies are needed to understand the 3D characteristics of the circulation in the area; specifically of the mesoscale structures observed during some winter and summer periods. This study provides a comprehensive description of surface ocean current patterns and their variability in relation to some of the main forcings in the area. It highlights the potential of this technique applied to HF radar data for model validation and further research of surface ocean transport paths.

CHAPTER VI

CONCLUSIONS AND FUTURE RESEARCH

A HF radar system has been working operationally in the SE Bay of Biscay since 2009. The resulting data, for 2009-2013, have been used in this thesis, to study the surface ocean dynamics and surface circulation patterns in the area. Satisfactory validation of HF radar data with *in-situ* data supports the present findings. Also, the data set used properly suites the purpose of this PhD thesis, since it adequately reproduces the known main characteristics of the spatio-temporal variability of the surface circulation in the study area.

6.1. CONCLUSIONS

- HF radar technology has been used successfully all around the world for more than three decades to study surface ocean processes. This PhD thesis provides further evidence of the advantages of this technology for improving knowledge and monitoring of coastal ocean areas.
- The agreement between the different available measurements and HF radar data is reasonably good, and data comparison results are consistent with those described previously by several authors. It is worth to note the comparisons in terms of spectral energy contents at the tidal and inertial bands performed, since they demonstrate the ability of the HF radar to measure the previously described spatial variability at these temporal scales. These comparisons reinforce the confidence in HF radar data to analyse the surface circulation in the SE Bay of Biscay and to give a new insight into the currents and their spatio-temporal variability.
- Different methodologies have been applied to HF radar data (e.g. EOF, KMA) and it has been demonstrated that they are useful analysis tools to extract surface current patterns and to study the different spatio-temporal scales. Taking into account the significant differences amongst them, the agreement in the results obtained by both approaches (note that EOFs provide theoretic mathematical patterns whilst KMA clustering technique classifies real observed patterns) reinforces the confidence in the methodology used in the thesis. It has also been demonstrated that the strategy of using KMA clustering analysis independently for predictor (wind) and predictand (currents) variables to subsequently obtain probabilistic relationships is an interesting approach to study surface ocean dynamics in the area.
- The results reveal the continuity of the along shelf/slope surface circulation in the SE corner of the Bay of Biscay, with east-west (north-south) surface circulation in front of the Spanish (French) coast, with a marked seasonality, in accordance to the previous observations. The current circulates eastward (north) over the slope off the Spanish (French) coast in winter, with speeds reaching up to 70 cm·s-1. In summer, the water circulation is reversed and has intensities 3 times

weaker than those observed in winter, with predominant westward currents over the Spanish slope.

- Vertically, the good agreement between surface HF radar data and deeper ADCP data, suggests that, most of the time, the most intense surface currents over the slope have a clear vertical signal affecting, at least, the first 100 m of the water column.
- The presence and persistence of eddy mesoscale circulations within the area has been observed, with cyclonic structures in winter and anticyclonic mesoscale eddies during summer.
- Most of the surface current patterns (66%) observed are clearly related to specific wind patterns, recurrent in the study area. However, there is high variability in terms of surface current spatial patterns and of wind–current interactions.
- Several current patterns not as clearly related with specific wind conditions have also been identified. These are patterns showing closed cyclonic circulation features with higher occurrence during winter months. These winter currents, with an along-slope circulation clearly intensified over the upper part of the slope, are the strongest westerly currents observed over the slope. Their higher occurrence during periods of winter along-slope currents (IPC) intensification is demonstrated. The presence of these patterns is, in consequence, related to the surface signature of the slope current (IPC) and its marked seasonality.
- Globally, inertial currents represent from 10 to 40% of the total variability, being their contribution significantly higher in summer. Spatially, their distribution presents an energy maximum over the deeper part of the slope in winter and centred around 44ºN and 2º 30'W in summer. Tides contribute much less to the total KE, mainly over the shelf, although their contribution can be higher than that of inertial oscillations during winter.
- Interannual variability has been observed in cyclonic and anticyclonic currents. Cyclonic patterns which do not show mesoscale cyclonic structures, have higher occurrences during 2011-13 whilst the current groups with closed cyclonic mesoscale structures have been more persistent during 2009-10. The anticyclonic summer pattern has also been more recurrent during 2009-10. (It

worth noting that this study is based in only 5 years of available data, the study of interanual variability being, thus, limited).

- Globally, the results obtained provide an insight to the global spatio-temporal complexity of the surface circulation in the study area and, thus, to the complexity and variability of the corresponding ocean surface transport paths in the area. Understanding and monitoring surface ocean transport is key for an improved management of coastal ocean related to different issues, as marine pollution and marine safety. Taking into account the complexity of circulation processes and transport patterns, it worth noting the potential benefits of HF radar to the integrated management of the study area. Indeed, the results in terms of lagrangian predictability point the benefits of using HF radar data to generate trajectories for search and rescue exercises, since they considerably improve the present search radius used in the study area for these operations.
- OMA technique is used to fill gaps in HF radar derived currents in order to make them more suitable for management purposes. The approach is based on physical theoretic modes of the currents and, thus, the resulting fields have higher inaccuracies. However, the small differences with total currents in terms of lagrangian predictability suggest that no-gap OMA surface current fields are more suited to operational trajectory and transport estimations.

6.2. FUTURE RESEARCH

The analysis carried out in this thesis is focused on improving our understanding of surface water circulation in the SE Bay of Biscay. Indeed, the 5 years of available data have provided an invaluable new insight into the surface circulation patterns in the study area. The ongoing addition of HF radar data to the present data set will permit in the future the analysis of additional processes, such as: the observed interannual variability of surface currents, and to obtain enhanced statistical description of the currents (i.e. long-term and extreme value distributions). Specifically, an extended data series covering more years will also permit the analysis of the relation of the variability of currents over the Bay of Biscay slope circulation to remote oscillations

Further research is needed to understand the physical mechanisms driving the previously described circulation patterns and also to evaluate their contribution to the total variance of the regional circulation. This thesis has focussed on analysing and describing current variability in a wide range of scales. Using similar approaches (i.e. KMA analysis) in combination with filtering techniques that permit to isolate specific scales (i.e. mesoscale) within HF radar currents is one of most promising future research lines. Likewise more research is also needed to understand the 3D characteristics of the circulation in the area, specifically of the mesoscale structures observed during some winter and summer periods. For this purpose, HF radar data could be analysed together with buoys at different depths, in order to explore 3D circulation.

Although near-real time total and OMA currents are suitable to use in operational purposes, the best suited products for search and rescue and marine pollution related situations should be based on forecasts. In this sense, we are presently working on the methodology described by Frolov *et al*. (2012) to provide short-term prediction (48 hours) of the surface currents only based on past and near-real time HF radar currents. Obtained results are promising, although this study has not been included in this manuscript since more analysis is required to its validation and implementation to the integrated management in the study area.

Applying ocean and coastal circulation models is, as well, a common practice to provide operational forecasts. In the Bay of Biscay, there are several operational modelling systems providing daily forecast of currents (amongst other variables) as input for oil spill models, for the study of river plumes, water quality models, biological models, etc. Having a long, high resolution and reliable database of HF radar derived surface currents represents an invaluable opportunity to increase the quality of these products through a better understanding of oceanic circulation processes and model calibration and validation. Finally, the operational assimilation of near-real time surface currents into coastal ocean models is other of the expected benefits of this technology in the area.

Bibliography

Abascal, A. J., Castanedo, S., Medina, R., Losada, I. J., Álvarez-Fanjul, E., 2009. Application of HF radar currents to oil spill modeling. Marine Pollution Bulletin, 58(2), 238-248.

Abascal, A., Castanedo, S., Fernández, V., Medina, R., 2012. Backtracking drifting objects using surface currents from high-frequency (HF) radar technology. Ocean Dynamics, 62, 7, 1073-1089.

Álvarez, I., Gomez-Gesteira., M., de Castro, M., Carvalho, D., 2014. Comparison of different wind products and buoy wind data with seasonality and interanual climate variability in the southern Bay of Biscay (2000-2009). Deep-Sea Research II, 106, 38-48.

Alvera-Azcárate, A., Barth, A., Rixen, M., Beckers, J.M., 2005. Reconstruction of incomplete oceanographic data sets using empirical orthogonal functions: application to the Adriatic Sea surface temperature, Ocean Modelling, 9, 325–346.

Alvera-Azcárate, A., Barth, A., Sirjacobs, D., Beckers, J.M., 2009. Enhancing temporal correlations in EOF expansions for the reconstruction of missing data using DINEOF, Ocean Science, 5, 475– 485, doi:10.5194/os-5-475-2009.

Bardey, P., Garnesson P., Moussu G., Wald L., 1999. Joint analysis of temperature and ocean colour satellite images for mesoscale activities in the Gulf of Biscay. International Journal of Remote Sensing, 7, 1329-1341.

Barrick, D. E., Evans M. W., Weber B.L., 1977. Ocean surface currents mapped by radar. Science, 198, 138-144.

Barrick, D E. and Lipa, B.J., 1986. Correcting for distorted antenna patterns in CODAR ocean surface measurements. IEEE Journal of Oceanic Engineering, OE-11, 304-309.

Beckers, J. M. and Rixen, M., 2003. EOF calculations and data filling from incomplete oceanographic datasets, Journal of Atmospheric and Oceanic Technology, 20, 1839-1856.

Benson, D.J, 1992. "Computational methods in lagrangian and eulerian hydrocodes," Computer Methods in Applied Mechanics and Engineering., 99 (2–3), 235-394.

Blanton, J.O., Atkinson, L.P., Fernández, F., Castillejo, F., Lavín, A., 1984. Coastal upwelling off the Rias Bajas. Galicia, northwest Spain. I. Hydrographic studies. Rapports et Procès-Verbaux des Réunions du Conseil International pour l'Exploration de la Mer, 183, 79-90.

Breivik, Ø, Allen, A.A., Maisondieu, C., Olagnon, M., 2013. Advances in Search and Rescue at Sea. Ocean Dynamics, 63, Issue 1, 83-88. doi:10.1007/s10236-012-0581-1.

Caballero, A., Pacual, A., Dibarboure, G., Espino, M., 2008. Sea level and Eddy Kinetic Energy variability in the Bay of Biscay, inferred from satellite altimeter data. Journal of Marine Systems, 72, 116-134.

Caballero, A., Ferrer, L., Rubio, A, Charria, G, Taylor, B. H., Grima, N., 2014. Monitoring of a quasi-stationary eddy in the Bay of Biscay by means of satellite, in situ and model results, Deep- Sea Research II, http://dx.doi.org/10.1016/j.dsr2.2013.09.029.

Camus, P., Mendez, F.J., Medina, R., Cofiño, A.S., 2011: Analysis of clustering and selection algorithms for the study of multivariate wave climate. Coastal Eng., 58, 453–462, doi:10.1016/j.coastaleng.2011.02.003.

Charria, G., Lazure, P., Le Cann, B., Serpette, A., Reverdin, G., Louazel, S., Batifoulier, F., Dumas, F., Pichon, A., Morel, Y., 2013. Surface layer circulation derived from lagrangian drifters in the Bay of Biscay, Journal of Marine Systems, 109-110, S060-076. doi:10.1016/j.jmarsys.2011.09.015.

Crombie, D.D., 1955. Doppler spectrum of sea echo at 13.56 Mc/s. Nature, 175, 681-682.

Emery, W.J. and Thomson, R.E., 2001. Data Analysis Methods in Physical Oceanography. Amsterdan, Elsevier Science.

Emery, B.M., Washburn, L., Whelan, C., Barrick, D., Harlan, J., 2014. Measuring Antenna Patterns for Ocean Surface Current HF Radars with Ships of Opportunity. Journal of Atmospheric and Oceanic Technology, 31, 1564–1582.

Esnaola, G., Sáenz, J., Zorita, E., Lazure, P., Ganzedo, U., Fontán, A., Ibarra-Berastegi, G., Ezcurra, A., 2013. Coupled air-sea interaction patterns and surface heat-flux feedback in the Bay of Biscay, Journal of Geophysical Research-Oceans, 117, C06030, doi:10.1029/2011JC007692.

Espejo, A., Camus, P., Losada, I.J., Méndez, F.J., 2014. Spectral Ocean Wave Climate Variability Based on Atmospheric Circulation Patterns. Journal of Physical Oceanography, 44 (8), 2139-2152.

Ferrer, L., González, M., Cotano, U., Uriarte, A., Sagarminaga, Y., Santos, M., Uriarte, Ad., Collins, M., 2004. "Physical controls on the evolution of anchovy in the Bay of Biscay: a numerical approximation," ICES Annual Science Conference, 22-25 September 2004, Vigo, Spain, 20pp.

Ferrer, L., Fontán, A., Mader, J., Chust, G., González, M., Valencia, V., Uriarte, Ad., Collins, M.B., 2009. Low-salinity plumes in the oceanic region of the Basque Country. Continental Shelf Research, 29, 970-984.

Ferrer, L., Liria, P., Bolaños, R., Balseiro, C., Carracedo, P., González-Marco, D., González, M., Fontán, A., Mader, J., Hernández, C., 2010. Reliability of coupled meteorological and wave models to estimate wave energy resource in the Bay of Biscay. In: Proceedings of the 3rd International Conference on Ocean Energy (ICOE), 6-8 October 2010, Bilbao, Spain, 6 pp.

Fontán, A., 2009. Physical processes governing water circulation in the southeastern limit of the Bay of Biscay. University of Southampton, MPhil thesis in Physical Oceanography, 136 pp.

Fontán, A., González, M., Wells, N., Collins, M., Mader, J., Ferrer, L., Esnaola, G., Uriarte, Ad., 2009. Tidal and wind-induced circulation within the southeastern limit of the Bay of Biscay: Pasaia Bay, Basque coast. Continental Shelf Research, 29 (8), 998-1007.

Fontán, A., Esnaola, G., Sáenz, J., González, M., 2013. Variability in the air–sea interaction patterns and time-scales within the Southeastern Bay of Biscay, as observed by HF radar data, Ocean Science, 9, 1-12, doi:10.5194/osd-9-1-2012.

Frolov S., Paduan J.D., Cook, M., Bellingham, J., 2012. Improved statistical prediction of surface currents based on historic HF-radar observations. Ocean Dynamics, 62, Issue 7, 1111-1122.

Frouin, R., Fiúza, A.F.G., Âmbar, I., Boyd, T.J., 1990. Observations of a poleward surface current off the coasts of Portugal and Spain during winter. Journal of Geophysical Research, 95(C1), 679-691.

Ganzedo, U., Alvera-Azcárate, A., Esnaola, G., Ezcurra, A., Sáenz, J., 2011. Reconstruction of sea surface temperature by means of DINEOF: a case study during the fishing season in the Bay of Biscay. International Journal of Remote Sensing, 32, 933–950.

García-Soto, C., 2004. Prestige Oil Spill and Navidad flow. Journal of the Marine Biological Association of the U.K., 84, 297-300.

García-Soto, C., Pingree, R.D., Valdés, L., 2002. Navidad Development in the Southern Bay of Biscay: Climate change and swoddy structure from remote sensing and in situ measurements. Journal of Geophysical Research, 107(C8), 3118, doi:10.1029/2001JC001012.

García-Soto, C. and Pingree, R.D, 2012. Atlantic Multidecadal Oscillation (AMO) and sea surface temperature in the Bay of Biscay and adjacent regions. Journal of the Marine Biological Association of the United Kingdom, 92, pp 213-234 doi:10.1017/S0025315410002134.

Gil, J. and Sánchez, R., 2001. ¿Es determinante la dinámica en los niveles superiores de la columna de agua sobre la abundancia y distribución de peces en el mar Cantábrico? Física de la Tierra, 13, 55-70.

González, M., Gyssels, P., Mader, J., Fontán, A., Del Campo, A., Uriarte, A., 2002. Estudio de la dinámica marina y del medio físico de la costa comprendida entre Donostia-San Sebastián y Baiona. Diputación Foral de Gipuzkoa.

González, M., Uríarte, A., Fontán, A., Mader, J., Gyssels, P, 2004. Chapter 6, Marine dynamics. Borja A. y Collins M. (Eds.). Oceanography and Marine Environment of

the Basque Country, Elsevier Oceanography Series nº 70, 133-157, Elsevier, Amsterdam.

González, M., Ferrer, L., Fontán, A., Rubio, A., Mader, J. Del Campo, A., Liria, P., Hernández, C., Cuesta, L., Berregui, J., Uriarte, Ad., Collins, M., 2009. Explosive cyclogenesis of extra-tropical cyclone Klaus and its impact on the water column stability in the Bay of Biscay. GLOBEC International Newsletter, 15(2), 59(S).

González-Pola, C., Ruiz-Villarreal, M., Lavín, A., Cabanas, J.M., Alvarez-Fanjul, E., 2005. A subtropical water intrusion spring-event in the shelf-slope of the south western Bay of Biscay after strong wind-forcing pulses. Journal of Atmospheric and Ocean Science 10, 343-359.

Gough, M. K., Garfield, N., McPhee-Shaw, E., 2010. An analysis of HF radar measured surface currents to determine tidal, wind-forced, and seasonal circulation in the Gulf of the Farallones, California, United States. Journal of Geophysical Research, 115(C4), C04019.

Guanche, Y., Mínguez, R., Méndez, F.J., 2013. Autoregressive logistic regression applied to atmospheric circulation patterns. Climate Dynamics 42, 537–552. Doi: 10.1007/s00382-013-1690-3.

Gurgel, K.W., Essen, H.H., Schlick, T., 2001. The University of Hamburg WERA HF Radar - Theory and Solutions. First International Radiowave Oceanography Workshop, ROW 2001, Proceedings.

Hastie, T., Tibshirani R., Friedman J., 2001. The Elements of Statistical Learning: Data Mining, Inference, and Prediction. Springer, 533 pp.

Haynes, R. and Barton, E.D., 1990. A poleward flow along the Atlantic coast of the Iberian Peninsula. Journal of Geophysical Research, 95(C7), 11425-11441.

Helzel, T., Kniephoff, M., Petersen, L., 2006. WERA: Remote Ocean Sensing for Currents, Waves and Wind Direction. Introduction to the Principle of Operation. http://www.helzel.com/files/432/upload/Papers/WERA-Basics-Paper-6605.pdf

Ibáñez, M., 1979. Hydrological studies and surface currents in the coastal area of the Bay of Biscay. Lurralde, 2, 37-75.

Kaihatu, J.M., Handler R.A., Marmorino G.O. and Shay, L.K., 1998. Empirical Orthogonal Function Analysis of Ocean Surface Currents Using Complex and Real-

Vector Methods. Journal of Atmospheric and Oceanic Technology (American Meteorological Society), 15. Issue 4, 927-941.

Kaplan, D.M., Largier, J., Botsford, L.W., 2005. HF Radar observations of surface circulation off Bodega Bay (northern California, USA). Journal of Geophysical Research, 110, C10020, doi:10.1029/2005JC002959.

Kaplan, D. M. and Lekien, F., 2007. Spatial interpolation and filtering of surface current data based on open-boundary modal analysis. Journal of Geophysical Research-Oceans 112(C12). doi:10.1029/2006JC003984.

Kohut, J.T., Glenn, S.M., 2003. Improving HF Radar Surface Current Measurements with Measured Antenna Beam Patterns. Journal of Atmospheric and Oceanic Technology, 20(9), 1303-1316.

Kohut, J.T., Roarty, H.J. and Glenn S.M., 2006. Characterizing Observed Environmental Variability with HF Doppler Radar Surface Current Mappers and Acoustic Doppler Current Profilers: Environmental Variability in the Coastal Ocean. IEEE Journal of Oceanic Engineering, 31, No. 4, October 2006, 876-884.

Kosro, P.M., 2005. On the spatial structure of coastal circulation off Newport, Oregon, during spring and summer 2001 in a region of varying shelf width. Journal of Geophysical Research, 110, C10S06, doi:10.1029/2004JC002769.

Koutsikopoulos, C. and Le Cann, B., 1996. Physical processes and hydrological structures related to the Bay of Biscay anchovy. Scientia Marina, 60 (Supl. 2), 9-19.

Lavín, A., Valdés L., Gil J., Moral M., 1998. Seasonal and interannual variability in properties of surface water off Santander (Bay of Biscay) (1991-1995). Oceanologica Acta, 21(2), 179-190.

Lavín, A., Valdes L., Sánchez F., Abaunza P., Forest A., Boucher J., Lazure P., Jegou A.M., 2006. The Bay of Biscay: the encountering of the ocean and the shelf. En: Robinson A.R. y Brink K. (Eds.). The Sea, 14B: The Global Coastal Ocean. Interdisciplinary Regional Studies and Syntheses. Harvard University Press, 933-1001.

Laws, K., 2001. Measurements of near surface ocean currents using HF radar. M.S. thesis, University of California.

Lazure, P., 1997. La circulation des eaux dans le Golfe de Gascogne. En: 10émes rencontres interregionales de l´AGLIA. Saint Jean de Luz, 83-88.

Lazure, P. and Jégou, A.M., 1998. 3D modelling of seasonal evolution of Loire and Gironde plumes on Biscay Bay continental shelf. Oceanologica Acta, 21(2), 165-177.

Le Boyer, A., Charria, G., Le Cann, B., Lazure, P., Marie, L., 2013. Circulation on the shelf and the upper slope of the Bay of Biscay. Continental Shelf Research, 55, 97-107.

Le Cann, 1990. Barotropic tidal dynamics of the Bay of Biscay Shelf: observations, numerical modelling and physical interpretation. Continental Shelf Research, 10(8), 723-758.

Le Cann, B. and Serpette, A., 2009. Intense warm and saline upper ocean inflow in the southerna Bay of Biscay in autumn-winter 2006-2007. Continental Shelf Research, 29, 1014-1025.

Lekien, F., Coulliette, C., Bank, R., Marsden, J., 2004. Open-boundary modal analysis: Interpolation, extrapolation, and filtering, 2004. Journal of Geophysical Research, 109, C12004, doi:10.1029/2004JC002323.

Liu, Y., Weisberg, R.H., Shay L. K., 2006. Current Patterns on the West Florida Shelf from Joint Self-Organizing Map Analyses of HF Radar and ADCP Data. Journal of Atmospheric and Oceanic Technology, 24(4), 702-712.

Liu, Y., Weisberg, R.H., Merz, C. R., 2014. Assessment of CODAR SeaSonde and WERA HF Radars in Mapping Surface Currents on the West Florida Shelf. Journal of Atmospheric and Oceanic Technology, 31, 1363-1382.

Lomb, N.R., 1976. Least-squares frequency analysis of unequally spaced data. Astrophysics and Space Science, 39, 447-462.

Lorente, P., Piedracoba, S., Álvarez Fanjul, E., 2015. Validation of high-frequency radar ocean surface current observations in the NW of the Iberian Peninsula. Continental Shelf Research, 92, 1-15.

Maillard, C., 1986. Atlas Hydrologique de l´Atlantique Nord-Est. IFREMER, Brest, 260 pp.

North, G.R., Bell, T.L., Cahalan, R.F., Moeng, F.J., 1982. Sampling errors in the estimation of empirical orthogonal functions. Monthly Weather. Review 110, 699-706.

Ohlmann, C., White, P., Washburn, L., Emery, B., Terrill, E., Otero, M., 2007. Interpretation of Coastal HF Radar–Derived Surface Currents with High-Resolution Drifter Data. Journal of Atmospheric and Oceanic Technology, 24(4), 666-680.

OSPAR, 2000. OSPAR Quality Status Report 2000, Region IV. Bay of Biscay and Iberian Coast. OSPAR Commission, London, 134 pp.

Paduan, J.D. and Rosenfeld, L.K., 1996. Remotely sensed surface currents in Monterey Bay from shore-based HF radar (Coastal Ocean Dynamics Application Radar. Journal of Geophysical Research, 101(C9), 20669-20686.

Paduan, J.D. and H.C. Graber, 1997. Introduction to high-frequency radar: Reality and myth, Oceanography, 10, 36-39.

Paduan, J.D. and Washburn, L. HFR observation of Ocean Surface Currents, 2013. Annual Review of Marine Science, 5,115-36.

Peliz, A., Dubert, J., Haidvogel, D. B., Le Cann, B., 2003. Generation and unstable evolution of a density-driven Eastern Poleward Current: The Iberian Poleward Current, Journal of Geophysical Research-Oceans, 108, 3268, doi:10.1029/2002JC001443.

Pingree, R.D., 1993. Flow of surface waters to the west of the British Isles and in the Bay of Biscay. Deep Sea Research II, 40(12), 369-388.

Pingree, R.D., 1997. The eastern Subtropical Gyre (North Atlantic): Flow Rings Recirculations Structure and Subduction. Journal of the Marine Biological Association of the U.K., 78, 351-376.

Pingree, R.D. and Le Cann, B., 1990. Structure, strength and seasonality of the slope currents in the Bay of Biscay region. Journal of the Marine Biological Association of the U.K., 70, 857-885.

Pingree, R.D. and Le Cann, B., 1992a. Anticyclonic Eddy X91 in the Southern Bay of Biscay, May 1991 to February 1992. Journal of Geophysical Research, 97(C9), 14353-14367.

Pingree, R.D. and Le Cann, B., 1992b. Three anticyclonic Slope Water Oceanic eDDIES (SWODDIES) in the southern Bay of Biscay in 1990. Deep-Sea Research, 39, 1147-1175.

Pollard, R.T., Griffiths, M.J., Cunningham, S.A., Reid, J.F., Perez, F.F., Rios, A., 1996. Vivaldi 1991 - A study of the formation, circulation, and ventilation of Eastern North Atlantic Central Water. Progress in Oceanography, 37, 167-192.

Press, W.H., Flannery, B.P., Teulosky, S.A. and Vettelrling, W.T., 1989. Numerical Recipes. Cambridge University Press, 702 pp.

Reverdin, G., Marié, L., Lazure, P., d'Ovidio, F., Boutin, J., Testor, P., Martin, N., Lourenco, A., Gaillard, F., Lavín, A., Rodriguez, C., Somavilla, R., Mader, J., Rubio, A., Blouch, P., Rolland, J., Bozec, Y., Charria, G., Batifoulier, F., Dumas, F., Louazel, S., Chanut, J., 2013. Freshwater from the Bay of Biscay shelves in 2009, Journal of Marine Systems, 109–110, Supplement, January 2013. Pages S134-S143, ISSN 0924-7963, http://dx.doi.org/10.1016/j.jmarsys.2011.09.017.

Rubio, A., Reverdin, G., Fontán, A., González, M., Mader, J., 2011. Mapping near-inertial variability in the SE Bay of Biscay from HF radar data and two offshore moored buoys. Geophys. Res. Lett., 38(19), L19607.

Rubio, A., Fontán, A., Lazure, P., González, M., Valencia, V., Ferrer, L., Mader, J., Hernández, C., 2013a. Seasonal to tidal variability of currents and temperature in waters of the continental slope, southeastern Bay of Biscay. Journal of Marine Systems, 109-110, S121-S133.

Rubio, A., Solabarrieta, L., González, M., Mader, J., Castanedo, S., Medina, R., Charria, G., Aranda, J. A. 2013b. Surface circulation and lagrangian transport in the SE Bay of Biscay from HF radar data. OCEANS - Bergen, 2013 MTS/IEEE. doi: 10.1109/OCEANS-Bergen.2013.6608039.

Sánchez, F. and Olaso, I., 2004. Effects of fisheries on the Cantabrian Sea shelf ecosystem. Ecological Modelling, 172 (2-4), 151-174.

Saunders, P.M., 1982. Circulation in the Eastern North Atlantic. Journal of Marine Research, 40, 641-657.

Scargle, J., 1982. Studies in astronomical time-series analysis. II - Statistical aspects of spectral analysis of unevenly spaced data. The Astrophysical Journal, 263, 835-853.

Schmidt, R.O., 1986. Multiple emitter location and signal parameter estimation. IEEE Transactions Antennas Propagation., AP-34, 276-280.

Schaeffer, A., Molcard, A., Forget, P., Fraunié, P., Garreau, P., 2011. Generation mechanisms for mesoscale eddies in the Gulf of Lions: radar observation and modeling. Ocean Dynamics, 61(10), 1587-1609.

Serpette, A., Le Cann, B., Dolas, F., 2006. Lagrangian circulation of the North Atlantic Central Water over the abyssal plain and continental slopes of the Bay of Biscay: description of selected mesoscale features. Scientia Marina, 70(S1), 27-42.

Skamarock, W.C., Klemp, J.B., Dudhia, J., Gill, D., Barker, D., Wang, W., Powers, J.G, 2005. A description of the Advanced Research WRF Version 2, NCAR Technical Note NCAR/TN-468+STR.

Smith, N.P., 1981. An investigation of seasonal upwelling along the Atlantic coast of Florida. Proc. 12th Internat. Liege Colloque Ocean Hydrodynamics, 79-98.

Solabarrieta, L., 2011. Patrones medios mensuales de la corriente superficial obtenidos a partir de datos de radar HF en el sureste del Golfo de Bizkaia. University Master Thesis, Cantabrian University.

Solabarrieta, L., Rubio A., Castanedo S., Medina R., Charria G. and Hernández C., 2014. Surface water circulation patterns in the southeastern Bay of Biscay: New evidences from HF radar data. Continental Shelf Research 74, 60-76.

Solabarrieta, L., Rubio, A., Cárdenas, M., Castanedo, S., Esnaola, G., Méndez, F.J., Medina, R., Ferrer, L. Probabilistic relationships between wind and surface water circulation patterns in the SE Bay of Biscay. Submitted to Ocean Dynamics.

Solabarrieta, L., Cook, M., Frolov, S., Paduan, J., Rubio, A., Charria, G. Comparison of real drifters and simulated trajectories using differently processed HF radar data in the Bay of Biscay. In preparation.

Somavilla, R., González-Pola, C., Rodriguez, C., Josey, S.A., Sánchez, R.F., Lavín, A., 2009. Large changes in the hydrographic structure of the Bay of Biscay after the extreme mixing of winter 2005. Journal of Geophysical Research, c01001.

Somavilla, R., González-Pola, C., Lavín, A., Rodríguez, C., 2013. Temperature and salinity variability in the south-eastern corner of the Bay of Biscay (NE Atlantic).

Journal of Marine Systems, 109-110, S105-S120. doi:10.1016/j.jmarsys.2012.02.010

Thompson, K. R., Sheng J., Smith P.C., Cong L., 2003. Prediction of surface currents and drifter trajectories on the inner Scotian Shelf, Journal of Geophysical Research, 108(C9), 3287, doi:10.1029/2001JC001119.

Ullman, D. S., O'Donnell J., Kohut J., Fake T., Allen A., 2006. Trajectory prediction using HF radar surface currents: Monte Carlo simulations of prediction uncertainties, Journal of Geophysical Research, 111, C12005, doi:10.1029/2006JC003715.

Valdés, L. and Lavín, A., 2002. 10 Dynamics and human impact in the Bay of Biscay: An ecological perspective. Large Marine Ecosystems, 10, 293-320.

Valencia, V., Franco J., Borja Á., Fontán A., 2004. Hydrography of the southeastern Bay of Biscay. En: Borja Á. y Collins M. (Eds.), Oceanography and Marine Environment of the Basque Country. Elsevier Oceanography Series nº 70, Elsevier, Amsterdam, 159-194.

van Aken, H.M., 2002. Surface currents in the Bay of Biscay as observed with drifters between 1995 and 1999. Deep Sea Research. I, 49, 1071-1086.

von Storch, H. and Zwiers, F. W., 2004. Statistical Analysis in Climate Research. Cambridge University Press.

Whelan, C.W., Barrick, D.E., Lilleboe, P.M., Kjelaas, A., Breivik, Ø., Fernandez, V., Alonso-Martirena A., 2010. Rapid Deployable HF Radar for Norwegian Emergency Spill Operations. Oceans 2010 IEEE, 1 -3.

Wilks, D.S., 2006. Statistical Methods in the Atmospheric Sciences, in: International Geophysics Series, 59, Academic Press, doi:10.1002/met.16, 2006.

Wooster, W, Bakun, A., Mclain, D.R.., 1976. Seasonal upwelling cycle along eastern boundary of North Atlantic. Journal of Marine Research, 34, 131-141.

Wyatt, L.R., Atwater, D., Prytz, A., Rehder, S., 2013. A comparison between SeaSonde and WERA HF radar current measurements. OCEANS - Bergen, 2013 MTS/IEEE.

Wyatt, L.R., 2014, "High frequency radar applications in coastal monitoring, planning and engineering", Australian Journal of Civil Engineering, 12(1).